Synthesis and Characterization of Structurally Well-Defined Polymer-Layered Silicate Nanocomposites

Qinghui Mao

Department of Chemistry

University of Mainz

Max-Planck-Institute for Polymer Research

A thesis submitted for the degree of

Ph.D. Thesis

Submit date: January 22, 2007

Abstract

Polymer-layered silicate (PLS) nanocomposites are often based on natural clays such as montmorillonite. In EPR and NMR studies of the surfactant layer that compatibilizes the silicate and the polymer, we found that the iron content in these natural clays is detrimental, as it broadens spectra and shortens relaxation times. The problem was overcome by using as a layered silicate iron-free and structurally well defined magadiite, which was synthesized by a hydrothermal method. The morphology of the magadiite and the extent of intercalation in melt-prepared polymer-organo-magadiite nanocomposites were characterized by scanning electron microscopy (SEM) and wide-angle x-ray scattering (WAXS) respectively. Among different types of polymers, those with carbonyl groups appear to intercalate more easily. With iron-free magadiite, polycaprolactone (PCL) was found to intercalate into both ammonium surfactant modified and phosphonium surfactant modified organomagadiites. By using site-specific nitroxide spin probes and applying CW EPR (Continuous Wave Electron Paramagnetic Resonance) and pulse EPR techniques the dynamics and spatial structure of surfactant layers in such nanocomposites, were studied. Static ^{2}H Nuclear Magnetic Resonance (NMR) on specifically deuterated cationic surfactants was also applied to access surfactant motion on a complementary time scale (milliseconds to microseconds) compared to EPR (nanoseconds).

By CW EPR and ^{2}H NMR, fast motion of surfactant layers was found to be pronounced by intercalation of PCL while it diminishes in non-intercalated microcomposites with polystyrene (PS). The rotational correlation times τ_c and activation energies E_a reveal different regimes of reorientation of surfactant molecules with increasing temperature. The transition temperature between the regimes is related to T_g of PS in microcomposites and to the melting temperature T_m of PCL in nanocomposites. The iron-free magadiite leads to substantially longer electron spin relaxation times and thus allows for pulse EPR experiments such as four-pulse double electron electron resonance (DEER), electron spin echo envelope modulation (ESEEM) and electron nuclear double resonance (ENDOR) on spin-labeled and specifically deuterated surfactants. ENDOR results suggest a model of the surfactant layers with a well-defined middle layer. This model can explain the dilution effects caused by PCL and PS polymers in the hybrids. Comprehensive information from these techniques nicely complements information from conventional characterization techniques such XRD and TEM and provides a much more detailed picture of structure and dynamics of the surfactant layer in polymer-layered silicate nanocomposites.

Contents

Chapter 1

Introduction

1.1 Introduction

Nanocomposites attract more and more researchers interest because of their improved properties such as thermal resistance, gas barrier behaviour, mechanical strength and flame retardance compared with normal polymers.(1)-(3) Organically modified clay (*organoclay*) or modified minerals (*organosilicates*) are one of the most widely used types of nanofillers since the publication of the Toyota research group during the early 1990's of an industrial application to Nylon 6. (4)-(5)

There is a vast amount of literature on giving preparation methods for polymer layered silicate (PLS) nanocomposites and corresponding characterization techniques. (6) X-Ray Diffraction (XRD) and Transmission Electron Microscopy (TEM) are widely used to characterize the degree of intercalation of the polymer and the morphology of organoclay in polymer matrices. However, both of them give little information on dynamics and molecular structure of the interface between polymer and organoclay. Such information is required to gain a better understanding of the interactions between silicate and polymer.

Solid-state Nuclear Magnetic Resonance (NMR) and Electron Paramagnetic Resonance (EPR) are powerful methods to characterize dynamics of molecules over a wide time scale (ms to ps). In previous work, CW (Continuous Wave) EPR and ^{31}P MAS (Magic Angle Spinning) NMR were introduced to study dynamics of surfactant layers, and dynamic heterogenity of surfactant layers in organoclays based on the commercial material Somasif and in their nanocomposites with polystyrene (PS) was observed. (6) However as described in Sec.1.6 paramagnetic ions in natural layered silicates, mainly Fe^{3+} ($3d^5$), broadened EPR and NMR signals because of dipole-dipole coupling between electron spins or between electron and nuclear spins. In pulse EPR paramagnetic species shorten the relaxation time of electrons and make the spectra harder to interprete. In electron-nuclear double resonance (ENDOR) experiments, they cause a drastic reduction of the signal-to-noise ratio. In this thesis an iron-free layered silicate , so called magadiite, is synthesized with a hydrothermal method. (9) The product is characterized with Wide-Angle X-Ray Scattering (WAXS) and Scanning Electron Microscopy (SEM) to study morphology and layer structure. The optimum synthesis conditions were established with which an appropriate product with a layered and well defined structure can be obtained. The iron-free magadiite is then organically modified with two types of cationic surfactants, hexadecyltrimethylammonium (HTMA) chloride and hexadecyltributylphosphonium

(HTBP) bromide. Intercalation of a range of polymers with different dielectric constants is attempted. In constrast to previous work on the commercial layered silicate Somasif, where intercalation was observed only with PS and the HTMA surfactant, the studies could now be extended to polycaprolactone (PCL), which intercalates into magadiite modified with both HTMA and HTBP. In contrast to PS, PCL has a glass transition temperature (-60°C, 213 K) that is below the order-disorder transition temperature (T_{ODT}) of the surfactant layer in organomagadiite.

By using magadiite that is free from paramagnetic impurites, ^{2}H NMR can now also be applied to deuterated surfactants so that access to different time scales of surfactant motion is obtained. Magadiite also allows for application of pulse EPR techniques such as Electron Spin Echo Envelope Modulation (ESEEM), Double Electron Electron Resonance (DEER) and Electron Nuclear Double Resonance (ENDOR) to study the dipolar coupling between electrons (DEER), the hyperfine coupling between electrons and deuterons (ESEEM), and the hyperfine coupling between electrons and ^{31}P nuclei (ENDOR). With site-specific nitroxide surfactant spin probes (ammonium and phosphonium) and site-specific deuterated surfactants both dynamic and spatial information on the surfactant layers can be obtained, which is supplemental to that from the conventional techniques (WAXS and TEM). This will be discussed in detail in the experimental and conclusion part Chapter 5 and Chapter 6.

In this thesis, with lab-made magadiite and site-specific spin probes, novel characterization is performed on PLS hybrids which can be summarized as follows:

1. ^{2}H NMR on site-specifically labeled surfactants.
2. CW EPR for a nanocomposite with T_g of the polymer (PCL) lower than T_{ODT} of the surfactant layer.
3. ^{31}P ENDOR on polymer nanocomposites (with PCL) and microcomposites (with PS).
4. A systematic DEER study of surfactant distribution in organosilicates, and polymer nanocomposites (with PCL) and polymer microcomposites (with PS).
5. An ESEEM study of contact between site-specific spin labels on a surfactant molecule and deuterated head groups or parts of the alkyl chain near the head group.

In the remaining part of the introduction, the basics of nanocomposites and organoclay will be explained. In Chapter 2 the theoretical background of the related silicon chemistry and hydrothermal synthesis method will be described. In Chapter 3 basics of EPR and then in Chapter 4 of NMR will be introduced. The experimental results are presented in Chapter 5 and the final discussion will be given in Chapter 6.

1.2 Basics of nanocomposites and organoclay

Polymers are commonly admixed with a variety of both natural and synthetic compounds to improve their performance. (19) Inorganic compounds used for this purpose are called *fillers* and give rise to *filled polymers*. There are three types of fillers commonly used in nanocomposite materials depending on the size of the fillers: ultra small spheres, nanotubes and nanoplatelets. A *nanocomposite* is any material which is a composite made of a polymer

and a dispersed filler whose particles have one or more dimensions in the nanometer range. These nano-sized particles can improve many properties when compared with the virgin polymer or conventional micro- and macro-composites. (32) The improvements can include high moduli, increased strength and heat resistance, decreased gas permeability and flammability, and increased biodegradability of the polymers.

Polymer Layered Silicate Nanocomposites (PLS nanocomposites) are hybrids that consist of a polymer and nanoplatelets, namely nanoscopically dispersed layered silicate. *Phyllosilicates*, which are layered silicates such as mica, talc, montmorillonite, vermiculite, and hectorite, are the most commonly used nanoplatelets. Among them, hectorite and montmorillonite are the most commonly used smectite-type layered silicates for the preparation of nanocomposites. Smectites are generally a valuable mineral class for industrial applications because of their high *cationic exchange capacities*, surface area, surface reactivity, adsorption properties, and in the case of hectorite, high viscosity and transparency in solution. As the phase of highly polar clay particles which are hydrophilic in nature would separate from unpolar polymers (hydrophobic) if they are mixied directly without any modification, the nanocomposites can only be obtained by compatibilizing clay and polymer with the help of surfactants. By addition of surfactant the modified clay (now referred to as an *organoclay* or OLS (organically modified layered silicate)) is much more compatible with the polymer than the unmodified clay. Hence usually PLS nanocomposites consist of three components: polymer, layered silicate and surfactant, and the two latter components are combined as organoclay.

There are two classes of hybrids between a polymer and nanoscopically dispersed organoclay: *intercalated* nanoplatelets and *exfoliated* nanoplates (as shown in Fig. 1.1). (19) In intercalated nanocomposites the single polymer chains are intercalated between unaltered silicate layers with their regular alternation of galleries and laminae. In exfoliated nanocomposites the organoclay is totally exfoliated and dispersed in the polymer matrix. In intercalated PLS nanocomposites the distance between the layers is on the order of a few nanometers. In exfoliated PLS nanocomposites the ordered structure of organoclay is lost and the distance between the layers is of the order of the radius of gyration of the polymer R_g.

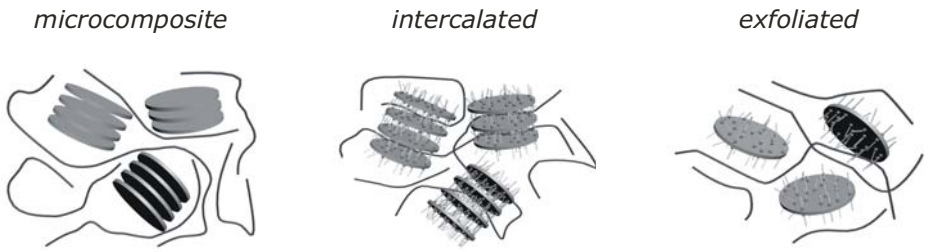

Figure 1.1: Types of hybrids. Microcomposites are the hybrids where the polymer chains surround unaltered layered silicates without intercalation. Unmodified layered silicates keep their structure and the system is immiscible. *Intercalated nanocomposites* are hybrids in which the *single* polymer chains are intercalated between unaltered silicate layers. *Exfoliated nanocomposites* are hybrids in which the silicate is totally delaminated and dispersed in the polymer matrix.

The idealized 2:1 layered silicate structure is shown in Fig.1.2. One silicate layer consist of two tetrahedral sheets which are fused to one octahedral sheet. For each tetrahedral cell of oxygen (O) atoms there is a silicon (Si) atom (only one Si atom is shown in the left side of the unit cell in (A) and others are omitted.). Each

layer is separated from its neighors by a van der Waals gap called a *gallery* or *interstratum*. Because in natural phyllosilicate octahedral sites are usully occupied by metal atoms such as aluminum (Al), magnesium (Mg), iron (Fe) or lithium (Li) whose formal cationic charge are less than silicon, also because of deficiency of some of the silicon atoms, the surface of the layers is anionically charged. These anionic charges are balanced by counter ions (usually sodium (Na^+))which are located in the galleries. The layer thickness is around 1 nm, and the lateral dimensions of these layers may vary from 30 nm to several microns or larger, depending on the particular layered silicate.

Organoclay is produced by replacing the cations originally present in the galleries with organic cations. The cationic surfactants (e.g. ammonium or phosphonium) are preferred to be attached to the wall of the gallery via Coulombic interaction. The aliphatic tails render the normally hydrophilic silicate surface unpolar (hydrophobic), so that the silicate is compatabilized with polymers. Moreover, expansion of the distance between layers of organoclay makes it easier to intercalate the galleries with polymer chains.

The *Cation Exchange Capacity* (CEC) is often used to measure the capacity of the clay for alkylammonium uptake by neutralization of surface charges. For example, the CEC of Somasif, one type of fluorite mica, is around 70–80 mmol/100g (mmol charges that can be substituted per 100 grams of clay). The CEC is a property of the clay. However the actual amount of surfactant that a clay can absorb depends also on the types and concentration of surfactant that is used in preparation. Some examples are listed in Tab.1.1.

2:1 phyllosilicate	Chemical formula	CEC (mmol/100g)	Particle length (nm)
Montmorillonite	$M_x(Al_{4-x}Mg_x)Si_8O_{20}(OH)_4$	110	110-150
Hectorite	$M_x(Mg_{6-x}Li_x)Si_8O_{20}(OH)_4$	120	200-300
Saponite	$M_xMg_6(Si_{8-x}Al_x)Si_8O_{20}(OH)_4$	86.6	50-60
Somasif*	$Na_{0.66}Mg_{2.68}(Si_{3.98}Al_{0.02})O_{10.02}F_{1.96}$	70-80	600
Magadiite**	$Na_2Si_{14}O_{29} \cdot 11H_2O$	80-120	∼1500

Table 1.1: Chemical formula and characteristic parameters of commonly used 2:1 phyllosilicates with M as monovalent cation and x as degree of isomorphous substitution (between 0.5 and 1.3). $*$ (Somasif) data is taken from (34). $**$ (Magadiite) data is taken from experimental measurements in this thesis and the particle length is approximated from SEM. Other data is taken from (32).

1.3 Preparation and characterization of organoclay

Usually organoclay is prepared by mixing of cationic surfactant solution and clay solution (or suspension). The ion-exchange reactions between cationic surfactants, including primary, secondary, tertiary and quaternary alkylammonium or alkylphosphonium cations, and the negatively charged clay surface is spontaneous via electrostatic interaction. Alkylammonium or alkylphosphonium cations in the organosilicates lower the surface energy of the inorganic host and improve the wetting characteristics of the polymer matrix and result in a larger interlayer spacing. Additionally, the alkylammonium or alkylphosphonium cations can provide functional groups that can react with the polymer matrix, or in some cases initiate the polymerization of monomers to improve the strength of the interface between the inorganic and the polymer matrix. (32)

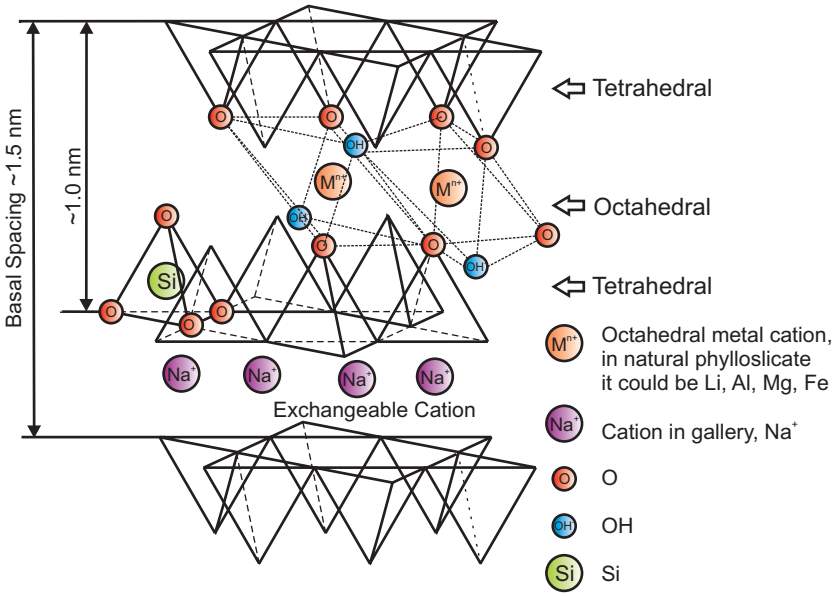

Figure 1.2: Ideal structure of 2:1 of phyllosilicate. One silicon coordination tetrahedron is shown with four oxygen atoms and one silicon atom in the center. All other silicon atoms are not shown in the picture. In the octahedral unit structure, metal ions have ligands with oxygen and hydroxyl groups. These metal ions could be Li, Al, Fe, or Mg in natural silicate. The dashed lines between the layers show the octadetral symmetry. Synthesized iron free magadiite contains only sodium ions as metal ions. The gallery between layers is usually occupied by exchangeable cations that counterbalance the negative charge by the isomorphous substitution of the atoms forming the charge (e.g. Mg^{2+} in montmorillonite, Li^{1+} in hectorite.)

WAXS and XRD are commonly used to characterize the structure of organoclay. However, little information can be obtained on the long range order (more than 10 nm) from WAXS or on the conformation of the surfactant molecules. Vaia et al. used Fourier Transfer Infrared Spectroscopy (FTIR) experiments to study the adsorbed surfactants. (35) Atomic Force Microscopy (AFM) was also applied to have direct images of surfactant aggregates at solid surfaces in aqueous solutions. (36) The adsorption of surfactants on the surface can also be studied by adsorption isotherms and HRTEM (High Resolution Transmission Electron Microscopy). Different models of packing of surfactant aggregates on the clay surface have been presented including a bilayer model, liquid-like and solid-like model (35) or cylindrical aggregates model if the surfactant concentration is above its CMC (Critical Micelle Concentration). In our experiment, NMR and EPR techniques are applied with appropriate site-specific spin probes such as deuterated surfactants and nitroxide labeled surfactants to study dynamics and spatial distributions between specific sites in surfactant layers. With pulse EPR techniques the distance range between 0.5 nm and 10 nm can be accessed and rotational correlation times of surfactant molecules can be determined in the nanosecond to microsecond range. With site-specific deuterated surfactants, time scales between microseconds and milliseconds can be accessed. Hence magnetic resonance techniques give complementary information to that from scattering and microscopy techniques.

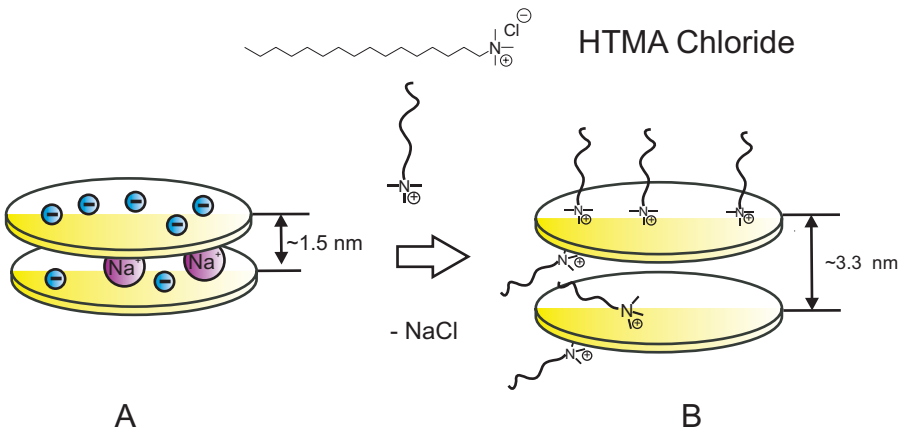

Figure 1.3: Formation of organically modified layered silicates (OLS). The negative charge formed on the surface of the silicate implies that the cationic head of alkylammonium is preferentially attached to the wall of gallery via Coulombic interaction and its aliphatic tail renders the normally hydrophilic silicate surface hydrophobic. The example is taken from experiments with HTMA and magadiite. The distance shown in the figure is measured from WAXS. (A) phyllosilicate (B) organically modified layered silicate

1.4 Types of polymers used for nanocomposites

The large variety of polymer systems used in nanocomposite preparation with layered silicates can be conventionally classified as below: (32)

1. Vinyl polymers. These include the vinyl addition polymers derived from monomers like methyl methacrylate, methyl methacrylate copolymers, other acrylates, acrylic acid, acrylonitrile, styrene, 4-vinylpyridine, acrylamide, poly(N-isopropylacrylamide) and tetrafluoro ethylene. Corresponding structures of polymers are shown in Fig.1.4.

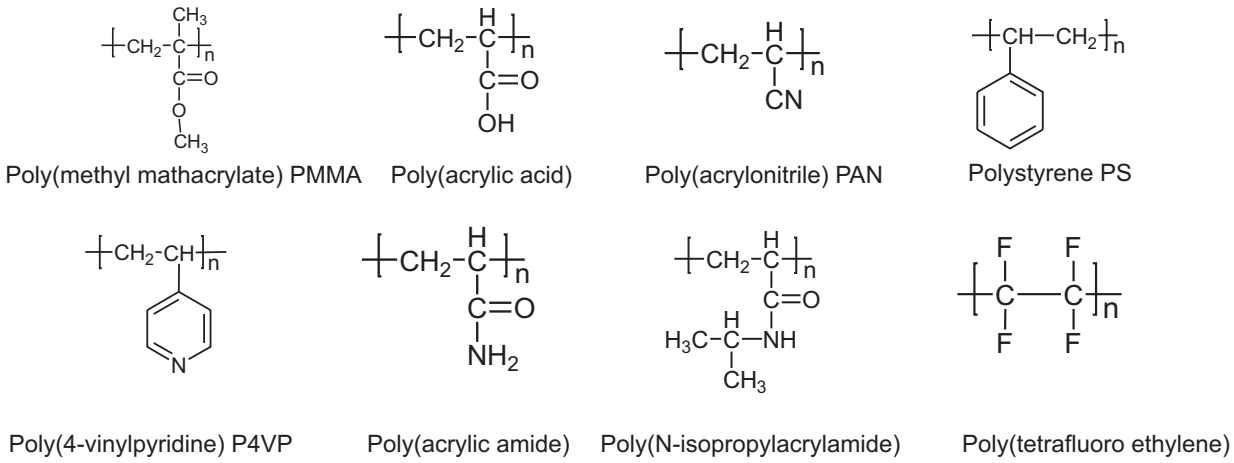

Figure 1.4: Structures of vinyl polymers

2. Condensation (step) polymers. Several technologically important polycondensates have been used in nanocomposite preparation with layered silicate. These include Nylon 6 (N6), several other polyamides, poly(ϵ-

caprolactone) (PCL), poly(ethylene terephthalate), poly(trimethylene terephthalate), poly(butylene terephthalate), polycarbonate (PC), poly(ethylene oxide) (PEO), ethylene oxide copolymers, poly(ethylene imine), poly(dimethyl siloxane), epoxidized natural rubber, epoxy polymer resins (EPR), phenolic resins, polyimides, poly(amic acid), polysulfone, polyetherimide, polyurethanes (PU), polyurethane urea, and fluoropoly(etherimide). Corresponding structures of some polymers are shwon in Fig.1.5.

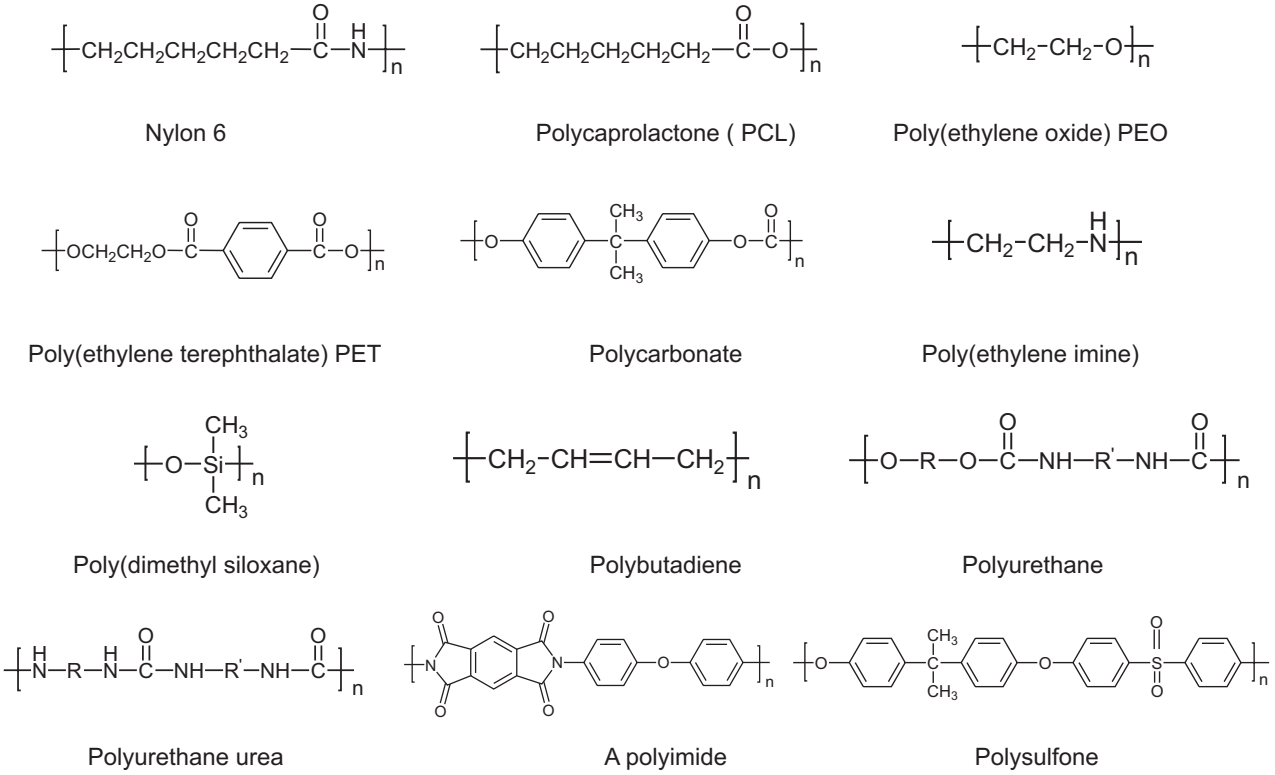

Figure 1.5: Structures of condensation (step) polymers

3. Polyolefins such as polypropylene (PP), polyethylene (PE), polyethylene oligomers, copolymers such as poly(ethylene-co-vinyl acetate) (EVA), ethylene propylene diene methylene linkage rubber (EPDM), poly(1-butene), polybutadiene and butadiene copolymers have been used.

4. Specialty polymers. In addition to the above mentioned conventional polymers, several interesting developments occurred in the preparation of nanocomposites of layered silicated with specialty polymers including the N-heterocyclic polymers like polypyrrole (PPY), poly(N-vinylcarbazole) (PNVC), and polyaromatics such as polyaniline (PANI), poly(*p*-phenylene vinylene) and related polymers. Corresponding structures of some polymers are shown in Fig.1.6. PPY and PANI are known to display electric conductivity, and PNVC is well known for its high thermal stability and characteristic optoelectronic properties. Research has also been performed on liquid crystalline polymer (LCP)-based nanocomposites, hyper-branched polymers, and cyanate esters.

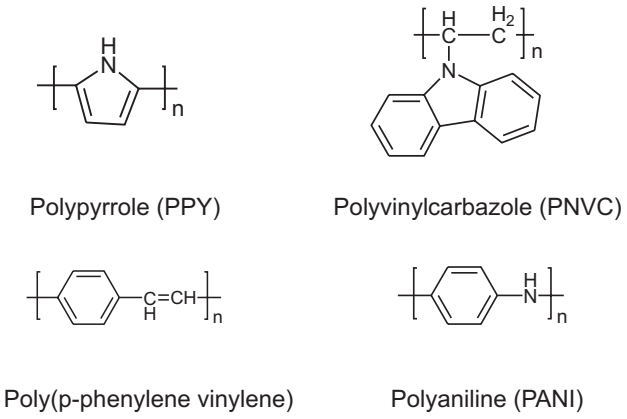

Figure 1.6: Structures of specialty polymers

5. Biodegradable polymers. Polyactide (PLA), poly(butylene succinate) (PBS), PCL, unsaturated polyester, polyhydroxy butyrate and aliphatic polyester lead to have biodegradable polymer/layered silicate nanocomposites or so-called green polymeric materials that would not involve the use of toxic or noxious components in their manufacture, and could allow degradation via a natural composting process.

1.5 Preparation of nanocomposites

From (32) three different preparative methods of nanocomposites are discussed:

1. Intercalation of polymers or pre-polymer from solution. Water soluble polymers, such as PEO, poly(vinyl alcohol) (PVA), poly(N-vinyl pyrrolidone) (PVP), and poly(ethylene vinyl alcohol) (PEVA), have been intercalated into the clay galleries using this method. (38) Examples from non-aqueous solvents are nanocomposites of PCL/clay (39) and PLA/clay in chloroform as a co-solvent (40), and high-density polyethylene (HDPE) with xylene and benzonitrile (41).

2. In situ intercalative polymerization method. The report of N6/MMT nanocomposites obtained via this route by the Toyota research group (2) introduced nanocomposites to industrial practice. They first reported the ability of Na^+-MMT (montmorillonite) modified by α,ω-amino acids (COOH-$(CH_2)_{n-1}$-NH_2^+, with n = 2, 3, 4 5, 6, 8, 11, 12, 18) to be swollen by the ϵ-caprolactam monomer at 100°C. Subsequent ring opening polymerization lead to N6/MMT nanocomposites.

3. Melt intercalation. Melt intercalation has advantages over solution intercalation. For example, direct melt intercalation is highly specific for the polymer, leading to new hybrids that were previously inaccessible. In addition, the absence of solvent makes direct melt intercalation an environmentally sound and an economically favorable method for industry from a waste perspective. This method is applied in this thesis as a standard preparative method for the tested polymer/clay hybrids.

1.6 Characterization of polymer/clay nanocomposites

Conventional characterization methods for the structure of nanocomposites are X-Ray Diffraction (XRD) and Transmission Electron Microscopy (TEM). Although the XRD technique WAXS offers a convenient method to determine the interlayer spacing of the silicate layers in the original layered silicates and in the intercalated nanocomposites in the range of 1-4 nm, little can be said about the spatial distribution of silicate layers or any structural inhomogeneties in nanocomposites. Therefore, conclusions concerning the mechanism of nanocomposite formation and their structure based solely on WAXS patterns are only tentative. TEM allows a qualitative understanding of the internal structure, spatial distribution of the various phases, and structural defects through direct visualization. However special care must be exercised to guarantee a representative cross-section of the sample. Furthermore TEM only gives qualitative information on the sample as a whole.

VanderHart et al. (37) used solid-state nuclear magnetic resonance (NMR) (^{1}H and ^{13}C) as a tool for gaining greater insight about the morphology, surface chemistry and to a limited extent, the dynamics of exfoliated polymer clay nanocomposites. The main objective in their solid-state NMR measurements is to connect the measured longitudinal relaxation time T_1 of protons (and ^{13}C nuclei) with the quality of clay dispersion.

The surface of naturally occuring layered silicates such as MMT are mainly made of silica tetrahedra while the central plane of the layers contains octahedrally coordinated Al^{3+} with frequent non-stoichiometric substitutions, where Al^{3+} is replaced by Mg^{2+} and , somewhat less frequently, by Fe^{3+}. As Fe^{3+} is strongly paramagnetic (spin = 5/2 in this distorted octahedral environment), the concentration of Fe^{3+} is critical in NMR. Typical concentrations of Fe^{3+} in naturally occuring clays produce nearest-neighbour Fe-Fe distance of about 1.0-1.4 nm. (42) At such distances, the spin-exchange interaction between the unpaired electrons on different Fe atoms is expected to produce magnetic fluctuations in the vicinity of the Larmor frequencies for protons or ^{13}C nuclei. Thus the relaxation time of these nuclei (protons or ^{13}C nuclei) depends on the distance of the polymer chain from the clay surface.

In previous experiments in our group, ^{31}P solid state MAS NMR was applied to study states of ^{31}P nuclei in surfactant layers in organoclay prepared with Somasif (synthetically modified hectorite) and phosphonium surfactants. Temperature dependent ^{31}P NMR spectra clearly show that for an excess of surfactant with respect to the CEC mobile and less mobile ^{31}P nuclei can be observed. (6) CW EPR was also used to study dynamics of surfactant layers with site-specific nitroxide spin probes and to obtain rotational correlation times τ_c. For detected temperatures (from 300 K to 450 K) τ_c values correspond to the slow tumbling region (a few nanoseconds). With NMR and EPR heterogeneity of the surfactant layers in organoclay prepared with ammonium and phosphonium surfactants and in corresponding hybrids with PS was studied. (6)-(7)

1.7 The design of this project

As described in Sec.1.1, in this project magadiite was obtained by a hydrothermal synthesis method. The design of the experiments for synthesis of magadiite, preparation of organomagadiite (organically modified magadiite) and of the corresponding polymer hybrids is shown in Fig.1.7. With a fixed composition of reactants (amorphous silica :

NaOH : H_2O = 3 : 1 : 200 in molar ratio) and autogeneous pressure during annealing in an autoclave, temperature-dependent and annealing-period-dependent experiments have been performed and the products were characterized with WAXS and SEM to study the morphology and crystal structure to find optimum synthesis conditions. Once magadiite was successfully synthesized, as shown in Fig.1.7, the CEC and amount of absorbed surfactants were characterized. For the HTBP series, the amount and states of surfactants could be studied with ^{31}P MAS NMR because of a nice signal/noise ratio of the ^{31}P NMR signal.

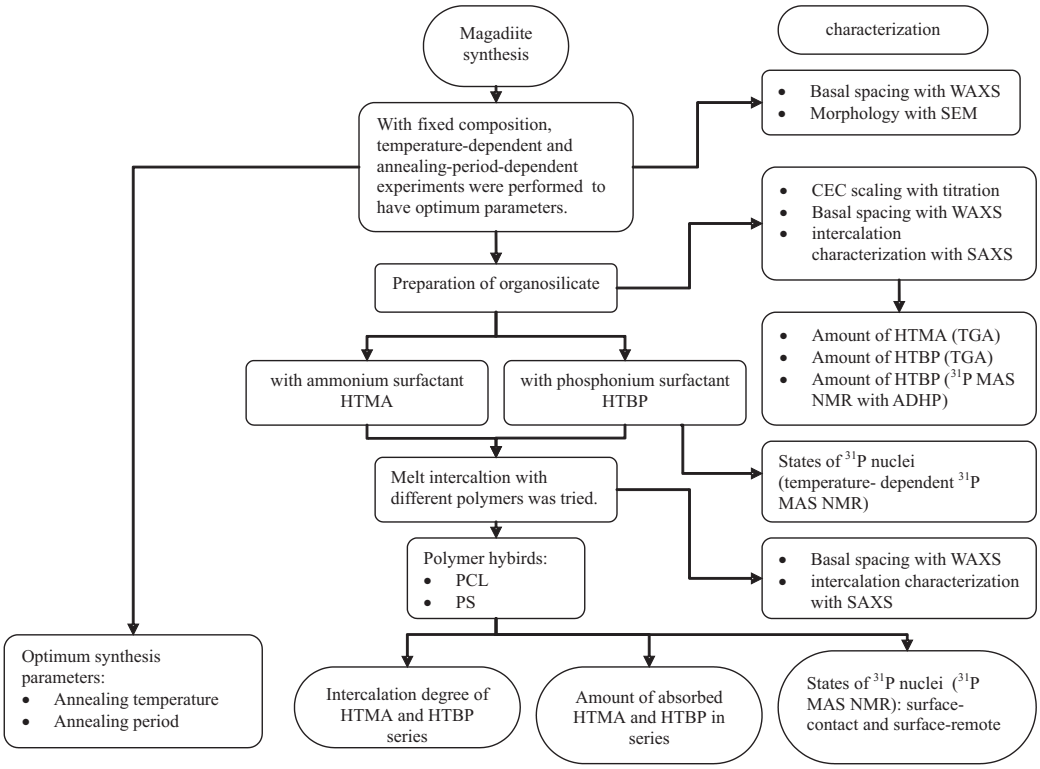

Figure 1.7: Flow chart of synthesis experiments and characterization

The design of the spectroscopic experiments is shown in Fig.1.8 and Fig.1.9. The purposes of experiments are given in Fig.1.8 and the sample series prepared are given in Fig.1.9. Totally four series of samples were prepared and the details are described in the experimental and conclusion part (Chapter.5 and Chapter.6). The site-specific nitroxide surfactants are based on undecyltrimethylammonium (UTMA) bromide and undecyl phosphonium (UTBP) bromide. (7) According to the position of the spin label (SL) in the alkyl chain they are designated as 11-SL-UTMA and 11-SL-UTBP (end-labeled), 9-SL-UTMA, 9-SL-UTBP, 7-SL-UTMA and 7-SL-UTBP and the corresponding chemical structures are shown in Fig.1.9.

1. Samples prepared for DEER measurements. The composition of these samples is magadiite, ammonium surfactant spin probes (11-SL-UTMA, 9-SL-UTMA, and 7-SL-UTMA), HTMA chloride and corresponding PCL and PS hybrids (Fig.1.9. (A)).

2. Samples prepared for ENDOR measurements. The composition of these samples is magadiite, phosphonium spin probes (11-SL-UTBP, 9-SL-UTBP and 7-SL-UTBP), HTBP and corresponding PCL and PS hybrids

(Fig.1.9. (B)).

3. Samples prepared for ESEEM measurements. The composition of these samples is magadiite, ammonium spin probes (11-SL-UTMA, 9-SL-UTMA, and 7-SL-UTMA), deuterated surfactants (d9, dα and dβHTMA bromide) and corresponding PCL and PS hybrids (Fig.1.9. (C)).

4. Samples prepared for ^{2}H NMR measurements. The composition of these samples is magadiite, deuterated surfactants and corresponding PCL and PS hybrids (Fig.1.9. (D)).

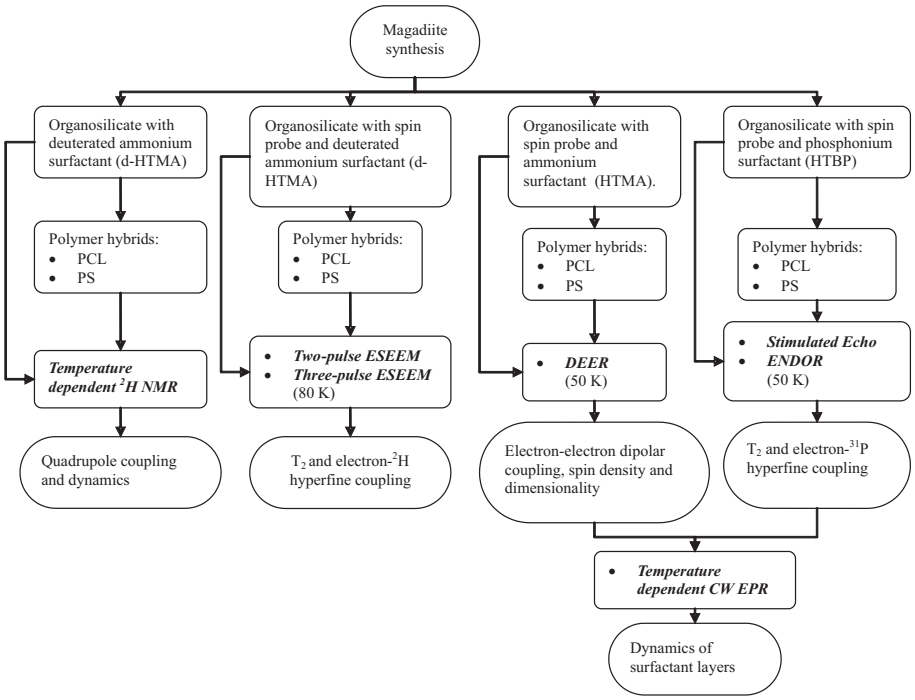

Figure 1.8: Flow chart of spectroscopic characterization experiments

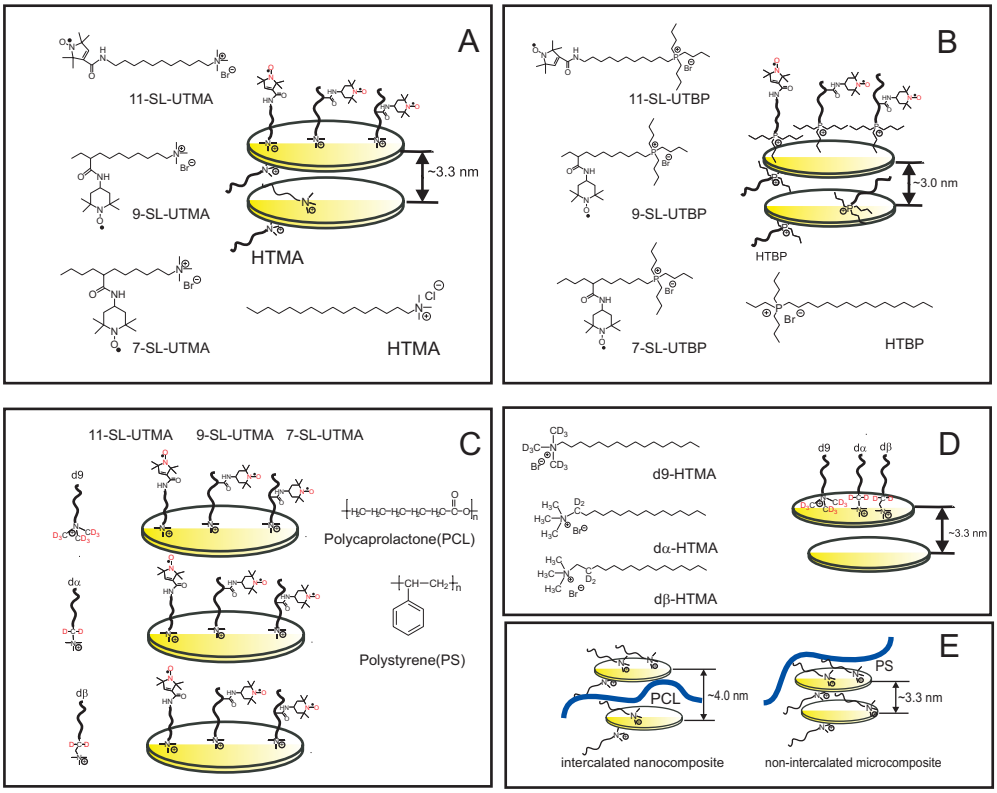

Figure 1.9: Schematic illustration of the design of spectrocopic experiments. (A) Samples for DEER. (B) Samples for ENDOR. (C) Samples for ESEEM. (D) Samples for ^{2}H NMR. (E) Illustration of PCL nanocomposites and PS microcomposites.

Chapter 2

Introduction of the synthesis of silicates

2.1 The crystal structure of silicates

2.1.1 Introduction

The basis for extending the application range of magnetic resonance experiments for polymer-layered silicate nanocomposites is to synthesize an iron-free layered silicate. There are several kinds of layered silicate that can be synthesized from amorphous silica. Beneke and Lagaly listed five alkali silicate minerals, which are potentially layered and have exchangeable cations, as opposed to the large number of other silicate minerals: the anhydrous sodium disilicate *natrosilicate* ($Na_2Si_2O_5$), hydrous silicates including *magadiite* ($Na_2Si_{14}O_{29}{\cdot}11H_2O$), *kenyaite* ($Na_2Si_{22}O_{45}{\cdot}10H_2O$), *makatite* ($Na_2Si_4O_9{\cdot}5H_2O$), and *kanemite* ($NaHSi_2O_5{\cdot}3H_2O$). (8) M41S, a family of silicate/aluminosilicate mesoporous molecular sieves, can also have a lamellar structure under appropriate reaction conditions (MCM-50). (44) The structure of such mesoporous materials (pore dimension between 20 Å and 500 Å) strongly depends on the presence of *structure-directing agents* such as surfactants, as described by the biomineralization model which uses the organic assembly as a template to grow the inorganic-organic hybrids. (46) Not only the lamellar structure of the synthesized silicate is important, but also the stability of the structure, the exchange capability of the interlayer sodium ions by organic long-chain cations (CEC), the innercrystalline swelling of these organic derivatives, and the surface properties need to be taken into account to select the silicate that is most appropriate for the purpose of this work. In this chapter, the basics of silicates will be introduced and the synthesis principle will be discussed.

2.1.2 Introduction of silicon compounds

Silicic acid ($Si(OH)_4$) is a parent substance from which a large family of structures is derived, such as silicate minerals, salts, and esters. The silicic acid itself can be prepared only as an unstable solution in water. Its molecules readily condense with one another to form water and polymeric chains, rings, sheets, or three-dimensional materials.

$$nSi(OH)_4 \rightarrow nSiO_2 + 2nH_2O \tag{2.1}$$

The chemical structures of some silicon compounds are shown in Fig.2.1.

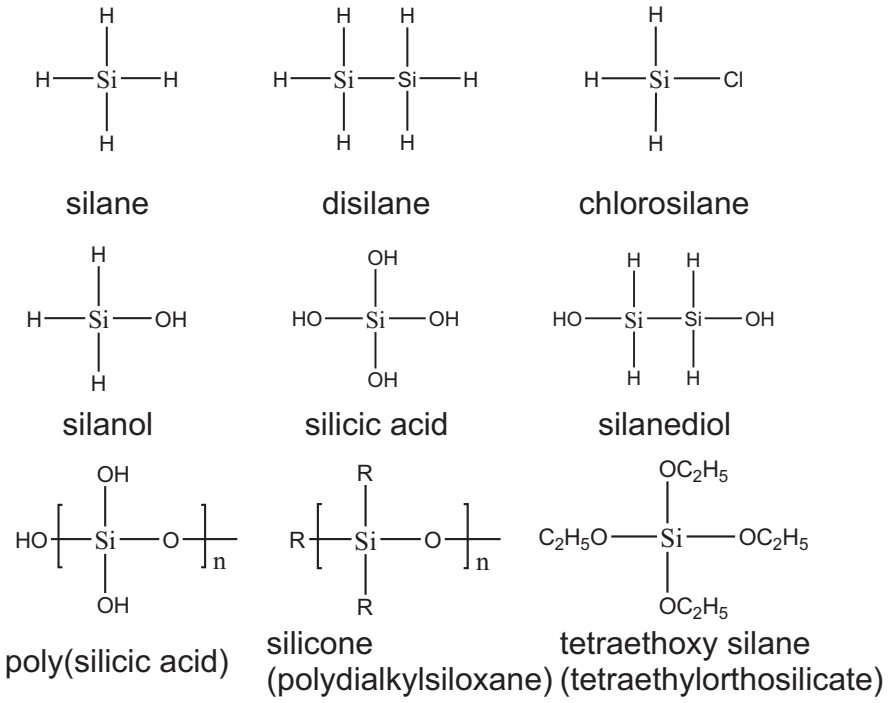

Figure 2.1: The chemical structures of some silicon compounds.

2.1.3 Basics of silicates

95% of the Earth's crust is composed of mineral groups of silicates such as *feldspars*, *quartz*, *amphiboles*, *pyroxenes*, and *micas* because the Si–O bond is considerably stronger than that between any other element and oxygen. The Si–O bond has ionic and covalent properties (50/50%). The high affinity of silicon for oxygen accounts for the existence of a vast array of silicate minerals and synthetic silicon-oxygen compounds, which are important in mineralogy, industrial processing, and laboratory synthesis. *Silicates* are built up on the basis of sharing oxygen atoms of tetrahedral SiO_4 units in which the Si atom is at the center and the O atoms are at the vertices. Aside from rare high-temperature phases, the structures of silicates are confined to tetrahedral four-coordinate Si. The SiO_4 tetrahedron shape is defined by the Si–O bond lengths and O–Si–O bond angles (ϕ in Fig.2.2. (B)). By X-ray and neutron diffraction, the mean Si–O bond length is 1.63 Å. The strength of the Si–O bond limits the range of the bond lengths from about 1.60 Å to 1.63 Å. When [SiO_4] tetrahedra are linked in a structure, the bond length of the Si–O_{bridge} is larger than the one of the Si–$O_{nonbridge}$ by 0.025 Å. The bond angle ϕ of an O_{bridge}–Si–O_{bridge} motif is less than the bond angle γ of an $O_{nonbridge}$–Si–$O_{nonbridge}$ motif. So in linkage structures the silicon atoms are displaced from the centers of the tetrahedra, away from the bridging oxygens, as a result of repulsion between the two silicon atoms. The bond angle θ of Si–O–Si defines the orientation of the tetrahedra relative to one another. Angle θ is on the scale between 120° and 180° and depends on the local structure environment, temperature and pressure.

The complicated silicate structures are often easier to comprehend if they are treated as a combination of the SiO_4 units and formal charges of Si^{4+} and O^{2-} are assigned to ensure charge balance in the formula. In general,

these tetrahedra share vertices and (much more rarely) edges or faces. The oxo anions where 2, 3, or 4 oxygen atoms are attached to a central atom to give a discrete anion are called *mononuclear oxo anions* (Fig.2.2. (A)). If one or more of these oxygen atoms are shared between two silicon atoms to give a bridge oxygen the anions are called *polynuclear oxo anions* (e.g. Fig.2.2. (B)). *Orthosilicate* ($[SiO_4]^{4-}$) is shown in Fig.2.2. (A) and *disilicate* ($[O_3SiOSiO_3]^{6-}$) is shown in Fig.2.2. (B). Rankinite ($Ca_3Si_2O_7$) is an example of a mineral that has a dimer structure.

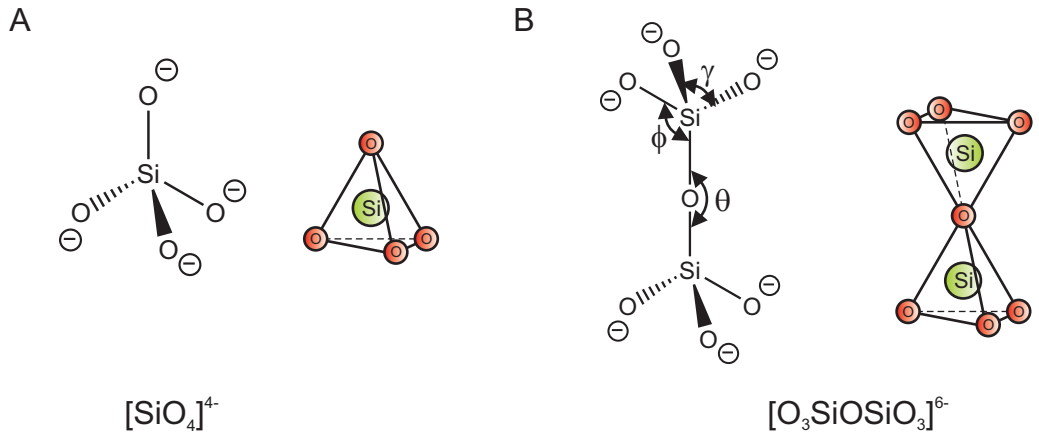

Figure 2.2: The silicate structure of (A) orthosilicate. (B) disilicate.

Another example of polynuclear oxo anions of silicates is the infinite chain of SiO_4 units, which has two shared O atoms for each Si atom (Fig.2.3. (A)) and is called *chain metasilicate* or *pyroxene*. The mineral jadeite ($NaAl(SiO_3)_2$) has such a structure. A ring of SiO_4 units has the same formula with $n = 6$ and is shown in (Fig.2.3. (B)) and is called *cyclic metasilicate*. The mineral beryl ($Be_3Al_2Si_6O_{18}$) contains such a $[Si_6O_{18}]^{12-}$ unit.

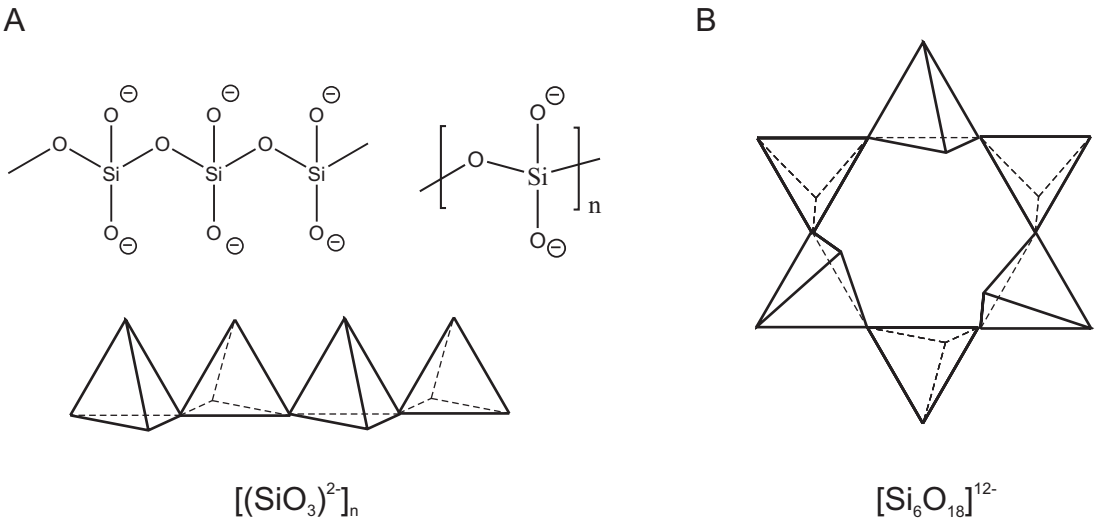

Figure 2.3: Silicate structures of (A) an infinite chain of SiO_4 units ($[(SiO_3)^{12-}]_n$). (B) a ring of SiO_4 units ($[Si_6O_{18}]^{12-}$).

An infinite sheet of SiO_4 units hexagonally linked in a 2-dimensional network having a formula as $[(Si_2O_5)^{2-}]_n$ forms a *sheet* (ring structure in Fig.2.3. (B) extended infinitely in two dimensions, three of the oxygen atoms are shared with three neighbouring units). The formular is derived from two SiO_4 units: two independent oxygen atoms (each one has one negative formal charge) and six shared oxygen atoms give rise to 5 oxygen atoms in the unit cell. For example, talc $(Mg_6Si_8O_{20}(OH)_4$ in the mica group has such a structure.

Silica (SiO_2) has a structure in which all oxygen atoms of SiO_4 units are shared. Pure silica occurs in two forms: quartz and cristobalite. In cristobalite the silicon atoms are placed as the carbon atoms in diamond (cubic close-packed (ccp) with half of the tetrahedral holes occupied), with the oxygen atoms midway between each pair of silicon atoms. Quartz is built up of SiO_4 tetrahedra as in silicates with each oxygen atom shared by two silicon atoms so that the empirical formula is SiO_2. Quartz and cristobalite can be interconverted when heated. The interconversion process is slow because breaking and reforming of bonds is required and the activation energy is high. However, the rates of conversion are profoundly affected by the presence of impurities, or by the introduction of alkali-metal oxides.

Silica and many silicates crystallize slowly. Amophous solids known as *glass* can be obtained instead of crystals by cooling the melt of silica at an appropriate rate. (21) Glass is a material with no long-range order but, instead, a disordered array of polymeric chains, sheets, or three-dimensional units. In some respects these glasses resemble liquids. As with liquids, their structures are ordered over distances of only a few interatomic spacings (such as within a single SiO_4 tetrahedron). Unlike for liquids, their viscosities are very high, and for most practical purposes they behave like solids.

Silicon polymers which have a –Si–O–Si– backbone have a quite different set of properties. A typical silicone polymer has the polydimethylsiloxane repeat unit and end-capping alkyl groups (Fig.2.4). The properties vary from mobile high boiling liquids to flexible high polymers. The liquids are used as lubricants and the high polymers are used for a wide variety of applications, including weather- and chemical-resistant flexible sealants. The unusual property of these polymers is their very low glass transition temperature, the temperature at which they become rigid. The origin of the low transition temperature appears to be the highly compliant nature of the –Si–O–Si– linkage.

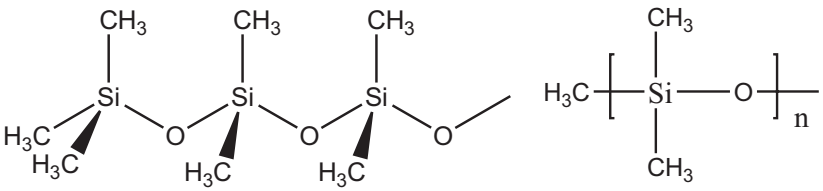

Figure 2.4: The structure of polydimethyl siloxane.

2.1.4 Aluminosilicates

If some of the formally Si^{4+} 'ions' are replaced by Al^{3+}, its presence in place of Si^{4+} in an aluminosilicate renders the overall charge negative by one unit. An additional cation, such as H^+, Na^+, or $1/2Ca^{2+}$, is therefore required for each Al tom that replaces an Si atom. Then the framework must have a negative charge, and positive charged counter ions must be distributed through it. These additional cations have a profound effect on the properties of the materials. Such framework minerals are the aluminosilicates. In aluminosilicates Al may substitute Si in tetrahedral sites, enter an octahedral environment external to the silicate framework, or, more rarely, occur with other coordination numbers. They are among the most diverse, widespread, and useful natural silicate minerals. Many synthetic aluminosilicates can be made, and several are manufactured industrially for use as ion-exchanger (when wet) and *molecular sieves* (when dry). Generally three types of aluminosilicates are commonly found in nature.

1. Layered aluminosilicates.
2. Three-dimensional aluminosilicates.
3. Molecular sieves.

Layered aluminosilicates contain also metals such as lithium, magnesium, and iron. Examples of such materials include clay, talc, and various micas. In one class of layered aluminosilicate (1:1 layered aluminosilicate), the repeating unit consists of a silicate layer whose linkage of $[SiO_4]$ units is shown in Fig.2.3. (B) (infinite extension). The edge view of the net is shown in Fig.2.5. In MO_6 octahedral, if M is Mg, then this structure is for the mineral chrystoile. When M is Al^{3+} and each of the atoms on the bottom is replaced by an OH group, this structure is close to that of the 1:1 clay mineral kaolinite ($Al_2(OH)_4Si_2O_5$). The electrically neutral layers are held together by rather weak hydrogen bonds, so the mineral readily cleaves and incorporates water between the layers. A larger class of aluminosilicate has Al^{3+} ion sandwiched between silicate layers.

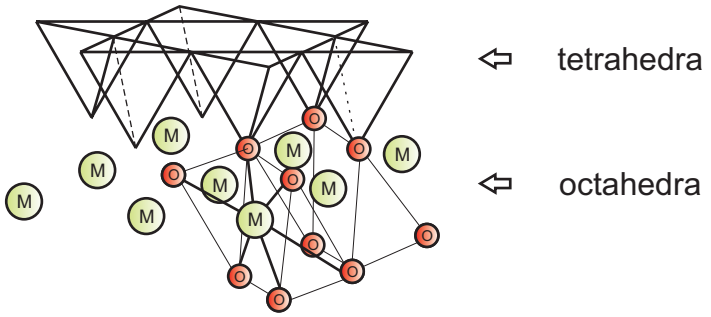

Figure 2.5: Edge view of the 1:1 layered aluminosilicate (One layer of $[SiO_4]$ incorporates with one net of $[MO_6]$ octahedra). Individually one O of a $[SiO_4]$ unit incorporates with a $[MO_6]$ octahedron. Two units of octahedra are shown.

The structure of the other type (2:1 layered aluminosilicate) is shown in Fig.1.2 with two tetrahedral sheets fused to an octahedral sheet. One example is muscovite mica ($KAl_2(OH)_2Si_3AlO_{10}$), in which K^+ resides between

the charged layers (exchangeable cation sites), Si^{4+} resides in sites of coordination number 4 and Al^{3+} in sites of coordination number 6. In talc, Mg^{2+} ions occupy the octahedral sites and O atoms on the top and bottom are replaced by OH groups. For example, the mineral talc ($Mg_3(OH)_2Si_4O_{10}$) is obtained when three Mg^{2+} ions replace two Al^{3+} ions in the octahedral sites in pyrophyllite ($Al_2(OH)_2Si_4O_{10}$). In talc (and in pyrophyllite) the repeating layers are neutral, and as a result talc readily cleaves between them. Muscovite mica is not soft like talc because of the electrostatic cohesion, but it is readily cleaved into sheets. More highly charged layers with dications between the layers lead to greater hardness. The friable layered aluminosilicates are the primary constituents of clay and some common minerals.

The hard three-dimensional aluminosilicates are common rock-forming minerals. Feldspars (orthoclase with formula $KAlSi_3O_8$ and albite with formula $NaAlSi_3O_8$) have aluminosilicate frameworks which are built up by sharing all vertices of $[SiO_4]$ or $[AlO_4]$ tetrahedra. The cavities in this three-dimensional network accommodate ions such as K^+ and Ba^{2+}.

Molecular sieves are crystalline aluminosilicates having open structures with apertures of molecular dimensions. The name 'molecular sieves' is prompted by the observation that these materials adsorb only molecules that are smaller than the aperture dimensions and so can be used to separate molecules of different sizes.

Zeolites, which are a subclass of molecular sieves, have an aluminosilicate framework with cations (typically from Groups 1 or 2) trapped inside tunnels or cages. In addition to their function as molecular sieves, zeolites can exchange their ions for those in a surrounding solution. The cages in zeolite are defined by the crystal structure, so they are highly regular and of precise size. Consequently, molecular sieves capture molecules with greater selectivity than high surface area solids such as silica gel or activated carbon, where molecules may be caught in irregular voids between the small particles. Zeolites are also used for shape-selective heterogeneous catalysis. One example is that the molecular sieve ZSM-5 is used to synthesize 1,2-dimethylbenzene (o-xylene) for use as an octane booster in gasoline. The other o-xylenes are not produced because the catalytic process is controlled by the size and shape of the zeolite cages and tunnels.

2.2 Introduction of mesoporous silicate materials

2.2.1 Synthesis of mesoporous silicates

Beck, Vartuli and their coworkers reported synthesis of a silicate material in the mesoporous range and its potential application in catalysts and PLS nanocomposites. (44)–(45) *M41S* is a family of silicate/aluminosilicate mesoporous molecular sieves. The characteristics of M41S are that they have large surface areas and very narrow pore size distributions, with pore diameters tunable from 15 to 100 Å. The M41S family consists of MCM-48, which has a cubic ordered pore structures, MCM-41, which has a hexagonally ordered pore structure, and MCM-50, which has an unstable lamellar structure.

Generally porous materials can be classified into three groups as shown in Tab.2.1.

Material	pore diameters (Å)
microporous	$\leq$20
mesoporous	between 20 and 500
macroporous	$\geq$500

Table 2.1: Classification of porous materials

Microporous materials embrace materials from amorphous silica (SiO_2) and inorganic gels to crystalline materials such as zeolite (aluminosilicates), aluminophosphates (e.g. $AlPO_4$), gallophosphates (e.g. $GaPO_4$) and related minerals. The hydrothermal synthesis of zeolite generally uses the following reactants:

1. water as the solvent;
2. a silicon source;
3. an aluminum source;
4. a mineralizing agent;
5. a surfactant-directing agent.

The most important properties of the structure-directing agents are moderate hydrophobicity and the ability to form strong, non-covalent inorganic-organic interactions. When the structure-directing agents are brought in contact with water, hydrophobic hydration spheres, fully connected by hydrogen bonds, surround the structure-directing agents. Then interactions between the structure-direcing agents and silicate species will entail replacement of water by the inorganic species. This leads to an organic-inorganic assembly, and the geometry of the structure-directing agent will be reflected in the inorganic pore structure. The thermodynamic driving force of such a mechanism derives from the release of the structural water as the organic-inorganic assembly is formed.

One group of mesoporous materials, designated M41S, are fundamentally different from zeolite. These materials are characterized by narrow pore size distributions tunable from 15 to 100 Å and have large surface areas (typically above 700 m^2/g). Compared with zeolite, the pore walls of M41S are amorphous and the ordering lies in the pore arrangement. Researchers of Mobile Inc. ((44)–(45)) used four main components in the M41S synthesis:

1. Structure-directing surfactants: alkyltrimethyl ammonium halides;
2. Silica source: a combination of sodium silicate (Na_2SiO_3), TEOS ($(C_2H_5O)_4Si$, tetraethoxy silicates), fumed silica (SiO_2), and Ludox (spherical silica (SiO_2) sol nanoparticles with an average particle diameter of 8 nm).
3. Sovent: aqueous solution.
4. Catalyst: basic additives such as sodium hydroxide (NaOH) or TAH ($(C_2H_5)_4N^+(OH)^-$, tetraethyl ammonium hydroxide).
5. In the case of aluminosilicates materials, an aluminum source was added as well.

The synthesis solutions were kept at temperatures ranging from 100°C to 150°C for 24–144 hours. Then the solid products were filtered, washed and dried. The materials were calcined at 540°C under a gas-flow of alternately nitrogen and air, thus removing the surfactant so that porous structures were formed.

The importance of structure-directing agents can be explained by a *liquid crystal templating mechanism* (LCT) as surfactant liquid crystal structures serve as organic templates (44)–(45). Firouzi et al. present a biomineralization model which is similar to the LCT model. (46) In this biomineralization model nucleation, growth, and the final morphology of the inorganic species are determined by preorganized assemblies of organic molecules. In Fig.2.6 a silicatropic liquid crystal (SLC) in which dilute isotropic aqueous silicate species are combined with a dilute isotropic surfactant solution is shown. Long-range order in typical mesophase synthesis is achieved only after dilute isotropic aqueous silicate species are combined with a dilute isotropic surfactant solution.

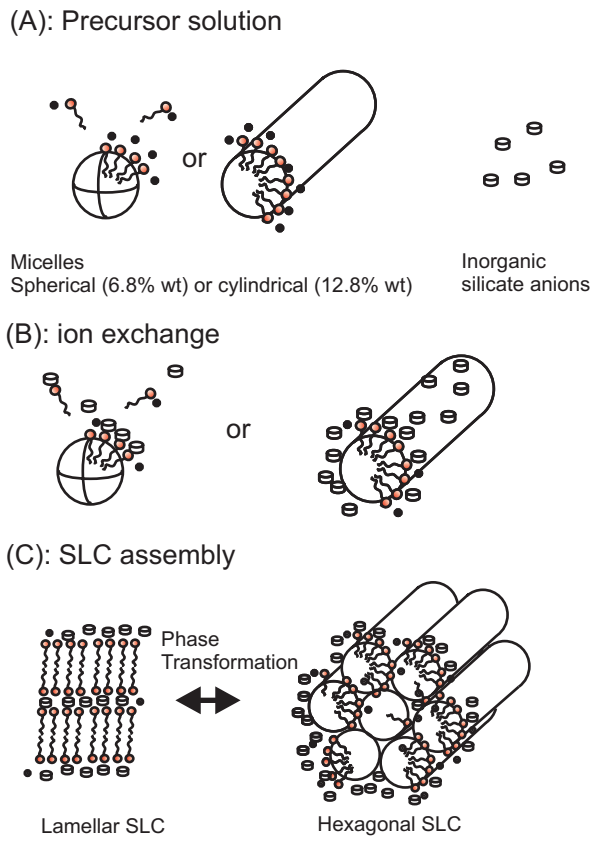

Figure 2.6: Schematic diagram of the cooperative organization of silicate-surfactant mesophases. (A) Organic and inorganic precursor solutions. Depending on the concentration of the surfactant, the initial organic precursor consists of spherical or cylindrical (or ellipsoidal) micelles that are in dynamic equilibrium with single surfactant molecules. The inorganic precursor solution at high pH contains predominantly multiply charged silicate anions. (B) Immediately after the two precursor solutions are mixed, silicate oligomers ion exchange with counter ions of surfactants to form inorganic-organic aggregates, whose structure can be different from that of the precursor micelles. (C) Multidentate interactions of oligomeric silicate units with the surfactant molecules has several implications. In particular, the screening of the electrostatic double-layer repulsion among aggregates can induce self-assembly of SLC mesophases. The processes of ion exchange and self-assembly appear to occur on comparable time scales. (46)

In (44) a conclusion on the dependence of the dominant synthesized product on the surfactant/silicon ratio is derived for the hydrothermal synthesis method. If $C_{16}H_{33}(CH_3)_3N^+$/Si is less than 1, the predominant product appears to be the hexagonal phase (MCM-41). If $C_{16}H_{33}(CH_3)_3N^+$/Si is larger than 1, a cubic phase can be produced. The diffraction data of the cubic phase are consistent with space group I_a3d. If $C_{16}H_{33}(CH_3)_3N^+$/Si increases further, another material is formed. The as-synthesized form exhibits a fairly well defined XRD patterns. After calcination of as-synthesized product, all XRD pattern definition is lost. The XRD patterns of these as-synthesized products characteristicall display multiple peaks that have higher orders of the first peak, suggesting a lamellar type material. So under this situation ($C_{16}H_{33}(CH_3)_3N^+$/Si$\gg$ 1) a lamellar material is obtained that is unstable with respect to calcination.

2.2.2 Characterization methods

Mesoporous materials can be characterized with XRD, HRTEM (High Resolution Transmission Microscopy) and SEM to study crystal structure and morphology. To study absorption behaviour of porous materials benzene sorption isotherms, argon physisorption isotherms, and temperature programmed amine desorption (TPAD) can also be used. (44) Solid-state ^{13}C NMR and solution ^{13}C NMR are applied to study surfactant molecules and ^{29}Si-NMR is used to study states of ^{29}Si nuclei. Usually MAS ^{29}Si-NMR is measured using cross polarization (CP) techniques to enhance sensitivity.

2.2.3 States of Si atoms in silicate

Depending on the number of *bridged* oxygen atoms attached to the silicon of interest, silicon atoms in the structure can be defined as Q^0, Q^1, Q^2, Q^3 and Q^4.

1. Q^0: No bridged oxygen atoms are attached to Si meaning Si is in an isolated [SiO_4] tetrahedron. For example, the silicon atom in silicic acid ($Si(OH)_4$) is in Q^0 state.

2. Q^1: One bridged oxygen atom (–Si–O–Si–) is attached to the silicon (Fig.2.7) and Q^1 can be interpreted as structures with pairs of tetrahedra sharing corners (Fig.2.8).

3. Q^2: Two bridged oxygen atoms are attached to the silicon (Fig.2.7) and Q^2 can be interpreted as structures with chains of tetrahedra. (Fig.2.8).

4. Q^3: Three bridged oxygen atoms are attached to the silicon (Fig.2.7) and Q^3 can be interpreted as structures of sheet silicates. (Fig.2.8).

5. Q^4: Four bridged oxygen atoms are attached to the silicon (Fig.2.7) and Q^4 can be interpreted as a three-dimensional framework of silicates.

These different states of silicon atoms present in the structure can be determined by ^{29}Si NMR because they have different chemical shifts due to different electron environments (see Fig.2.9). Since the natural abundance of ^{29}Si, which has a spin quantum number $I = 1/2$, is very small (4.685%), the signal/noise ratio is rather poor

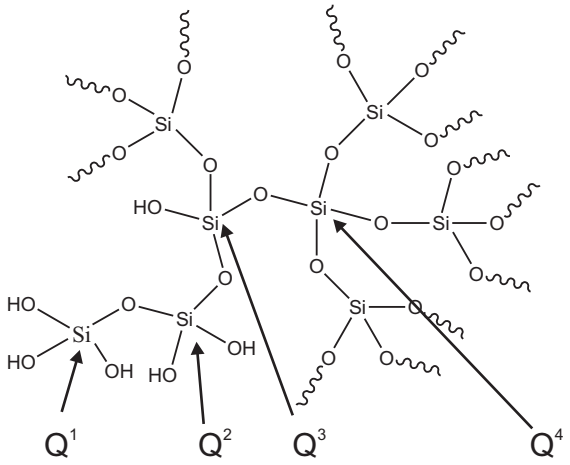

Figure 2.7: Assignment of silicon depending on its states in a silicon network (e.g. hydrolysis product of TEOS). Silicon in the Q^1 state has one bridged oxygen atom. Silicon in the Q^2 state has two bridged oxygen atoms and so on.

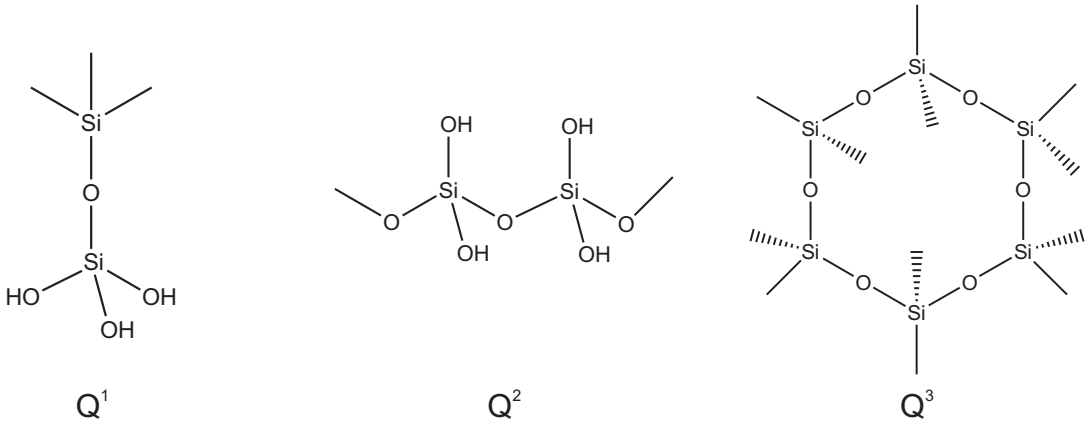

Figure 2.8: Interpretation of Q^1, Q^2, Q^3 states of silicon atoms. Q^1 states represent structures with pairs of tetrahedra sharing corners. Q^2 states represent structures with chains of tetrahedra. Q^3 represents sheet silicates.

and relaxation time is very long. Generally the signal of ^{29}Si can be enhanced with cross polarization (CP) MAS NMR techniques. One example of a ^{29}Si CP MAS NMR spectrum of synthesized magadiite is shown in Fig.2.9. (B). It should be noticed that CP MAS NMR is not a quantitative measurement because the technique transfers magnetization from more abundant (often ^{1}H) to the less abundant nucleus (^{29}Si in this case) via dipolar coupling between ^{1}H and ^{29}Si. Silicon nuclei surrounded by less ^{1}H give a smaller amplitude of the signal, so that the ratio of Q^n groups cannot be determined quantitatively by CP MAS NMR.

2.3 Alkali silicate minerals: kanemite, magadiite and kenyaite

As introduced in Sec.2.1.1, five alkali silicate minerals, natrosilicate ($Na_2Si_2O_5$), magadiite ($Na_2Si_{14}O_{29}{\cdot}11H_2O$), kenyaite ($Na_2Si_{22}O_{45}{\cdot}10H_2O$), makatite ($Na_2Si_4O_9{\cdot}5H_2O$), and kanemite ($NaHSi_2O_5{\cdot}3H_2O$) are distinct from the

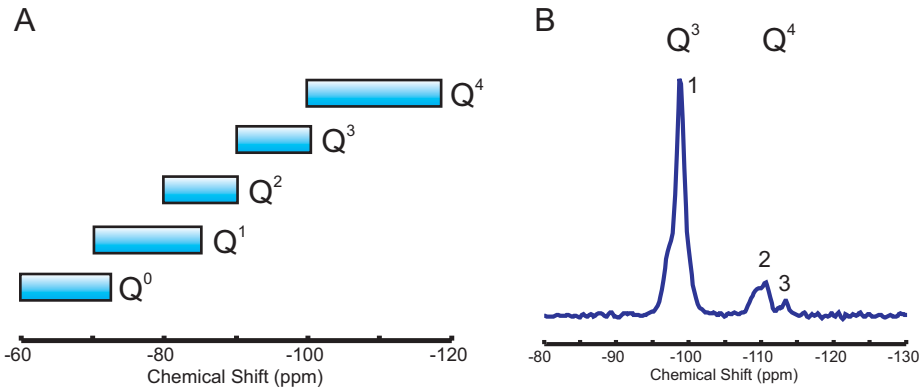

Figure 2.9: (A) The variation of the ^{29}Si NMR chemical shift for Si in tetrahedral coordination with the degree of polymerization of the tetrahedra. (B) An example of ^{29}Si CP MAS NMR of magadiite with a $\pi/2$ pulse length for protons of 5 microseconds and a contact time of 5 milliseconds. Peak 1: -98.82 ppm. Peak 2: -111.12 ppm. Peak 3: -112.78 ppm.

large number of other silicate minerals because of their properties. Their physical properties include a high capacity for ion exchange, whereby sodium ions can be replaced by protons, other cations or large quaternary ammonium or phosphonium ions. Instead of anhydrous sodium disilicate (natrosilicate, $Na_2Si_2O_5$), Almond and coworkers studied octasilicate and four other silicate minerals (Makatite, kanemite, magadiite, and kenyaite) which form a series of sodium polysilicate hydrates with a common formula, $Na_2O{\cdot}(4-22)SiO_2 \cdot (4-22)H_2O$. Characteristic structure properties are listed in Tab.2.2. (47)

silicate	formula	Basal spacing (nm)	connectivity ratio Q^3: Q^4
makatite	$Na_2O{\cdot}4SiO_2 \cdot 5H_2O$	0.903	1:0
kanemite	$Na_2O{\cdot}4SiO_2 \cdot 7H_2O$	1.03	1:0
octosilicate	$Na_2O{\cdot}8SiO_2 \cdot 9H_2O$	1.10	1:1
magadiite	$Na_2O{\cdot}14SiO_2 \cdot 10H_2O$	1.56	1:3[a]
kenyaite	$Na_2O{\cdot}22SiO_2 \cdot 10H_2O$	2.00	unknown[b]

Table 2.2: Formulae and structural details for five layered sodium polysilicate hydrates (Basal spacing values are obtained from powder X-Ray diffraction and Q^3: Q^4 ratios come from solid-state ^{29}Si NMR studies. [a] Conflicting values have been reported, but when T_1 of ^{29}Si is considered this is the most appropriate result. [b] Again conflicting values have been reported. By Almond and coworkers this value is 1:5. (47)

Kanemite, magadiite and kenyaite are the most interesting of these minerals because well-developed methods for synthesis of these minerals in the lab exist. (8)–(10) It should be noticed that only the structure of makatite is known, which consists of silicate layers separated by hydrated sodium ions. (11) Powder X-Ray diffraction suggests that this is also a reasonable model for the other four silicates and values of the basal spacing are listed in Tab.2.2. (49)-(50)

Beneke and Lagaly described the synthesis method of kanemite in detail in (8). An optimized method is described as following. One mole SiO_2 was dispersed in 100 ml methanol. Then cold NaOH solution (one mole in 35 ml H_2O, nearly saturated) was added slowly with the temperature was controlled below room temperature. The mixture was dried at 100°C and then calcined at 700°C for 5.5 hours. After cooling to room temperature the

product was dispersed in water. The product was filtered and dried to have kanemite. The authors also described hydrothermal methods with which kenyaite was synthesized. (9) Depending on the annealing temperature and period, mixtures of kenyaite, magadiite and the high temperature product quartz can be obtained.

Fletcher and Bibby studied synthesis of kenyaite and magadiite in presence of various anions. (12) Generally the synthesis of magadiite and kenyaite is based on hydrothermal methods. The hydrothermal synthesis method will be discussed in detail in Chapter 5. An autoclave is used to create supercritical conditions under which reactants (silica or sodium silicate, water and NaOH) are in a confined space and under high pressure. The supercritical condition is critical for the nucleation of solids and therefore obtaining the appropriate product, magadiite or kenyaite, depends on the supercritical condition in the autoclave.

Basics of supercritical fluids are introduced here. The *phase diagram* of a substance shows the regions of pressure and temperature at which its various phases are thermodynamically stable (Fig.2.10. (A)). When a liquid is heated in an open vessel, vaporization is free and the temperature at which the vapour pressure is equal to the external pressure is called *boiling temperature* T_b at that pressure. When a liquid is heated in a closed vessel boiling does not occur as it occurs in an open vessel. Instead, the vapour pressure, and hence the density of the vapour, rise continuously as the temperature is raised. At the same time, the density of the liquid decreases slightly as a result of its expansion (Fig.2.10. (B)). There comes a stage when the density of the vapour is equal to that of remaining liquid and the interface between the two phases disappears. The temperature at which the interface disappears is the *critical temperature*, T_c, of the substance. The vapour pressure at the critical temperature is called the *critical pressure*, p_c. At and above the critical temperature, a single uniform phase called a *supercritical fluid* fills the container. (20)

In hydrothermal synthesis, in an autoclave when a supercritical state or close to a supercritical state is achieved with heating (e.g. 150°C), the solubility of the solute changes dramatically resulting in nucleation of well-structured crystallized solids. With fixed composition of reactants and autogeneous pressure, annealing temperature and period are the critical parameters. The influence of these parameters will be studied in detail in the experimental part (Chapter. 5). The characterization methods are similar to that described in Sec.2.2.2.

In this thesis magadiite was synthesized based on the hydrothermal method. The reason for selecting alkali layered silicate to synthesize for our further studies of polymer-layered silicate hybrids system are follows:

1. The method to synthesize magadiite, kenyaite and kanemite is well developed. Compared with layered aluminosilicate it contains less metal ions which will simiplify the interpretation of NMR and EPR spectra. The three-component composition of reactants is easier to control.

2. The product has a similar structure to that of aluminosilicate utilized in PLS systems in industry or in science. The properties such as CEC and surface of layered silicate are comparable to that of natural layered silicates. The results obtained from further NMR and EPR characterization can thus be compared with that from our previous work.

3. Synthesis of MCM-50 type mesoporous materials was also tried. Control of the surfactant-directing agent is critical. Reproducibility of a stable lamellar structure was poor.

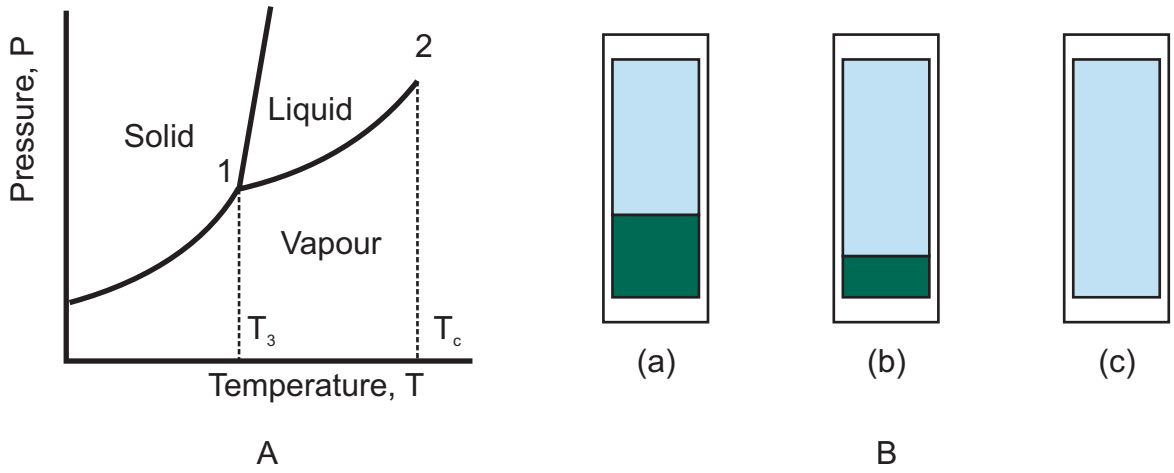

Figure 2.10: (A) The general regions of pressure and temperature where solid, liquid, or gas is stable (that is, has minimum molar Gibbs energy) are shown on this phase diagram. Point 1 is the triple point and T_3 is the temperature at triple point (coexistence of solid, liquid and gas phase). Point 2 is the critical point and T_c is the temperature at critical point. (B) (a) A liquid in equilibrium with its vapour. (b) When a liquid is heated in a sealed container, the density of the vapour phase increases and that of the liquid decreases slightly. (c) Above such temperature at which the two densities are equal and the interface between the fluids disappears, the surpercritical state is achieved. The pressure in supercritical state is very large: for water T_c is 374°C and the vapour pressure is then 218 atm (221 bar).

4. The synthesis of magadiite has a large yield (61%) and need shorter reaction time (48 to 72 hours) compared with synthesis of MCM-50 and other layered silicates (e.g. kanemite). The synthesized products proved to have nice WAXS patterns and SEM images indicating a well-defined layered structure.

Chapter 3

Electron Paramagnetic Resonance

3.1 Basics of Electron Paramagnetic Resonance

3.1.1 Energy levels of the free electron in a magnetic field

Electron Paramagnetic Resonance is the study of molecules and ions containing unpaired electrons by observing the magnetic fields at which they come into resonance with monochromatic radiation. (20) Like NMR focusses on behaviour of nuclei in magnetic fields, EPR studies electron behaviour in magnetic fields. Just as many nuclei possess spin angular momentum, the electron also has spin angular momentum $\vec{S}$, and in addition orbital angular momentum $\vec{L}$ if the electron is in an orbital with $l > 0$. Orbital and spin angular momentum of the electron give rise to a magnetic moment. Classically the value of the magnetic moment is expressed by the loop current and its area as Eqn.3.1 with i as loop current (Ampere), A as area of the current loop (m^2) and μ as *magnetic dipole moment* (Am^2).

$$\vec{\mu} = \vec{i} \cdot \vec{A} \tag{3.1}$$

Classically the energy E of a magnetic moment in a magnetic field is expressed as Eqn.3.2 with **B** as magnetic flux density of the magnetic field in unit of Tesla ($1\ T = 1\ V\ s/m^2$).

$$E = -\vec{\mu} \cdot \vec{B} \tag{3.2}$$

Quantum mechanically the Hamiltonian is given by Eqn.3.3.

$$H = -\hat{\mu}\mathbf{B} \tag{3.3}$$

As shown in Fig.3.1.(A) for an electron the magnetic moment arising from orbital angular momentum is antiparallel but proportional to it. The magnetic moment operator $\hat{\mu}_l$ that arises from orbital angular momentum is expressed as Eqn.3.4 with **L** as orbital angular momentum and γ_e as *magnetogyric ratio* of the electron:

$$\hat{\mu}_l = \gamma_e \hat{\mathbf{L}} \tag{3.4}$$

If the magnetic moment is treated as arising from the circulation of an electron of charge -e, from standard electromagnetic theory the magnetogyric ratio of the electron can be expressed as Eqn.3.5 with m_e as mass of electron. The negative sign means that the orbital moment μ_l is antiparallel to its orbital angular momentum $\vec{L}$.

$$\gamma_e = -\frac{e}{2m_e} \tag{3.5}$$

Similarly, the magnetic moment operator $\hat{\mu}_s$ that arises from spin angular momentum $\mathbf{S}$ is also proportional to spin angular momentum. However, the *g value (g_e)* has to be introduced which arises from relativistic effects and from interactions of the electron with electromagnetic fluctuations in the vacuum that surrounds the electron. $\widehat{\mu}_s$ can be expressed as Eqn.3.6. For the free electron $g_e = 2.002319...$

$$\widehat{\mu}_s = g_e \gamma_e \widehat{\mathbf{S}} \tag{3.6}$$

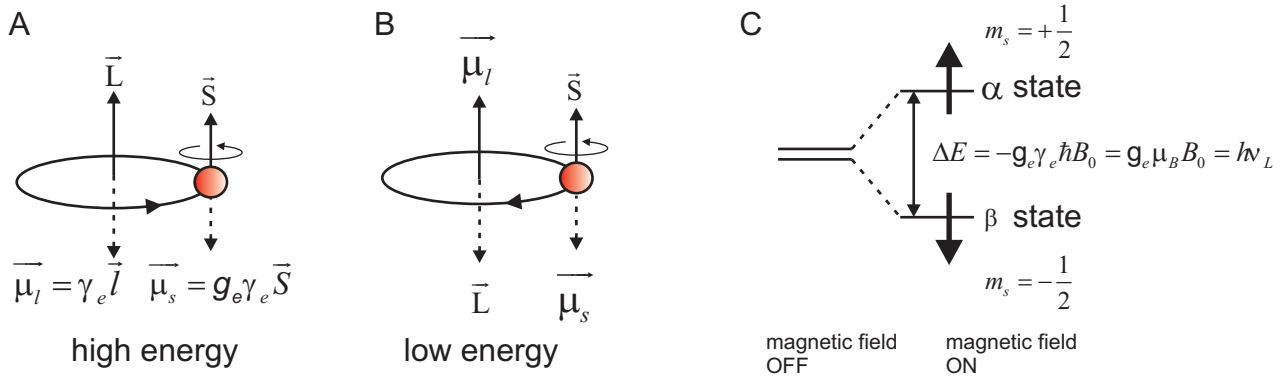

Figure 3.1: (A) and (B) Magnetic moment of free electron from spin angular momentum ($\vec{S}$) and orbital angular momtum ($\vec{L}$). *spin-orbital coupling*, the interaction of the spin magnetic moment with the magnetic field arising from the orbital angular momentum, results in energy difference between states in which the two magnetic moments are parallel and antiparallel to each other with (A) parallel (B) antiparallel. (C) For a free electron with $l = 0$, the energy levels split in presence of an external magnetic field $\vec{B}_0$. Because $\gamma_e < 0$, and from Eqn.3.2 the energy corresponding to the $|\beta\rangle$ state is lower than that for the $|\alpha\rangle$ state.

In solids usually only the magnetic moment arising from spin angular momentum is considered because of a *quenching* process which results in a shortening of the lifetime of the excited state. In solids the electronic orbital motion interacts strongly with the crystalline electron fields and becomes decoupled from spin. Thus orbital motion is usually quenched by the ligand field, resulting in spin only magnetism such as Cr^{3+} ($3d^3$), Mn^{2+} ($3d^5$) compounds.

If the system is not a spin only system ($l \neq 0$), the strength of the *spin-orbital coupling* (the interaction of the spin magnetic moment μ_s with the magnetic field arising from the orbital momentum $\mathbf{L}$) and its effect on the energy levels of the atom depends on the relative orientation of the spin and orbital magnetic moments, and therefore on the relative orientation of the two magnetic momenta. The *Total angular momentum J* of the electron, the vector sum of its spin and orbital momenta $\vec{j} = \vec{l} + \vec{s}$, can be used in the above formalism. When the spin and orbital angular momenta are nearly parallel, the total angular momentum is high, resulting in a high energy level

(unfavourable). When the two angular momenta are opposed, the total angular momentum is low, resulting in a low energy level which is a favourable state. (Fig.3.1. (B))

The free electron can be considered as a spin-only system ($l = 0$ as in an s-orbital). The Hamiltonian of the free electron in a magnetic field is expressed in Eqn.3.7 from Eqn.3.3 and Eqn.3.6:

$$H = -g_e \gamma_e \mathbf{B}\hat{\mathbf{S}} \tag{3.7}$$

From quantum mechanics, $\hat{\mathbf{S}}_z$, the z-component of $\hat{\mathbf{S}}$, has two eigenfunctions representing the two states α (also denoted as $\uparrow$ with eigenvalue $m_s\hbar = +\frac{1}{2}\hbar$) and β (also denoted as $\downarrow$ with eigenvalue $m_s\hbar = -\frac{1}{2}\hbar$). The degenerate states α and β have energy E_{m_s} which is the eigenvalue of Eqn.3.7 is expressed in Eqn.3.8 with $m_s = \pm\frac{1}{2}$:

$$E_{m_s} = -g_e \gamma_e m_s \hbar B_0 = g_e \mu_B m_s B_0 \tag{3.8}$$

with μ_B as *Bohr magneton* defined in Eqn.3.9 together with Eqn.3.5.

$$\mu_B = -\gamma_e \hbar = \frac{e\hbar}{2m_e} = 9.274 \times 10^{-24} \quad J \cdot T^{-1} \tag{3.9}$$

If we put $m_s = \pm\frac{1}{2}$ in Eqn.3.8 the energy difference $\triangle E$ between two states α and β can be calculated as Eqn.3.10 (Fig.3.1. (C)) with ν_L as the *Larmor frequency*.

$$\triangle E = E_\alpha - E_\beta = -g_e \gamma_e \hbar B_0 = g_e \mu_B B_0 = h\nu_L \tag{3.10}$$

3.1.2 Classical description of motion of an ensemble of electron spins (system with spin $S = \frac{1}{2}$)

The *macroscopic magnetization* M, resulting from an ensemble of electron spins which give rise to individual magnetic moments μ_i, at thermal equilibrium, is given by Eqn.3.11 with unit volume V:

$$\vec{M}_0 = \frac{\vec{\mu}}{V} \tag{3.11}$$

with the macroscopic moment $\vec{\mu} = \sum_{i=1}^{N} \vec{\mu}_i$ and N as the number of electrons.

According to classical physics, a magnetic field $\vec{B}_0$ acting on a magnetic moment $\vec{\mu}$ induces a torque $\vec{T}$ as $\vec{T} = \vec{\mu} \times \vec{B}$ (Fig.3.2. (A) and (B)). As shown in Fig.3.2. (A), the torque on a bar magnet in an external magnetic field rotates the bar until its plane is parallel to the field direction. In analogy to the magnetic bar, the torque $\vec{T}$ rotates the moment μ according to the right-hand-rule. The motion is described by Eqn.3.12 with **J** as macroscopic angular momentum.

$$\frac{d\vec{J}}{dt} = \vec{\mu} \times \vec{B} \tag{3.12}$$

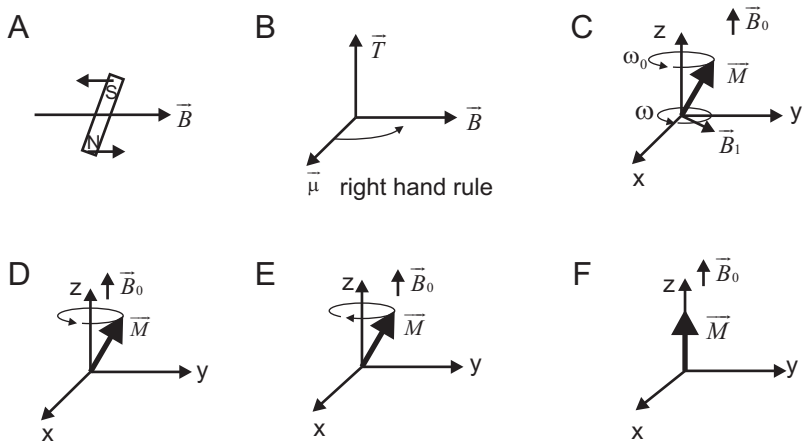

Figure 3.2: Classical description of a magnetic moment and magnetization behaviour in an external magnetic field. (A) The torque acts on a bar magnet in magnetic field. (B) The torque $\vec{T}$ rotates the magnetic moment $\vec{\mu}$ according to the right-hand-rule. (C) The precession of magnetization with Larmor frequency ω_0. This magnetization can interact with the introduced weak perturbation field $\vec{B}_1$ which is rotating in the xy-plane at frequency ω. (D) For $\omega_0 > 0$ which applies for electron and nuclear spin with $g_n < 0$, the precession proceeds counter clockwise. (E) For $\omega_0 < 0$ which applies for most nuclear spins, the precession proceeds clockwise. (F) After relaxation the equilibrium state is achieved.

From Eqn.3.6 ($\vec{J}$ is used as total angular momentum instead of $\vec{L}$), Eqn.3.11 and Eqn.3.12, the equation of motion of an angular momentum associated with a magnetic moment is given by Eqn.3.13.

$$\frac{d\vec{M}}{dt} = g_e \gamma_e \vec{M} \times \vec{B} \tag{3.13}$$

For nuclei with total angular momentum $\vec{J}$, this equation is $\frac{d\vec{M}}{dt} = \gamma_n \vec{M} \times \vec{B}$ (as now Eqn.3.4 is valid) and $\gamma_n = \frac{g_n e}{2m_p}$ with g_n as *nuclear g-value* which is usually in the range from -6 to +6 and m_p as mass of the nucleus. To solve the equation of motion, the differential equation can be represented by a matrix and expanded with the determinant as Eqn.3.14 for a possibly time dependent magnetic field $\mathbf{B}(t)$.

$$\begin{aligned} \vec{M} \times \vec{B} &= \begin{vmatrix} \vec{i} & \vec{j} & \vec{k} \\ M_x & M_y & M_z \\ B_x(t) & B_y(t) & B_z(t) \end{vmatrix} \\ &= \vec{i}(M_y B_z(t) - M_z B_y(t)) - \vec{j}(M_x B_z(t) - M_z B_x(t)) + \vec{k}(M_x B_y(t) - M_y B_x(t)) \end{aligned} \tag{3.14}$$

From Eqn.3.13 and Eqn.3.14 each equation of motion for the x-, y- and z-component, respectively, can be derived.

$$\frac{dM_x}{dt} = g_e \gamma_e (M_y B_z(t) - M_z B_y(t)) \tag{3.15}$$

$$\frac{dM_y}{dt} = g_e \gamma_e (M_z B_x(t) - M_x B_z(t)) \tag{3.16}$$

$$\frac{dM_z}{dt} = g_e\gamma_e(M_xB_y(t) - M_yB_x(t)) \tag{3.17}$$

For a static magnetic field $\vec{B}_0$ along the z-direction, as $B_z = B_0 =$ constant and $B_x = B_y = 0$, the equation of motion for each component becomes:

$$\frac{dM_x}{dt} = g_e\gamma_e M_yB_0 \tag{3.18}$$

$$\frac{dM_y}{dt} = -g_e\gamma_e M_xB_0 \tag{3.19}$$

$$\frac{dM_z}{dt} = 0 \tag{3.20}$$

From Eqn.3.20 it turns out that the z-component of M_z of the magnetization during motion is constant. The harmonic differential equation Eqn.3.18 and Eqn.3.19 can be solved as follows with *angular Larmor frequency* $\omega_0 = -\gamma_eB_0 = 2\pi\nu_L$ which is consistent with Eqn.3.10.

$$M_x(t) = M_x(0)\cos(\omega_0 t) \tag{3.21}$$

$$M_y(t) = M_x(0)\sin(\omega_0 t) \tag{3.22}$$

These equations of motion describe a *precession* of the magnetization vector on a cone (Fig.3.2, (D), (E)) in presence of an external static magnetic field ($\vec{B}_0$). This precession is characterized by the angular Larmor frequency ω_0. For electrons and nuclei with $g_n < 0$ the precession proceeds counter clockwise (Fig.3.2, (D)). For most nuclear spins with $g_n > 0$ the procession proceeds clockwise (Fig.3.2, (E)). After relaxation the equilibrium state is achieved with macroscopic magnetization $\vec{M}$ parallel to the direction of the magnetic field (Fig.3.2, (F)).

3.1.3 The effects of an additional small magnetic field $\vec{B}_1$ ($B_1 \ll B_0$)

From the classical vector model of magnetic resonance it is known that the additional pertubation field $\vec{B}_1$ must be perpendicular to the external field $\vec{B}_0$ to give rise to transitions between the quantum states. In a resonance experiment, a linearly polarized magnetic field $\vec{B}_1$ (for NMR, it is in the radio frequency, for EPR, it is in the microwave frequency range) is applied in the xy-plane to induce transitions between the two spin states (Fig.3.2, (C)). This linearly polarized field can be considered as a superposition of two circularly polarized fields, one of them rotating clockwise, the other one rotating counter clockwise. Only the component which has the same sense of rotation as the spin precession interacts with the spin. The macroscopic magnetization can interact with the weak pertubation magnetic field $\vec{B}_1$ if its oscillatory frequency ω is close to the precession frequency ω_0. If ω differs strongly from ω_0, the precessing magnetic moment will not seriously be affected by $\vec{B}_1$ for the $\vec{M}$ component in xy-plane will pass in and out of phase with $\vec{B}_1$ and there will no resultant interaction.

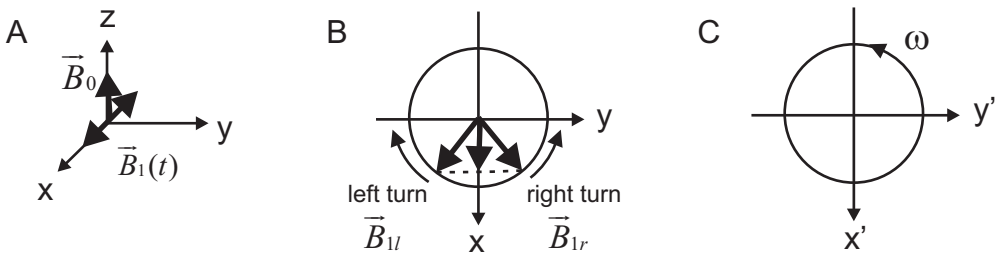

Figure 3.3: (A) A linearly polarized field $\vec{B}_1$ is applied. For EPR, the oscillatory transverse magnetic field $\vec{B}_1$ is generated by a microwave cavity. For NMR it is generated by a coil in the xy-plane. (B) The oscillating field $\vec{B}_1$ consists of two components: left turn $\vec{B}_{1l}$ which turns clockwise; and right turn $\vec{B}_{1r}$ which turns counter clockwise. (C) For the rotating frame the z'-axis coincides with the original laboratory z-axis and x'-, y'-axis are rotating about the z'-axis at a frequency ω which is the same as that of the oscillating field $\vec{B}_1$. In the rotating frame $\vec{B}_{1r}$ is time-independent.

In Fig.3.3. (A) it shows that a linearly polarized magnetic field $\vec{B}_1$ is applied in xy-plane. Experimentally in EPR the oscillatory transverse magnetic field is generated by a microwave cavity. In NMR this field is generated in radio frequency by a coil at in the xy-plane. This linearly polarized field can be written as a sum of right-handed and left-handed circularly polarized fields with $\vec{B}_{1l}$ clockwise and $\vec{B}_{1r}$ counter clockwise (Fig.3.3. (B)).

$$\vec{B}_{1x}(t) = 2B_1 \cos(\omega t)\vec{e}_x = \vec{B}^l_{1x}(t) + \vec{B}^r_{1x}(t) \tag{3.23}$$

As shown in Fig.3.3. (B), the $\vec{B}_{1l}$ and $\vec{B}_{1r}$ can be expressed by Eqn.3.24 and Eqn.3.25 respectively.

$$\vec{B}_{1l}(t) = B_1 \cos(\omega t)\vec{e}_x - B_1 \sin(\omega t)\vec{e}_y \tag{3.24}$$

$$\vec{B}_{1r}(t) = B_1 \cos(\omega t)\vec{e}_x + B_1 \sin(\omega t)\vec{e}_y \tag{3.25}$$

The left turn component $\vec{B}_{1l}(t)$, which is counter rotating with the spin precession (Fig.3.2. (D)), can be neglected in a good approxiamtion. The right turn component $\vec{B}_{1r}(t)$ interacts with the spin, as it rotates with the same sense as the magnetization vector precesses (Fig.3.2. (D)). Only this right turn component is effective in inducing resonance transitions.

From Eqn.3.25 the total time-dependent magnetic field $\vec{B}_0 + \vec{B}_{1r}$ is now given by the components in the *laboratory frame*;

$$\text{in the laboratory frame} \begin{cases} B_x(t) = B_1 \cos(\omega t) \\ B_y(t) = B_1 \sin(\omega t) \\ B_z(t) = B_0 \end{cases} \tag{3.26}$$

To simplify the equation of motion, the *rotating frame* is introduced which rotates counter clockwise with angular frequency ω about the z-axis of the original laboratory frame (Fig.3.3. (C)). In the rotating frame, the

z'-axis is the same as the original laboratory z-axis. The x' and y'-axes rotate about the z'-axis at a frequency ω. In the rotating frame, $\vec{B}_{1r}$ is time independent. The magnetic field $\vec{B}_0 + \vec{B}_{1r}$ is now given by the components:

$$\text{in rotating frame} \begin{cases} B_x = B_1 \\ B_y = 0 \\ B_z = B_0 \end{cases} \tag{3.27}$$

The strength of the oscillatory field is quantified by $\omega_1 = \gamma_e B_1$. The resonance offset Ω_0 is defined by Eqn.3.28 with ω_0 as Larmor frequency of magnetization.

$$\Omega_0 = \omega_0 - \omega \tag{3.28}$$

In case of $|\Omega_0| \gg \omega$, the irradiation is called *off-resonance* (Fig.3.4. (A),(D)). The spin system is not significantly perturbed by the induced field $\vec{B}_1$ and the precession remains the same as that in a static field $\vec{B}_0$. *On-resonance* irradiation occurs if ω equals ω_0 ($\Omega_0 = 0$, Fig.3.4. (B),(E)). The precession due to the static field vanishes in the rotating frame. Only the oscillatory field drives the motion of the magnetization vector which precesses with angular frequency ω_1 about the x'-axis of the rotating frame (Fig.3.4. (E)). In the frame rotating with the Larmor frequency, the induced field $\vec{B}_1$ appears to be stationary. If the resonance offset Ω_0 is on the ω_1 scale ($|\Omega_0| \approx \omega_1$) the slightly off-resonance motion is called *nutation*. The magnetization vector precesses about an effective field that can be pictured as the vector sum of $\vec{\Omega}_0$ and $\vec{\omega}_1$ (Fig.3.4. (C),(F)). The precession cone is characterized by an angle θ with $\theta = \arctan(\omega_1/\Omega_0)$.

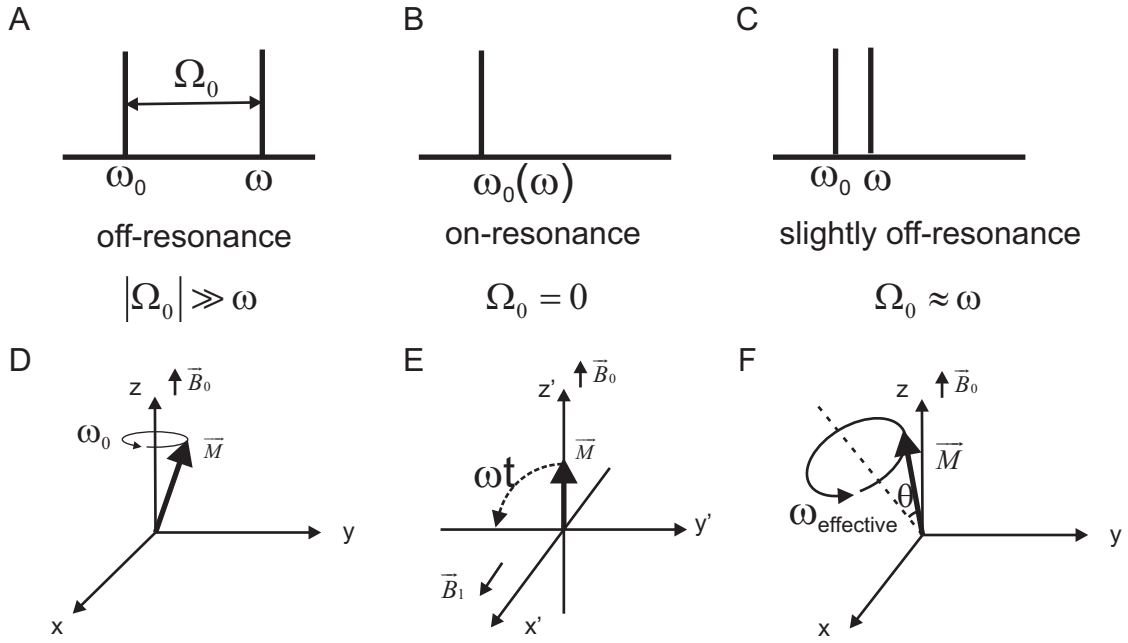

Figure 3.4: (A) Off-resonance irradiation. (B) On-resonance irradiation. (C) Slightly off-resonance irradiation. (D) The spin system is not significantly perturbed under off-resonance irradiation. (E) Under on-resonance irradiation, in the rotating frame with Larmor frequency, the magnetization rotates about the x'-axis at the Larmor frequency. (F) Under slightly off-resonance irradiation, the magnetization vector precesses about an effective field.

3.1.4 Spin relaxation and Bloch equations

After the spin system is excited by an oscillatory magnetic field in the radio frequency (NMR) or microwave frequency (EPR) range, the macroscopic magnetization vector will undergo precession. As we assumed that the experiments start with the magnetization vector $\vec{M}_0$ at thermal equilibrium (along the direction of the static magnetic field $\vec{B}_0$, Fig.3.2. (F)), the process that returns from excited state to equilibrium state is called *spin relaxation*.

At thermal equilibrium under the static magnetic field $\vec{B}_0$ the spins have a Boltzmann distribution, with more β spins than α spins (for electrons) (Fig.3.5). By irradiation of $\vec{B}_1$ the equilibrium is disturbed. As long as irradiation continues, equilibrium is not attained. If the irradiation is switched off again, the precessing spins will find their way back to the thermal equilibrium distribution (relaxation).

There are two processes contributing to relaxation: *longitudinal relaxation (spin-lattice relaxation)* and *transverse relaxation (spin-spin relaxation)* (Fig.3.6). The z-component of magnetization reverts to its equilibrium state $\vec{M}_0$ with a time constant called the longitudinal relaxation time T_1 (Fig.3.5). It is also called spin-lattice relaxation time because this relaxation process involves giving up energy to the surroundings (the 'lattice') as β spins revert to α spins. The longitudinal relaxation process can be expressed as:

$$M_z(t) - M_0 \propto e^{-t/T_1} \tag{3.29}$$

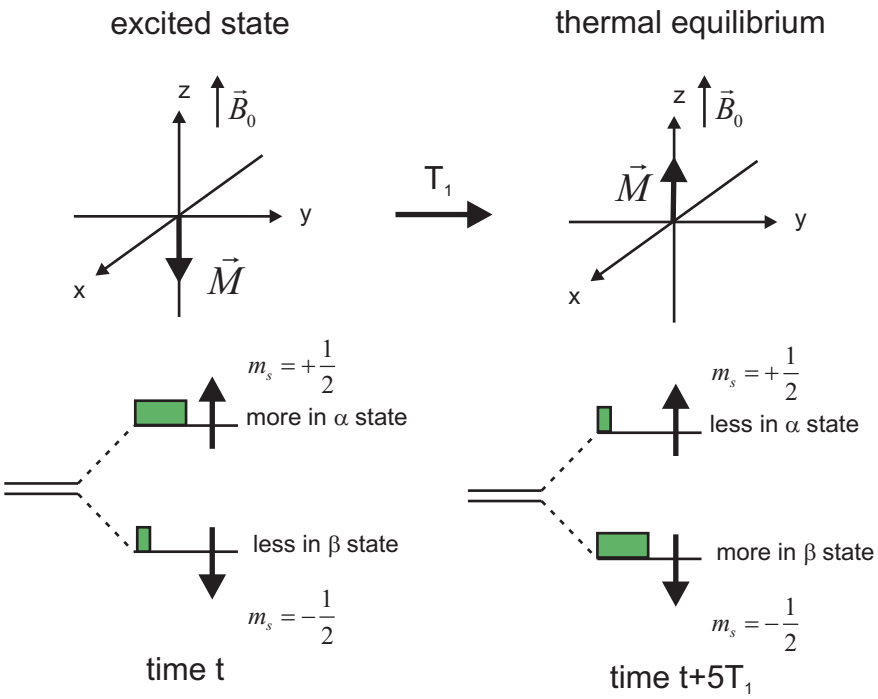

Figure 3.5: Longitudinal relaxation (spin-lattice relaxation). After irradiation with duration $t = \frac{\pi}{\omega_1}$, the magnetization is flipped meaning $|\beta\rangle$ is more populated. After a time that is a small multiple of T_1 (e.g. $5 \times T_1$), the magnetization vector has returned back to the thermal equilibrium with the lower energy state $|\alpha\rangle$ being more populated.

As shown in Fig.3.5, after an irradiation time t ($t = \frac{\pi}{\omega_1}$), the net magnetization vector is flipped to the -z-direction. The populations revert to their thermal equilibrium values with less spins in the β state and more in the α state. After the longitudinal relaxation time T_1[1], the magnetization vector has returned back to the thermal equilibrium (+z-direction). The populations are back to their thermal equilibrium values with more in the β state and less in the α state.

At thermal equilibrium the transverse components of the magnetization vector are zero ($M_x = M_y = 0$). After the resonance irradiation the spins are bunched together immediately resulting in an orderly arrangement of spins in the excited state (Fig.3.6). After the irradiation, the individual spins spread out until they are randomly distributed with all possible angles around the z-axis (phase relaxation). Such transverse relaxation towards the equilibrium values ($M_x = M_y = 0$) does not necessarily require energy exchange with the surroundings. It can also arise from energy exchange between spins in the same ensemble. As shown in Fig.3.6, the populations of the states remain the same, only the relative phase of spins relaxes. Because the transverse relaxation involves the relative orientation of the spins, the transverse relaxation is also called spin-spin relaxation. The randomization of the spin direction occurs exponentially with a time constant called the transverse relaxation time T_2:

$$M_{x \text{ or } y}(t) \propto e^{-t/T_2} \tag{3.30}$$

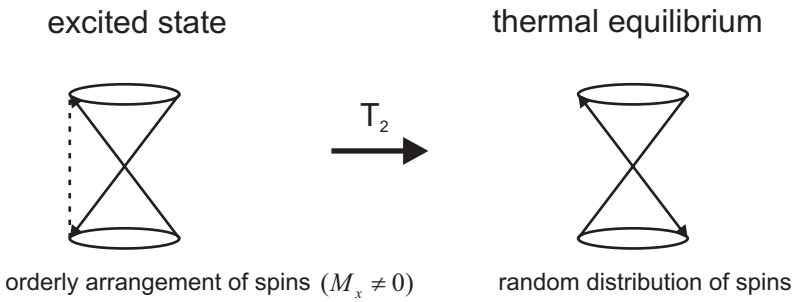

Figure 3.6: Transverse relaxation (spin-spin relaxation). The population of the states remains the same, only the relative phase of spins relaxes.

The equations of motion can be rewritten in the laboratory frame by introducing the relaxation processes into Eqn.3.15, Eqn.3.16 and Eqn.3.17.

$$\frac{dM_x}{dt} = g_e\gamma_e(M_yB_z(t) - M_zB_y(t)) - \frac{M_x}{T_2} \tag{3.31}$$

$$\frac{dM_y}{dt} = -g_e\gamma_e(M_xB_z(t) - M_zB_x(t)) - \frac{M_y}{T_2} \tag{3.32}$$

[1]The relaxation is not complete at time T_1, but to a good approximation at time $5 \times T_1$. The motion back to equilibrium is not a precession

$$\frac{dM_z}{dt} = g_e\gamma_e(M_xB_y(t) - M_yB_x(t)) - \frac{M_z - M_0}{T_1} \tag{3.33}$$

In the rotating frame with Eqn.3.27 and Eqn.3.28 the equations of motion are called *Bloch equations* and can be written as Eqn.3.34, Eqn.3.35 and Eqn.3.36 with $\omega_1 = \gamma_e B_1$:

$$\frac{dM_x}{dt} = -\Omega_0 M_y - \frac{M_x}{T_2} \tag{3.34}$$

$$\frac{dM_y}{dt} = \Omega_0 M_x - \frac{M_y}{T_2} \tag{3.35}$$

$$\frac{dM_z}{dt} = \omega_1 M_y - \frac{M_z - M_0}{T_1} \tag{3.36}$$

When the irradiation time is much longer than the longitudinal relaxation time T_1 and the transverse relaxation time T_2, the spin ensemble should attain a steady state with $\frac{dM_x}{dt} = 0$, $\frac{dM_y}{dt} = 0$ and $\frac{dM_z}{dt} = 0$. By solving Eqn.3.34, Eqn.3.35 and Eqn.3.36 for M_x, M_y and M_z, we obtain the following equations in the rotating frame:

$$M_x = M_0\omega\frac{\Omega_0 T_2^2}{1 + \Omega_0^2 T_2^2 + \omega_1^2 T_1 T_2} \tag{3.37}$$

$$M_y = M_0\omega\frac{T_2}{1 + \Omega_0^2 T_2^2 + \omega_1^2 T_1 T_2} \tag{3.38}$$

$$M_z = M_0\frac{1 + \Omega_0^2 T_2^2}{1 + \Omega_0^2 T_2^2 + \omega_1^2 T_1 T_2} \tag{3.39}$$

If the system is irradiated on resonance ($\Omega_0 = 0$), the components of magnetization during irradiation can then be calculated from Eqn.3.37, Eqn.3.38 and Eqn.3.39 in the rotating frame:

$$M_x = 0 \tag{3.40}$$

$$M_y = M_0\omega\frac{T_2}{1 + \omega_1^2 T_1 T_2} \tag{3.41}$$

$$M_z = M_0\frac{1}{1 + \omega_1^2 T_1 T_2} \tag{3.42}$$

If $\omega^2 T_1 T_2 \ll 1$, from Eqn.3.41 and Eqn.3.42 we get $M_y \approx M_0\omega T_2$ and $M_z \approx M_0$. The signal M_y is linear proportional to the strength of magnetic field ω_1 and this regime is called *linear regime* (Fig.3.6. (A)). If $\omega_1^2 T_1 T_2 \gg 1$, from Eqn.3.41 we will have $M_y = M_0\frac{1}{\omega_1 T_1}$ and for ω_1 to infinity M_y vanishes. The system in this regime is said to be *saturated* when the rate of upward and of downward transitions is equalized and no net energy is transferred between the irradiation field $\vec{B}_1$ and the spin system. Hence too much power of the irradiation field will result in less signal and the lineshapes are distorted. Usually the experiment is performed in the linear regime.

Consider the lineshapes of the resonance lines corresponding to M_x and M_y, i.e. the dependence of these magnetization vector components on Ω_0 in the linear regime. From Eqn.3.37 the dependence of M_x on Ω_0 as $M_x(\Omega_0)$ is a *Lorentzian dispersion line* as expressed by Eqn.3.43 with $\omega^2 T_1 T_2 \ll 1$. The lineshape is shown in Fig.3.6. (C).

$$M_x(\Omega_0) = M_0\omega\frac{\Omega_0 T_2^2}{1+\Omega_0^2 T_2^2} \tag{3.43}$$

From Eqn.3.38 and $\omega^2 T_1 T_2 \ll 1$, $M_y(\Omega_0)$ can be expressed by Eqn.3.44. The so called *absorption* lineshape of $M_y(\Omega_0)$ is shown in Fig.3.6. (B).

$$M_y(\Omega_0) = M_0\omega\frac{T_2}{1+\Omega_0^2 T_2^2} \tag{3.44}$$

By analyzing the absorption lineshape, *FWHH* (Full Width of Half Height) is $\frac{1}{2}M_0\omega T_2$ at $\Omega_0^2 T_2^2 = 1$ ($\Omega_0 = \pm\frac{1}{T_2}$) as shown in Fig.3.6. (B). If the absorption lineshape is plotted on a $\Omega_0 T_2$ scale the FWHH equals 2. If it is plotted on a Ω_0 scale the FWHH equals $\frac{2}{T_2}$.

As a consequence of the phase sensitive detector in a CW EPR spectrometer, the derivative of the absorption line ($\frac{dM_y}{dB}$) is measured as a function of the swept magnetic flux density B of the static field (Fig.3.6. (D)). Although the derivative absorption line looks similar as a dispersion line, it is much narrower. In fact, resolution in derivative absorption spectra is significantly better than in pure absorption spectra, while resolution in dispersion spectra is significantly worse.

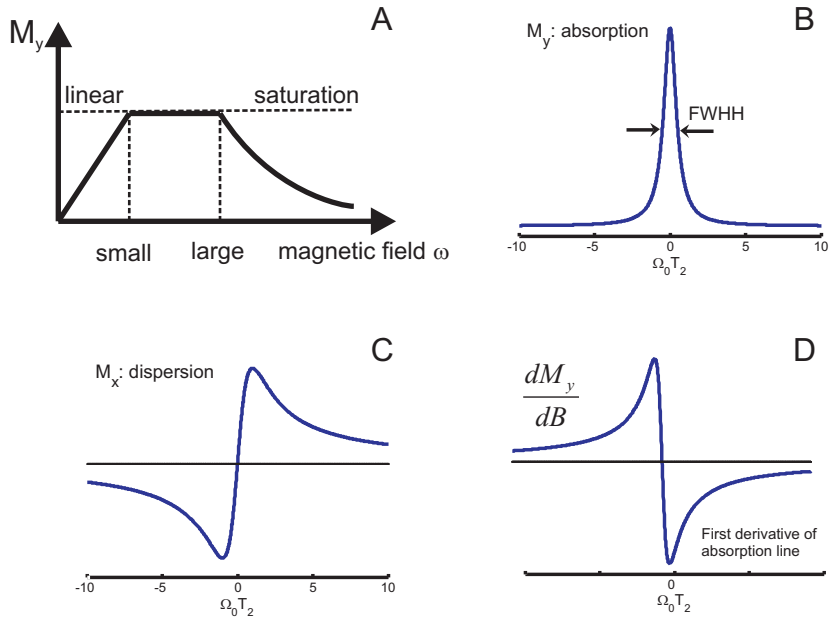

Figure 3.7: (A) Linear regime and saturation of the signal with respect to the irradiation frequency ω. (B) Absorption spectrum in which the line shape is a Lorentzian absorption line. In ω scale FWHH is $2/T_2$ and in ν scale FWHH is $1/(\pi T_2)$. (C) Dispersion spectrum in which the line shape is a Lorenzian dispersion line. (D) The spectrum in which the first derivative of the absorption line is measured.

3.2 Spin Hamiltonian of radicals in a static external magnetic field

3.2.1 General spin Hamiltonian

In Section.3.1. a classical description of the resonance transition of an ensemble of electrons with a macroscopic magnetization is given. However this classical picture does not work for multiple-pulse EPR if the interval between pulses is shorter than the longitudinal relaxation time T_1. Pulse EPR is applied as it reveals more detailed information on paramagnetic species by evaluating spin-spin or spin-orbital couplings which can not be pictured by classical description even in single pulse EPR. Such interactions must be examined by quantum mechanics.

If we have a system with an effective electron spin **S** and m nuclei with spin quantum number **I** in an external static field $\vec{B}_0$, the *static spin Hamiltonian* H_0 is described by Eqn.3.45. (23)

$$H_0 = H_{EZ} + H_{ZFS} + H_{HF} + H_{NZ} + H_{NQ} + H_{NN} \tag{3.45}$$

with the term H_{EZ} as the *electron Zeeman interaction*, H_{ZFS} as the *zero field splitting*, H_{HF} as the *hyperfine coupling*, H_{NZ} as the nuclear Zeeman interaction, H_{NQ} as the nuclear quadrupole coupling for nuclear spin quantum numbers $I > 1/2$, H_{NN} as the nuclear spin-spin interactions between pairs of nuclear spins. All these terms contribute to effective static spin Hamiltonian. These interactions are either *anisotropic* or *isotropic* depending on whether this interaction is orientation dependent or not. It should be noticed that a certain interaction could be isotropic or anisotropic depending on the state of the system. For example, electron Zeeman interaction is isotropic in a liquid sample however anisotropic in a solid sample. Fig.3.8 provides an overview of time scales and length scales that can be accessed by NMR and EPR.(23)

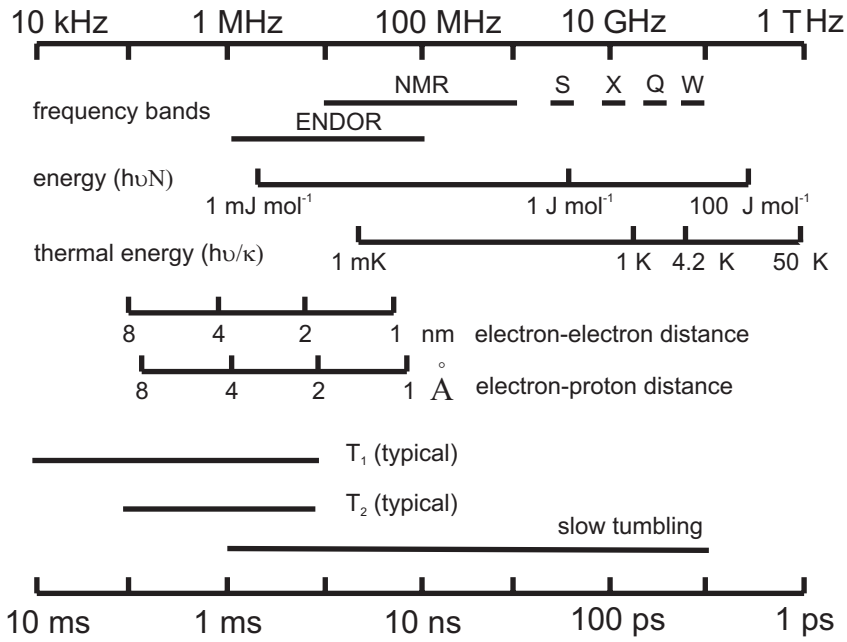

Figure 3.8: Frequencies, time scales, energies, and length scales in EPR experiments. (30)

3.2.2 The g-factor for radicals in a static magnetic field

As the systems of interest in this thesis are nitroxide radicals in solids, to a good approximation, the electron Zeeman interaction, which is the interaction of magnetic moments arising from electron spins with the external magnetic field $\vec{B}_0$, and the hyperfine interaction, the interaction between the electron spin and the magnetic dipole moments of nuclei present in the radical, dominate the spin Hamiltonian while other terms can be neglected. The Hamiltonian for the electron Zeeman interaction can be written as Eqn.3.46.

$$H_{EZ} = -\gamma_e \mathbf{B_0} g \hat{\mathbf{S}} = \frac{\mu_B}{\hbar} \mathbf{B_0} g \hat{\mathbf{S}} \tag{3.46}$$

Compared with Eqn.3.7 that applies for a free electron, now the g-factor (g) is represented by a tensor due to its orientation dependence. The g-tensor in EPR plays a similar role to the shielding constant in NMR, for it takes into account the presence of local fields induced by the applied field. In the liquid state the electron Zeeman interaction in such a system is isotropic because the molecule is tumbling rapidly. Then only the average g-value is observed (Eqn.3.47). The deviation of the average g-factor from the g-value of free electron ($g_e \approx 2.0023$) depends on the ability of the applied field to induce local electron currents in the radical, therefore its value gives some information about electronic structure. However, because g-values differ very little from g_e in many radicals in liquids (for example, 2.003 for H, 1.999 for NO_2, 2.01 for ClO_2), the isotropic g-value is mainly used in chemical applications to aid the identification of the species present in a sample.

$$H_{EZ} = -g_e \gamma_e \mathbf{B_0} \widehat{\mathbf{S}} = g_e \frac{\mu_B}{\hbar} \mathbf{B_0} \widehat{\mathbf{S}} \tag{3.47}$$

For radicals in solids, the g-tensor is anisotropic and it can be represented by a second-rank tensor ($3^{\text{rank}} = 9$ components). From matrix calculus, it is known that such a matrix can be diagonalized (this is equivalent to the determination of the eigenvalues of a matrix). Such a diagonalization is a rotation of the matrix in space until the non-diagonal elements vanish. The eigenvalues (energes) will not depend on the orientation of the reference axes frame, so the choice of the reference system is a completely arbitrary one. The axes system in which the tensor is diagonalized is called *principal axis system of the tensor* and denoted as { X, Y, Z } . In case of the g-tensor, the principal axes always coincide with the axes of molecular symmetry, if such symmetry exists (Fig.3.9. (A)). In the principal axes system, the Hamiltonian of electron Zeeman interaction can be written in matrix representation as Eqn.3.48.

$$\begin{aligned} H_{EZ} &= g_e \frac{\mu_B}{\hbar} \begin{bmatrix} B_x & B_y & B_z \end{bmatrix} \begin{bmatrix} g_{xx} & & \\ & g_{yy} & \\ & & g_{zz} \end{bmatrix} \begin{bmatrix} S_x \\ S_y \\ S_z \end{bmatrix} \\ &= g_e \frac{\mu_B}{\hbar} (g_{xx} B_x \widehat{S}_x + g_{yy} B_y \widehat{S}_y + g_{zz} B_z \widehat{S}_z) \end{aligned} \tag{3.48}$$

If the g-tensor is axially symmetric and the symmetry axis is chosen along the z-axis, we will have $g_{xx} = g_{yy} = g_\perp$ and $g_{zz} = g_{//}$.

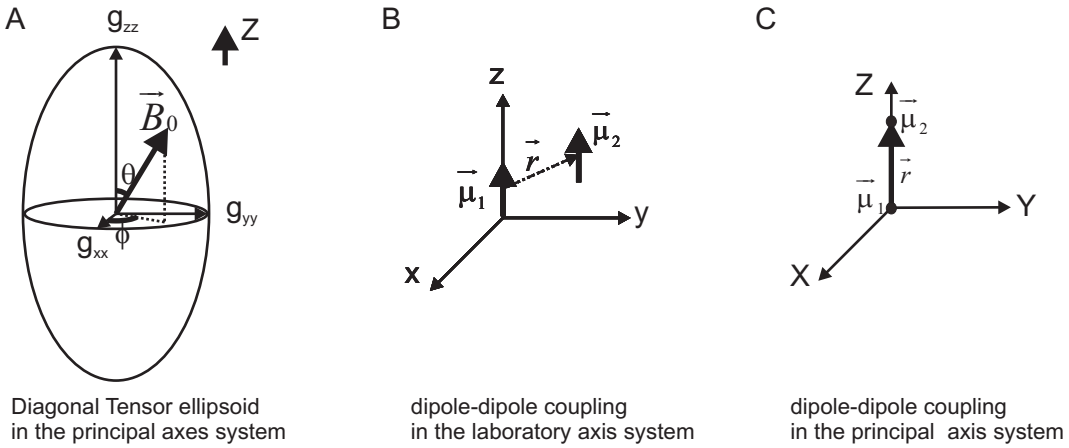

Figure 3.9: (A) Illustration of a g-tensor. The axes system is choosen to be the molecular axes system (principal axes system) in which the g-tensor is diagonal. (B) Dipole-dipole coupling in the laboratory axis system. (C) Dipole-dipole coupling in the principal axis system in which the dipolar coupling tensor is diagonalized.

3.2.3 The hyperfine tensor

There are two contributions to the hyperfine coupling: One is *isotropic hyperfine interaction* which is also called *Fermi contact interaction* arising from contact interaction between electrons in s-orbitals and nuclei. This part contributes to energies both for liquids and solids. The other part is the *anisotropic hyperfine interaction* which is a *dipole-dipole interaction* between the electron and nuclear spin and contributes only for solids.

Classically in the laboratory axes frame (x, y, z) (the z-axis coinciding with the direction of the static magnetic field $\vec{B}_0$), the energy U of dipole-dipole coupling between two magnetic *point* dipoles $\vec{\mu}_1$ and $\vec{\mu}_2$ is expressed by Eqn.3.49 with μ_0 as vacuum permeability ($\mu_0 = 4\pi \times 10^{-7}\ J^2 J^{-1} m^3$). (Fig.3.9. (B))

$$U = \frac{\mu_0}{4\pi}\left\{\frac{\vec{\mu}_1\vec{\mu}_0}{r^3} - 3\frac{(\vec{\mu_1}\vec{r})(\vec{\mu_2}\vec{r})}{r^5}\right\} \tag{3.49}$$

The appropriate quantum mechanical expression is obtained as Eqn.3.50 by using Eqn.3.6 ($\hat{\mu}_1 = g_e\gamma_e\hat{\mathbf{S}}$ for electron) and Eqn.3.4 ($\hat{\mu}_2 = \gamma\hat{\mathbf{I}}$ for nucleus) with γ as the characteristic value of the magnetogyric ratio for the nucleus under study and $\mathbf{I}$ as the spin angular momentum of the nucleus:

$$H_{HF}^{DD} = \frac{\mu_0}{4\pi} g_e\gamma_e\gamma\left\{\frac{\hat{\mathbf{S}}\,\hat{\mathbf{I}}}{r^3} - 3\frac{(\hat{\mathbf{S}}\,\mathbf{r})(\hat{\mathbf{I}}\,\mathbf{r})}{r^5}\right\} \tag{3.50}$$

In the laboratory axes frame (x, y, z), the product can be expanded as :

$$\hat{\mathbf{S}}\,\hat{\mathbf{I}} = \hat{S}_x\hat{I}_x + \hat{S}_y\hat{I}_y + \hat{S}_z\hat{I}_z \qquad \text{with} \quad \mathbf{S} \quad \text{as} \quad \begin{bmatrix} S_x & S_y & S_z \end{bmatrix} \quad \text{and} \quad \mathbf{I} \quad \text{as} \quad \begin{bmatrix} I_x \\ I_y \\ I_z \end{bmatrix} \tag{3.51}$$

$$\hat{\mathbf{S}}\,\mathbf{r} = \hat{S}_x x + \hat{S}_y y + \hat{S}_z z \qquad \text{with} \quad \mathbf{r} \quad \text{as} \quad \begin{bmatrix} x \\ y \\ z \end{bmatrix} \tag{3.52}$$

$$\hat{\mathbf{I}}\,\mathbf{r} = \hat{I}_x x + \hat{I}_y y + \hat{I}_z z \tag{3.53}$$

By inserting Eqn.3.51, Eqn.3.52 and Eqn.3.53 in Eqn.3.50 the Hamiltonian can be rewritten as Eqn.3.54:

$$H_{HF}^{DD} = \hat{\mathbf{S}}\,\mathbf{D}\,\hat{\mathbf{I}} \tag{3.54}$$

with $\mathbf{D}$ as the *dipolar coupling tensor* expressed by Eqn.3.55.

$$\mathbf{D} = \frac{\mu_0}{4\pi}\frac{\gamma_e\gamma}{r^5}\begin{vmatrix} r^2-3x^2 & -3xy & -3xz \\ -3xy & r^2-3y^2 & -3yz \\ -3xy & -3yz & r^2-3z^2 \end{vmatrix} \tag{3.55}$$

It is noticed that the dipolar coupling tensor $\mathbf{D}$ is symmetric and the trace of $\mathbf{D}$ is zero because $x^2+y^2+z^2 = r^2$.

$$Tr\mathbf{D} = \sum_i D_{ii} = (r^2-3x^2) + (r^2-3y^2) + (r^2-3z^2) = 0 \tag{3.56}$$

In the principal axes frame (X, Y, Z) (Fig.3.9. (C)), the dipolar coupling tensor $\mathbf{D}$ is a diagonalized matrix as Eqn.3.57 with the principal values D_{XX}, D_{YY} and D_{ZZ}.

$$\mathbf{D} = \begin{vmatrix} D_{XX} & 0 & 0 \\ 0 & D_{YY} & 0 \\ 0 & 0 & D_{ZZ} \end{vmatrix} \tag{3.57}$$

The Hamiltonian of anisotropic hyperfine coupling can be expressed as Eqn.3.58.

$$H_{HF}^{DD} = D_{XX}\hat{S}_X\hat{I}_X + D_{YY}\hat{S}_Y\hat{I}_Y + D_{ZZ}\hat{S}_Z\hat{I}_Z \tag{3.58}$$

The Hamiltonian of this dipole-dipole coupling between two aligned dipoles with angle θ in laboratory axes system with z-direction along the direction of static external magnetic field $\vec{B}_0$ is expressed as Eqn.3.59. μ_b is Bohr magneton as in Eqn.3.9 and μ_N is nuclear magneton with $\mu_N = \gamma\hbar/g_N$ (g_N is nuclear g-value described in Sec.3.1.2).

$$H_{HF}^{DD} = \left(\frac{\mu_0 g_e\gamma_e\gamma}{4\pi r^3}\right)(1-3\cos^2\theta)\widehat{S}_z\widehat{I}_z = -\left(\frac{\mu_0\, g_e\, g_N\, \mu_B\, \mu_N}{4\pi r^3\hbar^2}\right)(1-3\cos^2\theta)\widehat{S}_z\widehat{I}_z \tag{3.59}$$

The first-order contribution to the energy is the expectation value of this Hamiltonian for the ground-state wavefunction (without pertubation correction of $\vec{B}_1$).

$$E_{HF-DD}^{(0)} = -\left(\frac{g_e\, g_N\, \mu_B\, \mu_N\, \mu_0}{4\pi}\right)\left\langle\frac{1-3\cos^2\theta}{r^3}\right\rangle m_s m_l \tag{3.60}$$

For an anisotropic hyperfine coupling between a nucleus and an electron in an s-orbital, the angular integration can be performed immediately, with the result that the integral over $1-3\cos^2\theta$ vanishes as shown in Eqn.3.61 meaning that electrons in s-orbitals do not have an anisotropic hyperfine coupling with neighbouring nuclei.

However, in an s-orbital the electron can be found at the nucleus and consequently the point-dipole approximation is invalid. Isotropic hyperfine coupling arising from *Fermi-contact interaction* should be taken into account.

$$\int_0^{\pi} (1 - 3\cos^2\theta)\sin\theta\, d\theta = \int_{-1}^{1} (1 - 3x^2)\, dx = (x - x^3)\big|_{-1}^{1} = 0 \tag{3.61}$$

Because a magnetic nucleus and an electron may have a magnetic interaction by virtue of their contact, such magnetic interaction is called the Fermi-contact interaction. Only electrons in s-orbitals can show a Fermi-contact interaction since only they have a density at nucleus. As s-electrons have a spherically symmetrical distribution it also follows that the interaction is isotropic. The Hamiltonian for the Fermi-contact interaction is expressed by Eqn.3.62 with a as the *hyperfine constant* which is proportional to the probability density to find the electron at the nucleus ($a \propto |\psi_s(0)|^2$).

$$H_{HF}^{contact} = a\hat{\mathbf{S}}\,\hat{\mathbf{I}} \tag{3.62}$$

By combining the anisotropic and isotropic interaction the Hamiltonian of hyperfine coupling can be expressed by Eqn.3.63.

$$H_{HF} = \hat{\mathbf{S}}\,\mathbf{A}\,\hat{\mathbf{I}} \tag{3.63}$$

From discussion of Sec.3.2.2 and Sec.3.2.3 (Eqn.3.46 and Eqn.3.63), under a strong stationary external magnetic field approximation the total spin Hamiltonian of radicals will be:

$$H = \frac{\mu_B}{\hbar}\mathbf{B_0}\, g\,\hat{\mathbf{S}} + \hat{\mathbf{S}}\,\mathbf{A}\,\hat{\mathbf{I}} \tag{3.64}$$

3.3 Basics of Pulse EPR techniques

3.3.1 Energy levels of coupled spins with one electron S=1/2 and one nucleus I=1/2

The samples measured by CW and pulse EPR in this thesis are of nitroxide radicals which can be considered as a one-electron and one-nitrogen (^{14}N) system. However as for the nitrogen nucleus I=1, which has triplet states, the nucleus can not be desribed by a classical magnetic moment vector any more. To simplify the basics of pulse EPR we can start from the system with one electron ($S = 1/2$) and one nucleus with $I = 1/2$, such as a proton and thus have a classical picture of its energy levels.

For an $S = 1/2$ and $I = 1/2$ system with an isotropic g tensor and an anisotropic hyperfine interaction, the static Hamiltonian in the laboratory frame may be written as Eqn.3.65 with $\omega_S = g_e\mu_B B_0/\hbar$ as angular Larmor frequency of electron and $\omega_I = g_n\mu_B B_0/\hbar$ as the angular Larmor frequency of the nucleus. (23)

$$H_0 = \omega_S\mathbf{S}_z + \omega_I\mathbf{I}_z + \mathbf{S}\,\mathbf{A}\,\mathbf{I} \tag{3.65}$$

The first and second term arise from electron and nuclear Zeeman interaction. The third term arises from hyperfine coupling that is associated with dipole-dipole coupling (Sec.3.2.3). It is shown in Fig.3.10 that dipole-dipole coupling can shift the energy levels of corresponding states. If the hyperfine coupling is isotropic, the splitting of energy levels can be plotted as shown in Fig.3.11. The degenerate four states of the sytem will split in the presence of an external magnetic field. From Fig.3.1 because $\gamma_e < 0$ for the electron (magnetic moment antiparallel to spin angular momentum) the $|\beta_S\rangle$ state has lower energy lever than the $|\alpha_S\rangle$ state. For nuclei, because $\gamma_e > 0$ (magnetic moment parallel to spin angular momentum), the $|\beta_I\rangle$ state has higher energy than the $|\alpha_I\rangle$ state. So for a positive hyperfine coupling (dipole-dipole coupling) the system state $|\beta_S\alpha_I\rangle$ has lowest energy. In the *weak-coupling* case, energy levels retain the same order after being shifted by hyperfine coupling. However in the *strong-coupling* case, the $|\alpha_S\alpha_I\rangle$ state is shifted to the highest level. In Fig.3.11 the hyperfine coupling is simply plotted as $1/4a$ with 'a' as hyperfine coupling constant if the hyperfine coupling is isotropic and can be evaluated. In this case the eigenvalue of the hyperfine coupling term is am_Sm_I in angular frequency units. So for the $|\beta_S\alpha_I\rangle$ state the total energy is shifted by $-1/4a$ in angular frequency units.

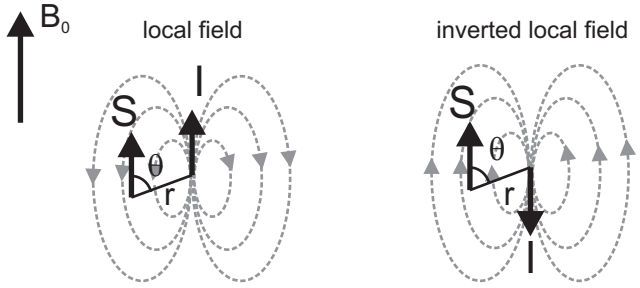

Figure 3.10: Dipole-dipole coupling between two spins **I** and **S**. The dipole moment arising from spin **S** can feel the local field imposed by the presence of the dipole moment of nucleus **I** nearby. The magnetic moment from **S** can either be shielded (left) or deshielded (right) from the external field resulting in shifts of corresponding energy levels.

It can be derived quantum-mechanically that in EPR the selection rule for resonance transitions in a coupled system with an electron spin and a nuclear spin follows Eqn.3.66.(20)

$$\triangle m_S = \pm 1 \qquad \triangle m_I = 0 \qquad \text{for EPR} \tag{3.66}$$

And for NMR the selection rule is:

$$\triangle m_I = \pm 1 \qquad \triangle m_S = 0 \qquad \text{for NMR} \tag{3.67}$$

The EPR stick spectra for the weak- and strong-coupling case are shown in Fig.3.12.(23) The allowed transitions in EPR (marked as 'a') follow selection rule as Eqn.3.66 and the fobidden transitions (marked as 'f') are called *double quantum transitions* (DQ). ω_{12} and ω_{34} characterize the transitions in the radiofrequency range in NMR. The filled blocks represent the populated states and the blank blocks represent the unpopulated states. This energy

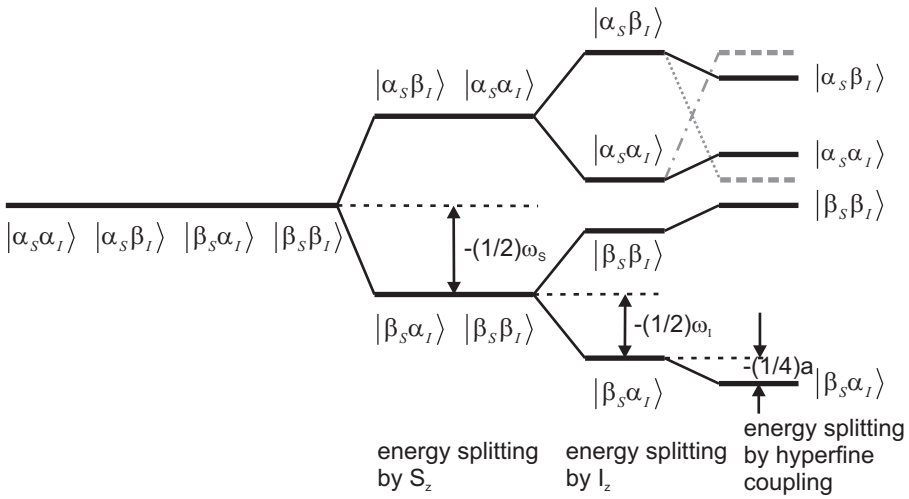

Figure 3.11: Energy level splitting of coupled spins as electron spin **S** and **I**. Four degenerate states split in presence of an external magnetic field. Energy splitting caused by electron Zeeman interaction results in the $|\beta_S\rangle$ state as the lower energy state. Then nuclear Zeeman interaction results in further splitting with the $|\alpha_I\rangle$ state as the lower energy state. Hyperfine coupling causes shift of energy levels and the dotted line represents the strong-coupling case.

splitting model is very useful for pulse EPR experiments such as *ENDOR* (Electron Nuclear Double Resonance) and *ESEEM* (Electron Spin Echo Envelope Modulation) which will be discussed later.

From (23) it can be derived that the splitting energy ω_+ (Fig.3.12.(B)) between two forbidden transitions in EPR and the the splitting energy ω_- between the two allowed transitions (DQ) are approximately the hyperfine coupling and twice the nuclear Zeeman frequency. They are defined by Eqn.3.68 and Eqn.3.69.

$$\omega_+ = \omega_{12} + \omega_{34} \tag{3.68}$$

$$\omega_- = \omega_{12} - \omega_{34} \tag{3.69}$$

3.3.2 Primary echo (Hahn echo) and phase cycling

Before we start to introduce the EPR double resonance technique, the magnetic vector picture in the spin echo experiment can help to understand macroscopic magnetization behaviour in pulse EPR experiments. As we have seen in Fig.3.4. (E), the induced magnetic field $\vec{B}_1$ in the xy-plane (laboratory frame) drives the motion of the overall magnetization vector (as an ensemble of a number of different magnetization with similar precession frequencies) to rotate about x'-axis in rotating frame with frequency ω_1. If the pulse starts at thermal equilibrium and lasts for a certain time with $\omega_1 t = \pi/2$ the magnetization is driven to the -y'-axis.

The *Hahn Echo* experiment is shown in Fig.3.13. (F). (20) At thermal equilibrium when the overall macroscopic magnetization vector is along the same direction as the external static magnetic field $\vec{B}_0$, a $\pi/2$ pulse (with the irradiation power in frequency units ω_1 and duration t so that $\omega_1 t = \pi/2$) is applied. In the rotating frame (rotating

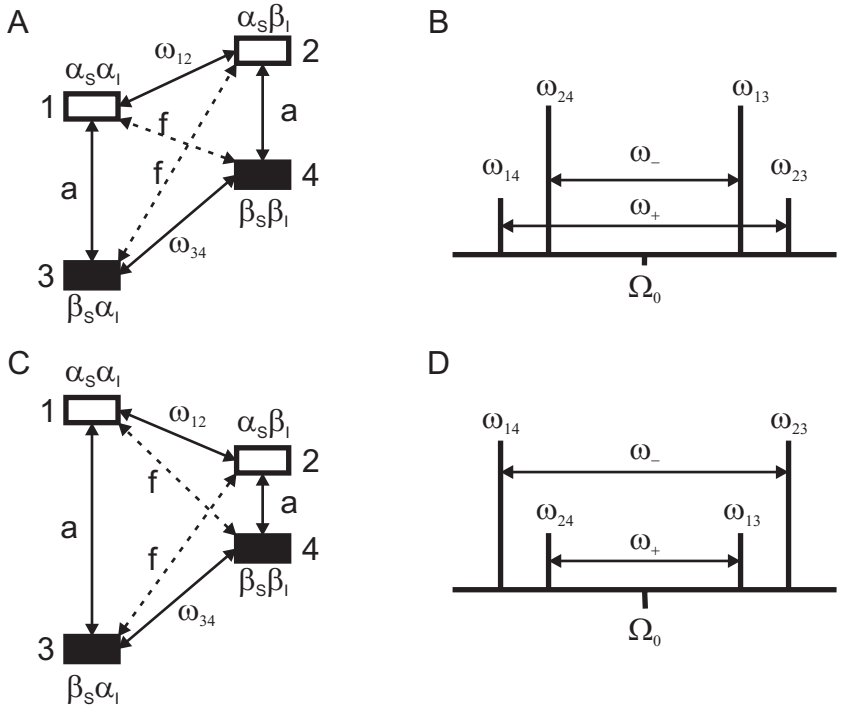

Figure 3.12: Energy level diagram (A), (C) and corresponding schematic EPR spectrum (B), (D) for an $S = 1/2$, $I = 1/2$ system with 'a' as allowed transitions and 'f' as forbidden transitions. ω_{12} and ω_{34} represent nuclear transitions. (A) and (B) weak-coupling case. (C) and (D) strong-coupling case.

at the same rate as the induced field of the pulse $\vec{B}_1$), $\vec{B}_1$ is stationary along the x'-axis. The magnetization is rotated about the x'-axis to the -y'-axis (Fig.3.13. (A)). The magnetization of the vector at time point 1 is given by Eqn.3.70.

$$\mathbf{M}(t=0) = -M_0\,\mathbf{e}_y \tag{3.70}$$

Now the individual spins of the ensemble begin to fan out because they have different Larmor frequencies, with some above the frequency ω_0 and some below. In the absence of $\vec{B}_1$ the spin ensemble also undergoes relaxation process to its thermal equilibrium state. After time τ the magnetization vector (at time point 2) for a spin packet with resonance offset Ω_0 is described by Eqn.3.71. The signal that is detected at this point has decayed with a time constant T_2^* because of the combined effects of field inhomogeneity and spin-spin relaxation (T_2) (Fig.3.13. (B)).

$$\mathbf{M}(\tau) = -M_0\cos(\Omega_0\tau)e^{-\frac{\tau}{T_2}}\,\mathbf{e}_y + M_0\sin(\Omega_0\tau)e^{-\frac{\tau}{T_2}}\,\mathbf{e}_x \tag{3.71}$$

After an evolution period τ, a $(\pi)_y$ pulse (with irradiation power ω_1 in angular frequency units lasting for a time so that $\omega_1 t = \pi$, and applied along the y-axis) is applied to the sample, the magnetization vectors are driven to rotate about the y'-axis of the rotating frame (Fig.3.13. (C)). When the $(\pi)_y$ pulse ends (at time point 3) the magnetization vectors are in the xy-plane: the x-component of the magnetization vector remains unchanged while

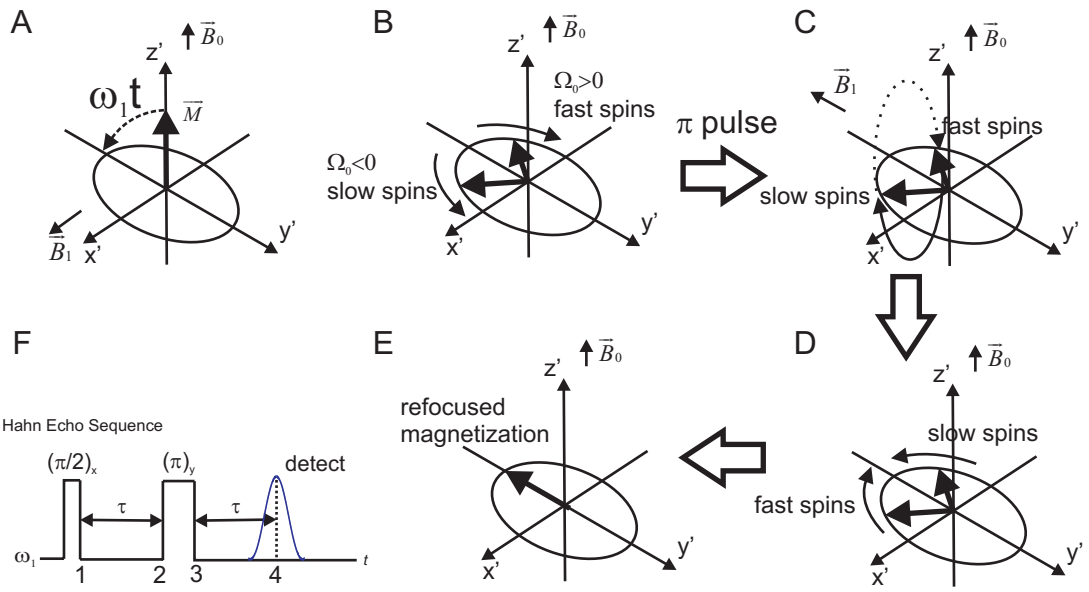

Figure 3.13: Primary echo (Hahn echo) pulse sequence and corresponding magnetization vector behaviour. (A) at time point 1. (B) during first evolution time τ until time point 2. (C) at time point 3. (D) during second evolution time τ. (E) at detection time point 4. (F) Primary echo pulse sequence.

the y-component is inverted (Eqn.3.72 with δ as infintesimal time).

$$\mathbf{M}(\tau+\delta) = M_0 \cos(\Omega_0\tau) e^{-\frac{\tau}{T_2}} \mathbf{e}_y + M_0 \sin(\Omega_0\tau) e^{-\frac{\tau}{T_2}} \mathbf{e}_x \tag{3.72}$$

Then the magnetization vectors start to precess in the same direction as that before the $(\pi)_y$ pulse (Fig.3.13. (D)). Thus the fan begins to close up again and the resultant signal begins to grow back into an echo. At time 2τ, all the vectors will be once more along the y'-axis, and the fanning out caused by the field inhomogeneity is *refocused*. The spin echo has reached its maximum (Fig.3.13. (E)). At time $t = 2\tau$ the magnetization vector is described by Eqn.3.73, independent from Ω_0.

$$\mathbf{M}(2\tau) = M_0 \, e^{-\frac{2\tau}{T_2}} \mathbf{e}_y \tag{3.73}$$

After the time 2τ, the magnetization will continue to precess, fanning out once again, giving a resultant signal that decays with time constant T_2^* which is the effective transverse relaxation time.

By this technique because the effects of field inhomogeneities have been suppressed by the refocusing, the echo signal as a function of time τ decays by the factor $e^{-2\tau/T_2}$ caused by spin-spin relaxation alone. The Hahn echo is applied in solid state EPR also because it is not possible to detect the *FID* (Free Induction Decay) signal immediately after a high power pulse. There is some deadtime t_d. If the FID decays significantly during this deadtime, it is no longer possible to compute the correct spectrum from the remaining signal by Fourier transformation. In partiular in solid state EPR the signal often decays almost completely during deadtime. In such situations, an echo experiment is required to detect any signal. It should be noticed that in the Hahn echo

experiment the evolution time τ should ideally be less than T_2 or at least not much longer than T_2.[1]

Just as the Hahn echo experiment, more pulse sequences can be designed in appropriate ways to have a better signal or separate interactions. The procedure to design multiple-pulse sequences by varying the phase of pulses and combining the signals to eliminate the overlap of signals is called *phase cycling*.

3.3.3 The stimulated echo

The maximum time after which a primary echo can be detected is limited by T_2. Interactions that are much smaller than the inverse of T_2 can not be separated by a primary echo experiment, and dynamic processes with characteristic times much shorter than T_2 can not be studied by a primary echo experiment alone. However, in solids, where usually $T_1 \gg T_2$, the natural limit of magnetic resonance experiments with respect to the magnitude of interactions and with respect to the timescale of dynamic processes is given by T_1. As T_1 is the longitudinal relaxation time corresponding to the magnetization vector component along the z-axis, the *stimulated echo experiment* described below is designed to store the magnetization along the z direction to have signals after long evolution time T.

The pulse sequence is shown in Fig.3.14 (A). The magnetization vector distributions corresponding to each time point from 1 to 6 are also shown in the (B) to (G) plots. As shown in (B) the magnetization vector is driven to the -y'-axis after a $(\pi/2)_x$ pulse. After a free evolution period of duration τ, a $(\pi/2)_x$ pulse is applied again. At time point 1 the magnetization vector after the first pulse can be expressed in the rotating frame by Eqn.3.74.

$$\mathbf{M}(\tau) = -M_0 \cos(\Omega_0 \tau) e^{-\frac{\tau}{T_2}} \mathbf{e}_y + M_0 \sin(\Omega_0 \tau) e^{-\frac{\tau}{T_2}} \mathbf{e}_x \tag{3.74}$$

At time point 3 after the $(\pi/2)_x$ pulse, the fanned-out magnetization vectors are forced to rotate about the x'-axis from the x'y'-plane to the x'z'-plane. For instance the magnetization vector labeled as 'a' rotates counter clockwise between time point 2 and time point 3. At this point the x'-component is the same as at time point 2 and the y'-component before the pulse now is changed to the z'-component. The magnetization vector after the second pulse can be expressed in the rotating frame by Eqn.3.75 with δ as infinitesimal time after the second pulse.

$$\mathbf{M}(\tau + \delta) = -M_0 \cos(\Omega_0 \tau) e^{-\frac{\tau}{T_2}} \mathbf{e}_z + M_0 \sin(\Omega_0 \tau) e^{-\frac{\tau}{T_2}} \mathbf{e}_x \tag{3.75}$$

At time point 4 when after free evolution time ($T_2 \ll T \ll T_1$), the x'-component is completely lost because of precession and T_2 relaxation towards its equilibrium value zero (Fig.3.14 (E4)). Neglecting the equilibrium polarization that is built up by longitudinal relaxation, the magnetization vector before the third pulse is described by Eqn.3.76.

$$\mathbf{M}(\tau + T) = -M_0 \cos(\Omega_0 \tau) e^{-\frac{\tau}{T_2}} e^{-\frac{T}{T_1}} \mathbf{e}_z \tag{3.76}$$

[1] In ENDOR we use $\tau = T_2$ in the stimulated echo experiment. In DEER we usually have $\tau > T_2$. This will be explained later.

At time point 5 another $(\pi/2)_x$ pulse again forces the magnetization vectors to rotate about x'-axis towards the x'y'-plane. The z'-component now changes to the -y'-component (Eqn.3.77).

$$\mathbf{M}(\tau + T + \delta) = M_0 \cos(\Omega_0 \tau) e^{-\frac{\tau}{T_2}} e^{-\frac{T}{T_1}} \mathbf{e}_y \tag{3.77}$$

In the final free evolution period of duration τ, the magnetization vector precesses in the x'y'-plane. The magnetization vectors can be described as Eqn.3.78.

$$\mathbf{M}(2\tau + T) = M_0 \, e^{-\frac{\tau}{T_2}} \, e^{-\frac{T}{T_1}} \, (\mathbf{e}_y \, \cos^2(\Omega_0 \tau) - \mathbf{e}_x \cos(\Omega_0 \tau) \sin(\Omega_0 \tau)) \tag{3.78}$$

At time point 6 (detection time), because half of the magnetization is lost as x'-component during time T, the stimulated echo signal has half the amplitude of the primary echo signal if longitudinal relaxation during time T is neglected.

$$\mathbf{M}_\infty(2\tau + T) = \frac{1}{2} M_0 \, e^{-\frac{\tau}{T_2}} \, e^{-\frac{T}{T_1}} \, \mathbf{e}_y \tag{3.79}$$

The derivation of the stimulated echo signal given from Eqn.3.79 neglects other dynamic processes that might change the resonance offset Ω_0 during time T, for instance reorientation of the molecule or chemical exchange. If such dynamic processes are relevant during the interpulse delay T, such processes can be characterized and more information on chemical structure or dynamics can be obtained.

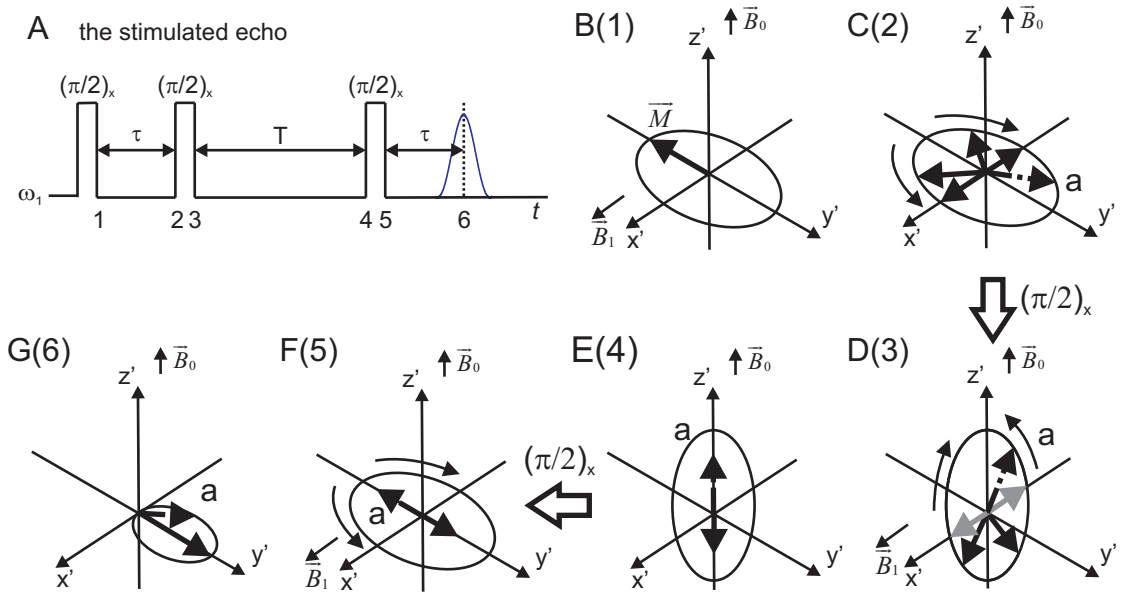

Figure 3.14: The stimulated echo pulse sequence and corresponding magnetization vector behaviour. (A) the stimulated echo pulse sequence. (B) at time point 1. (C) during first evolution time τ until time point 2. (D) at time point 3. (E) at time point 4. (F) at time point 5. (G) at detection time point 6.

3.4 Nuclear modulation experiments: ESEEM

3.4.1 Introduction of the density operator and coherence

For spin probe samples such as nitroxides, the CW EPR technique can give information on dynamics by lineshape analysis and yield the rotational correlation time. However, except for $2A'_{zz}$, the largest principal value of the hyperfine tensor, hyperfine coupling is not resolved due to overlap of signals. To quantitatively analyze intermolecular interactions and strucural information on a long range scale (0.5 nm–8 nm by EPR corresponding to electron-nuclear or electron-electron coupling between 100 kHz and a few megahertz (MHz)), pulse EPR is very useful to separate the hyperfine coupling from other interactions by well designed pulse sequence techniques. As shown in Fig.3.7, pulse EPR is suitable for a wide range of time scales from microseconds to pisoseconds. Among pulse EPR techniques *electron spin echo envelope modulation* (ESEEM) is a well-established technique to study hyperfine coupling and nuclear quadrupole couplings in solids.

Just as the magnetization vector pictures (Fig.3.13 and Fig.3.14), the more formal density matrix description is often used to understand exprimental behaviour. With the density matrix it is easier to describe the probability of transitions and polarization (population difference) between different states.

For one isolated spin with S=1/2, the general description for its state is its wavefunction $|\psi\rangle$.

$$|\psi\rangle = c_\alpha|\alpha\rangle + c_\beta|\beta\rangle \tag{3.80}$$

c_α and c_β are complex coefficients of the linear combination of eigenfunctions $|\alpha\rangle$ and $|\beta\rangle$. c_α and c_β meet the *normalization condition* as Eqn.3.81.

$$|c_\alpha|^2 + |c_\beta|^2 = 1 \tag{3.81}$$

For a large ensemble of spins that all have the same wavefunction $|\psi\rangle$ (*pure state*), the three Cartesian components (real numbers) of the magnetization vector can be expressed by Eqn.3.82, Eqn.3.83 and Eqn.3.84 with g as appropriate g-value, μ as appropriate magneton (g_B or g_N), N as the number of spins in the ensemble and V as unit volume.

$$M_x = -\frac{g\mu N}{2V}(c_\alpha^* c_\beta + c_\alpha c_\beta^*) = -\frac{g\mu N}{2V}|c_\alpha|\,|c_\beta|\cos\phi \tag{3.82}$$

$$M_y = -\frac{g\mu N}{2V}(c_\alpha^* c_\beta - c_\alpha c_\beta^*) = -\frac{g\mu N}{2V}|c_\alpha|\,|c_\beta|\sin\phi \tag{3.83}$$

$$M_z = -\frac{g\mu N}{2V}(|c_\alpha|^2 - |c_\beta|^2) \tag{3.84}$$

The phase angle ϕ is shown in Fig.3.15 (A) and (B). The complex c_α and c_β can be plotted in the complex plane as shown in Fig.3.15 (B). In a *mixed state*, in which different spins in the ensemble may have different

wavefunctions, the magnetization components are measured as their averaged value as expressed by Eqn.3.85, Eqn.3.86 and Eqn.3.87.

$$M_x = -\frac{g\mu N}{2V}(\overline{c_\alpha^* c_\beta} + \overline{c_\alpha c_\beta^*}) \tag{3.85}$$

$$M_y = -\frac{g\mu N}{2V}(\overline{c_\alpha^* c_\beta} - \overline{c_\alpha c_\beta^*}) \tag{3.86}$$

$$M_z = -\frac{g\mu N}{2V}(\overline{|c_\alpha|^2} - \overline{|c_\beta|^2}) \tag{3.87}$$

The averaged value is defined with its probabilities p_i with $p_i = n_i/N$ (n_i is the number of spins with same wavefunction $|\psi_i\rangle$ in a total number of spins N).

$$\overline{c_\alpha^* c_\beta} = \sum_{i=1}^{N} p_i c_\alpha^* c_\beta \tag{3.88}$$

$$\overline{c_\alpha c_\beta^*} = \sum_{i=1}^{N} p_i c_\alpha c_\beta^* \tag{3.89}$$

$$\overline{|c_\alpha|^2} = \sum_{i=1}^{N} p_i \, |c_\alpha|^2 \tag{3.90}$$

$$\overline{|c_\beta|^2} = \sum_{i=1}^{N} p_i \, |c_\beta|^2 \tag{3.91}$$

In analogy to *Pauli matrices*, the *density matrix* is defined by Eqn.3.92.

$$\delta = \begin{vmatrix} \overline{|c_\alpha|^2} & \overline{c_\alpha c_\beta^*} \\ \overline{c_\alpha^* c_\beta} & \overline{|c_\beta|^2} \end{vmatrix} \tag{3.92}$$

The time-dependent diagonal elements of the density operator $\overline{|c_\alpha|^2}$(t) and $\overline{|c_\beta|^2}$(t) are the populations of the $|\alpha\rangle$ and $|\beta\rangle$ states. Their difference corresponds to longitudinal magnetization or to *polarization of the transition*. The time dependent off-diagonal elements of the density operator $\overline{c_\alpha^* c_\beta}$(t) and $\overline{c_\alpha c_\beta^*}$(t) are related to transverse magnetization and a *coherent* superposition of the two states. Coherence means the wavefunctions of a number of spins are characterized by the same phase parameter ϕ. It should also be noticed that $\overline{c_\alpha^* c_\beta}$(t) and $\overline{c_\alpha c_\beta^*}$(t) are complex conjugates.

The *density operator* $\hat{\sigma}$ is defined by the Eqn.

$$\hat{\sigma} = \sum_{i=1}^{N} p_i |\psi_i\rangle\langle\psi_i| \tag{3.93}$$

The quantum-mechanical equation of motion is the *Liouville-von-Neumann equation* with $[H(t), \widehat{\sigma}(t)]$ as the

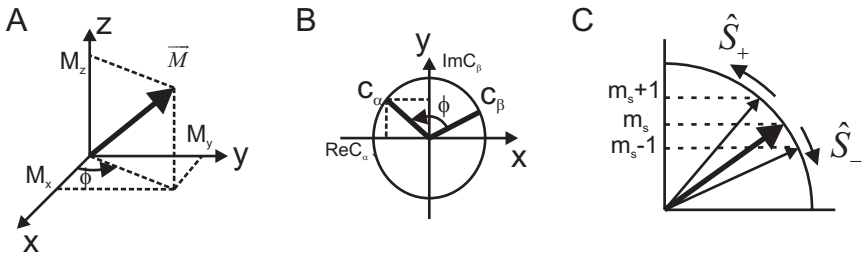

Figure 3.15: (A) Magnetization in the laboratory axis system. (B) c_α and c_β in complex plane. (C) Shift operators. The raising operator $\hat{S}_+$ results in a state with the same magnitude of angular momentum but with a z-component one unit greater as $\hat{S}_+|m_S\rangle = |m_S + 1\rangle$. The lowering operator $\hat{S}_-$ results in state as $\hat{S}_-|m_S\rangle = |m_S - 1\rangle$.

commutator of the Hamiltonian and density operators.

$$\frac{d\hat{\sigma}}{dt} = -i[H(t), d\hat{\sigma}(t)] \tag{3.94}$$

The general formula for the computation of the expectation value of operator $\hat{A}$ from the density operator $\hat{\sigma}$ is expressed by Eqn.3.95.

$$\langle \hat{A} \rangle = \text{Trace}\{\hat{A}\,\hat{\sigma}\} \tag{3.95}$$

The expectation values of $\hat{S}_x$, $\hat{S}_y$ and $\hat{S}_z$ are proportional to the magnetization vector components M_x, M_y and M_z, respectively.

3.4.2 Principles of two pulse ESEEM

ESEEM is suitable for the measurement of the hyperfine coupling if the hyperfine coupling and the nuclear Zeeman frequency are of the same order of magnitude. Nuclear modulation due to this hyperfine coupling can be measured quantitatively and in turn structural information can be obtained.

The pulse sequence of two pulse ESEEM is shown in Fig.3.16. (A). Just like Hahn echo, the sample is irradiated with a $(\pi/2)_x$ pulse first. Instead of the π_y pulse in the Hahn echo, two pulse ESEEM uses a π_x pulse and detects the amplitude of the echo signal as a function of time variable τ. For simplicity we consider the weak-coupling case which is shown in Fig.3.16. (C) (as from Fig.3.12. (A)). Density matrix elements are shown in Fig.3.16. (B). Diagonal elements are populations of corresponding states and the off-diagonal elements represent coherences. *Single quantum coherences* (SQ) labeled (1) ($\triangle m_S = \pm 1$) are EPR allowed transitions. SQ labeled as (2) ($\triangle m_I = \pm 1$) are NMR allowed transitions. *Double quantum coherences* (DQ) and *zero quantum coherences* (ZQ) are forbidden transitions.

Immediately after the $(\pi/2)_x$ pulse, the coherence on one selected transition can be visualized as a vector $\vec{M}^{(13)}$ of length $\cos\eta$ which is the weighting factor interpreted as the transition amplitude of the allowed transitions (just as in Fig.3.13. (A))[1]. (23) The vector is driven to the -y-axis just as in the Hahn echo. During the first free evolution

[1] Coherence on a forbidden transition can be pictured as a vector of length $\sin\eta$.

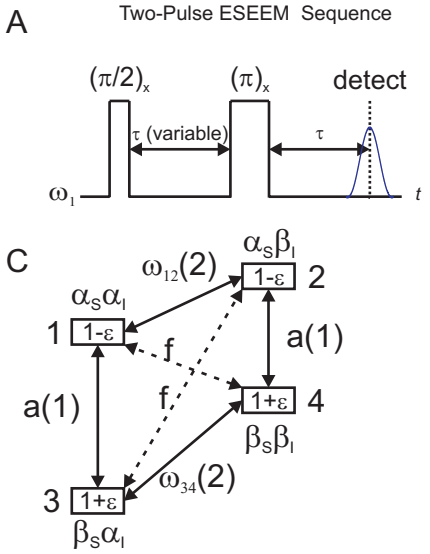

B

$\lvert\alpha_S\alpha_I\rangle$	$\lvert\alpha_S\beta_I\rangle$	$\lvert\beta_S\alpha_I\rangle$	$\lvert\beta_S\beta_I\rangle$	
1 $P_{\alpha\alpha}$	$SQ^{(2)}$	$SQ^{(1)}$	DQ	$\langle\alpha_S\alpha_I\rvert$
$SQ^{(2)}$	2 $P_{\alpha\beta}$	ZQ	$SQ^{(1)}$	$\langle\alpha_S\beta_I\rvert$
$SQ^{(1)}$	ZQ	3 $P_{\beta\alpha}$	$SQ^{(2)}$	$\langle\beta_S\alpha_I\rvert$
DQ	$SQ^{(1)}$	$SQ^{(2)}$	4 $P_{\beta\beta}$	$\langle\beta_S\beta_I\rvert$

Figure 3.16: Two-pulse ESEEM (A) Pulse sequence of the two-pulse ESEEM experiment with variable time τ as the free evolution time (and interpulse delay). (B) Density matrix elements of the system. Numbered diagonal elements correspond to the states shown in (C). P is the population of the state. The number in bracket represents the corresponding transition label in (C). SQ is the single quantum transition; DQ the double quantum transition; ZQ the zero quantum transition. (C) Energy levels of the system and transitions between states. 'a' denoted as allowed transition and 'f' a forbidden transition. The states are indicated with population factor ϵ.

period of length τ, the vector precesses and gains a phase $\phi_{13} = \Omega_S^{(13)}\tau$ with $\Omega_S^{(13)} = \Omega_S - \omega_-/2$ (Fig.3.17. (A)). The $(\pi)_x$ pulse of the primary echo sequence rotates the phase about the x-axis counter clockwise to the x(+y)-plane (Fig.3.17. (B)). With microwave irradiation, it is possible to transfer the coherence from transition SQ (1,3) to all four electron spin transitions including SQ (1,3), DQ (1,4), ZQ (2,3) and SQ (2,4) transitions with different weighting factors $\cos^2\eta$, $\sin\eta\cos\eta$, $-\sin\eta\cos\eta$, and $-\sin^2\eta$, respectively.

Immediately after the $(\pi)_x$ pulse, all four coherences are in phase (Fig.3.17. (B)). The magnetization vectors corresponding to the different coherences now begin to precess with different frequencies. As shown in Fig.3.17. (C), after time $\triangle t$, the coherence on transition (2,3) gains a phase $\triangle\phi_{23} = (\omega_{23} - \omega_{13})\triangle t = -\omega_{12}\triangle t$ (vector picture in Fig.3.16. (C)) with respect to the coherence on transition (1,3). So the component of $\vec{M}^{23}$ along the direction of $\vec{M}^{13}$ is given by $\cos(\omega_{12}\triangle t)\vec{M}^{23}$.

At time τ after the $(\pi)_x$ pulse, $\vec{M}^{13}$ is directed along the +y-axis and contributes to the usual primary echo (Fig.3.17. (D)). Dectection of the allowed coherence imposes another weighting factor $p_d = \cos\eta$, hence the total weighting of this pathway is $\cos^4\eta$ ($\cos\eta\cos^2\eta\cos\eta$). The directions of $\vec{M}^{23}$, $\vec{M}^{24}$, and $\vec{M}^{14}$ do not depend on the offset frequency Ω_0. Any defocusing of these magnetization components due to a distribution of Ω_0 thus vanishes, and echoes along y-axis are formed. Such *coherence-transfer echoes* are observed when coherence refocuses on a transition different to the one which has defocused. Their contribution to the total echo amplitude is the origin of *nuclear modulations* in the two pulse ESEEM experiment. As the magnetization components for these coherence-transfer echoes along the observation direction y oscillate with $\cos(\omega_{kl} - \omega_{13})$ when (kl) is (2,3), (1,4) or (2,4), the signal is modulated by the oscillation.

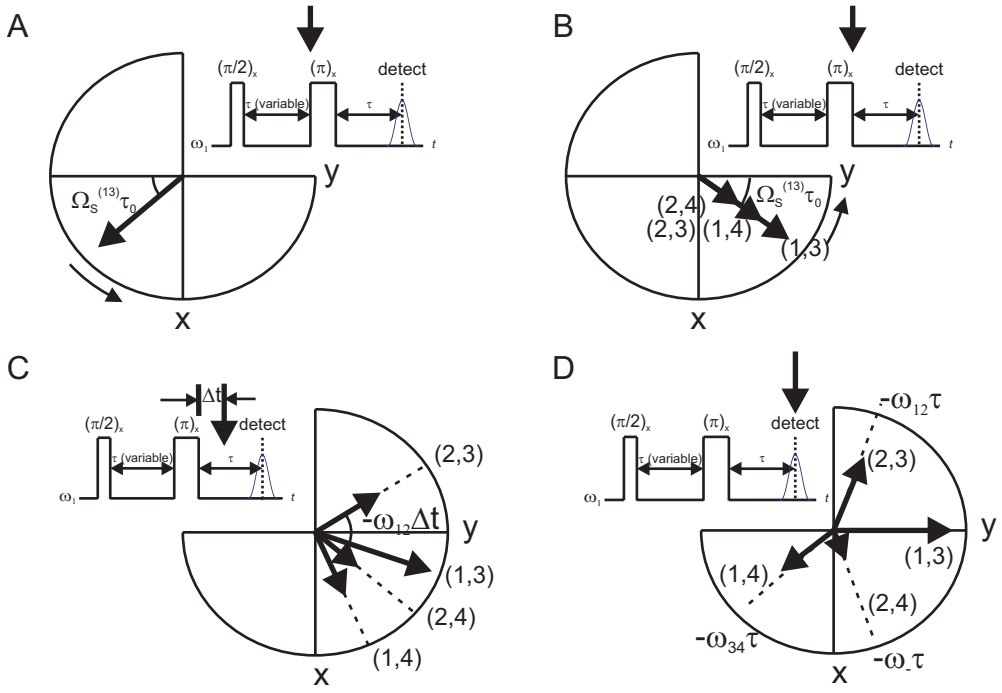

Figure 3.17: Evolution of coherence that is initially on the allowed transition (1,3) during a two-pulse ESEEM experiment. (A) Coherence immediately before the π pulse. The magnetization has a phase $\phi_{13} = \Omega_S^{13}\tau$ with respect to -y-direction immediately after the $(\pi/2)_x$ pulse. (B) The $(\pi)_x$ pulse inverts the phase and distributes the magnetization between all four electron spin transitions. (C) At time $\triangle t$ after the π pulse, the coherence on resonane has gained a phase $\triangle\phi_{23} = \phi_{23} - \phi_{13} = -\omega_{12} \triangle t$ with respect to the coherence on transition (1,3). (D) At time of echo formation, only part of the magnetization on the transitions (1,4), (2,4), and (2,3) contributes to the echo along y. (23)

It can be derived that the *modulation depth parameter* in two-pulse ESEEM is given by Eqn.3.96. (23)

$$k = \sin^2 \eta \tag{3.96}$$

The modulation depth parameter k can also be written as Eqn.3.97 with B as the pseudo-secular part of the hyperfine coupling in equation of $H_0 = \omega_s S_z + \omega_I I_z + A S_z I_z + B S_z I_x$. (23)

$$k = \left(\frac{B\omega_I}{\omega_\alpha \omega_\beta}\right) \tag{3.97}$$

For weak couplings k approaches $(B/\omega_I)^2$, the depth parameter can also be expressed by Eqn.3.98. r is the distance between the electron and nuclear spin. θ is the angle between $\vec{B}_0$ and the vector of hyperfine coupling.

$$k = \frac{9}{4}\left(\frac{\mu_0}{4\pi}\right)^2 \left(\frac{g\mu_B}{B_0}\right)^2 \frac{\sin^2(2\theta)}{r^6} \tag{3.98}$$

The modulation formula for the signal of the two-pulse ESEEM experiment is given by Eqn.3.99 with ω_α and ω_β as the absolute values of the nuclear frequencies $|\omega_{12}|$ and $|\omega_{34}|$ respectively.

$$V_{2eseem}(\tau) = -\langle S_y \rangle = 1 - \frac{1}{4}[2 - 2\cos(\omega_\alpha \tau) - 2\cos(\omega_\beta \tau) + \cos(\omega_- \tau) + \cos(\omega_+ \tau)] \tag{3.99}$$

Relaxation can be taken into account by assuming the same phase memory time T_m for all electron transitions, which is often a good approximation:

$$V'_{2eseem}(\tau) = \exp\left(-\frac{2\tau}{T_m}\right) V_{2eseem}(\tau) \tag{3.100}$$

In most paramagnetic compounds several nuclei are coupled to the electron spin. The density operator at any time during the experiment is a *product* in which each of the factors contains terms involving **S** and *one* of the nuclear spins $\mathbf{I}_1 \cdots \mathbf{I}_N$, resulting in the ESEEM signal:

$$V'_{2eseem}(\tau) = \exp\left(-\frac{2\tau}{T_m}\right) \prod_{l=1}^{N} V_{2eseem,l}(\tau) \tag{3.101}$$

From Eqn.3.100 the relaxation time T_m can be obtained by fitting expontenial decay to the signal. This relaxation time can be approximated as transverse relaxation T_2 under the high field approximation for dilute samples. So from two-pulse ESEEM we can have information on relaxation time and on nuclear modulation.

3.4.3 Principle of three-pulse ESEEM

The pulse sequence of three-pulse ESEEM is shown in Fig.3.18. (A) and the building blocks are shown in Fig.3.18. (B). The technique is very similar to the stimulated echo except that the interval τ between the second and the third $(\pi)/2_x$ pulse is variable. Nuclear coherence (NC) is generated after the second pulse. After the incremented evolution time the third $(\pi)/2_x$ pulse is applied. The signal modulated by nuclear coherence is detected.

With its dependence on Ω_S, τ_0 and variable evolution time τ, three-pulse ESEEM is considerably more complex than two-pulse ESEEM.

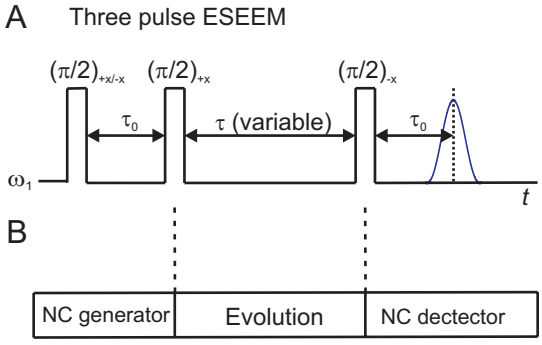

Figure 3.18: Three-pulse ESEEM. (A) Pulse sequence. (B) Building blocks. NC denotes nuclear coherence.(23)

The sequence $(\pi/2)_x - \tau_0 - (\pi/2)_x - \tau - (\pi/2)_x - \tau_0$ generates a s stimulated echo, whose envelope as a function of variable time τ is modulated with the two nuclear frequencies ω_α and ω_β. The combination frequencies ω_+ and ω_- are not observed. The *modulation depth* k, as shown in Fig.3.19. (A), which is the separation between the dashed lines, divided by the echo amplitude is also $\sin^2\eta$. The longer relaxation time in the stimulated echo results in narrower lines and thus better resolution compared to two-pulse ESEEM.

From (23), for an $S = 1/2$ and $I = 1/2$ spin system, the modulation formula of the three-pulse ESEEM experiment is given by Eqn.3.102.

$$V_{3eseem}(\tau_0, \tau) = 1 - \frac{1}{4}\{[1 - \cos(\omega_\beta \tau_0)][1 - \cos(\omega_\alpha(\tau_0 + \tau)] + [1 - \cos(\omega_\alpha \tau_0)][1 - \cos(\omega_\beta(\tau_0 + \tau)]\} \tag{3.102}$$

Relaxation effects are consided in the modulation formula by assuming a common phase memory time $T_m^{(n)}$ for all the nuclear transition and T_m for all the electron transitions:

$$V'_{3eseem}(\tau_0, \tau) = \exp\left(\frac{-\tau}{T_m^{(n)}}\right) \exp\left(\frac{-2\tau_0}{T_m}\right) V_{3p}(\tau_0, \tau) \tag{3.103}$$

The Eqn.3.102 and Eqn.3.103 for three-pulse ESEEM is only valid for an infinitely broad inhomogeneous line, while Eqn.3.99 and Eqn.3.100 for the two-pulse ESEEM experiment applies for each particular spin packet. For the three-pulse ESEEM experiment, more scans are required to measure a precise averaged modulation depth, but the modulation is more simple, as it does not contain the combination frequencies ω_+ and ω_-.

3.4.4 Analysis and interpretation of ESEEM

A typical two-pulse ESEEM time-domain signal is shown in Fig.3.19. (A). This signal is from the end-labeled nitroxide that is used in this thesis as a spin probe to characterize the surfactant layer in organoclay and nanocomposites (Fig.1.9. (A)). The sample preparation method is described in Chapter 5.

From the expontential data fitting shown as a dashed line in the middle in Fig.3.19. (A), the relaxation time T_m approximated as T_2 can be calculated. In this case it is 374 ns. There are two main parameters of the experimental data: the modulation depth k at frequency $|\omega_I|$ and the function describing the decay of this modulation component, which may be characterized by the time-dependent ratio as Eqn.3.104.

$$R_{exp}(\tau) = \frac{V_{max}(\tau)}{V_{min}(\tau)} \tag{3.104}$$

V_{max} and V_{min} are curves that interpolate between the maxima and minima of the modulation with frequency $|\omega_I|$ (dashed line in outer-frame in Fig.3.19. (A)), respectively.

The time-domain signal of three-pulse ESEEM of the same sample is shown in Fig.3.19. (B). After exponential decay data fitting, the nuclear modulation is extracted as shown in Fig.3.19. (D) by substracting the fitting curve from the signal-intensity. The time-domain nuclear modulation can be Fourier transformed to give a frequency-domain signal. As g_n of proton is 5.586, its Larmor frequency can be calculated in analogy to the one of electrons in Eqn.3.10. The *nuclear magneton* μ_N is defined by Eqn.3.105 with m_p as mass of proton and its value is $5.051 \times 10^{-27} \quad JT^{-1}$.

$$\mu_N = \frac{e\hbar}{2m_p} \tag{3.105}$$

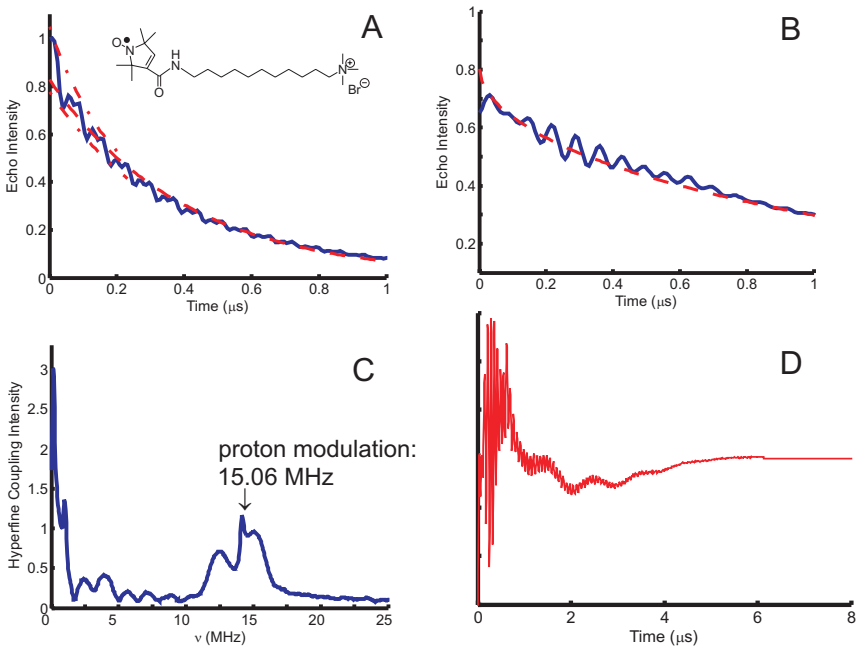

Figure 3.19: Example of data treament of ESEEM measured at 80 K. The sample is organoclay prepared from magadiite and HTMA with spin probe 11-SL-UTMA. (A) Signal from two-pulse ESEEM. The center dashed line is an expontential data fitting curve. The modulation depth is the distance between the two dashed lines in the outer frame of the signal curve. (B) Signal from three-pulse ESEEM. It is obvious that for the same sample three-pulse ESEEM has a longer relaxation time. The dashed line is expontential data fitting. (C) Fourier Transform of the signal in frequency domain as shown in (D). Hyperfine coupling intensity and position can be clearly identified in the spectrum. (D) The remaining signal in time-domain after subtracting the exponential fitting curve from the signal intensity.

The magnetogyric ratio γ_n of protons is calculated by by Eqn.3.106. For protons by Eqn.3.106 its value is $2.675 \times 10^7 \quad T^{-1}s^{-1}$.

$$\gamma_n = \frac{g_n \mu_N}{\hbar} \tag{3.106}$$

The Larmor frequency is calculated by Eqn.3.107 from $\triangle E_{proton} = g_n \mu_N B_0 = \gamma_n \hbar B_0 = h\nu_L$. As shown in Fig.3.19. (C), at the experimental static magnetic field $B_0 = 0.35$ Tesla, the maximum in the range is 15.06 MHz, very close to the calculated value of 15 MHz.

$$\nu_L = \frac{\gamma_n B_0}{2\pi} \tag{3.107}$$

With Eqn.3.98 the modulation depth k can be related to the electron-nuclear distance. Hence from the modulation depth, information on the proximity of nuclei of certain elements (e.g. ^{2}H) to the electron spin can be obtained. In principle the number and distance of the nuclei can be computed. (23)

3.5 Double resonance techniques: ENDOR

3.5.1 Principle of ENDOR

Apart from the ESEEM methods, *electron nuclear double resonance* (ENDOR) spectroscopy is the other well-established magnetic resonance technique for measuring nuclear transition frequencies of paramagnetic compounds. All ENDOR experiments rely on a polarization transfer from electron spin transitions to nuclear spin transitions. The idea of ENDOR is to use the EPR population difference (polarization) on an NMR transition to enhance sensitivity. As shown in Fig.3.20, compared with conventional spectroscopy, the double resonance experiment introduces a second perturbation P_2 with amplitude B_2. According to *perturbation theory*, there are two main effects of the pertubation P_2: firstly even a relatively weak perturbation P_1 of S spins may change the population of energy levels. And the corresponding change of population changes the intensity of the resonance lines of I spins giving rise to enhanced signal of I transitions. For ENDOR, P_1 influences only electron spins S, while P_2 influences only nuclear spins I. In case of *Double Electron Electron Resonance* (DEER) (Sec.3.6), P_1 influences one kind of electron spins S_1, while P_2 influences a different kind of electron spins S_2.

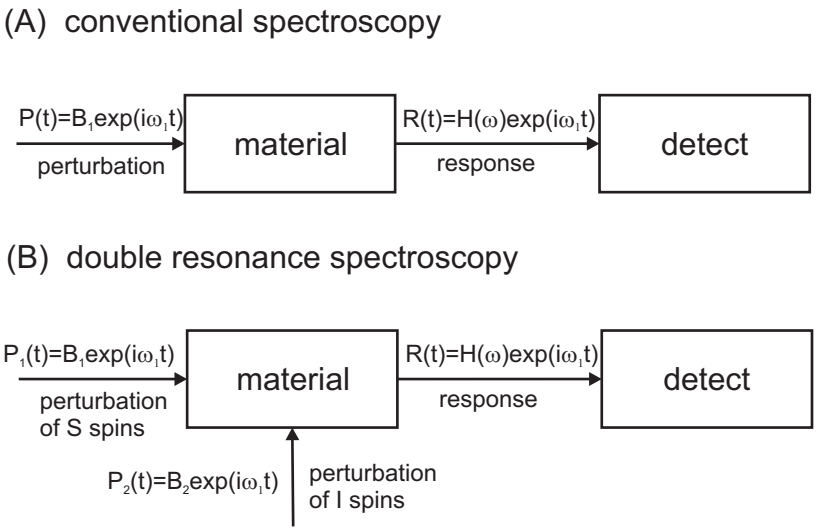

Figure 3.20: Illustration of the double resonance experiment in comparison with a conventional pulse experiment. (A) Conventional spectroscopy. (B) Double resonance spectroscopy.

The Hamiltonian of the dipole-dipole interaction as expressed by Eqn.3.54 can be rewritten by Eqn.3.108.

$$H_{dd} = 2\pi\nu_{dd}[\hat{A} + \hat{B} + \hat{C}] \tag{3.108}$$

The dipolar frequency ν_{dd} defines the magnitude of the dipole-dipole interaction for two spins at a distance r from each other by Eqn.3.109.

$$|\nu_{dd}| = \frac{1}{r^3}\frac{\mu_0}{4\pi h}\mu_B\mu_N g_e|g_n| \tag{3.109}$$

The operator terms $\hat{A}$, $\hat{B}$, $\hat{C}$ are defined by Eqn.3.110, Eqn.3.111 and Eqn.3.112.

$$\hat{A} = \hat{S}_z \hat{I}_z (1 - 3\cos^2\theta) \tag{3.110}$$

$$\hat{B} = \frac{1}{2}(\hat{S}_x \hat{I}_x + \hat{S}_y \hat{I}_y)(1 - 3\cos^2\theta) \tag{3.111}$$

$$\hat{C} = -3\hat{S}_z \hat{I}_x \sin\theta\cos\theta \tag{3.112}$$

As shown in Fig.3.21. (A), the hyperfine coupling arising from dipole-dipole interaction causes line splittings in EPR spectra. The complexity of dipole-dipole coupling in paramagnetic centers makes spectra hard to interprete (in (A) there are five dipole-dipole interactions for the electron). However for each one nuclear spin I there is only one electron S coupled.

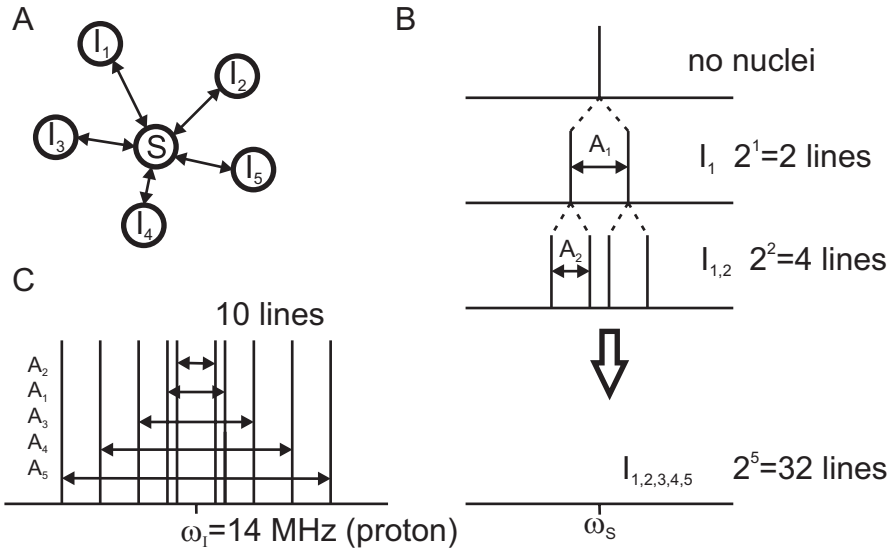

Figure 3.21: (A) One electron coupled with five different nuclei nearby. (B) Line splittings in EPR spectrum (product effects, Eqn.3.113). (C) Line splittings in NMR spectrum (sum effects as Eqn.3.114).

The number of EPR transitions, N_{EPR}, as shown in Fig.3.21. (B), increases multiplicatively with the number of nuclear spins and the frequency of each transition is influenced by all the hyperfine couplings A_k. For protons with $I = 1/2$, five nuclei give rise to $2^5 = 32$ lines.

$$N_{EPR} = \prod_{k=1}^{m} (2I_k + 1) \tag{3.113}$$

In contrast, the number of NMR transitions, N_{NMR}, increases only additively with the number of nuclear spins and the frequency of each transition is influenced by only one hyperfine coupling (Fig.3.21. (C)). In case of five

protons, $N_{NMR} = 2 \times 2 \times ((1/2) \times 5) = 10$ lines. The frequency of each line depends on only one of the hyperfine couplings. ENDOR spectra are thus better resolved and easier to interpret than EPR spectra.

$$N_{NMR} = 2(2S+1)\sum_{k=1}^{m} I_k \tag{3.114}$$

There are several techniques using different pulse sequences and radio frequency pumping methods to measure nuclear transition frequencies by ENDOR: frequency-domain Mims ENDOR, time-domain Mims ENDOR, and time-domain Davies ENDOR. In our experiment frequency-domain Mims ENDOR was applied to measure the distance between nitroxide spin probe radicals and phosphorus nuclei of phosphonium head group surfactants in organoclay and nanocomposites. Accordingly, basics of frequency-domain Mims ENDOR are introduced here.

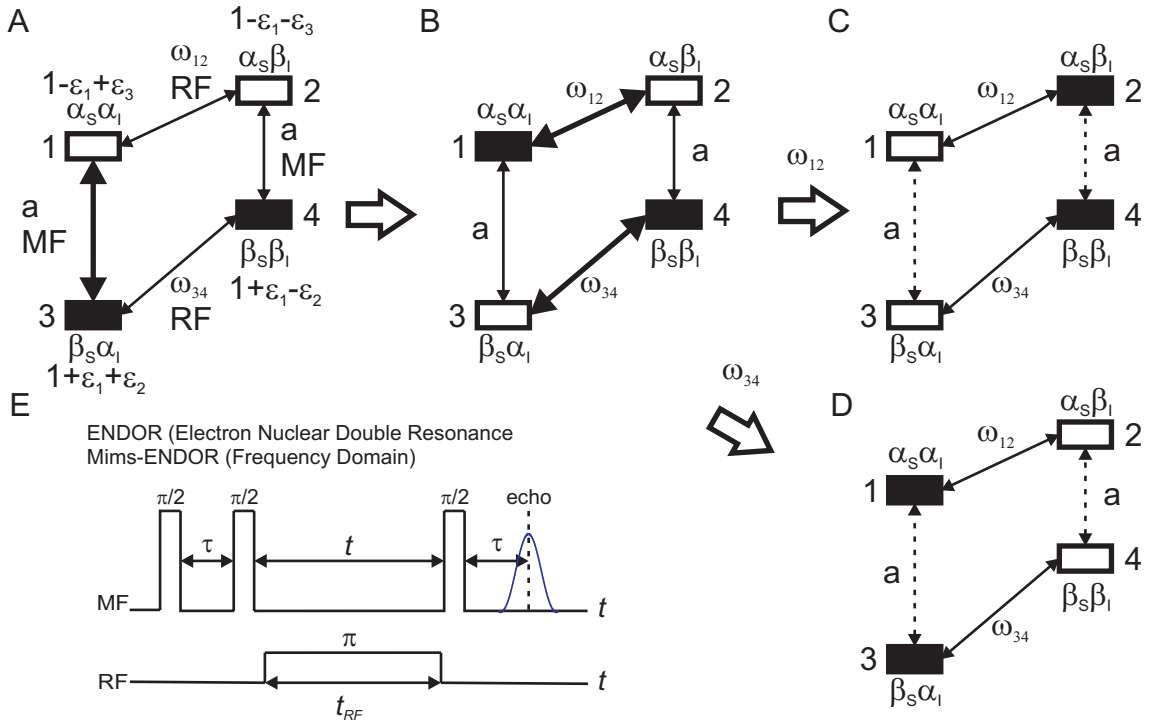

Figure 3.22: Energy transitions in ENDOR and pulse sequence (A) (1,3) transition (bolded line) after microwave irradiation. (B) As population reversed from 3 to 1, polarization on the NMR transitions (1,2), (3,4) can be generated by selective r.f. irradiation either to (C) or to (D). (C), (D): Equal population of EPR transitions result in a saturated situation. No EPR transition should be detected. (E) Mims ENDOR pulse sequence.

Mims ENDOR is based on the stimulated echo sequence (Sec.3.3.3) as shown in Fig.3.22. (E). After the preparation sequence, $\pi/2$-τ- $\pi/2$, the magnetization vectors are restored in the z'-direction in antiphase (Fig.3.14. (D3)). As shown in Fig.3.22. (A), at thermal equilibrium both states $|\beta_S\alpha_I\rangle$ and $|\beta_S\beta_I\rangle$ are populated, however to a different degree ($\epsilon_1 \gg \epsilon_2$ and ϵ_3). After this preparation sequence with microwave irradiation (also called NC generator), as shown in Fig.3.22. (B), state $|\alpha_S\alpha_I\rangle$ is populated. During the mixing period t, the polarization is changed either to Fig.3.22. (C) pathway or to Fig.3.22 (D) by a selective radio frequency pulse irradiation that is resonant with transition (1,2) or with transition (3,4). If the radio frequency is off-resonant, the populations

remain unchanged. In both (C) and (D) EPR transitions are saturated. For detection the NMR spectrum is recorded by observing the change of EPR signal as a function of the frequency of the r.f. pulse. For example, to detect protons in ENDOR r.f. is swept around $\nu_L = 15$ MHz at 0.35 T and echo signal is recorded as same as in stimulated echo experiment.

In Mims ENDOR, the relative change of the echo amplitude by a resonant r.f. pulse can be expressed in terms of F_{ENDOR} with a_{iso} as isotropic hyperfine coupling constant.(23)

$$F_{ENDOR} = \frac{1}{4}(1 - \cos(a_{iso}\tau)) = \frac{1}{2}\sin^2\left(\frac{a_{iso}}{2}\tau\right) \tag{3.115}$$

The optimized interpulse delay τ, for which there is maximum signal/noise ratio, can be derived from Eqn.3.79 and Eqn.3.115. (23)–(24) It is found that τ approximates T_{2e} which is the transverse relaxation time of electrons ($\tau \approx T_{2e}$). As the EPR detection in Mims ENDOR is done by a stimulated echo, whose signal can determine T_{2e} from Eqn.3.79, the optimum value for τ should thus be determined by varying τ in a stimulated echo experiment with the same interpulse delay t as is used in the Mims ENDOR experiment.(24) In the limit of small, purely dipolar hyperfine couplings, $\sin(a_{iso}\tau)/2 \approx (a_{iso}\tau)/2$. F_{ENDOR} can be approximated by Eqn.3.116.

$$F_{ENDOR} = \frac{1}{2}\sin^2\left(\frac{a_{iso}}{2}\tau\right) \approx \frac{a_{iso}^2}{8}\tau^2 \tag{3.116}$$

Because $a_{iso} \propto r^{-3}$ with r as distance between dipoles, it can be derived as Eqn.3.117:

$$F_{ENDOR} \propto r^{-6} \tag{3.117}$$

By Eqn.3.98 the modulation depth from ESEEM is also proportional to r^{-6}, the scaling of the ENDOR efficiency with distance r is the same as for the modulation depth in ESEEM experiments.

3.5.2 Data analysis of Mims ENDOR

Mims ENDOR lineshapes can be simulated by different models depending on the system measured. In (24) two models are described: a spin probe at fixed distance from a planar layer of nuclei (Fig.3.23), and a spin probe coupled to discrete objects arranged in a hexagonal pattern in a plane. The latter is suitable for a spin-labeled lipid doped into a lipid bilayer while the former is appropriate for the system we are interested in: spin probe in surfactant layers adsorbed in layered silicate.

For the model in which a spin probe is situated at a fixed distance d from a single planar layer of nuclei, it can be derived that for $\tau < 4\ \mu s$ averaging up to $r = 4$ nm is sufficient for numerical simulation. The simulated lineshape of Mims ENDOR can be calculated corresponding to different fixed distance d from a plane of homogeneously distributed ^{31}P nuclei. (24) Distance distributions obtained from Mims ENDOR data overemphasize the shortest distance to a lesser extent than those obtained from ESEEM data although both of them have the same order of distance dependence (r^{-6}).

One example of data analysis of Mims ENDOR is shown in (Fig.3.24). The sample is an end-labeled spin probe with phosphorous head group mixed into phosphonium surfactant HTBP absorbed by layered silicate (magadiite).

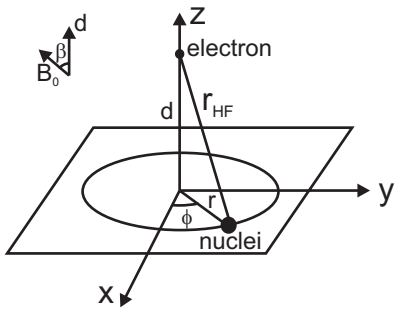

Figure 3.23: Models for calculating Mims ENDOR line shapes. A spin probe at a fixed distance from a planar object. (24)

The optimized interpulse delay τ is obtained by a stimulated echo experiment before ENDOR is perfomed. As shown in Fig.3.24. (A), by expontential data fitting, the optimized interpulse delay is found to be 297 ns. The ENDOR signal of this sample is shown in Fig.3.24. (B), with $\nu_L(^{31}P) = 6$ MHz in $B_0 = 0.35$ T.

The reversed signal which is treated as a nuclear transition signal is then fitted with precomputed spectra based on the model described above (Fig.3.24. (D)). The distance distribution is then found with the corresponding precomputed dataset (Fig.3.24. (C)). The distance between the electron spin and ^{31}P nuclei has two preferable distributions as shown in (Fig.3.24. (C)). As these two distances are much smaller than the length of the alkyl chain of the spin probe molecule, it means that the surfactant molecules are not perpendicular to the head group layer but strongly tilted. This will be discussed later in the experimental part. Hence ENDOR can give information on the distance between paramagnetic centers and nuclei of interest. Mims ENDOR is suitable for small and moderate hyperfine coupling, while for larger hyperfine coupling it is better to use Davies ENDOR.

3.6 Double resonance techniques: four-pulse DEER

3.6.1 Principle of DEER

Double electron electron resonance (DEER) is an experimental technique designed to separate the coupling between electron spins from other contributions to the spin Hamiltonian, namely, resonance offset due to g-value dispersion, hyperfine couplings, and for $S > 1/2$, zero-field splitting (ZFS).(23) This is achieved by refocusing all interactions, including the coupling between the two electron spins, in an echo experiment on the observer spin S. The spin-spin coupling is then reintroduced by a pump pulse that ideally exclusively excites the other spin I. The pulse sequence is shown in Fig.3.25. (A). Just as in ENDOR, observe and pump excitation use different frequencies. However four-pulse DEER starts with a primary echo sequence, after an adjustable interpulse evolution time $(\tau_1 + \tau_2)$, a third π pulse is applied to refocuse the magnetization vectors. Such a refocused echo created by the observer sequence coincides with a stimulated echo if $\tau_1 = \tau_2$ (Fig.3.14).(23) In the second channel, a microwave pulse is applied at a variable time t after formation of the first primary echo of the observer spins. The starting point of the pump pulse at ν_2 can be treated as zero mixing time as at this point the coherence has zero phase. This pump pulse flips the spin I from its $|\alpha\rangle$ to its $|\beta\rangle$ state, thus transferring the coherence to the other transition of spin

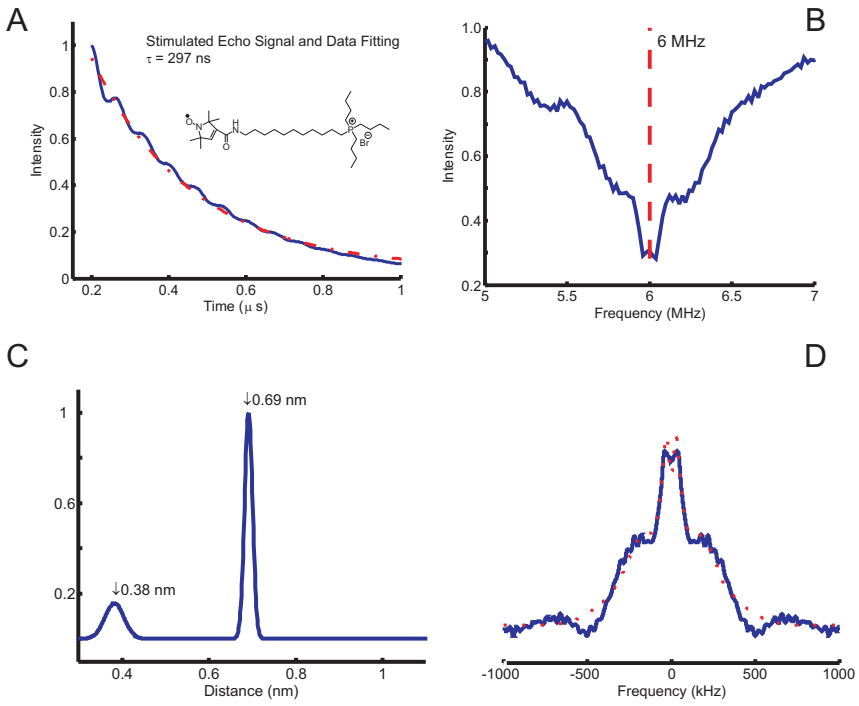

Figure 3.24: Example of data treatment for Mims ENDOR measured at 50 K. The sample is organomagadiite prepared from magadiite, HTBP and spin probe 11-SL-UTBP. (A) The step that is used to determine the optimum interpulse delay τ for ENDOR. The dashed line is expontential data fitting. The exponential decay time constant found is the τ used in ENDOR. (B) Signal of ENDOR in frequency domain. The signal is nearly symmetrical to ^{31}P Larmor frequency 6 MHz in 0.35 T. (C) Distance between electron and ^{31}P after best model fitting from (D). (D). Normalized signal in frequency domain with dotted line as simulated spectrum from precomputed dataset.

S and changing the resonance frequency of spin S by -d. Here d is the spin-spin coupling including dipole-dipole *and* exchange contributions.

Selection of the observer and pumped spin requires excitation pulses at two different frequencies. The observer frequency ν_1 is set to the local maximum at low field obtain to maximum echo amplitude while avoiding overlap with the excitation at pump frequency ν_2 ($h\upsilon_1 = g_a\mu_B B_0^a$)(Fig.3.25. (B)). ν_2 should excite as many spins as possible so it is set to the maximum of the absorption spectrum ($h\upsilon_2 = g_b\mu_B B_0$). This maximizes the influence of the electron spin-spin coupling on the echo. Because the actual four-pulse DEER is run at external static field B_0 ($B_0 > B_0^a$), if $g_a \approx g_b$, ν_1 should be set at larger frequency than ν_2 to have resonance: $\nu_1 - \nu_2 = g_e\mu_B(B_0 - B_0^a)/h$. Experimentally it is found that $\nu_1 - \nu_2 = 65$ MHz. In Fig.3.25. (B) the echo-detected EPR spectrum of the sample containing an end-labeled spin probe is shown. The microwave tuning mode is shown in (D). The structure of the spin probe is shown in (C).

For a single pair (i,k) of localized electron spins with distance r_{ik}, the dipolar time evolution signal is expressed by Eqn.3.118.(25)

$$V(t) = V_0[1 - \lambda_{ik}(1 - \cos(\omega_{ik}t))] \tag{3.118}$$

λ_{ik} is the modulation depth which quantifies the fraction of the echo signal that is due to excited spin pairs

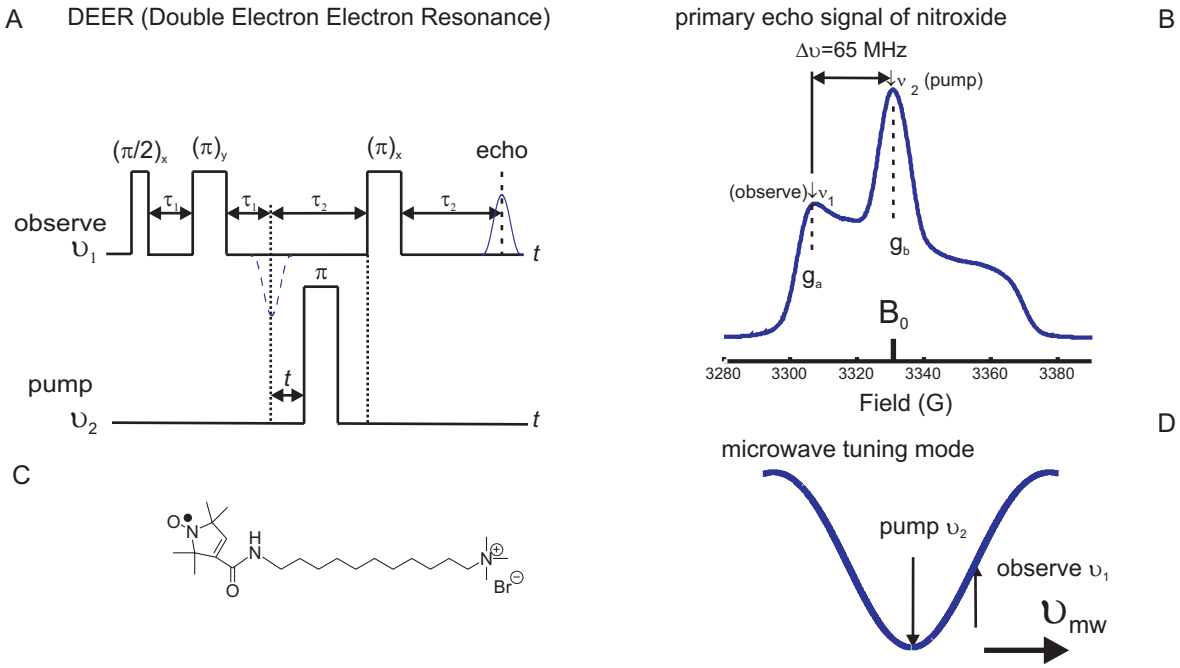

Figure 3.25: Pulse sequence and double resonance frequencies of DEER. (A) Pulse sequence (B) Echo-detected EPR spectrum of organosilicate prepared from magadiite, HTMA and spin probe 11-SL-UTMA. The pump frequency and observe frequency are indicated. (C) Chemical structure of the spin probe 11-SL-UTMA. (D) Both frequencies are indicated in the microwave tuning mode.

(i,k). ω_{ik} is defined by Eqn.3.119 from Eqn.3.60.

$$\omega_{ik} = \omega_{dd}^{(ik)}(3\cos^2\theta_{ik} - 1) \tag{3.119}$$

with ω_{dd}^{ik} as dipolar evolution frequency:

$$\omega_{dd}^{(ik)} = \frac{\mu_0}{4\pi\hbar}\frac{g_i g_k \mu_B^2}{r_{ik}^3} \tag{3.120}$$

In DEER, 'i' can be seen as observer spin (S spin), 'k' can be seen as pumped spin (I spin) and θ_{ik} is the angle between the static field vector $\vec{B}_0$ and the vector $\vec{r}_{ik}$.

For an ensemble containing systems with multiple pumped spins, the signal for the S observer spin follows a product law (as in ESEEM):

$$V_i(t) = V_{0,i}\prod_{k\neq i}[1 - \lambda_{ik}(1 - \cos(\omega_{ik}t))] \tag{3.121}$$

The total signal is the sum of all S spins as $\sum_i V_i(t)$. If the spins are distributed homogeneously in three dimensions, the signal is a monoexponential decay:

$$V(t) = V_0 \exp\left(-\frac{t}{T_{hom}}\right) \tag{3.122}$$

T_{hom} is expressed by Eqn.3.123 with C as the concentration of spins and λ as the modulation depth parameter which is the fraction of excited I spins.

$$T_{hom} = \frac{9\sqrt{3}\hbar}{2\pi g^2 \mu_B^2 \mu_0 \lambda C} \tag{3.123}$$

3.6.2 Data analysis of four-pulse DEER

In analogy to the form factor and structure factor in scattering techniques, dipolar evolution data can be converted to a distance distribution. The range of distances that can be characterized by four-pulse DEER is from 1 to 10 nm, with precise measurements being possible between 1.5 and 8 nm. Hence pulse EPR can complement results from scattering techniques which either access long range order as from micrometer to 80 nanometer (light scattering), or on the angstrom (Å) scale (small angle X-ray scattering (SAXS) and small angle neutron scattering (SANS)). For systems with intermediate order, the pair distance distribution function P(r), which corresponds to the probability to find distance r within the particle being studied, is given by Eqn.3.124 with $G(r)$ as radial distribution function.

$$P(r) = 4\pi r^2 G(r) \tag{3.124}$$

This can be derived from Eqn.3.121, if the product is expanded under the approximation that $\lambda \ll 1$ which is usually fulfilled in DEER on nitroxide spin probes. The dipolar time evolution is then dominated by effects of the radial distribution function $G(r)$. This corresponds to a situation where multiple scattering can be neglected.

The primary result of the DEER experiment is a distribution of dipolar couplings d. The signal is detected in time-domain (Fig.3.26. (A)). Within the linear approximation and using the shell factorization model, the signal is related to $G(r)$ by Eqn.3.125. (25)

$$V(t) = \prod_k [1 - 4\pi r^2 \lambda \triangle r G(r_k)(1 - V_k(t))] \tag{3.125}$$

The validity of this equation depends on proper limits of r. For $r < r_{min}$, the linear approximation is not valid. When $r > r_{max}$, by Eqn.3.125, V_{rmax} is saturated to 1. It can be computed that for typical electron spin relaxation times the Eqn.3.125 is applicable for 1 nm$< r <$8 nm. (25)

As in ESEEM, the modulation depth is extracted by eliminating nonlinear contributions with appropriate data fitting. The dot line in Fig.3.26. (A) is a stretched exponential data fitting after cutoff time (straight line in (A)). Then the time domain data (smooth line in Fig.3.26. (B)) is transfered to distance domain. The linear contribution to the signal is written as Eqn.3.126 with $B(t)$ as fitting function of the background.

$$V_{lin}(t) = \frac{V(t) - B(t)}{B(t)} \approx \frac{\lambda}{1 - \lambda} \int_{rmin}^{rmax} 4\pi r^2 G(r) V_r(t) dr \tag{3.126}$$

The integration can be substituted by discretized summation (Eqn.3.127) with the discrete integration transform dePakeing model. N is the number of spins.

$$V_{lin}(t) = \sum_{k=1}^{N} \lambda' G(r_k) V_k(t) \tag{3.127}$$

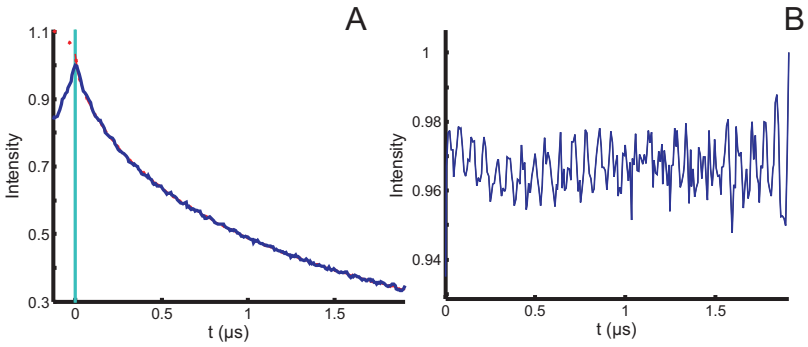

Figure 3.26: Example of data treatment of four-pulse DEER. The sample is organoclay prepared from magadiite, HTMA and spin probe 11-SL-UTMA. (A) Signal in time domain. The straight line is the cutoff time left to which the signal is ignored. The dotted line is background fitting. (B) This signal should be treated by Fourier Transform. The oscillation is from deviation from a homogeneous distribution and from proton modulation.

Mathematically converting P(d) (dipolar coupling space in time domain or frequency domain) to P(r) (distance space) is an ill-posed problem because a slight distortion of P(d) by noise can cause a strong distortion of P(r). This problem is solved by Tikhonov regularization. (26) In Fig.3.26. (B) the residual after background fitting is a flat line corresponding to a homogeneous distribution of nitroxide spin probes on the surface of organomagadiite.

In light scattering, the form factor $P(q)$, which is defined in q (scattering vector in unit of m^{-1}) space, has a meaningful power dependence of q. A plot of the scattering intensity I(q) in q space as $\log I(q) \sim \log q$ reveals information on the shape of particles. For example, for rodlike particles, the scattering intensity I(q) shows a q^{-1} dependence, and for disc particles intensity it shows a q^{-2} scaling. In DEER, dimensionality x of the spin probe distribution in space can also be obtained from the dipolar evolution function $D_x(t)$ from Eqn.3.128 with $\alpha = k\lambda\rho$ proportional to the density ρ of the I spins. The dependence of the proportionality constant k on x can be inferred from (27).

$$D_x(t) = \exp\left(-\alpha t^{x/3}\right) \tag{3.128}$$

The fit in Fig.3.26 corresponds to $x = 1.90$, i.e. to a nearly two-dimensional distribution.

3.7 CW EPR spectrum of nitroxide spin probes

3.7.1 Spin Hamiltonian of nitroxides

Nitroxides are N,N-disubstituted > NO• radicals (alternatively termed nitroxyl radicals). They are widely used as spin probes and labels owing to the sensitivity of their EPR spectra to the microenvironment and their mobility,

as well as due to the high chemical stability of the nitroxide moiety (Fig.3.27. (A)). Nitroxides are stable because of the protective effect exerted by the four methyl groups. The delocalization of the unpaired electron between the nitrogen and oxygen atoms also contributes to the stability of nitroxides (Fig.3.27. (C)). The chemical structure of one example of nitroxide, TEMPO (2,2,6,6-tetramethylpiperidine-1-oxyl), is shown in Fig. 3.27. (B).

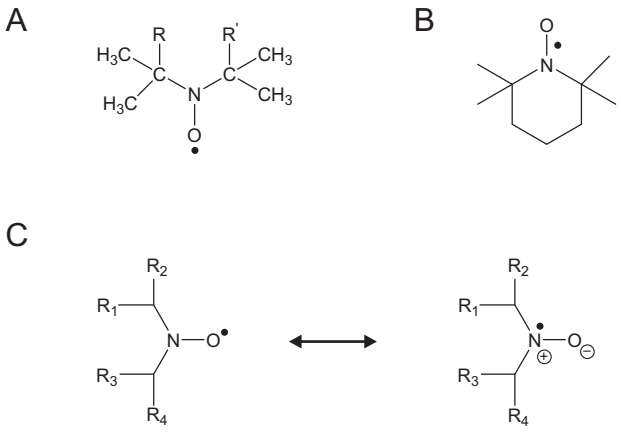

Figure 3.27: (A) General chemical structure of nitroxides. Nitroxides are stable and inert because of the protective effect exerted by the four methyl groups. (B) TEMPO (2,2,6,6-tetramethylpiperidine-1-oxyl) (C) The delocalization of the unpaired electron may be described by the mesomeric structures.

The EPR spectrum of the nitroxide radical is dominated by the hyperfine interaction of the electron spin with the nuclear spin of the ^{14}N atom and by g-shifts due to spin-orbit coupling mainly in the $2p_z$ orbital of the lone pair on the oxygen atom. From Eqn.3.64, to a good approximation, the spin Hamiltonian of a nitroxide in a static external field $\vec{B}_0$ can be expressed by Eqn.3.129 (in energy units).

$$H = \mu_B \mathbf{B_0}\, g\, \hat{\mathbf{S}} + \hat{\mathbf{S}}\, \mathbf{A}\, \hat{\mathbf{I}} \tag{3.129}$$

Three approximations are assumed for Eqn.3.129:

1. The nuclear Zeeman interaction is neglected.
2. The hyperfine interaction with protons and ^{13}C nuclei is neglected.
3. The interaction between spin labels is neglected.

For *dilute systems* under normal conditions all three approximations are reasonable. The nitroxide principal axes system (X, Y, Z) (also called the molecular axes system) is shown in Fig.3.28. (C). The orientation of the magnetic field $\vec{B}_0$ is given by the polar angles θ and ϕ. The X-axis coincides with the N–O bond and the Z-axis is along the $2p\pi$ orbital, which is occupied by the unpaired electron.

If nitroxide radicals are in solution, the anisotropic terms of the spin Hamiltonian can be averaged to zero due to very fast molecular reorientation by thermal motion (Sec.3.2.2 and Sec.3.2.3). The average values of the diagonal elecments of g tensor and $\mathbf{A}$ tensor can be evaluated. The axes system can be chosen as the laboratory

system (z-axis along the magnetic field). The spin Hamiltonian in fast motion in this system can be expressed by Eqn.3.130 with $g = \frac{1}{3}Tr(g)$ and $a = \frac{1}{3}Tr(\mathbf{A})$ as the isotropic hyperfine coupling constant.

$$\begin{aligned} H_{fast} &= g\mu_B \mathbf{B_0}\,\hat{\mathbf{S}}\,\hat{\mathbf{I}} + a\hat{\mathbf{S}}\,\hat{\mathbf{I}} \\ &= g\mu_B B_0\,\hat{S}_z + a(\hat{S}_x\,\hat{I}_x + \hat{S}_y\,\hat{I}_y + \hat{S}_z\,\hat{I}_z) \end{aligned} \tag{3.130}$$

Under the high-field approximation the spin Hamiltonian simplifies to Eqn.3.131.

$$H_{fast} = g\mu_B B_0\,\hat{S}_z + a\hat{S}_z\,\hat{I}_z \tag{3.131}$$

The first-order energy is the corresponding eigenvalue of the spin Hamiltonian with $m_s = \pm\frac{1}{2}$ and $M_I = 1,\ 0,\ -1$ because for the electron the spin quantum number is $S = \frac{1}{2}$ and for ^{14}N the spin quantum number is $I = 1$.

$$E = g\mu_B B_0 m_s + a m_s M_I \tag{3.132}$$

According to the selection rule, Eqn.3.66 and Eqn.3.67, $\Delta m_s = \pm 1$ and $\triangle M_I = 0$, due to the perburbation of $\vec{B}_1$, the splitting of energy levels in an external magnetic field is shown in Fig.3.28. (A) and (B). The energy separation of the splitting is calculated by Eqn.3.133. As M_I can only take the three values 1, 0, and -1, there are three allowed transitions and the CW EPR spectrum of nitroxide is a triplet. It should be noticed that Eqn.3.130, 3.131, 3.132, 3.133 are valid only for fast molecular motion. Under this situation from Eqn.3.133 the distance of the largest splitting is $2a$.

$$\triangle E = g\mu_B B_0 + a M_I \tag{3.133}$$

3.7.2 Powder spectrum of nitroxides

If nitroxides are in a single crystal host, and, if the molecular system coincides with the laboratory system (direction of external field), i.e. the Z-axis of the molecular frame is parallel to $\vec{B}_0$, the spin Hamiltonian is expressed by Eqn.3.134.

$$H = g_{zz}\mu_B\,B_0\hat{S}_z + A_{zz}\hat{S}_z\,\hat{I}_z \tag{3.134}$$

The same argument applies to $\vec{B}_0$ parallel to the X- or Y-axis of the molecular frame. The spectra for $A_{xx} = A_{yy} < A_{zz}$ with the magnetic field $\vec{B}_0$ directed along the principal axes X, Y, and Z at X-band microwave irradiation are shown in Fig.3.29. As the center transition corresponds to $M_I = 0$ and is thus not influenced by the hyperfine coupling according to Eqn.3.133, the anisotropy of the g-tensor determines the shift of the center field. g_{xx}, g_{yy} and g_{zz} can be calculated from each spectrum (Fig.3.29). When $\vec{B}_0$ coincides with one of the axes of the molecular frame, the energy levels can be calculated from Eqn.3.133 and $2A_{xx}$, $2A_{yy}$, $2A_{zz}$ can be evaluated from the corresponding spectrum. The maximum splitting is $2A_{zz}$ because A_{zz} is the largest principal value of the **A**-tensor (Fig.3.29. (A)).

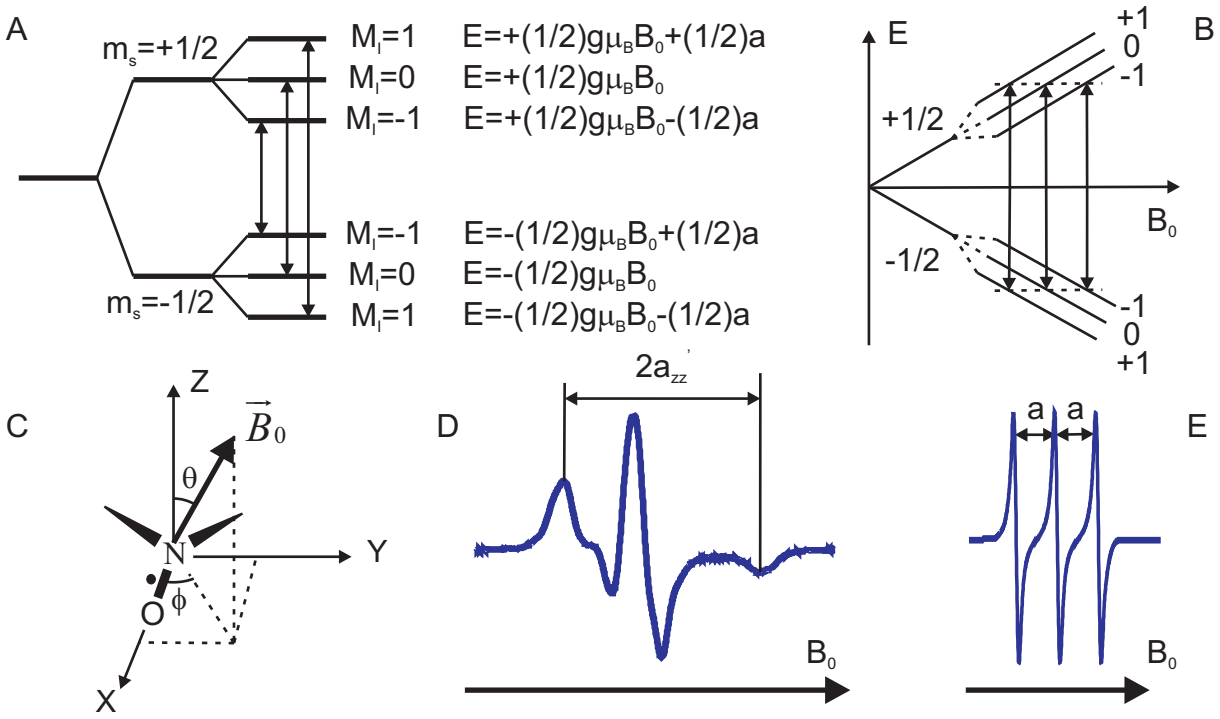

Figure 3.28: (A) Energy level scheme of the three allowed transitions of a nitroxide in presence of a magnetic field. (B) Another way to plot the energy levels which shows the same intensity of transition resonance lines with equal height and separation. (C) Nitroxide molecule and the principal axis frame of the g- and $\mathbf{A}$ tensors. (D) Powder spectrum of nitroxides. (E) EPR spectrum corresponding to transitions shown in (B).

Usually the samples are not oriented single crystals, but feature a random isotropic distribution of molecules. Then a so-called *powder spectrum* is obtained, which is a superposition of spectra of all orientations of $\vec{B}_0$ with respect to the molecule-fixed principal axes system. The spectrum consists of contributions from all possible orientations when the *rotational motion* is frozen on the time scale of the experiment. As EPR lines are derivative absorption lines (Fig.3.7. (D)), negative and positive contributions from neighboring orientations cancel. Powder spectra are thus dominated by contributions at the minimum and maximum resonance fields and by contributions at resonance fields that are common to many spins. The latter contribution provides the center line in the nitroxide powder spectrum (Fig.3.28. (D)). The outer extreme splitting measured directly in the powder spectrum is $2A_{zz}$.

3.7.3 Slow tumbling EPR spectra of nitroxides

To study diamagnetic materials such as polymers or organic-inorganic hybrids, nitroxide radicals can be used either as *spin probes*, which are just mixed with materials in interest, or *spin labels*, which are attached to backbones of the materials via covalent bonds. The mobility of a spin probe depends on the local viscosity (microviscosity) and on its connectivity to a larger, more immobile object. For spin labels, the mobility depends on the flexibility of the backbone and on the tumbling of the macromolecule as a whole. The mobility can be quantified by the *rotational correlation time* τ_c, which corresponds to the typical time during which a molecule maintains its spatial orientation. If the inverse of τ_c is of the same order of magnitude as the anisotropy of an interaction, this anisotropy is partially averaged and the EPR spectrum depends strongly on τ_c and on specific dynamics, such as the preference for a

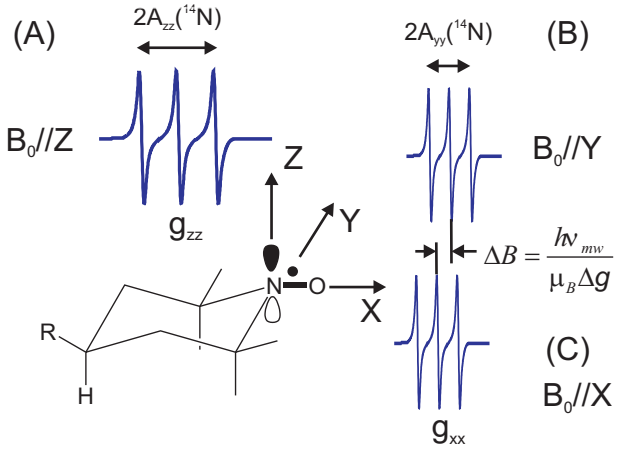

Figure 3.29: Simulated EPR spectra for a nitroxide radical in a single crystal. The anisotropic interaction makes spectra sensitive to orientation of molecules with respect to the magnetic field. The three cases are shown when the magnetic field is along one of the principal axes of the molecular frame: (A) $\vec{B}_0//Z$. (B) $\vec{B}_0//Y$. (C) $\vec{B}_0//Z$.

particular rotational axis or restrictions on the motion. For nitroxides at X-band, the EPR spectrum is dominated by the hyperfine anisotropy of about 150 MHz (corresponding to an anisotropy of the resonance field of ≈ 50 G). Hence tumbling effects can be observed on time scales of a few nanosceonds.

As shown in Fig.3.8, the slow tumbling region is such a range, in which the EPR spectrum can no longer be described as a simple superposition of Lorentzian lines as for fast motion, the single crystal, and the powder spectrum case. The outer extreme splitting measured directly in the spectrum is now $2A'_{zz}$, corresponding to the motionally averaged maximum hyperfine coupling (reduced from $2A_{zz}$ in powder spectrum due to rotational motion) however details of g-tensor and **A**-tensor are hard to obtain.

With the *Debye model* for rotational diffusion in Brownian rotational diffusion (Fig.3.30. (A)), the rotational correlation time τ_c is defined by Eqn.3.135. *Rotational diffusion* is a process by which the equilibrium statistical distribution of the overall orientation of molecules or particles is maintained or restored. Rotational diffusion may be compared to translational diffusion through which the equilibrium statistical distribution of position in space is maintained or restored.

$$\tau_c = \frac{1}{6D_{rot}} \tag{3.135}$$

D_{rot} is the *rotational diffusion coefficient* (s^{-1}) defined by Eqn.3.136 with R (with unit m) as radius of molecules which are modeled by rigid spheres in the Debye model, η as viscosity of the medium (with unit $kg\,m^{-1}\,s^{-1}$), k_B as the Boltzmann constant ($1.38 \times 10^{-23}\ JK^{-1}$) and T as the temperature (K).

$$D_{rot} = \frac{k_B T}{8\pi\eta R^3} \tag{3.136}$$

Different motional regimes are illustrated in Fig.3.30. (B). In the very fast motional region for $\tau_c < 10^{-11}$ s (not slow tumbling) the spectrum consists of three sharp lines of equal height (Lorentzian lines) as the fast limit. In this region the anisotropic terms of coupling are averaged to zero (e.g. in solution). The spectrum is

characterized by the isotropic values of magnetic parameters. No information on τ_c can be inferred from such spectra. In the fast motional region ($10^{-11} < \tau_c < 3 \times 10^{-9}$ s), there is a differential broadening of the lineshape while the line positions remain almost unchanged. The deviation of the relative height of the spectral lines from the expected lines is caused by the effect of the time-dependent part of the Hamiltonian. In this regime the transverse relaxation and thus the line width is dominated by effects of rotational motion. In the *slow motional region* ($3 \times 10^{-9} < \tau_c < 10^{-7} \sim 10^{-6}$ s) a distortion of the line positions and line shape is observed. The line shape reflects directly the random orientation distribution. EPR lineshape analysis is mostly applied if τ_c is in this regime and information on dynamics of the spin probe can be obtained. In the very slow motional region ($\tau_c > 10^{-7} \sim 10^{-6}$ s), the rigid powder spectrum is reached (a broadened line).

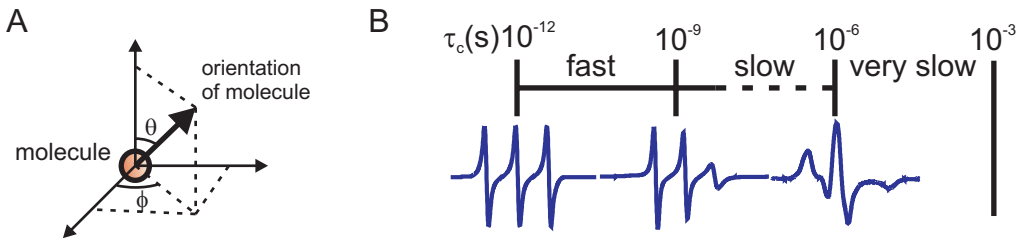

Figure 3.30: Debye reorientation model and motional regimes. (A) Debye reorientation model: The molecule is approximated by a rigid sphere of radius R. There are no interactions between molecules. The surroundings can be described as a viscous continuum, with viscosity η. Rotational diffusion controls the orientation of molecules. (B) Slow tumbling region. In different rotational correlational time regions, the nitroxide CW EPR spectrum has characteristic lineshapes. In the very fast motional region for $\tau_c < 10^{-11}$ s (not slow tumbling) the spectrum consists of three sharp lines of equal height (Lorentzian lines) as the fast limit. In the fast motional region ($10^{-11} < \tau_c < 3 \times 10^{-9}$ s), there is a differential broadenng of the lineshape while the line positions remain almost unchanged. In the *slow motional region* ($3 \times 10^{-9} < \tau_c < 10^{-7} \sim 10^{-6}$ s) a distortion of the line positions and line shape is observed. In the very slow motional region ($\tau_c > 10^{-7} \sim 10^{-6}$ s), the rigid powder spectrum is reached (a broadened line).

3.7.4 Line shape analysis for tumbling nitroxide radicals

The *relative anisotropy* r_a can be calculated by Eqn.3.137 if the outer-extrema separation $2A'_{zz}$ in the rigid limit and the isotropic hyperfine coupling, which can be calculated in fast-limit spectra, are known.

$$r_a = \frac{2A'_{zz} - 2A_{fast}}{2A_{rigid} - 2A_{fast}} \tag{3.137}$$

In the slow tumbling regime where τ_c is 1 to 10 ns, spectra are best analyzed by simulations. When relative anisotropy r_a is calculated, the corresponding τ_c can be derived from the simulation. Cameron reviewed EPR studies of polymers in the bulk phase and the analysis of nitroxide CW EPR spectra to relate T_{50G} to the glass transition point of a polymer T_g. (28) The empirical parameter T_{50G} is the temperature at which $2A'_{zz}$ equals 50 G (5 mT). Although an unknown T_g usually can not be determined by the spin probe method, T_{50G} is still a measure of the transition temperature at which a reordering of the surfactant layers in organoclays

or nanocomposites happens (T_{ODT}, order-disorder transition). Values of T_{50G} can be measured directly from temperature-dependent CW spectra.

Usually, dynamic information can be analyzed from temperature-dependent CW EPR measurements. The rigid limit of $2A_{rigid}$ is obtained from a low-temperature measurement or from a primary echo measurment at 50 K by pulse EPR. The fast limit of $2A_{fast}$ is obtained from high temperature CW EPR (e.g. 450 K).

One example of analyzing dynamics of an end-labeled spin probe in surfactant layers in organoclay, polycaprolactone (PCL) and polystyrene (PS) composites is shown is Fig.3.31. The rigid limit $2A_{rigid}$ is measured from the absorption spectrum at 50 K which is not shown. The absorption spectrum has to be transfered to a first derivative spectrum as dA/dB with an appropriate modulation parameter before $2A_{rigid}$ is obtained. In (A) CW EPR spectra at different temperature are shown. The slow component which is the outer maximum and minimum, and the fast component, which is the inner extrema in slow tumbling, are marked with a cross. By measuring the splitting of the slow and fast component, the temperature dependent $2A'_{zz}$ are obtained.

Using the Arrhenius equation expressed as Eqn.3.138, the plot of $\log \tau_c$ versus $1/T$ will give an activation energy E_a from the slope. A is a *pre-expontential factor* (also called frequency factor) and R is the gas constant (8.3145 $J\,K^{-1}\,mol^{-1}$). The activation energy can be interpreted as the minimum kinetic energy that the dynamic process needs to proceed.

$$\log \tau_c = \log A + \frac{E_a}{RT} \tag{3.138}$$

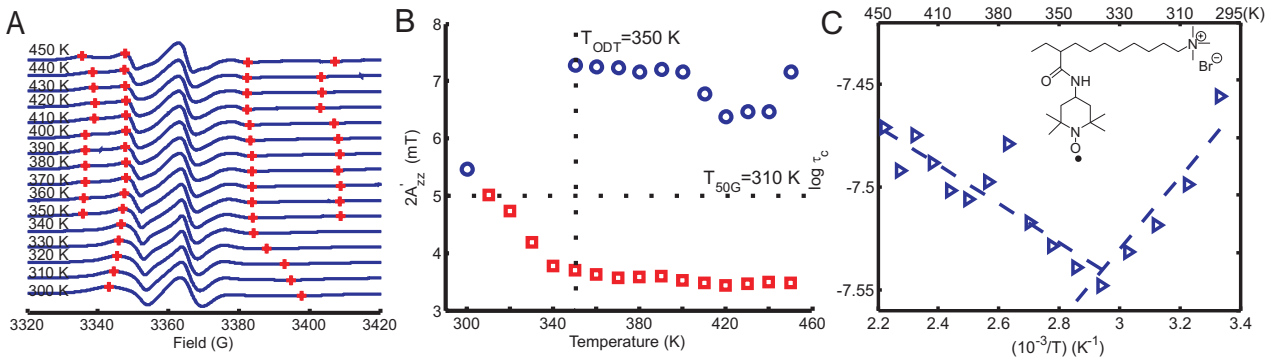

Figure 3.31: Temperature-dependent CW EPR of magadiite+(9-SL-UTMA)+HTMA. (A) CW EPR spectra at different temperature. The slow component which is the outer maximum and minimum, and the fast component, which is the inner extrema, are marked with crosses. (B) $2A'_{zz}$ measured from CW EPR spectra as a function of temperature. Circles indicate the corresponding τ_c in slow tumbling region. Squares indicate the corresponding τ_c is in the fast region. T_{ODT} and T_{50G} can be identified from temperature dependent CW EPR. (C) The Arrhenius plot of τ_c which is derived from r_a and simulation. From the plot the the activation energy E_a can be calculated. The chemical structure of 9-SL-UTMA is shown.

3.8 EPR and NMR spectrometers

The basic layouts of EPR and NMR spectrometers are shown in Fig.3.32. The layout of a continuous wave EPR spectrometer is shown in (A). A typical magnetic field is 0.3 T, which requires about 9 GHz microwaves for

resonance. Compared with an NMR spectrometer in which the radiofrequency field is generated by a coil around the probe, EPR uses waveguides and a cavity to create the microwave field. Pulse EPR can use the same basic setup but requires more units such as a pulse amplifier (travelling wave tube (TWT))and pulse detector (not shown). Usually pulse EPR is measured at low temperatures (from 50 K to 80 K) to freeze Brownian motion and achieve longer relaxation times. Usually liquid helium (for 50 K) and liquid nitrogen (80 K) are used as cooling media and are pumped to flow through the resonator under moderate vacuum.

In NMR a uniform, intense magnetic field is generated by a superconducting magnet capable of producing fields of the order of 7 T (300 MHz proton frequency) and more. Pulse techniques are generally used in NMR because an appropriate pulse can excite the whole spectral range of a given nuclear isotope, while only a small part of the spectrum of electron spins is excited by a single pulse. Hence CW EPR is often more sensitive. Furthermore it is technically easier to measure throughout the whole range of electron relaxation times than with pulse EPR, although the latter technique gives more information on structure and on relaxation mechanism.

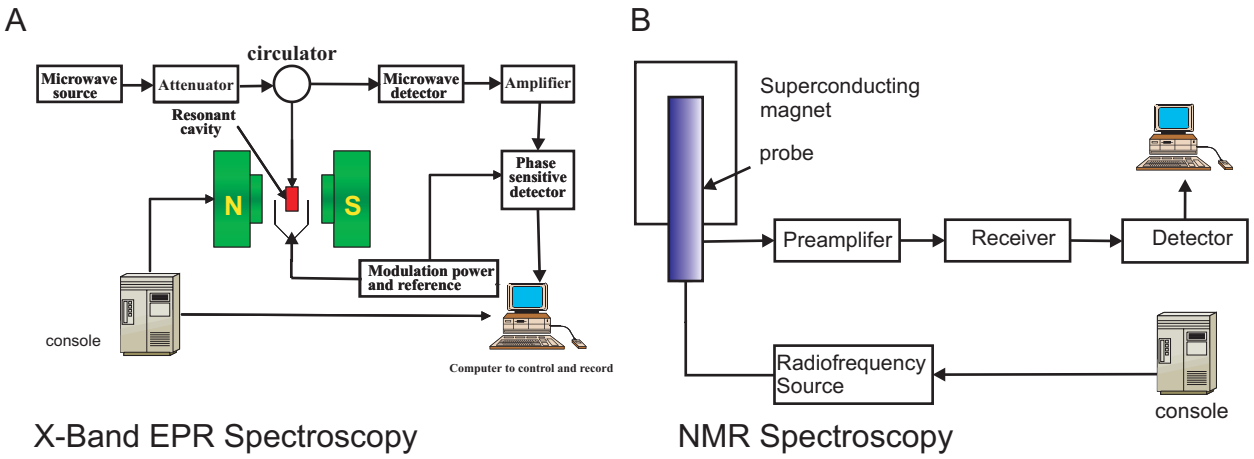

Figure 3.32: Layout of EPR and NMR spectrometer. (A) CW EPR spectrometer setup. (B) NMR spectrometer setup.

.

3.9 EPR methods applied in this thesis

Pulse Electron Paramagnetic Resonance techniques are very useful methods to characterize the interaction and structure information of paramagnetic centers such as radicals, transition metal ions, and crystal defects. (23) The dipole-dipole coupling arising from electron-electron (spin S) or electron (spin S)-nuclear (spin I) pairs is distance- and angular-dependent. If it can be separated from the total spin Hamiltonian, a model of the spatial distribution of the spins can be derived. Pulse EPR can access length scales between 0.5 and 10 nm corresponding to electron-electron or electron-nuclear couplings between 100 kHz and a few megahertz (MHz). (23) So pulse EPR can complement results from scattering techniques which require long range order and access length scales either can from micrometers to 80 nanometer (light scattering), or in the angstrom (Å) range (small angle X-ray scattering

(SAXS) and small angle neutron scattering (SANS)). For systems with intermediate order, expecially in polymer science in which intermolecular interactions and structural information on nanometer scales are important, pulse EPR is very suitable. This thesis focusses on its application on polymer-layered silicate (PLS) nanocomposites systems (Fig.1.8).

Two-pulse ESEEM is applied to measure the transverse relaxation time according to Eqn.3.101. Three-pulse ESEEM is used to measure deuterium modulation for samples with site-labeled deuterated surfactants and a site-labeled nitroxide spin probe. Four-pulse DEER is applied to measure dipole-dipole couplings between site-labeled nitroxides in surfactant layers. ENDOR is used to measure the hyperfine coupling between electron spins and ^{31}P nuclei for samples prepared with nitroxide spin probe and phosphonium surfactant. The signal of the stimulated echo experiment is also analyzed to have additional information on the relaxation mechanism.

As pulse EPR measurements are usually taken at low temperature (for ESEEM at 80K and for DEER and ENDOR at 50 K) to get minimum influence of dynamic effects, pulse EPR measurements do not lead to any thermal degradation and are performed first. These measurements yield structural information and are described in Chapter. 5. Then the samples are measured with temperature-dependent CW EPR (from 300 K to 450 K in 10 k increment) to obtain dynamic information such as τ_c, T_{50G}, T_{ODT} and E_a from which the mobility of surfactant layers can be inferred. This will also be described in detail in Chapter 5.

Chapter 4

^{2}H Solid State NMR

4.1 Basics of Nuclear Magnetic Resonance

4.1.1 Energy levels of nuclei in a magnetic field

As described in Sec.3.1 the electron gives rise to a magnetic moment due to its spin angular momentum and orbital angular momentum. A nucleus possessing a spin quantum number $I \neq 0$ also gives rise to a magnetic moment in an external magnetic field. The spin quantum number, I, is a fixed characteristic property of a nucleus and may be an integer or a half integer, but is never negative (Table.4.1). A nucleus with spin quantum number I has the following properties because the commutator of operators $\hat{I}^2$ and $\hat{I}_z$ follows $\left[\hat{I}^2,\ \hat{I}_z\right] = 0$ and both operate on a spin eigenfunction ψ of the state giving eigenvalues $I(I+1)\hbar^2$ and $m_I\hbar$ respectively: (20)

1. An angular momentum of magnitude $\sqrt{I(I+1)}\hbar$ because the state fulfills Eqn.4.1 with ψ representing an eigenfunction of the state.

$$\hat{I}^2\psi = I(I+1)\hbar^2\psi \tag{4.1}$$

2. A component of angular momentum $m_l\hbar$ on an arbitrary axis, where $m_l = I,\ I-1,\ \ldots,\ -I$. because the same state with eigenfunction ψ fulfills the Eqn.4.2. I_z is the z-component of the spin angular momentum I. So the magnetic moment of nucleus may lie in $2I+1$ different orientations relative to an axis.

$$\hat{I}_z\psi = m_I\hbar\psi \tag{4.2}$$

3. If $I > 0$, a magnetic moment with a constant magnitude $|I|$ and an orientation that is determined by the value of m_I.

Just as Eqn.3.4 for magnetic moments arising from electrons in a magnetic field $\vec{B}_0$, the energy of interaction between a nucleus with a magnetic moment $\vec{\mu}$ and an external field $\vec{B}_0$ can be calculated by Eqn.4.3 with **I** as spin

number of protons	number of neutrons	I	Example	Signal of NMR
even	even	0	${}^{12}_{6}$C, ${}^{16}_{8}$O	no signal
odd	odd	integer(1,2,3,...)	${}^{2}_{1}$D, ${}^{14}_{7}$N	except ${}^{2}_{1}$D, poor signal
even	odd	half-integer ($\frac{1}{2}$, $\frac{3}{2}$, $\frac{5}{2}$, ...)	${}^{13}_{6}$C	good for NMR
odd	even	half-integer ($\frac{1}{2}$, $\frac{3}{2}$, $\frac{5}{2}$, ...)	${}^{31}_{15}$P, ${}^{1}_{1}$H	good for NMR

Table 4.1: Nuclear constitution and the nuclear spin quantum number

angular momentum and γ_n as the magnetogyric ratio for the nucleus.

$$\hat{\mu} = \gamma_n \hat{\mathbf{I}} \tag{4.3}$$

The Hamiltonian, just as in Eqn.3.6, can be expressed by Eqn.4.4.

$$H = -\gamma_n \mathbf{B}_0 \hat{\mathbf{I}} \tag{4.4}$$

The *nuclear magneton* μ_N is defined by Eqn.4.5. It is noticed that the Bohr magneton is almost 2000 times larger than the nuclear magneton because of the larger mass of the proton m_p.

$$\mu_N = \frac{e\hbar}{2m_p} = 5.051 \times 10^{-27} \quad J\,T^{-1} \tag{4.5}$$

The magnetogyric ratio of nucleus γ_n is related to the nuclear magneton by Eqn.4.6 with g_n as *nuclear g-factor*, in analogy to the electron g-factor.

$$\gamma_n \hbar = g_n \mu_N \tag{4.6}$$

Nuclear g-factors vary between -6 and +6. Positive values of g_n and γ_n denote a magnetic moment that is parallel to the spin; negative values indicate that the magnetic moment and spin are antiparallel. From Eqn.4.3 and Eqn.4.4 the possible values of the z-component of the spin magnetic moment are:

$$\mu_n = \gamma_n m_I \hbar \tag{4.7}$$

Classically by Eqn.3.2, in a magnetic field B_0 in the z-direction, the $2I+1$ orientations (Fig.4.1. (A) for $I = 1$) of the nucleus have different energies, which are given by Eqn.4.8.

$$E_{m_I} = -\mu_z B_0 = -\gamma_n m_I \hbar B_0 \tag{4.8}$$

As shown in Fig.4.1. (B), for a nucleus with $I = 1/2$ (e.g. proton), the energy levels are split and the energy separation between levels is calculated by Eqn.4.9 if we put $m_I = \pm(1/2)$ into Eqn.4.8 here. ν_L is the Larmor frequency at which magnetic resonance is observed.

$$\triangle E = \gamma_n \hbar B_0 = g_n \mu_N B_0 = h\nu_L \tag{4.9}$$

Compared with NMR, the sensitivity of EPR is significantly better due to the larger magnetic moment of the electron spin (with larger magnetogyric ratio) compared to nuclear spins. The larger energy separation between energy levels in EPR gives resonance in the microwave frequency range. However, EPR is only used on paramagnetic species while NMR can be applied to most of nuclei with $I \neq 0$. The spectral resolution of NMR is very high despite the lower resonance frequency, as relaxation times of nuclear spins are much longer and the lines are thus much narrower. As each nucleus has its characteristic magnetogyric ratio the Larmor frequency is highly selective to each nucleus. It is in the radiofrequency range.

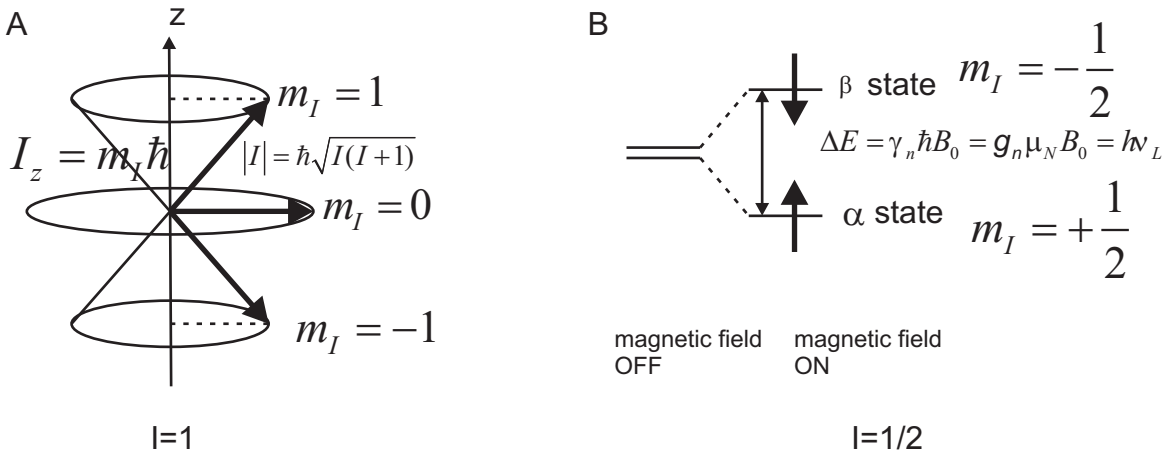

Figure 4.1: (A) The vector picture of spin angular momentum for $I = 1$. m_I can have value -1, 0, 1 giving rise to a triplet state. The z-component (or any of x- or y-) of spin angular momentum and the magnitude of the momentum $|I|$ can be defined simultaneously, however any two of axis components can not be defined simultaneously because $\left[\hat{I}_z,\ \hat{I}_x\right] = i\hbar\hat{I}_y$ but not zero. This uncertainty corresponds to a distribution of the vector on a cone. (B)The nuclear energy levels of a spin-$\frac{1}{2}$ nucleus with positive magnetogyric ratio γ_n in a magnetic field. Resonance occurs when the energy separation of the levels matches the energy of the photons in the electromagnetic field.

4.1.2 The chemical shift

Nuclear magnetic moments interact with the *local field* which differs from the applied field because the latter induces electronic orbital angular momentum (that is, the circulation of electronic currents) which gives rise to a small additional magnetic field dB at the nuclei. This additional field is proportional to the applied field and can be written by Eqn.4.10 with σ as the *shielding constant* of the nucleus. σ could be positive (additional field antiparallel to the applied field) or negative (parallel to the applied field).

$$dB = -\sigma B_0 \tag{4.10}$$

The local field is thus:

$$B_{local} = B_0 + dB = (1 - \sigma)B_0 \tag{4.11}$$

With Eqn.4.9 the Larmor frequency can be related to the shielding constant by Eqn.4.12. This frequency is different for nuclei in different environments. Hence the NMR signal can give information on the chemical environment of nuclei of interest.

$$\nu_L = \frac{\gamma_n B_{loc}}{2\pi} = (1-\delta)\frac{\gamma_n B_0}{2\pi} \tag{4.12}$$

Usually the position of NMR lines is expressed in terms of a *chemical shift* as a calibrated value which is independent of the applied field. The chemical shift δ is calculated by Eqn.4.13 with ν° as the Larmor frequency of a reference standard. Because the coefficient of 10^6 in the equation the unit of chemical shift is ppm. Usually the standard for protons is the proton resonance in tetramethylsilane (TMS) ($Si(CH_3)_4$). For ^{13}C, the reference frequency ν° is the ^{13}C resonance in TMS.

$$\delta = \frac{\nu - \nu^\circ}{\nu^\circ} \times 10^6 \tag{4.13}$$

The relation between the shielding constant σ and chemical shift δ is obtained by subtituting Eqn.4.12 into Eqn.4.13.

$$\delta = \frac{(1-\sigma)B_0 - (1-\sigma^\circ)B_0}{(1-\sigma^\circ)B_0} \times 10^6 = \frac{\sigma^\circ - \sigma}{1-\sigma^\circ} \times 10^6 \approx (\sigma^\circ - \sigma) \times 10^6 \tag{4.14}$$

If the shielding σ is smaller than σ°, meaning that the chemical shift δ increases, the nucleus is said to be *deshielded* indicating that the Larmor frequency is lower. The signal is then said to be shifted *downfield* (left side of the conventional NMR spectrum with δ decreasing from left to right). In this case, the additional magnetic field generated in the chemical environment is parallel to the applied magnetic field. If the shielding σ is larger than σ°, the nucleus is *shielded* and the additional field is antiparallel to the applied field. The shift δ is then *upfield* meaning that the Larmor frequency is higher. The standard signal on the δ-scale is at 0 ppm and usually corresponds to one that can be observed for this isotope of the strongest shielding effects.

The observed shielding constant can be expressed as the sum of three contributions:

$$\sigma = \sigma(\text{local}) + \sigma(\text{neighbour}) + \sigma(\text{solvent}) \tag{4.15}$$

The *local contribution*, σ(local), is essentially the contribution of the electron of the atom that contains the nucleus in question. The *neighbouring group contribution*, σ(neighbour), is the contribution from the groups of atoms that form the rest of the molecule. The *solvent contribution*, σ(solvent), is the contribution from the solvent molecules in liquids. The equivalent in solid-state NMR are contributions from neighbouring molecules.

The local contribution can be expressed by the sum of *diamagnetic contribution*, σ_d, and a *paramagnetic contribution*, σ_p.

$$\sigma(\text{local}) = \sigma_d + \sigma_p \tag{4.16}$$

A diamagnetic contribution σ_d opposes the applied magnetic field and shields the nucleus in question, whereas a paramagnetic contribution σ_p reinforces the applied magnetic field and deshields the nucleus in question. Therefore $\sigma_d > 0$ and $\sigma_p < 0$. The total local effect depends on which contribution dominates. The magnitude of σ_d depends on the electron density close to the nucleus and can be calculated from the *Lamb formula* (Eqn.4.17) with μ_0 as vacuum permeability and r as the electron-nucleus distance. If the electronegativity of nearby nuclei increases, σ_d will decrease due to less electron density resulting in an increase of the chemical shift (deshielding).

$$\sigma_d = \frac{e^2 \mu_0}{12\pi m_e} \left\langle \frac{1}{r} \right\rangle \tag{4.17}$$

The neighbouring group contribution arises from the currents induced in nearby groups of atoms. Consider the neighbouring group X on the proton H in a molecule such as H-X (Fig.4.2. (A)). The induced magnetic moment of X generated by the applied field is expressed by Eqn.4.18 with χ as the magnetic susceptibility of X (dimensionless), M as magnetization (A/m) and H_0 as the strength of applied magnetic field (A/m). Magnetization is defined by Eqn.3.11.

$$M = \chi H_0 \tag{4.18}$$

To a good approximation, the shielding constant σ(neighbour) can be expressed by Eqn.4.19.

$$\sigma(\text{neighbour}) \propto (\chi_{\parallel} - \chi_{\perp}) \left(\frac{1 - 3\cos^2\theta}{r^3} \right) \tag{4.19}$$

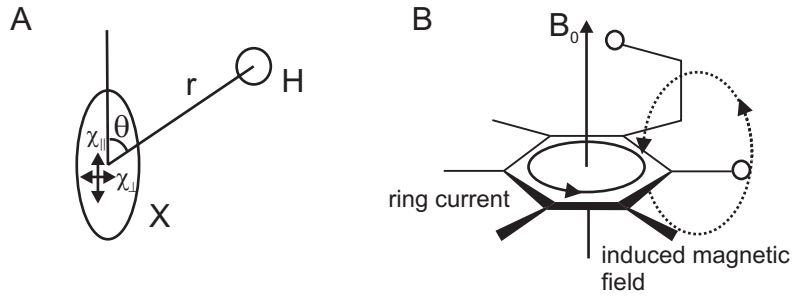

Figure 4.2: (A) Influence of neighbouring group X on proton H in question. The proton is affected by the induced magnetic moment arising from X. (B) The shielding and deshielding effects of the ring current induced in the benzene ring by the applied field. Protons attached to the ring are deshielded but a proton attached to a substituent that projects above the ring is shielded.

A special case of a neighbouring group effect is found in aromatic compounds (Fig.4.2. (B)). The strong anisotropy of the magnetic susceptibility of the benzene ring is ascribed to the ability of the field to induce a *ring current*, a circulation of electrons around the ring, when it is applied perpendicular to the molecular plane. Protons in the plane are deshielded, but protons that lie above or below the plane (as members of substituents of the ring) are shielded.

Just like the g-tensor in EPR, chemical shift takes into account the contributions of the local field. If the sample is in the solid state, the chemical shift is anisotropic (chemical shift anisotropy, CSA).

4.1.3 The spin Hamiltonian in solid state NMR

The spin Hamiltonian consists of three terms in solid state NMR: Zeeman interaction which is characterized by chemical shift anisotropy (CSA), *J-coupling* which is a scalar spin-spin interaction through bonding caused by *Fermi contact interaction* (Fig.4.3. (A)), and dipole-dipole coupling (Fig.4.3. (B)), which is through space.

$$H_0 = H_{CSA} + H_J + H_{DD} \tag{4.20}$$

The Hamiltonian for the Zeeman interaction term is given by Eqn.4.21.

$$H_{CSA} = \gamma_n \mathbf{B}_0 \left(\mathbf{1} - \hat{\sigma}\right) \mathbf{I} \tag{4.21}$$

J-coupling, which arises from spin-spin coupling between nuclei through bonds as shown in Fig.4.3, is often to a good approximation isotropic. This coupling is caused by the Fermi contact interaction of the nuclei with electrons in s orbitals. Through this polarization mechanism, the Fermi contact interaction with the second nucleus leads to different energies for the parallel and antiparallel configurations of the two nuclear spins.

The Hamiltonian for J-coupling is given by Eqn.4.22 with J as the coupling constant.

$$H_J = 2\pi\hbar J \hat{\mathbf{I}}_1 \hat{\mathbf{I}}_2 = 2\pi\hbar(\hat{I}_{1x}\hat{I}_{2x} + \hat{I}_{1y}\hat{I}_{2y} + \hat{I}_{1z}\hat{I}_{2z}) \tag{4.22}$$

The magnitude of J-coupling decreases with increasing number of bonds between the two nuclei. Usually the J-coupling for two nuclei connected by more than two bonds (for example, protons on H–C–H as $^2\mathrm{J_{HH}}$) can be neglected in solid-state NMR.

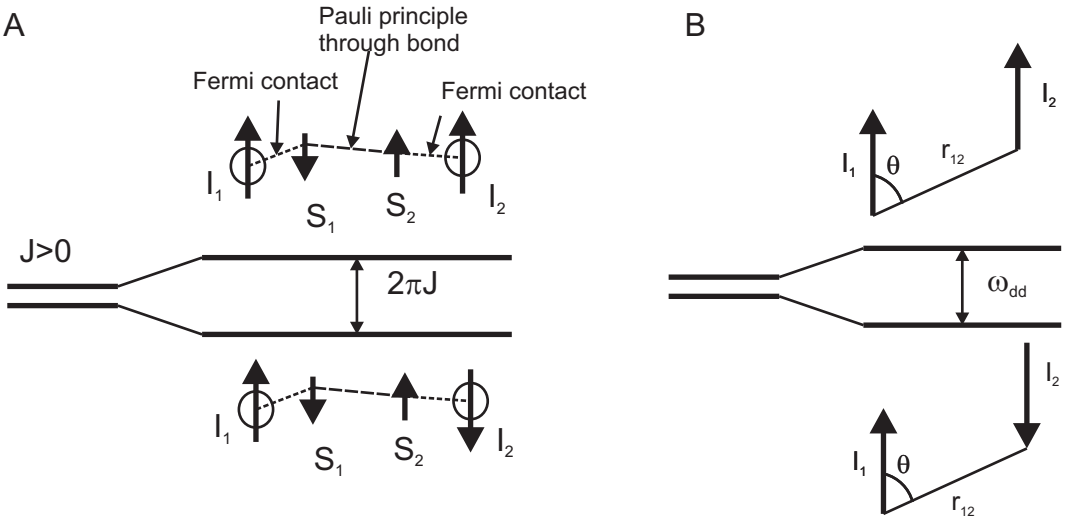

Figure 4.3: (A) Illustration of J-coupling ($^1J_{HH}$). The two arrangements have slightly different energies. In this case, J is positive, corresponding to a lower energy when the nuclear spins are antiparallel. (B) Dipole-dipole coupling between two magnetic moments arising from nuclear angular moments $\vec{I}_1$ and $\vec{I}_2$ results in splitting of energy levels. The dipolar coupling is through space while J-coupling is through bond.

In principle, the coupling mediated by the Fermi contact interaction and the Pauli principle (J-coupling) may also have an anisotropic contribution, but this can be neglected for light nuclei. The main contribution to the anisotropic part of the coupling between spins is the dipole-dipole coupling which is a through-space coupling(Fig.4.3. (B)). Just as derived for Eqn.3.59, in the high field approximation, the Hamiltonian for this term can be given by Eqn.4.23.

$$H_{DD} = \frac{\mu_0}{4\pi}\frac{\gamma_1\gamma_2\hbar^2}{r_{12}^3}(1-3\cos^2\theta)\left(\hat{I}_{1z}\hat{I}_{2z} - \frac{1}{2}\hat{I}_{1x}\hat{I}_{2x} - \frac{1}{2}\hat{I}_{1y}\hat{I}_{2y}\right) \tag{4.23}$$

If the two nuclei have Larmor frequencies that differ far from each other, e.g. ^{1}H and ^{13}C, the Hamiltonian can be simplified further by Eqn.4.24 with ω_{dd} as the dipolar coupling frequency (Fig.4.3. (B)).

$$H_{DD} = \frac{\mu_0}{4\pi}\frac{\gamma_1\gamma_2\hbar^2}{r_{12}^3}(1-3\cos^2\theta)\hat{I}_{1z}\hat{I}_{2z} = \omega_{dd}(1-3\cos^2\theta)\hat{I}_{1z}\hat{I}_{2z} \tag{4.24}$$

The dipolar coupling is anisotropic and averages to zero in solution NMR as Eqn.3.61. In solids the dipolar anisotropy can be described as a tensor which has the principal values as $-2\omega_{dd}$, ω_{dd} and ω_{dd}.

4.2 ^{2}H solid state NMR

4.2.1 The nuclear quadrupole interaction

In the case of nuclei with $I > 1/2$ such as ^{2}H, the solid state NMR spectra are usually dominated by *nuclear quadrupole interaction*. The nuclear quadrupole interaction between the electric quadrupole moment of nuclear spins ($I > 1/2$), Q, and the electric field gradient produced by surrounding electrons q, is a purely anisotropic interaction (Fig.4.4. (A)). (29) eq is referred to as the electric field gradient and eQ is referred to as the quadrupole moment. Their product in Hz units is defined as the *quadrupole coupling constant* by Eqn.4.25.

$$\text{quadrupole coupling constant} = \frac{e^2qQ}{h} \tag{4.25}$$

Usually the nuclear quadrupole coupling induces fast spin-spin relaxation (short T_2), so that the lines of quadrupole nuclei are significantly broader than the lines of $I = 1/2$ nuclei in NMR. The total Hamiltonian for quadrupole nuclei in magnetic field can be written as Eqn.4.27.

$$H = H_{Zeeman} + H_{quadrupolar} \tag{4.26}$$

The Hamiltonian for quadrupole coupling between a single nuclear spin I and the electric field gradient generated by surrounding electrons is given by Eqn.4.27 with $\mathbf{I}$ as the spin vector operator.

$$H_{quadrupolar} = \mathbf{I}\hat{Q}\mathbf{I} \tag{4.27}$$

$\mathbf{Q}$ is a 3×3 matrix or second rank tensor describing the three-dimensional nature of the quadrupole interaction. The tensor $\mathbf{Q}$ is expressed by Eqn.4.28 with V as electric field gradient at the nuclear site. The components of

V describe completely the orientation and magnitude of the electric field gradient. For example, in principal axis system the diagonal elements V_{11}, V_{22} and V_{33} in the diagonal form of V describe the size and shape of the field gradient.

$$\mathbf{Q} = \frac{eQ}{2I(2I-1)h}\dot{\mathbf{V}} \tag{4.28}$$

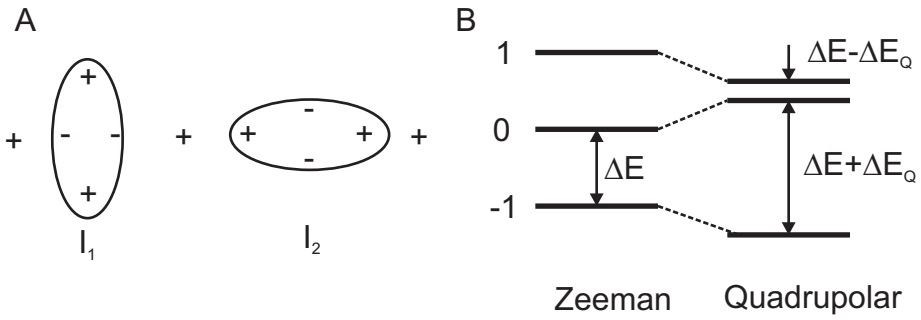

Figure 4.4: (A) Two orientations for a electric quadrupole moment in the electric gradient of a positive point charge. The orientation of I_1 has lower energy than that of I_2. (B) Energy levels of nucleus with $I = 1$. The allowed transitions are $\Delta m_I = \pm 1$

The *asymmetry parameter* η describing the electric field gradient is defined by Eqn.4.29.

$$\eta = \frac{V_{11} - V_{22}}{V_{33}} \tag{4.29}$$

In solution, as $\mathbf{V}$ can be evaluated by $V = \frac{1}{3}(V_{11} + V_{22} + V_{33})$ and since the $\mathbf{V}$ tensor is traceless, V=0. The quadrupole coupling is thus averaged to zero just as the dipolar interaction. In the solid state, if the electric field gradient is symmetric about the principal axis, $V_{11} = V_{22}$ and V_{33} is unique. From Eqn.4.29 $\eta = 0$. This is usually a good approximation for deuterium connected to carbon (C–D bond). The corresponding quadrupole coupling is said to be *axially symmetric*.

In the case of ^{2}H, under the high field approximation ($H_{Zeeman} \gg H_{quadrupole}$), the energy shifts due to the quadrupole coupling for the single nucleus may be obtained by first order perturbation theory. (15) For an axially symmetric coupling tensor the energy shift is given by Eqn.4.30 with ΔE_Q as the energy shift due to the quadrupolar coupling and θ as the angle between the principal component of the electric field gradient tensor and the magnetic field vector (Fig.4.4. (B)).

$$\triangle E_Q = \frac{3}{8}\left(\frac{e^2qQ}{h}\right)(3\cos^2\theta - 1) \tag{4.30}$$

The shifts of the energy levels are shown in Fig.4.4. (B). It should be noted that the ($m_I = -1$) and ($m_I = +1$) levels are affected equally and in the same direction by the quadrupole coupling. The selection law for the allowed transition is $\Delta m_I = \pm 1$. The separation between the resonance transition energies is $\Delta E + \Delta E_Q - (\Delta E - \Delta E_Q) = 2\Delta E_Q$. Thus the spectrum for a single spin $I = 1$ nucleus interacting with an axially symmetric field gradient

consists of a doublet with the peak separations given by Eqn.4.31. For deuterium in a C–D bond $\Delta\nu$ is about 170 $\backsim$ 200 kHz, for ^{14}N it is about 5 MHz and for ^{35}Cl it is about 80 MHz. Hence solid-state NMR has good resolution for deuterons (^{2}H nuclei). In particular, for aliphatic deuterons $\Delta\nu$ is about 165 kHz and for aromatic deuterons it is about 185 kHz.

$$\triangle\nu = \frac{3}{4}\left(\frac{e^2qQ}{h}\right)(3\cos^2\theta - 1) \tag{4.31}$$

4.2.2 The ^{2}H NMR experiment

Because spin-1 nuclei have three available spin states, it is not possible to represent the behaviour of the spins in terms of the simple magnetization vector behaviour, which we discussed for spin-1/2 nuclei or electrons. However the effect of pulses in the NMR experiment is similar. Generally in solid-state deuteron NMR the resonance angular frequency is given by Eqn.4.32. (14) The orientation of the magnetic field $\vec{B}_0$ in the principal axes system of the electric field gradient is specified by polar angles θ and ϕ (refer to Fig.3.28. (C)). ω_0 denotes the Larmor frequency and ω_Q denotes the frequency shift due to quadrupole coupling (Fig.4.4. (B)).

$$\begin{aligned}\omega &= \omega_0 \pm \frac{3}{8}\left(\frac{e^2qQ}{\hbar}\right)(3\cos^2\theta - 1 - \eta\sin^2\theta\cos 2\phi)\\ &= \omega_0 \pm \omega_Q\end{aligned} \tag{4.32}$$

Four different regimes can be distinguished with three important parameters: ω_Q as difference between resonance frequencies ($\Delta\nu$); the exchange rate k defined by rotational correlational time by $\tau_c = 1/(2k)$; and T_2^* which is the effective transverse relaxation time. (14)

1. In the *fast exchange* region ($\tau_c < 10^{-7}$ s, $k \approx \omega_0$ and $k \gg \omega_Q$), a lineshape with a Lorentzian at the center $\bar{\omega}$ is observed.

2. In the *intermediate exchange* region ($10^{-6} \leq \tau_c \leq 10^{-5}$s, $k \approx \omega_Q$), the signal is broadened and spread over the whole frequency range $\bar{\omega} \pm \omega_0$.

3. In the *slow exchange* region ($10^{-5} \leq \tau_c \leq 10^{-4}$ s, $k \leq \omega_Q$), a doublet Lorentzian centered at $\bar{\omega} + \omega_Q$ and $\bar{\omega} - \omega_Q$ respectively. The exchange imposed by the molecular motion causes an extra broadening of the lines observed in absence of moton.

4. In the *ultraslow exchange* region ($10^{-4} \leq \tau_c \leq 100$ s, $k \ll 1/T_2^*$), the doublet line shape becomes insensitive to the motion because the extra broadening is much smaller than the natural line width.

Different types of NMR experiments can measure different time-scales of dynamics of deuterons. This is shown in Fig.4.5. There are three basic experiment methods with different pulse sequences that are applied in ^{2}H solid state NMR (Fig.4.6). The solid-echo sequence (A) is used for the detection of ^{2}H NMR line shapes and spin-spin (T_2) relaxation. The timescale of solid-echo NMR in studying T_2 is in the microsecond scale and the line shape is in the MHz range. The spin-lattice (T_1) relaxation is probed with a modified inversion recovery experiment (B) from which fast molecular motions in the vicinity of the Larmor frequency, i.e. in the MHz to GHz region,

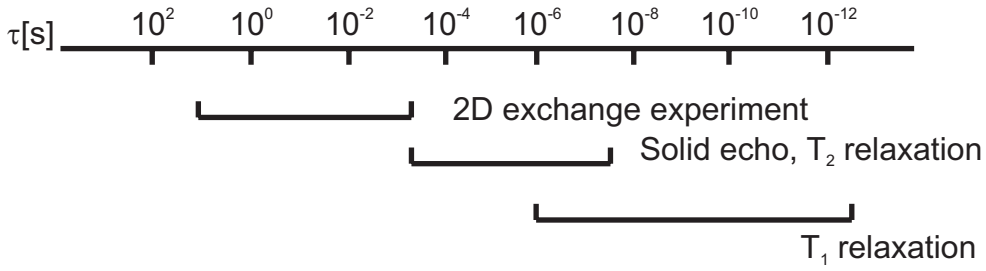

Figure 4.5: Sensitive time-scales of different types of dynamic NMR experiments.(18)

are accessible. 2D exchange experiments (C) can be used to study ultra-slow motional processes in the Hz- and sub-Hz range.

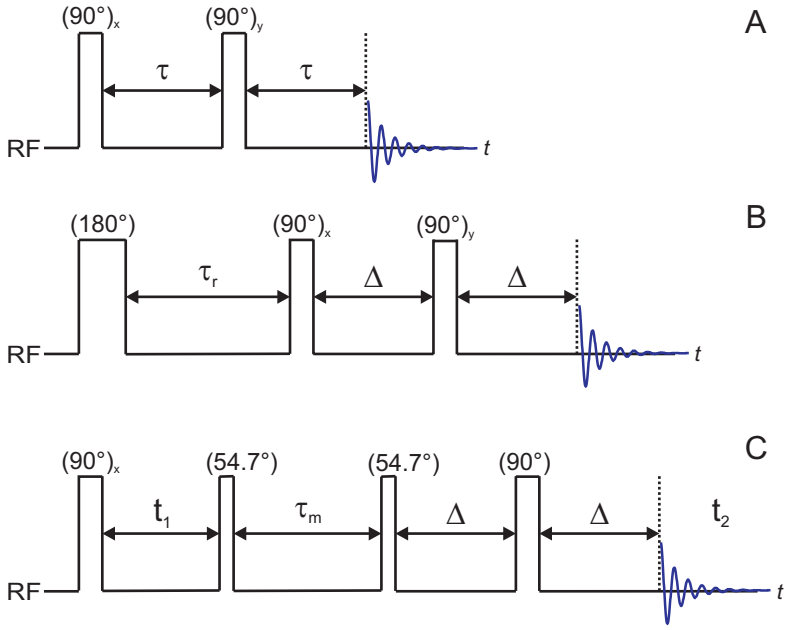

Figure 4.6: Basic pulse experiments in dynamic ^{2}H NMR spectroscopy. (A) Solid-echo pulse sequence. (B) inversion recovery sequence. (C) 2D exchange sequence. (18)

4.2.3 ^{2}H NMR spectra in the rigid limit

Just as one nitroxide orientation in single crystal in EPR was used to explain the powder spectrum (Sec.3.7.2), the explanation of the ^{2}H NMR spectrum begins with a single deuteron in a crystalline material. In the absence of motion (rigid limit), the ^{2}H NMR powder spectrum is the sum over all (static) orientations of the crystallites with respect to the external magnetic field and the resulting spectrum is a *Pake pattern*.

According to Fig.4.4. (B), for one deuteron in an external magnetic field two transitions obeying the selection rule $\triangle m_I = \pm 1$ are allowed. The difference frequency between these two transitions $\triangle\nu$ can be calculated by Eqn.4.32. For a rigid deuteron, the maximum splitting $\triangle\nu_1$ corresponding to $\theta = 0°$ can be calculated by Eqn.4.33.

The doublet spectrum obtained as a sum of the contributions over all possible crystal orientations is shown in Fig.4.7. (A).

$$\triangle\nu_1 = \frac{3}{2}\frac{e^2qQ}{h} \tag{4.33}$$

The splitting $\triangle\nu_2$ corresponding to $\theta = 90°$ is calculated by Eqn.4.34. At the orientation with $\theta = 54.7°$ the splitting is zero and the frequency corresponds to ω_0.

$$\triangle\nu_2 = \frac{3}{4}\frac{e^2qQ}{h} \tag{4.34}$$

In the solid-echo experiment, the spin-1 behaviour is found to be similar to that of a spin-1/2 in the primary echo experiment (Sec.3.3.2). The spins are refoused after the second $(90°)_y$ pulse (Fig.4.6. (A)) and an echo is produced after free evolution time τ. The Fourier transform of the signal gives a Pake pattern of ^{2}H nuclei in the rigid limit with asymmetry parameter $\eta = 0$ under the high field approximation (Fig.4.7. (B)).

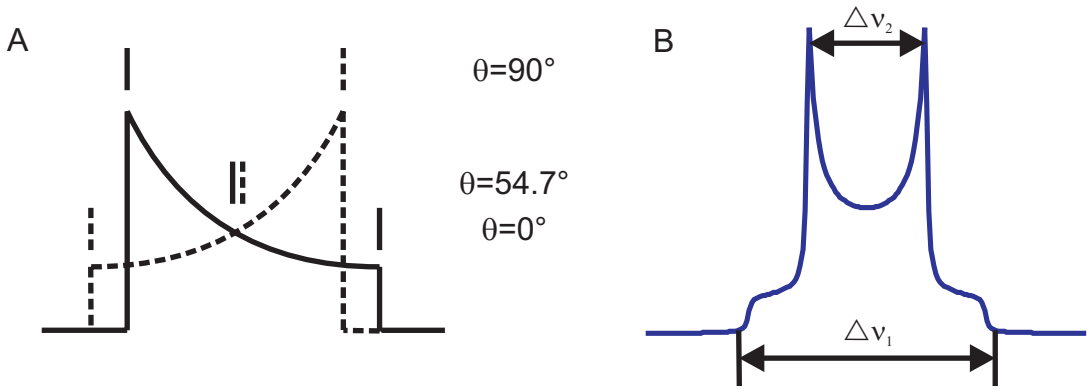

Figure 4.7: (A) Schematic representation of the Pake pattern resulting from the sum of the contributions from the random orientations of a spin-1 nucleus with respect to the magnetic field in a crystalline sample. (15) (B) Pake pattern of ^{2}H solid echo NMR experiment

4.2.4 Studies of molecular motion

The quadrupole coupling is sensitive to the presence of molecular motion as described in Sec.4.2.2. If the molecular motions are in the fast exchange region, then the inspection of the experimental line shapes gives an indication about the symmetry (or type) of the motional process of ^{2}H nuclei (Fig.4.8). (18)

If the molecular motions occurs in the intermediate time-scale ($10^{-6} \leq \tau_c \leq 10^{-5}$s, $k \approx \omega_Q$), solid-echo experiments can be used to study molecular motions. The FID (free induction decay) signal can be described by Eqn.4.35 with $S(t, 2\tau)$ as FID starting at the top of the solid echo. (18)

$$S(t, 2\tau) = \mathbf{1}\, e^{At} e^{A\tau} e^{A\tau *} P_{eq}(0) \tag{4.35}$$

τ is the interval between the r.f. pulses (Fig.4.6. (A)). $P_{eq}(0)$ is the vector that denotes the fractional populations of the N exchanging sites in thermal equilibrium and A is a complex matrix of size N with $A = i\Omega + K$.

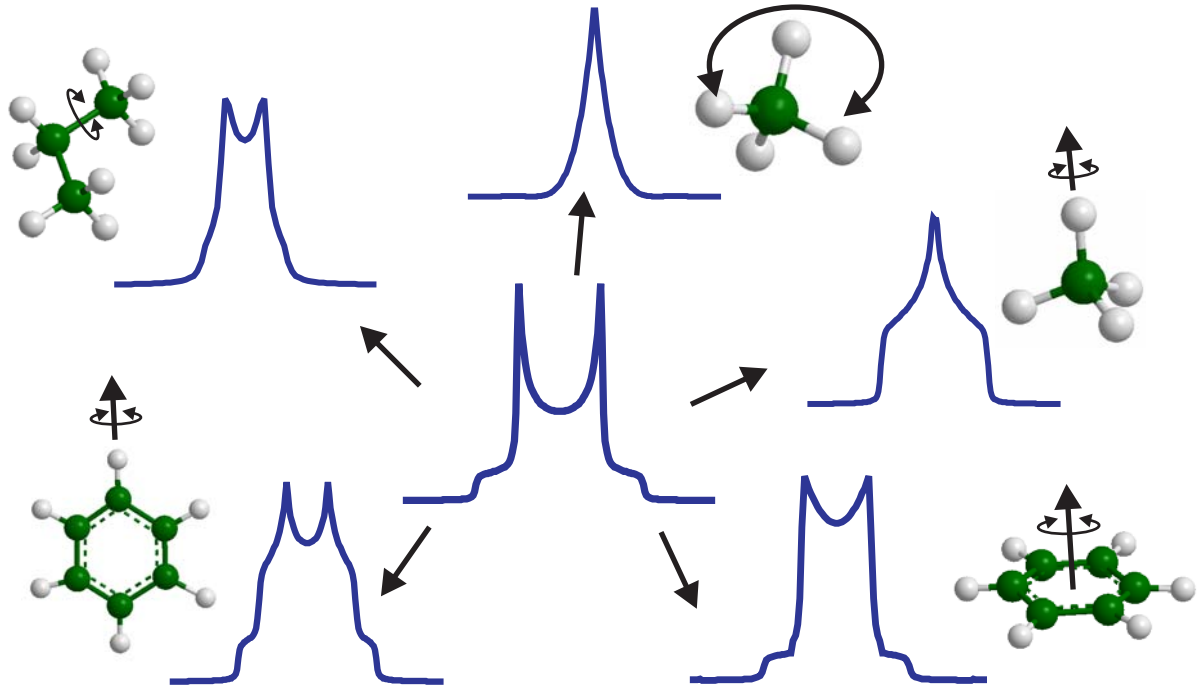

Figure 4.8: Theoretical fast exchange ^{2}H NMR spectra based on different motional models. (18)

The diagonal matrix Ω, which is the imaginary part of A, is defined by Eqn.4.36 with $\omega_{Q,i}$ describing the frequencies of the exchanging sites. The real part of A, K, corresponds to a kinetic matrix in which the non-diagonal elements are the jump rates from site j to i, and the diagonal elements represent the sums of the jump rates for leaving site i. Eqn.4.35 can be solved numerically using standard diagonalization routines, from which ^{2}H NMR line shapes and spin-spin relaxation time T_2 can be derived. (18)

$$\Omega = \begin{vmatrix} \omega_{Q,1} & & & \\ & \omega_{Q,2} & & \\ & & \ddots & \\ & & & \omega_{Q,N} \end{vmatrix} \tag{4.36}$$

The molecular motion process can be modeled by *continuous diffusion*, e.g. rotation of a surfactant molecule about its long axis, and *discrete processes* such as the jumping between gauche and trans conformations within the alkyl chain of the surfactant. Temperature dependent ^{2}H NMR can be used to characterize the molecular motion properties with appropriate motion models.

4.2.5 Analysis of the ^{2}H solid echo NMR spectrum

For ^{2}H NMR under static conditions, the chemical shift is unresolved and no other information in the spectrum can be used to identify the particular ^{2}H nucleus envolved. The quadrupolar splitting $\triangle\nu_1$ and $\triangle\nu_2$ can be measured to identify the quadrupole coupling constant depending on the resolution of spectrometer. Usually for ^{2}H NMR, the ^{2}H nucleus should be substituted into a specfic (and known) position in the molecule to study molecular motion at a specific position. Such site-specific spin labeling requires considerable synthetic efforts. In this thesis, three

site-specific deuterated surfactants were used, which were provided by H. Zimmermann[1], to characterize molecular motion of surfactant molecules in organoclay and corresponding polymer composites.

As shown in Fig.4.9, the samples can be measured with the solid-echo experiment, which can give information on molecular motion of the ^{2}H nuclei. From Fig.4.9. (A) it indicates clearly that motion of ^{2}H nuclei in PCL nanocomposites is faster than that in PS microcomposites and in organoclay. From Fig.4.9. (B) It is noticed that motion of ^{2}H nuclei at 80°C is in the fast exchange region while at room temperature or below it is in the slow motional region. From the FWHH plot (Fig.4.9. (C)) the quadrupole coupling can be inferred to be on the 12 kHz scale at room temperature which is much lower than that for C–D in aliphatic chain (165 kHz). This will be discussed in detail in the experimental part in Chapter 5.

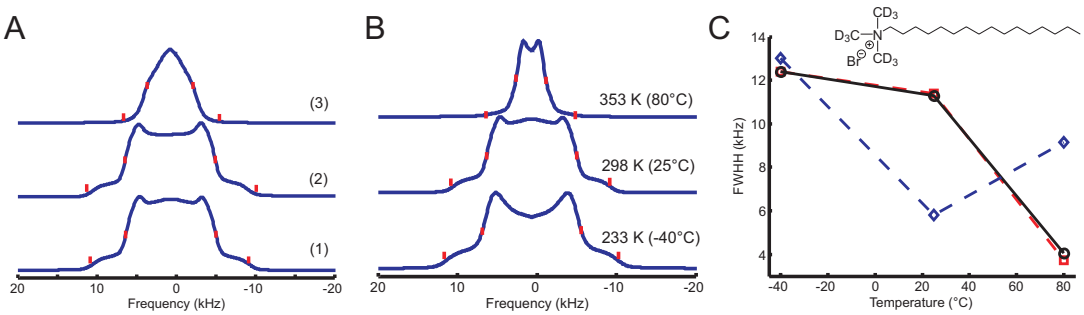

Figure 4.9: ^{2}H NMR spectra of organomagadiite prepared with d9HTMA and the corresponding PCL and PS composites. (A) Organomagadiite (1), with PS microcomposites (2) and with PCL nanocomposites (3) measured at room temperature. (B) Temperature-dependent ^{2}H NMR spectra spectra of d9HTMA organomagadiite. (C) Full width at half height (FWHH) of spectra versus temeprature. Because FWHH is more accurate to meaure than $\triangle\nu_1$ and $\triangle\nu_2$ ($\triangle\nu_2$ could be zero in some motion mode), we use FWHH as a measure of the quadrupole coupling. The chemical structure of d9HTMA is shown.

[1]Max–Planck–Institute for Medical Research, Jahnstrasse 29, 69120 Heidelberg, Germany

Chapter 5

Experimental results

5.1 Synthesis and characterization of magadiite

As introduced in Sec.1.1 iron-free layered silicate needs to be synthesized to prepare samples which are suitable for pulse EPR experiments. The hydrothermal synthesis method is widely used in synthesizing solids whose particle size distribution is on the nanometer scale, such as ceramic materials and molecular sieves. This method uses water as a solvent. An autoclave is usually used to achieve supercritical conditions, which change the solubility of the solute dramatically resulting in nucleation of well-structured crystallized solids. It is proposed that hydrothermal crystallization is driven by a drastic change of the dielectric constant in the vicinity of the critical point which in turn shifts the hydration reaction equilibrium toward metal oxide formation. (17) Hence reaction temperature and the composition of reactants are key parameters which influence the structure of final products. The mechanism of hydrothermal synthesis of magadiite ($Na_2Si_{14}O_{29} \cdot 11H_2O$) is as follows:

$$\text{hydrolysis of amorphous silica:} \quad SiO_2 + 2\,H_2O = Si(OH)_4 \tag{5.1}$$

$$\text{reorganization of structure:} \quad Si(OH)_4 + Na^+ \rightarrow Na_2\,Si_{14}\,O_{29} \cdot 11\,H_2O \tag{5.2}$$

Lagaly and coworkers described details of the synthesis of magadiite and kenyaite.(9) Firstly the three components silica (Acros, CAB-O-SilM5, Scintillation grade), water (MilliQ), and aqueous NaOH (adjusts pH and acts as a catalyst) were admixed. The suspension was sealed in a Teflon lined autoclave and heated between 100°C and 150°C for a certain time. The outcome would be a mixture of kenyaite and quartz depending on temperature and time. However, it took months for running an experiment to have a good product. Chyi-Ming Leu, Zhen-Wei Wu and coworkers gave an alternative hydrothermal method which shortened the experiment duration to 48 hours with a fixed molar ratio between three components (amorphous silica : NaOH : H_2O = 3 : 1 : 200) to synthesize kenyaite. In (9) the interconversion between magadiite and kenyaite depending on annealing temperature and period in the autoclave was described. Hence in this thesis temperature-dependent and annealing period-dependent experiments were performed to have an appropriate product as pure as possible rather than a mixture of kenyaite and magadiite.

In the our synthesis of magadiite, based on the latter hydrothermal method, different heating temperatures (focussing on the range between 140°C and 160°C) and annealing periods in the autoclave (48 hours to 72 hours) were tried. Very low and high temperature (larger than 180°C) were also tried. However it turns out that the product under such conditions is amorphous silica. The basic procedure is described in the following. Firstly 0.8 grams (0.02 *mol*) sodium hydroxide was dissolved in 72 grams distilled water (4.0 *mol*) (MilliQ) in three necked flask under stirring. Then 3.64 grams amorphous silica (Acros, CAB-O-SilM5, Scintillation grade) (0.06*mol*) was dispersed in the solution under strong stirring (200 rpm) and cooling with an ice bath. The suspension was kept stirring for 3 hours cooled by an ice bath to achieve a good dispersion. After testing pH ($pH = 12$) the white suspension was transferred to a Teflon-lined autoclave and was kept under autogeneous pressure at 150°C for 48 hours. The mixture after annealing was centrifuged (6000 rpm for 30 min) and washed with dilute NaOH solution (0.1 N). The white product was dried in a 60°C vacuum oven (yield: 61%).

The dried white powder was characterized with WAXS and SEM to find optimized conditions. With SEM morphology of the product can be studied and with WAXS fine structure of solids can be studied. Differential Scanning Calorimetry (DSC) and Thermal Gravimetric Analysis (TGA) were used to characterize thermal properties of the products such as melting points and decomposition conditions.

5.2 Preparation of organosilicates

5.2.1 Preparation of organosilicates without spin probes

After the appropriate layered silicate with nice SEM images and WAXS data showing the typical structure of magadiite was obtained, organoclay was prepared with either a cationic ammonium surfactant hexadecyltrimethylammonium (HTMA) chloride ($C_{16}H_{33}N^{+}(CH_3)_3Cl^{-}$, Fluka, 319.5 g/mol) or a cationic phosphonium surfactant hexadecyltributylphosphonium (HTBP) bromide ($C_{16}H_{33}P^{+}(C_4H_9)_3Br^{-}$, Fluka, 507.7 g/mol). The phosphonium cationic surfactant was chosen because it is accessible to ^{31}P NMR states and to ENDOR (Electron Nuclear Double Resonance).

To find the proper amount of surfactant that could be absorbed by magadiite, the scale of the *Cationic Exchange Capacity* (CEC) of magadiite should be found because too litte or to much excess of surfactant would result in poor intercalation with polymers. We used a titration method to define the rough range of the CEC. A 0.2% (*wt*) magadiite in water (MilliQ) solution was prepared in a three necked flask and stirred for 4 hours to achieve a good dispersion. A 0.2% (*wt*) (6.26 $mmol/l$) HTMA chloride solution was prepared and put into a titration tube. To decide how much HTMA should approximately be added we first assumed that the CEC is on a scale of 100 $mmol/100g$ because Somasif, one kind of phyllosilicate that was used in our previous research, has a CEC of 70 $mmol/100g$.(30) Furthermore exchange of the two sodium ions in magadiite ($Na_2Si_{14}O_{29} \cdot 11H_2O$) would correspond to a CEC of 182 $mmol/100g$. In steps of 3.20 ml (corresponding to 10 $mmol/100g$) of HTMA chloride solution, we titrated from 3.20 ml HTMA to 80 ml (corresponding to a CEC of 250 $mmol/100g$). After each step of adding HTMA and mixing for a certain time, the mixture was then kept stable without stirring for about 20 minutes to allow precipitation of the flocculated paricles and the turbidity of supernatant was measured

by a turbidity meter (Lovibond). We observed that at 30 $mmol/100g$ there were big flocculant and precipitation was very fast. The minimum turbidity of the supernatant was obtained at 120 $mmol/100g$ after which the fine coagulate was stable and distributed homogeneously in the solution. So we got the rough range of absorption behaviour that particles precipitate around 30 $mmol/100g$ and to prepare complete multilayer samples we should at least exceed 120 $mmol/100g$. In the following experiment, we took 200 $mmol/100g$ as surfactant to magadiite ratio to prepare organosilicate with multilayer absorption of surfactant molecules. From the titration experiment it was found that magadiite has a better solubility and larger CEC than somasif.

Organosilicate was prepared as follows. A 0.2% (wt) magadiite in water suspension was prepared and stirred for 4 hours to have a good dispersion. An amount of HTMA chloride corresponding to 200 $mmol/100g$ CEC was dissolved in water. The HTMA solution was then added to the magadiite solution and kept stirring and heated at 60°for 4 hours to achieve complete absorption. The mixture was then centrifuged (6000 rpm, 30 min). The residue was washed with water/ethanol (50/50 wt) once and then several times with water only because ethanol would wash out surfactant layers. The samples were washed until the supernatant from centrifuging was chloride free as tested with drops of 0.1 N $AgNO_3$. The final product was dried at 60° C in a vacuum oven (yield 22%). The same procedure was used to prepare organoclay with HTBP.

5.2.2 Characterization of the organosilicates

The distance between layers can be calculated from WAXS data. The intercalation degree could be calculated from the distance between layers in magadiite and organosilicate. TGA data were used to calculate the absorbed amount of surfactants by assuming that surfactant molecules were burned out at a high temperature (900°C) in an air flow (30 ml/min) and comparing the weight loss for magadiite and the organosilicate. For the phosphonium surfactant organosilicate the TGA method could be tested by a quantitative measurement with ^{31}P solid state single pulse MAS (Magic Angle Spin) NMR. In ^{31}P MAS NMR ammonium dihydrogenphosphate (ADHP, $(NH_4)H_2PO_4$), Aldrich) was used as a calibration standard (signal at 0.8 ppm). For such a quantative measurement ADHP was mixed with the organosilicate sample in a known ratio. By integration of the signal the amount of phosphorous atoms can be obtained. This will be discussed in Sec.5.5.3.3.

Because of the good signal/noise ratio in ^{31}P MAS NMR, temperature dependent ^{31}P MAS NMR could also be performed from 300 K to 400 K to study states of phosphorous nuclei in surfactant layers.

5.2.3 Preparation of organosilicates with spin probes for DEER and ENDOR

As described in Sec.3.9, pulse EPR can be used to obtain information on the localization and distribution of nitroxide radicals in surfactant layers. CW EPR can be applied to characterize dynamics of molecular motions. In this thesis, double resonance techniques, including Double Electron Electron Resonance (DEER) and Electron Nuclear Double Resonance (ENDOR) (for HTBP samples) are used to measure the dipole-dipole coupling between electrons and the hyperfine coupling between electron and ^{31}P nuclei, respectively, to obtain spatial information of surfactant distribution. After pulse EPR measurements which are usually carried out at low temperature (50 K for DEER and ENDOR), the samples were then mearured with CW EPR at temperatures from 300 K to 450

K in 10 K increments to obtain dynamic information. Such samples require one of the spin probes that are listed in Tab.5.1 to have an EPR signal.

The chemical structures of site-specific nitroxide spin probes used in EPR experiments are shown in Fig.5.1 (ammonium and phosphonium spin probes) and corresponding molar mass are listed in Tab.5.1. To prepare samples with spin probes, the spin probe was dissolved in a 1% molar ratio to the native surfactant in the surfactant solution and the same procedure was followed as in organosilicate preparation. For example, to prepare sample with the spin probe 11-SL-UTMA, 0.0028 g (0.006 mmol) were dissolved in 0.2% (wt) HTMA solution which was prepared from 0.19 g HTMA chloride (0.6 mmol) in 100 g H_2O. When exceeding 3% of spin-labeled surfactant aggregation of spin probes and broadening in EPR spectra was observed. The HTMA and 11-SL-UTMA solution then was added to a 0.2 % (wt) magadiite solution which was prepared from 0.3 g magadiite in 150 g H_2O with stirring at 60°C for 4 hours. The aggregated coagulents were separated by centrifuging (6000 rpm, 30 min) and washed with water/ethanol (50/50 wt) once and then several times with water only as described in Sec.5.2. The residue was dried at 60°C in a vacuum oven.

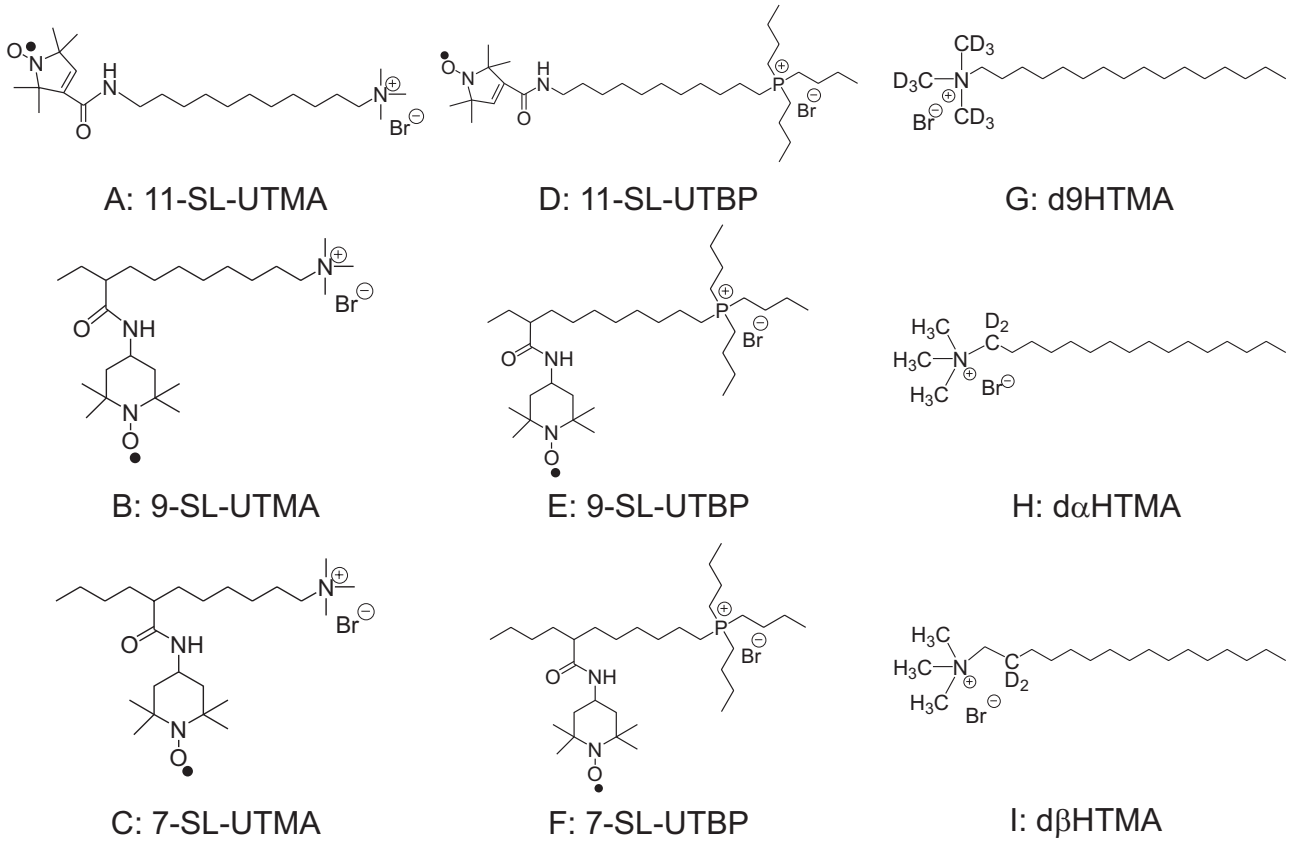

Figure 5.1: Site-specific nitroxide surfactants and site-specific deuterated surfactants. (A) 11-SL-UTMA (11: position in alkyl chain; SL: spin-labeled; UTMA: undecyltrimethylammonium) bromide (B) 9-SL-UTMA (C) 7-SL-UTMA (D) 11-SL-UTBP (UTBP: undecyltributylphosphonium) (E) 9-SL-UTBP (F) 7-SL-UTBP (G) d9HTMA (d9: nine deuterons in methyl groups.) (H) dαHTMA (dα: deuterated in α position in alkyl chain.) (I) dβHTMA (dβ: deuterated in β position in alkyl chain.)

ammonium spin probes		phosphonium spin probes		deuterated surfactants	
sample	M (g/mol)	sample	M (g/mol)	sample	M (g/mol)
11-SL-UTMA	475	11-SL-UTBP	618	d9HTMA	373
9-SL-UTMA	491	9-SL-UTBP	634	dαHTMA	366
7-SL-UTMA	491	7-SL-UTBP	634	dβHTMA	366

Table 5.1: Site-specific nitroxide spin probes used in EPR and site-specific deuterated surfactants used in ^{2}H NMR and ESEEM. The nomenclature of 11-SL-UTMA is explained as that: 11:the position that is labeled by the nitroxide; SL: spin-labeled; UTMA:undecyltrimethylammonium (undecyl: 11 carbon atoms in the backbone). For phosphonium surfactant spin probes UTBP referres to undecyltributylphosphonium.

5.2.4 Preparation of organosilicates with spin probes for ESEEM

The hyperfine coupling between the electron and deuterium nuclei can be measured with samples prepared with deuterated surfactants and a nitroxide spin probe by three-pulse ESEEM. The relative strength of the hyperfine coupling gives semi-quantitative information on the distance distribution between the electron and deuterium. Three-pulse ESEEM data also provide infomation on the relaxation mechanism of spin probes.

To prepare samples for three-pulse ESEEM measurements, we used ammonium spin probes (listed in Tab.5.1) to mix with deuterated surfactants and followed the same procedure to prepare organosilicates as Sec.5.2. The chemical structures of deuterated surfactants d9HTMA, dαHTMA and dβHTMA are shown in Fig.5.1 and corresponding molar lass are also listed in Tab.5.1.

5.2.5 Preparation of organosilicates for ^{2}H NMR

As described in Sec.4.2.4, ^{2}H NMR is applied to study molecular motion in surfactant layers of organosilicates and the corresponding polymer composites. To prepare samples with deuterated surfactant that are required for ^{2}H NMR, three site-specific deuterated surfactants: d9HTMA, dαHTMA and dβHTMA as listed in Tab.5.1 were prepared. The procedure to prepare these organosilicates is the same as the one described in Sec.5.2.1.

5.3 Intercalation of organosilicates with polymers

To disperse organosilicate in polymer matrices, the melt method was used.(30) 0.025 g organosilicate was mixed with 0.075 g polymer. After being grinded the mixture was put into the a Weber-Press (Maschinen Apparatebau) for 30 min at 160°C under 7 MPa (10 kN within 13mm diameter Telflon plates). The final pressed plates were characterized with WAXS/SAXS to infer the degree of intercalation. Commercial polymers with different dipolar properties as quantified by the dielectric constant were used.

5.4 Instrumental analysis

5.4.1 WAXS/SAXS measurements

WAXS was performed with a Siements X-Ray Scattering setup. The setup uses a CuKα radiation selected by a double graphite monochromator. The wavelength of the generated X-ray is thus about 1.54 Å. The setup consists of a X-ray generator and a X-ray mirror to parallelize the X-ray beam and therefore to minimize the beam divergence. Using a pinhole collimation system the beam diameter is about 0.7 nm. For data acquisition a two-dimensional detector (Bruker AXS) with 1024x1024 pixels was utilized. The sample-to-detector distance was 80 mm and the accessible scattering angle range was $2° < 2\theta < 32°$. After background subtraction the scattering intensity distributions were integrated over the azimuthal angles and are presented as a function of the scattering vector in q space using Eqn.5.3 derived from *Bragg's Law*.

$$q = \frac{4\pi}{\lambda} \sin \frac{2\theta}{2} \tag{5.3}$$

By the relationship between the Basal spacing d_{001}, which is the distance between layers, and the scattering vector corresponding to first order peak (Eqn.5.4).

$$d_{001} = \frac{2\pi}{q} \tag{5.4}$$

d_{001} can be calculated from the scattering angle 2θ and the wavelength from Eqn.5.5.

$$d_{001} = \frac{1}{2} \frac{\lambda}{\sin \frac{2\theta}{2}} \tag{5.5}$$

SAXS was performed with a home built spectrometer setup which consists of a Rigaku X-ray generator (RA-Micro7, Japan) and Siements detector.

5.4.2 SEM measurements

SEM was measured by a 'LEO 1530 Gemini FE-SEM' microscope. A high Efficiency In-lens Detector was used.

5.4.3 TGA and DSC measurements

TGA was measured with a Mettler TG 851 apparatus. An air flow of 30 ml/min and a temperature range from 25°C to 900°C in 10°C steps were used. DSC was measured with a Mettler DSC 30. A nitrogen flow of 30 ml/min and a temperature range from -150°C to 250°C in 10°C steps were used. For DSC the measuring process includes increasing (from -150°C to 250°C), decreasing(250°C to -150°C), and increasing of temperature again.

5.4.4 ^{31}P NMR measurements

^{31}P NMR measurements were performed with a Bruker AXS 500 spectrometer. 4-mm rotors were used as sample holders in MAS and sample spinning at 12 kHz was applied. Free-induction decay signals were recorded after a $\pi/2$ pulse. For quantitative measurements, ammoniumdihydrogen phosphate (ADHP, Aldrich) was used to calibrate

the chemical shift(δ_{ref} = 0.8 ppm). (31) Organosilicate prepared with HTBP surfactant was mixed with ADHP in a known ratio (i.e. 1:4 (wt)) and the repetition time was set to 1800s (d1) to have complete relaxation (T_1 was measured and found to be less than 60 s). (30)

Temperature dependent ^{31}P NMR measurements from 300 K to 400 K in 10 K increments were also performed with a Bruker AXS 500 spectrometer under the same MAS settings. The FID was recorded with a repetition time of 60s (d1) for both multilayer and monolayer samples.

5.4.5 ^{2}H NMR measurements

^{2}H static NMR measurements were performed with a Bruker AXS 300 spectrometer. The free evolution time τ and the repetition time were set to 0.3s (Fig.4.6. (A)).

5.4.6 EPR measurements

EPR spectra were recorded on a Bruker ELEXSYS E580 EPR spectrometer at X-band frequencies (9.3–9.8 GHz). Temperature dependent CW EPR was performed with a 4103 TM resonator using a glass dewar and the Bruker ER 4111 VT temperature controller. A microwave power of 2 mW, modulation amplitude of 0.1 mT, and a modulation frequency of 100 kHz were employed.

ESEEM experiments were performed at a temperature of 80 K with liquid nitrogen cooling medium. For the primary echo in two-pulse ESEEM the initial interval τ_0 between the $\pi/2_x$ and π_x pulses was set to 200 ns (Fig.3.16. (A)). The $\pi/2_x$ pulse length was set to 20 ns and the π_x pulse length was set to 40 ns. The acquisition time (d_0) for optimum integration after the π_x pulse was set to 440 ns. In three-pulse ESEEM τ_0 was set at 344 ns and d_0 was set to 508 ns.

Mims ENDOR experiments were performed at 50 K with liquid helium cooling medium. For ENDOR the E580 spectrometer was equipped with a DICE unit to provide radio frequency pulses which were amplified by a 200 W rf amplifier EN 3200L. A commercial double resonator from Bruker (EN 4118X-MD-4) was used. A stimulated echo experiment was performed prior to ENDOR to find the optimum interpulse delay τ between the first two $\pi/2_x$ pulses (Fig.3.23. (E)) from the exponential decay of the signal (Fig.3.20. (A)). The initial delay τ_0 in the stimulated echo experiment was set to 200 ns as in the primary echo. The time T between the second and third $\pi/2_x$ pulses is set to 27 μs (Fig.3.14. (A)) and d_0 was set at 476 ns in stimulated echo experiments. In Mims ENDOR the optimum interpulse delay τ between the first two $\pi/2_x$ pulses was set according to the expontential decay time T_m obtained from stimulated echo experiment signal (Sec.3.5.1). d_0 remained unchanged at 476 ns in Mims ENDOR.

Four-pulse DEER experiments were performed at 50 K with liquid helium cooling medium. The resonator used in DEER was a Bruker Flexline split-ring resonator ER 4118-MS3. Pump pulses at a secondary microwave frequency were generated by feeding the output of an HP 83508 sweep oscillator to one microwave pulse forming unit of the spectrometer. The pump frequency was set to the maximum of the nitroxide spectrum, and the observer frequency was 65 MHz higher (Fig.3.25). The interval τ_1 between the first $\pi/2_x$ and π_x pulses was set to 200 ns.

Both the $\pi/2_x$ and π_x pulses had a length of 32 ns and the dwell time was 8 ns. The interval τ_2 between the two observer π_x pulses was set to 2 μs and d_0 was set at 484 ns for integration of signal.

To summarize, magadiite was synthesized first and characterized with WAXS, SEM, DSC and TGA. Then the organosilicates without spin probes were prepared for WAXS and TGA characterization. Organosilicates with phosphonium surfactant HTBP were measured with quantitative ^{31}P single pulse MAS NMR by mixing with ADHP in a known ratio and the FID signal was recorded with a repetition time sufficient for complete relaxation (1800s). The integrated data were compared with TGA data of the same sample. This HTBP organosilicate was further characterized with ^{31}P single pulse MAS NMR with a shortened repetition time of 60s. The same HTBP organosilicate was washed with ethanol and measured with the same NMR experiments to have both multilayer and monolayer information.

The samples that were prepared for EPR measurements, including CW, ESEEM, DEER and ENDOR are listed in Fig.5.2. For ^{2}H NMR, the samples were prepared in the same series as organosilicate, PCL and PS composites for each deuterated surfactant as that for DEER or ENDOR ((B) and (C)) except that for ^{2}H NMR the organosilicates were prepared with deuterated surfactants only without any nitroxide spin probes or protonated HTMA or HTBP. All samples were first measured with WAXS before any further EPR or NMR measurements were performed to ascertain the correct intercalation situation. The experimental flow chart can be referred to Fig.1.7 and Fig.1.8 and the design of spectroscopic experiments can be referred to Fig.1.9 in Sec.1.7.

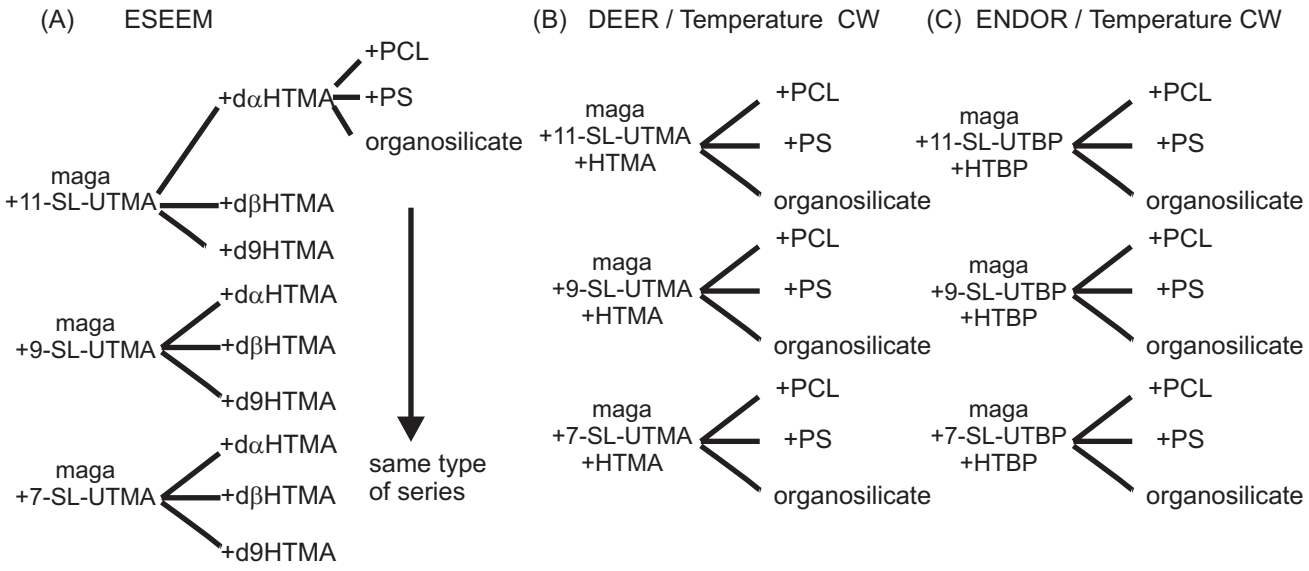

Figure 5.2: Samples prepared for EPR. (A) Samples prepared with site-specific deuterated surfactants and site-specific spin probes to have ESEEM measurements. (B) Samples prepared with ammonium site-specific labeled sufactants (nitroxides same as (A)) for DEER measurements and temperature dependent CW EPR. (C) Samples prepared with phosphonium site-specific labeled sufactants for ENDOR measurements and temperature dependent CW EPR. 'maga' represents magadiite.

5.5 Experiment results on sample preparation

5.5.1 Optimum parameters for synthesis of magadiite according to WAXS and SEM

With the fixed composition of three components of reactants (molar ratio: amorphous silica: NaOH: H_2O= 3 : 1 : 200), WAXS plots showed the final magadiite product was sensitive to temperature rather than to the annealing duration in the autoclave (Fig.5.4. (A) and (B)). However SEM showed that a longer annealing time would improve the macroscopic structure (morphology) of the final product (Fig.5.5. (C) and (F)). It turns out that there is a transition between magadiite and kenyaite in the range between 155°C and 160°C (Fig.5.4. (A)). If the temperature is not sufficient and far below 140°C there is no crystal nucleation and growth. Between 140°C and 155°C the product is mostly magadiite ($d_{001} \approx 1.5\ nm$). At 160°C or above kenyaite ($d_{001} \approx 2.0\ nm$) dominates which has a more loose and less well-structured morphology according to SEM (data not shown). When the temperature is far above 170°C , the final product is quartz with amorphous structure and the WAXS data is a broadened curve without any peaks. WAXS confirms nice reproducibility of the fine structure of the product under the same reaction conditions. It also indicates that the transition temperature between kenyaite and magadiite is at about 155–160°C. The synthesis experiments are summarized in Tab.6.1.

temperature (°C)	annealing duration (hours)	dominant product	Basal spacing (nm) (WAXS)	characteriaztion results (SEM)
$\ll 140$	any	amorphous structure	-	no
140	48	pure magadiite	1.5 (5.7°)	accepted
140	62–72	pure magadiite	1.5	preferred
145	48	magadiite	1.5	accepted
150	48	magadiite	1.5	preferred/accepted
150	72	magadiite	1.5	preferred
155	48	magadiite	1.5	accepted
160	48	kenyaite	2.0 (4.4°)	accepted
170–180	48	pure kenyaite	2.0	accepted
$\gg 180$	any	amorphous quartz	-	no

Table 5.2: Temperature and annealing period dependence of synthesis results under autogeneous pressure. Pure magadiite means no indication of scattering peaks from kenyaite (no peak (b) in Fig.5.3. (A1)). A magadiite dominant product is a admixure with a tiny scattering peak from kenyaite in WAXS. A kenyaite dominant product is a admixture with a tiny scattering peak from magadiite. WAXS curves of pure kenyaite do not have the scattering peak from magadiite (no peak (a) in Fig.5.3. (A4)). In SEM, preferred products have a well-defined layered structure while accepted products have a layered structure but not a high regularity over long distances.

Although the fine structure of the products is the same, SEM shows that the morphology is rather sensitive to small shifts of the reaction temperature. As described in Sec.5.1, with hydrothermal synthesis, at supercritical conditions in an autoclave, a small shift of temperature could result in drastic changes of the dielectric constant and the equilibrium of reactions (Eqn.5.1 and Eqn.5.2). WAXS indicates that the same thermodynamically stable phase is still obtained however SEM reveals that the morphology is influenced by the small inaccuracy of temperature control probably because of changes in the relative rates of nucleation and growth. For the preparation of organosilicates and composites with polymers, we choose samples that are pure magadiite according to WAXS with a first order scattering peak at $2\theta = 5.7°$ (as in Fig.5.4. (A1)) and have well ordered morphology according to

SEM. The annealing conditions of these samples were found to be at temperatures between 140°C and 155°C under autogeneous pressure. The optimum annealing conditions in the autoclave were at a relatively low temperature such as 140°C with a long reaction time from 62 hours to 72 hours. If the temperature was set between 150°C and 155°C, 48 hours of reaction time were sufficient. Longer times or higher temperatures result in an admixture of magadiite to the kenyaite.

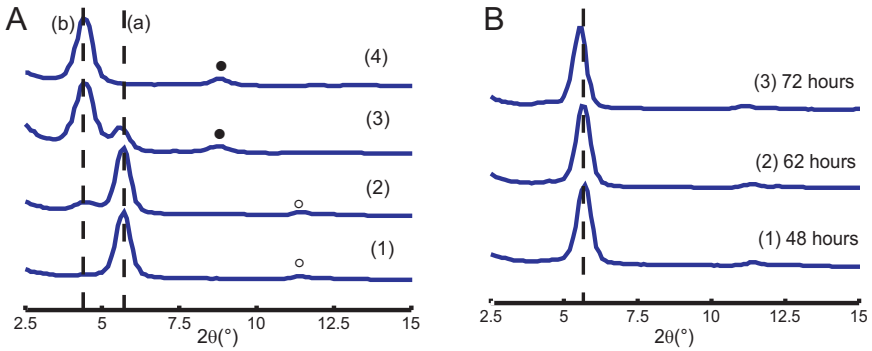

Figure 5.3: WAXS characterization of synthesized layered silicate. (A) Temperature dependence with the same annealing time of 48 hours in autoclave and autogeneous pressure. (1) 140°C. (2) 150°C. (3) 160°C. (4) 170°C. If the temperature exceeds more than 200 °C, the final product is an amorphous solid again and in WAXS there is only a broadened line without any peak. The same result is obtained if the temperature is too low. Peak (a) corresponds to $2\theta = 5.7°$ and 1.5 nm from Eqn.5.5. Peak (b) corresponds to $2\theta = 4.4°$ and 2.0 nm. The hollow dots in (1) and (2) shift to the positions of filled dots in (3) and (4) indicating secondary scattering layers shift from kenyaite dominant solids to magadiite dominant solids. According to Tab.2.2 in Sec.2.3 layered silicate with Basal spacing of 1.5 nm (5.7° in 2θ space in WAXS) corresponds to magadiite. Layered silicate with Basal spacing of 2.0 nm (4.4° in 2θ space in WAXS) corresponds to kenyaite. (B) WAXS plots of products with different annealing duration under the same temperature of 140°C. The temperature is more critical than the annealing duration for the fine crystal structure.

5.5.2 CEC scale of magadiite found by titration

As described in Sec.5.2.1, after the iron-free layered silicate magadiite was synthesized, it was titrated with HTMA chloride solution to find the approximate CEC scale. Some results of titration are listed in Tab.5.3. Magadiite solution was prepared with a concentration of 0.04% (wt) (0.2 grams of kenyaite dissolved in 500 ml H_2O) and HTMA chloride solution was prepared with a concentration of 0.2% (wt) (0.2 grams of HTMA chloride dissolved in 100 ml H_2O). The titration of HTMA into the magadiite solution started at 3.19 ml HTMA solution (corresponding to 10 mmol/100g cationic exchange) and HTMA solution was added in steps of 3.2 ml corresponding to an increment of the cation amount of 10 mmol/100g. The turbidity of the supernantant was measured with a turbidity meter (Lovibond). The method was described in Sec.5.2.1 in detail. From the titration experiment, the adsorption behaviour of the surfactant on the surface of magadiite can be described roughly. Between 30 mmol/100g and 40 mmol/100g big aggregates (flocculants) were formed fast and low turbidity of the supernatantas was observed. The reason could be that some magadiite sheets were so hydrophobic that they did no longer disperse in water. More adsorption of surfactants makes the flocculants redistributed and results in smaller particles. At 80 mmol/100g the multilayer adsorption reaches its maximum capacity. This point probably corresponds to electro-neutrality,

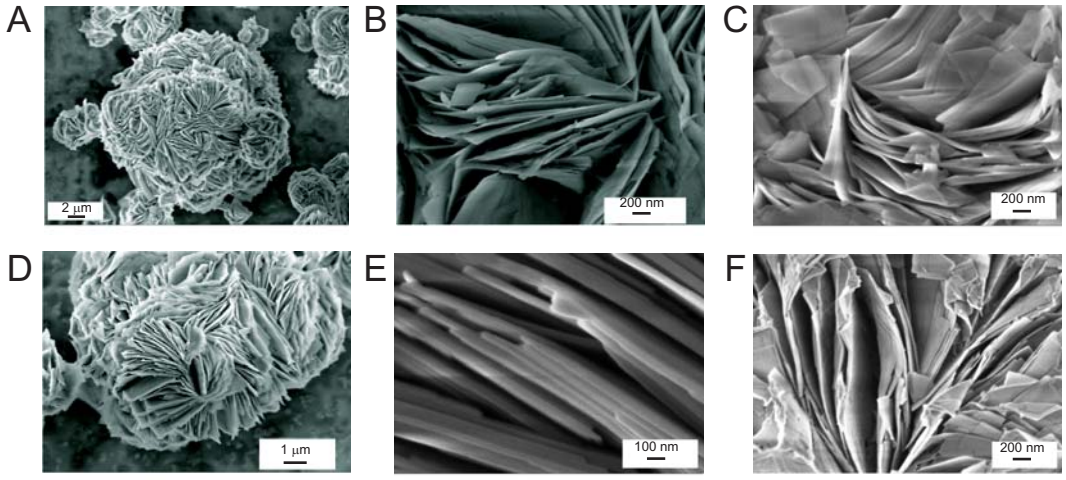

Figure 5.4: SEM images of synthesized magadiite. (A), (B), (D), and (E) are images of sample (A2) that is shown in Fig.5.3 (150°C, 48 hours). (C) Image of sample of (B1) (140°C, 48 hours). (F) Image of sample of (B3) (140°C, 72 hours). At the same temperature samples obtained by longer annealing have a more ordered macroscopic structure although by WAXS they have the same fine crystal structure as those obtained with shorter annealing time.

i.e. charge compensation between magadiite and cationic surfactants. Hence this point is most probably located close to the CEC. Further adding of surfactant leads to attachment of surfactant due to hydrophobic interaction. Above 120 mmol/100g no further changes were observed, the magadiite is then saturated by the surfactant. For further experiments, the amount of surfactant was taken in ratio of 200 mmol/100g to magadiite both for HTMA and HTBP to work in this saturation regime.

Compared to Somasif (CEC of 80 mmol/100g), a natural hectorite used in our previous experiments ((6)–(7)), the CEC of magadiite is on a similar scale. In the titration experiment of Somasif that were performed in our previous work, the first minimum turbidity of the supernatant corresponded to 42 mmol/100g. The multilayer adsorption (minimum turbidity in the range between 7 and 280 mmol/100g) corresponded to 112 mmol/100g and the apparent saturation was achieved after 210 mmol/100g. The adsorption of surfactant on surface of layered silicate is similar between Somasif and magadiite.

5.5.3 Characterization of organosilicates and polymer composites

5.5.3.1 Intercalation of organosilicates and polymer composites with HTMA

As described in Sec.5.4.1 and Sec.5.5.1 the distance between layers can be derived from WAXS data. So WAXS was used to characterize the degree of intercalation of organosilicates and corresponding nanocomposites or microcomposites. The basal spacing, which was assigned as d_{001}, can be calculated from the scattering data. Both WAXS and SAXS indicate intercalation of the polymer into organosilicate galleries as shown in Fig.5.5. In Fig.5.5 inter-

Total amount of CTAC added (ml)	in unit of CEC (mmol/100g)	Turbidity (FNU)	Phenomenon
3.19	10	141	no big changes
6.39	20	108	small fine precipitates
9.58	30	27	big precipitates
12.78	40	19.4	small particles floating
19.17	60	25	big and fast precipitation
25.26	80	6.5*	floating aggregates on surface
28.75	90	135	surfactant in excess
38.34	120	20	smaller fine particles
63.9	200	50	turbidity stable

Table 5.3: Titration of HTMA chloride to magadiite solution. Transition points are: 30, 80, 120 mmol/100g. $\star$At 80 mmol/100g, the turbidity of surpernatant has the minimum value indicating that the CEC of synthesized magadiite is on the scale of 80 mmol/100g (theoretical calculation gives CEC as 182 mmol/100g)

calation tests of polycaprolactone (PCL) and polystyrene (PS) into organosilicate are shown because the former (PCL) represents nanocomposites in which polymer chains do intercalate into the galleries between organosilicate sheets while the latter (PS) represents microcomposites in which the polymer has no influence on the fine structure of the organosilicate. The choice of PCL and PS will be explained later.

WAXS data show that 2θ of the d_{001} peak of organoclay in PCL nanocomposites shifts from that of pure organosilicate (2.7°) to 2.2° which corresponds to a change of the basal spacing from 3.2 nm to 4.0 nm, expanding 36% if the thickness of one sheet of magadiite is assumed as 1 nm (Fig.5.5. (A3), (A5)). The expansion degree, which is defined as intercalation degree in this thesis, is calculated by Eqn.5.6 with L as thickness of one sheet of magadiite ($L \approx 1$ nm).

$$\text{intercalation degree} = \frac{[(d_{001}(organoclay) - L) - (d_{001}(kenyaite) - L)]}{[(d_{001}(kenyaite) - L)]} \tag{5.6}$$

For PS microcomposites the distance between layers of organoclay does not change significantly indicating that PS chains have no intercalation with organoclay ((A3) and (A4)). The SAXS data also shows a peak at around 0.6° for PCL nanocomposites. The SAXS data of the mixture that was prepared from magadiite and PCL without HTMA, exhibits only a small shoulder, indicating that the magadiite structure was only slightly changed within the polymer matrix. The data of the nanocomposite show in comparision that addition of HTMA largely effects the structure. Hence from WAXS and SAXS data intercalation of PCL chains into organoclay layers is obvious. For PS microcomposites WAXS and SAXS indicate that the distance between layers in organosilicate remains unchanged and PS chains do not intercalate into organosilicate. Furthermore PCL can also intercalate into organosilicate prepared with the phosphonium surfactant HTBP, while PS can not (Sec.5.5.3.2). Hence PCL is a polymer that can intercalate into both HTMA and HTBP organosilicates giving rise to nanocomposites and PS can intercalate into neither of them and gives rise to microcomposites.

Apart from PCL and PS, other commercial polymers such as poly(ethyl methacrylate) (PEMA) (Aldrich),

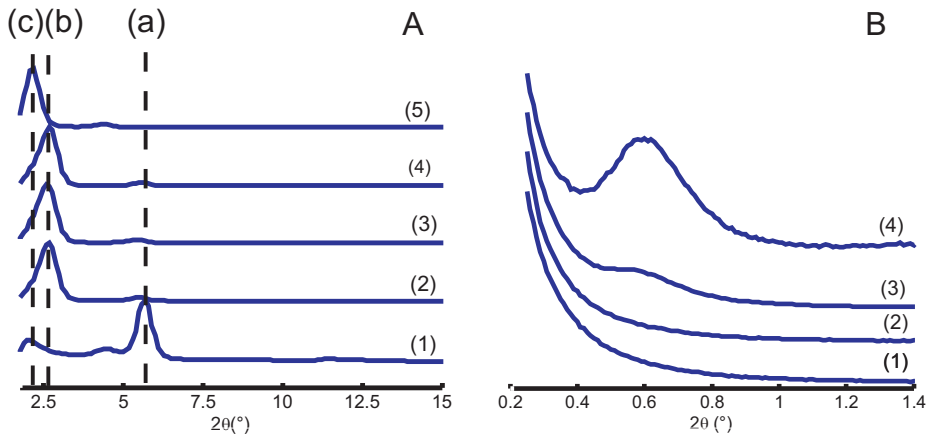

Figure 5.5: WAXS and SAXS of the HTMA intercalated series. (A) WAXS. (1) magadiite powder (2) organosilicate powder prepared from magadiite and HTMA (components: magadiite+HTMA). (3) organosilicate after melt annealing with 7 MPa pressure at 160°C for 30 min (components: magadiite+HTMA). (4) organosilicate in PS microcomposites (components: magadiite+HTMA+PS). (5) organosilicate in PCL nanocomposites (components: magadiite+HTMA+PCL). Peak (a) is at 5.7° corresponding to 1.5 nm. Peak (b) is at 2.7° correpsonding to 3.2 nm. Peak (c) is at 2.2° corresponding to 4.0 nm. The intercalation degree of PCL nanocomposites can be calculated from peak (b) and peak (c). (B) SAXS. (1) magadiite+HTMA after melt annealing. (2) magadiite+HTMA+PS (3) magadiite+PCL (without HTMA) (4) magadiite+HTMA+PCL. Compared with (3) and (4) it shows that in nanocomposites HTMA is a necessary component to compatabilize magadiite and PCL. In microcomposites in which PS chains do not intercalate into organosilicate HTMA has little influence on the crystal structure.

poly(ethylene oxide) (PEO) (Aldrich), poly(vinylidene fluoride) (PVDF) (Sigma), poly(4-vinylpyridine) (P4VP) (Sigma), were tested with the same melt method. Different molecular weights of PS and PEO were also tried and it turned out that the weight averaged molecular weight was not a critical factor for intercalation. To find polymers that could intercalate into organosilicates and were thus suitable for further NMR and EPR studies, the dielectric constant was considered as an important parameter rather than molecular weight and polydispersity. This assumption was suggested by a previous study of Younghoon Kim, White and coworkers using a different melt intercalation method. (13) The results of intercalation of different polymers into organosilicates according to WAXS are shown in Tab.5.4. PCL proved as a polymer which can intercalate with both of ammonium and phosphonium surfactants by the melt method. PEMA could be intercalated with HTMA to a slight degree however can not be intercalated with HTBP.

Compared to the results of Kim and White obtained by melt compounding in an extruder, in our case of melt intercalation in a press, it seemed that the dielectric constant is not a significant factor that influences melt intercalation. PEO with the largest dielectric constant does not exhibit intercalation into organosilicates. Neither does PVDF which is closely studied by Kim and White with their different melt method. (13) As PCL and PEMA intercalate more readily into magadiite modified by ammonium surfactants, one may consider that the carbonyl group in polymers could play an important role in intercalation in the melt method, probably because of hydrogen bonds between hydroxyl groups of the organosilicate and carbonyl groups in polymer chains. This agrees with the widespread industrial application of polyamide nanocomposites (2) that appear to form readily. The common property of PCL and polyamide is a carbonyl group in the main chain. This property may lead to formation of a

physical crosslink between the polymer and the organoclay resulting in more efficient in intercalation. However, this point is not studied further in this thesis.

For NMR and EPR experiments PCL and PS were chosen to prepare nanocomposites and microcomposites, respectively. The availability of data for both a nanocomposite and a microcomposite aids intepretation of the data. (6)

polymer	structure	dielectric constant ε	$\overline{M}_w$ (g/mol)	$\overline{PD}_n$	HTMA intercalation degree (%)	HTBP intercalation degree (%)
PEO	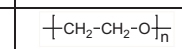	39	264,000	8.5	×	×
PVDF		8.4	270,000	2.6	×	×
PEMA		3.6	250,000	3.4	17	×
P4VP		2.56	45,000	2.9	×	×
PS		2.5	10,000	1.1	×	×
PCL	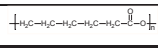	3.1–3.3	24,000	1.6	36	31

Table 5.4: Intercalation results of different polymers from WAXS spectra. PCL can intercalate into both HTMA and HTBP. PEMA can intercalate into HTMA to a smaller degree and not into HTBP. All other polymers tested can not intercalate into organomagadiite prepared with either surfactant.

5.5.3.2 Intercalation of organosilicates and polymer composites with HTBP

As shown in Tab.5.4, PCL can intercalate into organomagadiite prepared with the phosphonium surfactant HTBP and PS can not. The WAXS data for the HTBP series are shown in Fig.5.6. (A). The intercalation degrees both of the organosilicate and the PCL nanocomposites are less than that of the HTMA series. For HTMA, the intercalation degree of the organomagadiite compared with pure magadiite is 340% and the intercalation degree of PCL nanocomposites compared with organomagadiite is 36%. For HTBP the intercalation degree of organomagadiite compared with pure magadiite is 280% and the intercalation degree of PCL nanocomposites compared with organomagadiite is 31%.

5.5.3.3 TGA and ^{31}P single-pulse MAS NMR to determine the amount of absorbed surfactants

Quantative determination of the actual amount of surfactant absorbed in organomagadiite was done by TGA. With TGA (air flow 30ml/min, 25°C to 900°C in increment of 10°C/min) if we assume that surfactant layers are all burned out under very high temperature (900°C), we can calculate the amount of surfactant by the weight loss of magadiite and organomagadiite. The reliability of results from TGA can be tested with ^{31}P single pulse solid state MAS NMR for organomagadiite prepared with the phosphonium surfactant HTBP. The amount of HTBP can be calculated by integration of the signal from organomagadiite and ADHP (ammonium dihydrogenphosphate) (Fig.5.6 (B)). Organomagadiite and ADHP were mixed in a known ratio (4:1 in wt) and then placed in a 4 mm

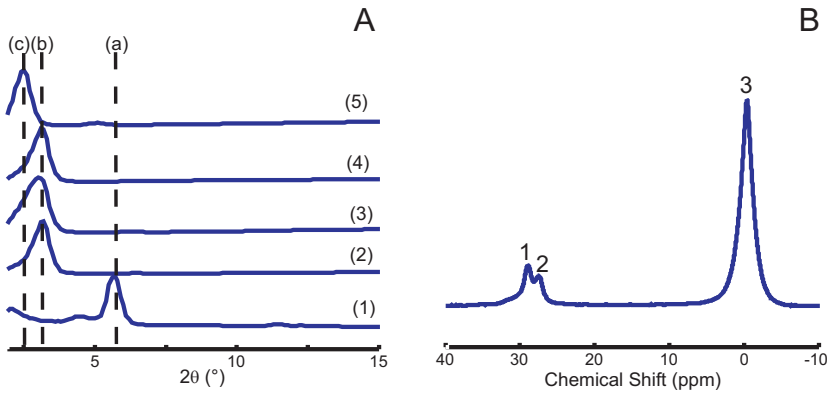

Figure 5.6: (A) WAXS of the HTBP intercalated series. (1) magadiite powder (2) organomagadiite powder prepared from magadiite and HTBP (components: magadiite+HTBP). (3) organomagadiite after melt annealing with 7 MPa pressure at 160°C for 30 min (components: magadiite+HTBP). (4) organomagadiite in PS microcomposites (components: magadiite+HTBP+PS). (5) organomagadiite in PCL nanocomposites (components: magadiite+HTBP+PCL). Peak (a) is at 5.7° corresponding to 1.5 nm. Peak (b) is at 3.0° correpsonding to 2.9 nm. Peak (c) is at 2.5° corresponding to 3.5 nm. The intercalation degree of HTBP is less than that of HTMA. (B) ^{31}P single pulse solid state MAS NMR spectrum of HTBP organoclay. By integration and the known amount of calibration standard compound ADHP the amount of HTBP surfactant layers can be determined. The parameters of the measurement are described in Sec.5.4.4. Peak 1 and peak 2 are from HTBP organomagadiite and correspond to 28.92 ppm and 27.47 ppm respectively. Peak 3 is from ADHP which is used as a shift calibration standard and for quantitatification of the surfactant content.

rotor and spun at an MAS frequency of 12 kHz. The results are shown in Table.5.5. We can conclude that TGA and NMR data are comparable and thus reliable.

The intercalation degrees of HTBP organomagadiite and HTMA organomagadiite are also compared. The intercalation degree and the amount of absorbed surfactants show that the ammonium surfactant is more efficiently absorbed on the clay surface than the phosphonium surfactant, probably because of the smaller head group that allows for closer packing and also leads to a stronger static electrical interaction. As we use as much as 200 $mmol/100g$ of surfactant to prepare organoclay, the saturation of adsorption is achieved. The multilayer of surfactant that can be absorbed stably in HTBP organomagadiite is about 60 $mmol/100g$ and in HTMA organoclay is about 85 $mmol/100g$. The latter value agrees nicely with the second transition point of the HTMA titration of magadiite.

Sample	intercalation degree from WAXS (%)	TGA ($mmol/100g$)	^{31}P NMR ($mmol/100g$)
kenyaite+HTBP	280	60	62
kenyaite+HTMA	340	85	-

Table 5.5: Intercalation degree and amount of absorbed surfactants. The value from TGA is very close to that from ^{31}P NMR for HTBP. The TGA data is thus reliable and can thus be applied to HTMA organomagadiite.

5.6 Molecular motion of ammonium surfactants

5.6.1 ^{2}H NMR results

5.6.1.1 ^{2}H NMR measured at room temperature

As described in Sec.5.6.1, ^{2}H NMR spectroscopy is a well established technique to study molecular motion of deuterons on a broad time scale between seconds and picoseconds. In this thesis, solid echo experiments which are suitable for time scales from milliseconds to microseconds were applied to investigate molecular motion of three different site-specifically deuterated ammonium surfactants in organomagadiite and corresponding PCL and PS composites. d9, dα and dβ–HTMA surfactants were used in our experiment (Tab.5.1). The ^{2}H NMR spectra of the samples measured at room temperature are shown in Fig.5.7. Because the Full Width at Half Height (FWHH) of normalized spectra is proportional to the residual quadrupole coupling and can be exactly measured in the spectra, we took the FWHH as a measure of the motionally averaged quadrupole coupling. FWHH are labeled in the spectra. The FWHH values can be directly compared between the samples prepared under the same conditions. The FWHH data measured at room temperature are listed in Table.5.6. Generally the wider the FWHH, the slower or more restricted is the molecular motion of the rH-C bond.

^{2}H NMR spectra of the dαHTMA series are shown in Fig.5.7. (A). Spectra of the dβHTMA series are shown in Fig.5.7. (B) and spectra of the d9HTMA series are shown in Fig.5.7. (C). As an overview, molecular motion of deuterons in all samples is in the intermediate exchange ($10^{-6} \leq \tau_c \leq 10^{-5}$ s, $k \approx \omega_Q$) or slow exchange regime ($10^{-5} \leq \tau_c \leq 10^{-4}$ s, $k \leq \omega_Q$) as the second pulse in the solid echo sequence can refocuse the signal after free evolution time $d_1 = 0.3\ s$.

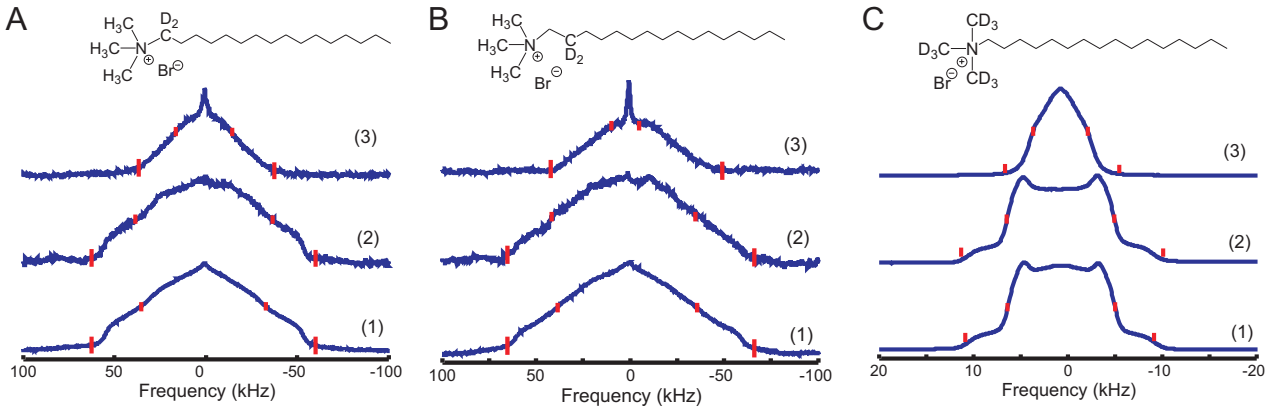

Figure 5.7: ^{2}H NMR spectra of organomagadiite with deuterated surfactants and their PCL and PS composites at room temperature. (A) dαHTMA series. (1) organomagadiite (magadiite+dαHTMA) (2) its PS microcomposite (magadiite+dαHTMA+PS) (3) its PCL nanocomposite (magadiite+dαHTMA+PCL) (B) dβHTMA series. (1) organomagadiite (magadiite+dβHTMA) (2) its PS microcomposite (magadiite+dβHTMA+PS) (3) its PCL nanocomposite (magadiite+dβHTMA+PCL) (C) d9HTMA series. (1) organomagadiite (magadiite+d9HTMA) (2) its PS microcomposite (magadiite+d9HTMA+PS) (3) its PCL nanocomposite (magadiite+d9HTMA+PCL)

FWHH data of the deuterated surfactant powder in the absence of magadiite are also shown in Tab.5.6. Unexpectedly, the FWHH of unperturbed original d9, dα and dβ HTMA powder indicates slower motion than for

the surfactant absorbed on organomagadiite (also in PCL and PS composites). Quadrupole coupling is reduced by almost a factor of two in organomagadiite compared to the pure surfactant. dαHTMA and dβHTMA powder have a typical aliphatic chain quadrupole coupling constant (165 kHz, if we assume that $\Delta\nu_2 \approx$ FWHH) while d9HTMA powder has much faster motion. This may result from a glassy state of the surfactant in the organomagadiite while the pure surfactant is crystalline.

Sample	powder (kHz)	organoclay (kHz)	+PS (kHz)	+PCL (kHz)
d9HTMA	21.4	11.4	11.3	5.8
dαHTMA	124	68.3	74.8	30.5
dβHTMA	125	73.9	76.5	22

Table 5.6: FWHH of original d9, dα, dβHTMA powder, organoclay and corresponding polymer composites at room temperature.

Fig.5.7. (C) shows, that the surfactant layers have higher mobility in PCL nanocomposites than in PS microcomposites and in organoclay as the spectra of PCL nanocomposites are much narrower than the other two in the same series. ^{2}H NMR spectra of deuterons in surfactant layers in non-intercalated PS microcomposites differ little from the ones of organomagadiite. The result for PCL nanocomposites coincides with that from CW EPR and pulse EPR which will be described later. The molecular motion of surfactants is supposed to be slower in nanocomposites because the surfactants are entangled with polymer chains. However in PCL nanocomposites this is not observed. In contrast to PS that was studied before ((6)–(7)) PCL is a polymer with a low melting point (60°C) and a low glass transition point (-60°C). This glass transition temperature is below the order-disorder transition temperature (T_{ODT}) of the surfactant layer in organomagadiite which will be explained in Sec.5.6.2.1. With such a polymer with low glass transition temperature the molecular motion of surfactant layers is accelerated.

Fig.5.7. (A) and (B) shows that molecular motion in the α-position is similar as in the β-position. At room temperature both positions exhibit a fast component (sharp peak in the spectrum) in PCL nanocomposites. More information on molecular motion of deuterons can be gained from temperature-dependent ^{2}H NMR. The dα and dβ deuterons on the backbone have larger quadrupole coupling because these deuterons are more rigid.

5.6.1.2 Temperature-dependent ^{2}H NMR

The results of temperature dependent ^{2}H NMR are listed in Tab.5.7. Temperature-dependent ^{2}H NMR was measured at -40°C, 25°C and 40°C. dα, dβ organomagadiite were also measured at -80°C. The FWHH at -80°C differs little from that at -40°C.

The temperature-dependent ^{2}H NMR spectra are shown in Fig.5.8 and the FWHH of these spectra are shown in Fig.5.10. Although at room temperature ^{2}H NMR spectra of dα and dβCTAB differ little, temperature dependent measurements reveal that the fast component in dβ is more mobile than that in dα in both PCL nanocomposites and PS microcomposites. The temperature dependence of the FWHH of dα and dβ in organomagadiite and PS microcomposites can be fitted linearly (Fig.5.10.(A) and (B)).

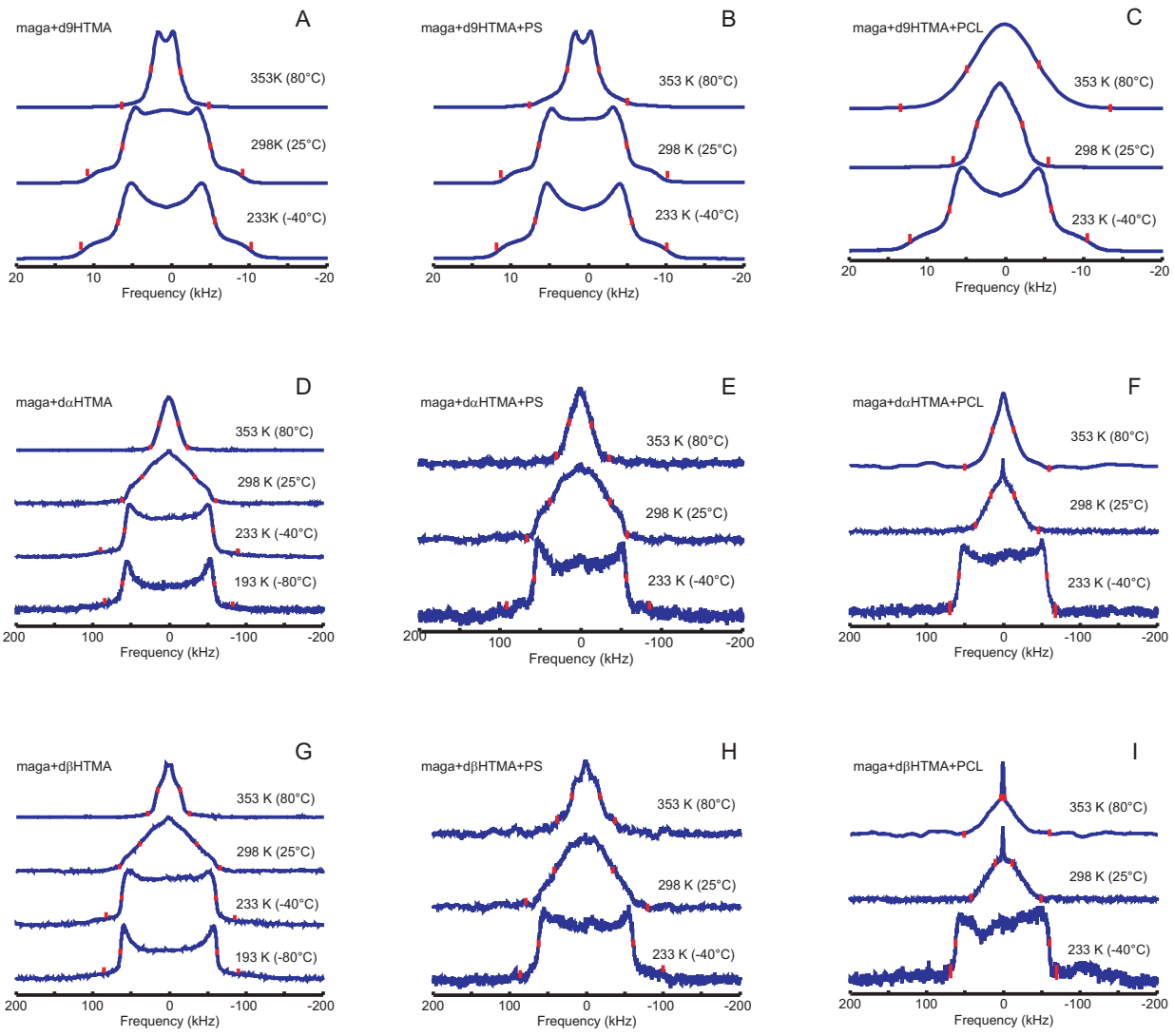

Figure 5.8: Temperature dependent ^{2}H static NMR. (A) d9 organomagadiite (B) d9 PS microcomposites (C) d9 PCL nanocomposites (D) dα organomagadiite (E) dα PS microcomposites (F) dα PCL nanocomposites (G) dβ organomagadiite (H) dβ PS microcomposites (I) dβ PCL nanocomposites

To analyze the motion of the deuterons in d9, dα andβ from spectra in Fig.5.8, the possible motion of substituted deuterons in organomagadiite can be divided into four different motions which are shown in Fig.5.9.

1. Rotation of methyl groups around the C–N bond which can be considered as a three-site jumping (motion labeled as '1' in Fig.5.9. (A)). This motion affects only d9HTMA and reduces the quadrupole coupling by a factor of 3.

2. Rotation of ammonium head groups around the $(CD)_3N$–C bond which is also a three-site jumping (motion labeled as '2' in Fig.5.9. (A)). This motion affects only d9HTMA and reduces the quadrupole coupling by another factor of 3.

3. Rotation of the alkyl chain around the symmetrical axes of the surfactant molecules (motion labeled as '3' in Fig.5.9). This motion affects d9HTMA, dαHTMA and dβHTMA. dαHTMA and dβHTMA are affected by this motion in the same way.

4. Wiggling of the alkyl chain with respect to the ammonium head group (motion labeled as '4' in Fig.5.9). This motion affects d9HTMA, dαHTMA and dβHTMA. dαHTMA and dβHTMA are affected by this motion in a different way. From Fig.5.9, for the same degree of motion with respect to the ammonium head group, deuterons at the β position undergo continuous diffusion with a larger amplitude than that of deuterons at the α position.

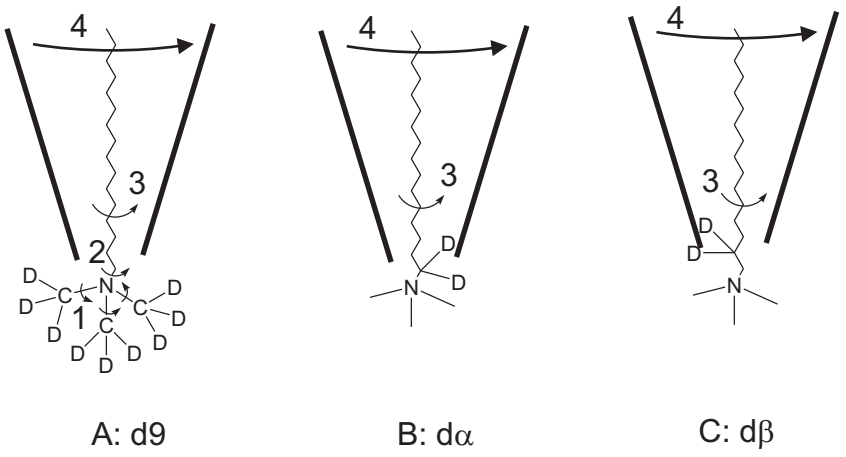

Figure 5.9: Illustration of motions of deuterons. Motion 1 is the rotation of methyl groups around C–N bond (three-site jumping motion). This motion affects only d9HTMA and reduces the quadrupole coupling by a factor of 3. Motion 2 is the rotation of ammonium head groups around $(CD)_3N$–C bond (three–site jumping motion). This motion affects only d9HTMA and reduces the quadrupole coupling by another factor of 3. Motion 3 is the rotation of the alkyl chain around the symmetrical axes of the surfactant molecules. This motion affects all deutrons in the surfactants. Motion 4 is the wiggling of the alkyl chain with respect to ammonium head group. This motion affects all deuterons in the surfactants. (A) d9HTMA (B) dαHTMA (C) dβ HTMA.

The overall ^{2}H spectra reflect the superposition of the different kind of motions that the deuterons have. For d9HTMA organomagadiite the dynamics of deuterons include motion 1, 2, 3 and 4. For dαHTMA organomagadiite motion 3 and 4 dominate the dynamics of deuterons and so they do for dβHTMA organomagadiite. The deuterons

can be regarded as rigid at -80°C (Fig.5.8. (D), (G)). For d9HTMA organomagadiite, motion 1 and 2 are present at -40°C, resulting in a reduction of the quadrupole coupling by a factor of nine compared to that of rigid deuterons substituted in alkyl chains. Motion 3 is not apparent at -40°C but is clearly visible at 25°C. From Fig.5.8. (D) and (G) a slight difference between dα and dβ at 80°C indicates that motion 4 is present at 80°C. Hence for organomagadiite, motion 1 and 2 are present at temperature as low as -40°C (for d9HTMA sample only). Motion 3 is present at 25°C and motion 4 can be observed at 80°C (for d9HTMA, dαHTMA, and dβHTMA organomagadiite).

Motion 4 is more clearly apparent in the PS and PCL composites (Fig.5.8. (E) and (H) spectra at 80°C). Generally dynamics of deuterons differs little between organomagadiite and PS microcomposites. However for PCL nanocomposites, motion 3 and 4 are observes at lower temperatures between -40°C and 25°C compared to organomagadiite and PS microcomposites. At -40°C the influence of PCL intercalation is not apparent as alkyl chains of surfactant molecules are rigid and discrete jumping is observed. At 25°C the effects of PCL intercalation can be clearly observed.

For PCL nanocomposites the FWHH of d9HTMA increases at 80°C which is in the melt state of the polymer (Fig.5.10. (C). (F) and (I)). The molecular motion of deuterons is thus strongly influenced by the melting of the polymer. In the melt state the solid echo experiment with an interpulse delay $\tau = 0.3\ s$ can not refocuse magnetization vectors correctly and the line shapes are distorted and spread over the resonance frequences. The molecular motion in the polymer melt could be in the intermediate exchange limit (Sec.4.2.2). The influence of the PCL melting is most pronounced for d9HTMA in which the FWHH of line shape for PCL nanocomposites at 80°C even increases compared to the data at 40°C (Fig.5.10. (C)).

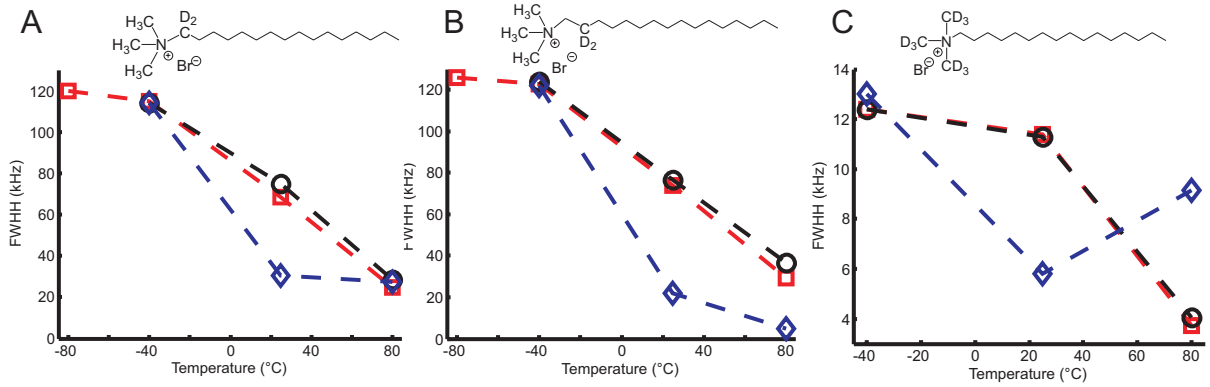

Figure 5.10: FWHH plot of temperature dependent ^{2}H NMR spectra. All surfactants were measured at -40°C, 25°C and +40°C. dα and dβ organomagadiite were also measured at -80°C and the FWHH at -80°C differs little from that at -40°C. (A) dα series. (B) dβ series. (C) d9 series with squares corresponding to organoclay, hollow circles corresponding to PS microcomposites and diamonds corresponding to PCL nanocomposites.

Sample	-80°C (193 K) FWHH (kHz)	-40°C (233 K) FWHH (kHz)	25°C (298 K) FWHH (kHz)	80°C (353 K) FWHH (kHz)
d9HTMA	-	12.4	11.4	3.74
d9HTMA+PS	-	12.4	11.3	4.04
d9HTMA+PCL	-	13	5.8	9.15
dαHTMA	120	115	68.3	24.8
dαHTMA+PS	-	114	74.8	28.7
dαHTMA+PCL	-	114	30.5	27.4
dβHTMA	126	123	73.9	29.4
dβHTMA+PS	-	124	76.5	36.7
dβHTMA+PCL	-	122	22	4.81

Table 5.7: FWHH of original d9, dα, dβHTMA powder, organomagadiite and corresponding polymer composites of temperature dependent ^{2}H NMR measurements.

5.6.2 CW EPR results

5.6.2.1 Temperature-dependent CW EPR spectra

The samples with nitroxide labels at different sites along the alkyl chain of the surfactant (11-SL-UTMA, 9-SL-UTMA and 7-SL-UTMA) were measured with CW EPR from 300 K to 450 K in 10 K steps. Selected spectra are shown in Fig.5.11. Generally we found that surfactant molecular motions are much faster in PCL nanocomposites than in PS microcomposites and organomagadiite. This result is consistent with that from ^{2}H static NMR measurements. In all PCL nanocomposites (Fig.5.11. (C). (F). (I)) the fast component dominates.

At high temperatures such as 450 K, EPR spectra of organomagadiite and PS microcomposites develop a new slow component which is not present at room temperature (Fig.5.11. (A). (D). (G) for organomagadiite and (B). (E). (H) for PS microcomposites). This probably is due to the partial decomposition of surfactants at high temperature. Spectra of PCL nanocomposites give little indication for decomposition, however spectra remeasured at 300 K after cooling down from 450 K indicate almost complete decomposition of the spin probes (the spectrum on the top). The spectra can thus be safely interpreted only up to the temperature of 430 K which is applied during melt intercalation. At this temperature the spin probes are obviously still stable.

The tail-labeled spin probe 11-SL-UTMA was somewhat different from the other two as its PCL nanocomposites had a slow component even at 440 K (not shown) and it is completely decomposited in PS microcomposites after heating (top spectrum in (B)).

Fig.5.12 provides a more detailed picture of molecular motion in surfactant layers as a function of temperature. As described in Sec.3.7.4, T_{50G} is the temperature at which $2A'_{zz}$ equals 50 G (5 mT). It is a empirical parameter that is used to correlate $2A'_{zz}$ with the glass transition temperature T_g of the sample. (28) The values of T_{50G} of all samples taken from the plots in Fig.5.11 are listed in Tab.5.8. Another parameter of interest is T_{ODT}, the order-disorder transition temperature which usually is derived from DSC. In EPR T_{ODT} can be approximated as the temperature at which the rotational correlation time τ_c of spin probe transfers from the slow tumbling region to the fast motional region and it is indicated in Fig.5.12 as well. For organomagadiite with the 11-SL-UTMA spin probe, $T_{50G} = 310$ K where the fast component appears. For organomagadiite with 9-SL-UTMA spin probe, $T_{50G} = 330$ K at which molecular motion of spin probe transfers from the slow tumbling region (cicle at 300

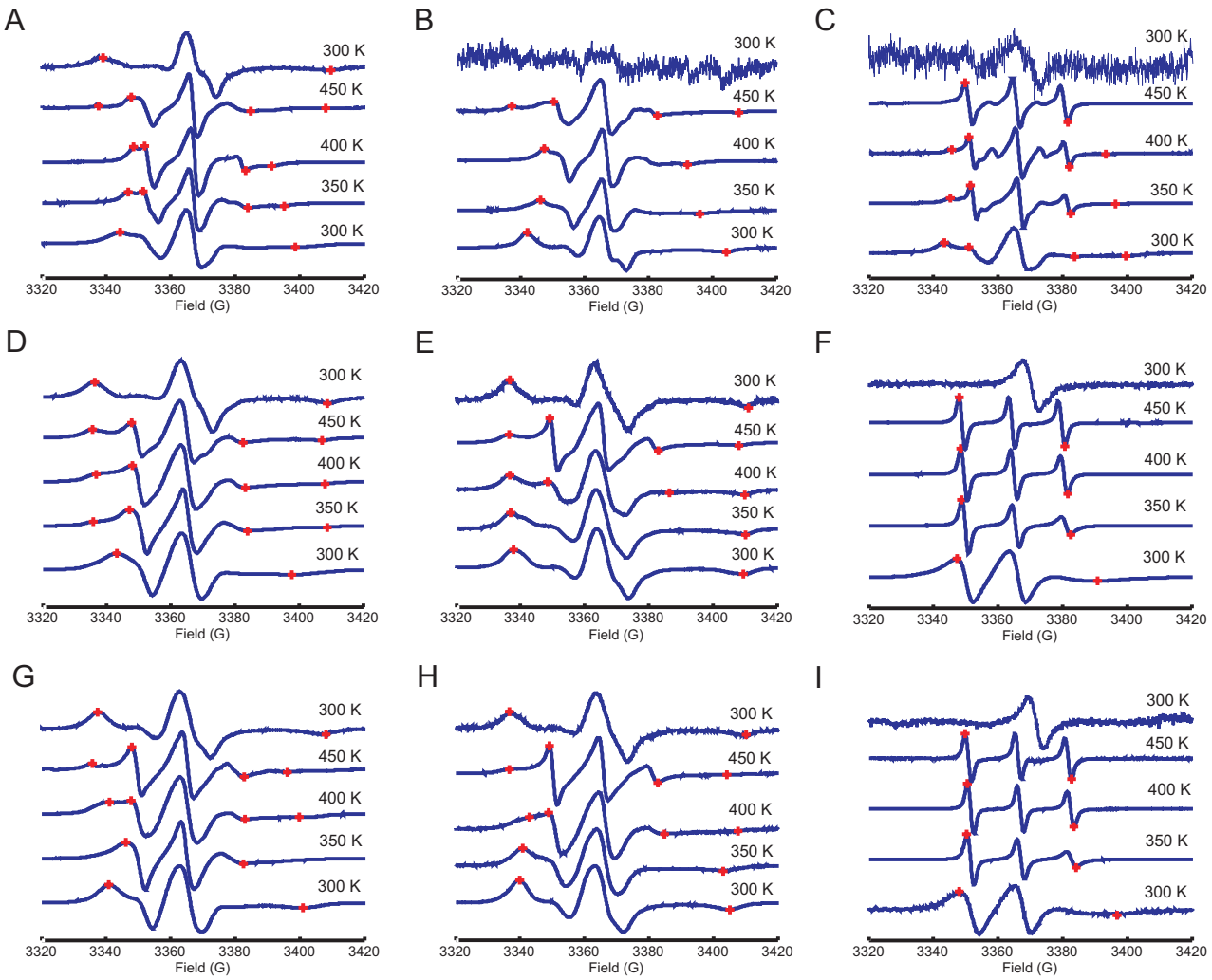

Figure 5.11: Temperature dependent CW EPR spectra of the ammonium surfactant HTMA series. (A) Organomagadiite with 11-SL-UTMA (magadiite+11-SL-UTMA+HTMA). (B) PS microcomposites (magadiite+11-SL-UTMA+HTMA+PS). (C) PCL nanocomposites (magadiite+11-SL-UTMA+HTMA+PCL). (D) Organomagadiite with 9-SL-UTMA (magadiite+9-SL-UTMA+HTMA). (E) PS microcomposites (magadiite+9-SL-UTMA+HTMA+PS). (F) PCL nanocomposites (magadiite+9-SL-UTMA+HTMA+PCL). (G) Organomagadiite with 7-SL-UTMA (magadiite+7-SL-UTMA+HTMA). (H) PS microcomposites (magadiite+7-SL-UTMA+HTMA+PS). (I) PCL nanocomposites (magadiite+7-SL-UTMA+HTMA+PCL). The spectra at 300 K on the top were measured after cooling down from 450 K.

Sample	T_{50G} (K)	Sample	T_{50G} (K)	Sample	T_{50G} (K)
11-SL-UTMA	315	9-SL-UTMA	310	7-SL-UTMA	330
11-SL-UTMA+PS	350	9-SL-UTMA+PS	400	7-SL-UTMA+PS	385
11-SL-UTMA+PCL	375	9-SL-UTMA+PCL	289	7-SL-UTMA+PCL	297

Table 5.8: T_{50G} values of the ammonium surfactant series.

Sample	τ_c (ns)	Sample	τ_c (ns)	Sample	τ_c (ns)
11-SL-UTMA	4.25	9-SL-UTMA	3.50	7-SL-UTMA	4.35
11-SL-UTMA+PS	5.20	9-SL-UTMA+PS	7.39	7-SL-UTMA+PS	5.24
11-SL-UTMA+PCL	3.98	9-SL-UTMA+PCL	2.40	7-SL-UTMA+PCL	2.36

Table 5.9: τ_c values of ammonium surfactant series at 300 K.

K in Fig.5.12. (B)) to the fast motional region (squares at 310K in (B)). For organomagadiite T_{50G} = 310 K is very close to T_{ODT}. The same conclusion applies to PS microcomposites. For PCL nanocomposites, actually $T_{ODT} < T_{50G}$ as the fast component is present already at 300 K. This indicates again the mobilization of the surfactant layer at a temperature below its own order-disorder transition due to the contacr with a polymer that is above its glass transition temperature.

In our previous work, PS was found to immobilize the surfactant layers significantly even if no intercalation took place. (30) This phenomenon is again reflected in Tab.5.8. The T_{50G} of PS microcomposites is larger than that of organomagadiite. In contrast, T_{50G} of PCL nanocomposites is smaller than that of organomagadiite except for the tail-specific spin probe 11-SL-UTMA. The series of 11-SL-UTMA is special because it has a slow component in PCL nanocomposites (Fig.5.11. (C) and Fig.5.12. (C)) however from the EPR spectrum a larger fraction of the fast component can still be noticed. Here it is also noticed that T_{50G} of surfactants in PCL nanocomposites is larger than T_g of the bulk PCL polymer.

5.6.2.2 Analysis of the reorientational correlation time τ_c

The CW EPR spectra can be fitted by simulated spectra and the reorientation correlation time τ_c can thus be derived based on the Debye model (3.7.3). The simulations were performed by Matlab (The MatWorks, Inc.) program that is based on EasySpin. (48) In Fig.5.13 both experimental and simulated spectra are shown. The deviation between experiment and simulation arises from a simplified model for the reorientation model. However by minimizing the mean square deviation between experimental and simulated data the reorientational correlation time τ_c can still be reliably determined. Tab.5.9 again shows that the fastest molecular motion of surfactant layers is observed in PCL nanocomposites.

After τ_c was obtained by spectra fitting for the whole series of temperatures, an Arrhenius plot according to Eqn.5.7 can provide the activation energy E_a. Although $2A'_{zz}$ plots in Fig.5.12 already give information on molecular motion trends with increasing temperature, Arrhenius plots reveal more details on different regimes of

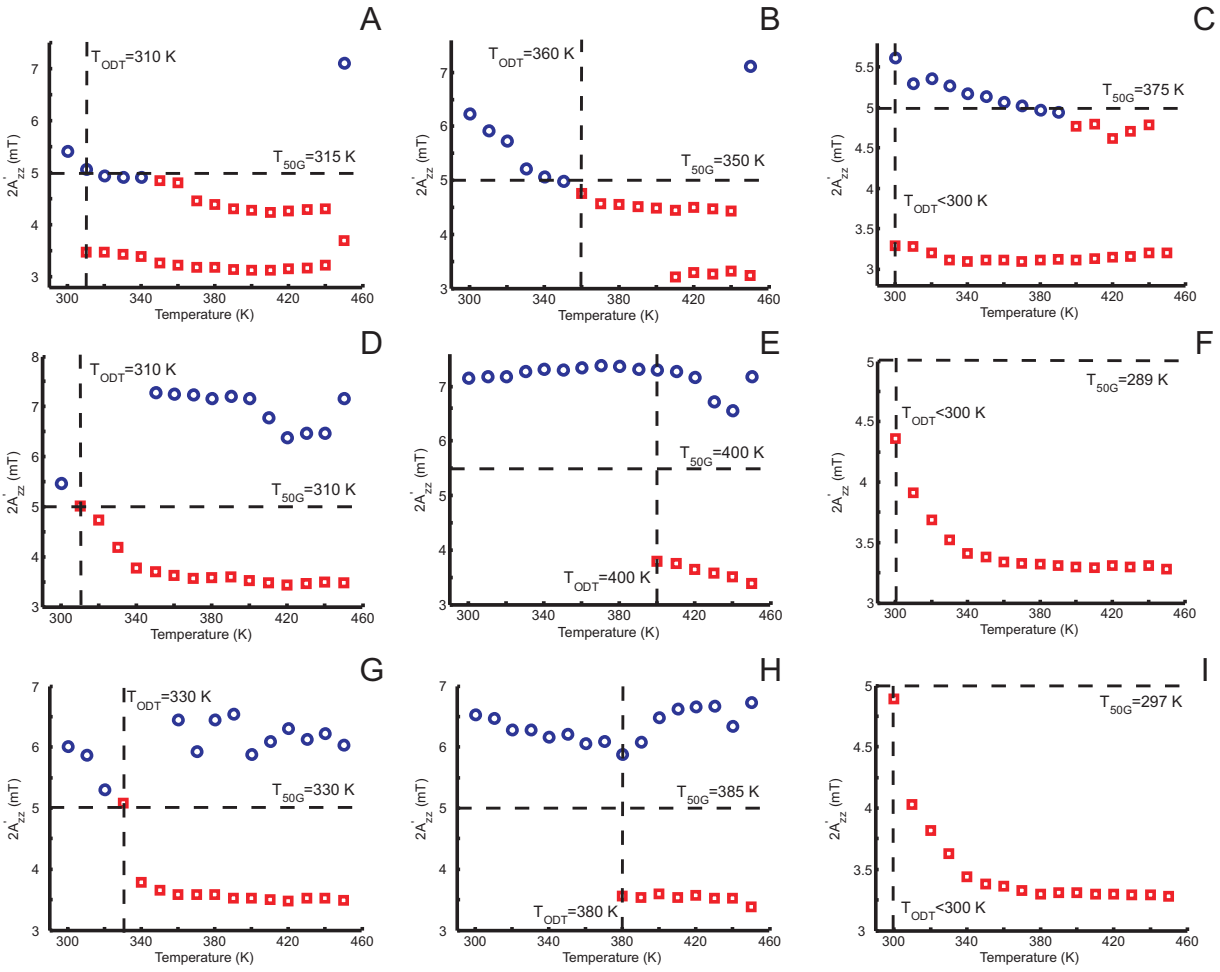

Figure 5.12: $2A_{zz}^{'}$ in CW EPR spectra of spin-labeled surfactants as a function of temperature. As shown in Fig.3.3, $2A_{zz}^{'}$ is the extrema separation in the CW EPR spectrum (first derivative dA/dB spectrum). (A) Organomagadiite with 11-SL-UTMA (magadiite+11-SL-UTMA+HTMA). (B) PS microcomposites (magadiite+11-SL-UTMA+HTMA+PS). (C) PCL nanocomposites (magadiite+11-SL-UTMA+HTMA+PCL). (D) Organomagadiite with 9-SL-UTMA (magadiite+9-SL-UTMA+HTMA). (E) PS microcomposites (magadiite+9-SL-UTMA+HTMA+PS). (F) PCL nanocomposites (magadiite+9-SL-UTMA+HTMA+PCL). (G) Organomagadiite with 7-SL-UTMA (magadiite+7-SL-UTMA+HTMA). (H) PS microcomposites (magadiite+7-SL-UTMA+HTMA+PS). (I) PCL nanocomposites (magadiite+7-SL-UTMA+HTMA+PCL). Circles represent molecular motion in the slow tumbling region and squares represent molecular motion in the fast motional region. T_{50G} and T_{ODT} are plotted for comparison.

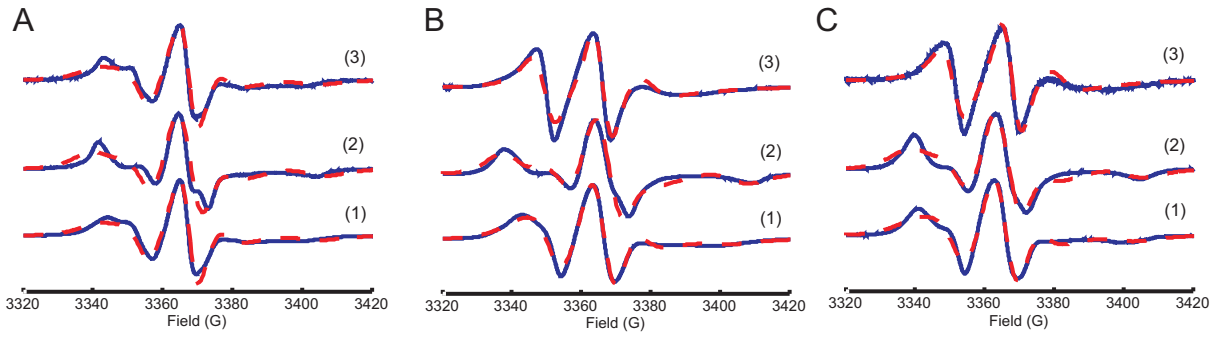

Figure 5.13: Experimental and simulated spectra of the HTMA series at 300 K. Solid lines are experimental spectra and dashed lines are simulated spectra. (A) 11-SL-UTMA series. (B) 9-SL-UTMA series. (C) 7-SL-UTMA series with (1) as organomagadiite, (2) as PS microcomposites and (3) as PCL nanocomposites.

the motion and quantify the activation energy for each regime.

$$\log \tau_c = \log A + \frac{E_a}{RT} \tag{5.7}$$

In Eqn.5.7, A is the pre-exponential factor and R the gas constant (8.3145 $J\,K^{-1}\,mol^{-1}$). By plotting $\log \tau_c$ versus $1/T$ the slope of the fitting curve is E_a/R.

For the tail-labeled spin probe 11-SL-UTMA series, τ_c of PCL nanocomposites is longer than that of organomagadiite because of its slow component in PCL nanocomposites (Fig.5.14. (A)). The Arrhenius plot shows that for 11-SL-UTMA organomagadiite with increasing temperature there are two different trends of molecular motion. In the first regime τ_c tends to be faster from 300 K to 400 K and E_a for this process is 6.3 $kJ\,mol^{-1}$. Compared with an overall E_a of spin-labeled polymer (low density polyethylene, (28)) in melt as 14.2 $kJ\,mol^{-1}$, the value is somewhat lower, which is reasonable for the short alkyl chain of surfactant. In the second regime from 400 K to 450 K the motion tends to slow down and the apparent E_a for this process is -20 $kJ\,mol^{-1}$. The existence of such two regimes of reorientation process is common to 11-SL-UTMA, 9-SL-UTMA and 7-SL-UTMA organomagadiite, however it is most obvious for the tail-labeled 11-SL-UTMA. The activation energy calculated from Fig.5.14 are listed Tab.5.10.

Generally with increasing temperature from 300 K to 450 K, the reorientation process of surfactant layers in organomagadiite, PS microcomposites and PCL nanocomposites can be divided into two regimes. Although for 7-SL-UTMA organomagadiite it can even be divided into three regimes corresponding to different activation energy E_a, the energy difference between the latter two is very small, so that an averaged E_a for one regime can be given (Fig.5.14. (C)). In the first regime, the activation energy E_{a1} is positive indicating an endothermic process. For organomagadiite, the reorientation process in this regime is driven by the activated motion in the disordered surfactant phase. The large negative activation energy E_{a2} (-20 $kJ\,mol^{-1}$) of 11-SL-UTMA organomagadiite (Fig.5.14. (A)) is unusual and could be related to decomposition of the spin probe.

For PS microcomposites a common property of the reorientation process with increasing temperature is that the process consists of one regime with a small positive E_{a1} followed by another regime with a larger positive

E_{a2}. The transition temperature between these two regimes for PS microcomposites is around the glass transition tempeature T_g of PS (373 K) (Tab.5.10). The positive activation energy in the first regime is explained by activated motion in the disordered surfactant phase. Above T_g of PS (around 373 K) the constraints from the polymer matrix are relieved and the mobility of the surfactants now increases together with the mobility of the polymer chains. As the activation energy is larger for the polymer chains, an increases in E_a is also observed for the surfactant.

For PCL nanocomposites, the sample with 11-SL-UTMA is an exception from the other two spin probes because of possible decomposition of the spin probe. For 9-SL-UTMA and 7-SL-UTMA PCL nanocomposites the transition temperature between regime 1 and regime 2 is about 330 K which is very close to the T_m (melting temperature) of PCL (60°, 333 K). In the first regime before the T_m of PCL the surfactant motion becomes faster with increasing temperature due to decreasing viscosity of the PCL. Above the T_m of PCL the polymer melt has almost constant viscosity and the activation energy of reorientation process with increasing temperature is close to zero.

Hence the temperature-dependent CW EPR spectra from 9-SL-UTMA and 7-SL-UTMA PS microcomposites in which PS chains do not intercalate into organomagadiite reveal that the glass transition temperature (T_g) of PS is still critical for the orientation of surfactant molecules. For 9-SL-UTMA and 7-SL-UTMA PCl nanocomposites the melting temperature (T_m) is critical for the orientation of surfactant molecules. The activation energy in regime 1 for these two nanocomposites is about 4 $kJ\,mol^{-1}$.

Sample	E_{a1} of regime1 ($kJ\,mol^{-1}$)	E_{a2} of regime2 ($kJ\,mol^{-1}$)	transition temperature (K)
11-SL-UTMA	6.3	-20	400
11-SL-UTMA+PS	2.4	11	400
11-SL-UTMA+PCL	2.6	-0.12	370
9-SL-UTMA	1.5	-0.78	350
9-SL-UTMA+PS	0.37	7.8	370
9-SL-UTMA+PCL	4	0.014	330
7-SL-UTMA	2.6	0.23	350
7-SL-UTMA+PS	1.9	3.3	380
7-SL-UTMA+PCL	4.1	-0.16	330

Table 5.10: Activation energy E_a calculated from Fig.5.10.

5.7 Pulse EPR results

5.7.1 Results from two-pulse ESEEM measurements

Now results from pulse EPR will be discussed. From ^{2}H NMR and temperature-dependent CW EPR, information on molecular motion of surfactant layers can be obtained. Pulse EPR with well designed pulse sequences can give information on the relaxation mechanism and relative strength of the hyperfine coupling (Electron Spin Envelope Echo Modulation (ESEEM)) or distance distribution of spin probes (Double Electron Electron Resonance (DEER)).

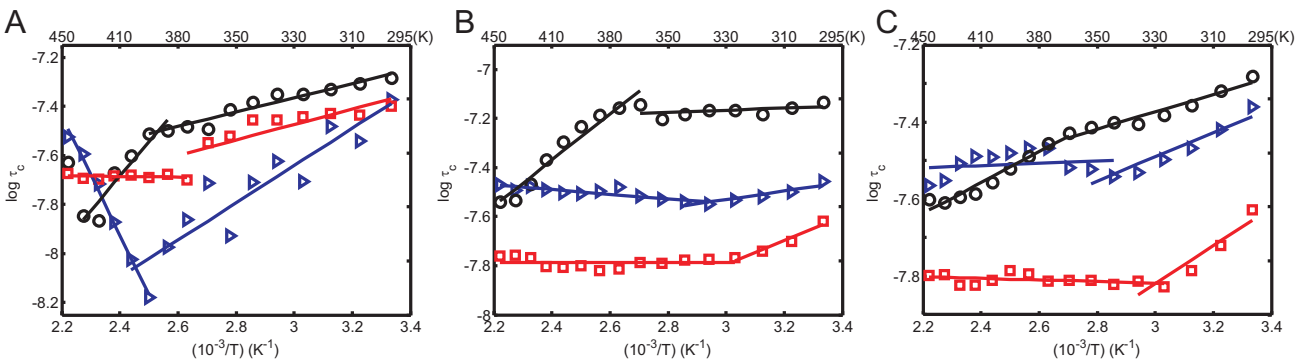

Figure 5.14: Arrhenius plots of the rotational correlation time τ_c. (A) magadiite+11-SL-UTMA+HTMA series. (B) magadiite+9-SL-UTMA+HTMA series. (C) magadiite+7-SL-UTMA+HTMA series. Triangles correspond to organomagadiite; circles correspond to PS micrcomposites and squares corresponds to PCL nanocomposites.

The samples measured with two-pulse and three-pulse ESEEM are shown in Fig.5.2. To study hyperfine coupling between electron and deuterated surfactants, organomagadiites were prepared like this: with each deuterated surfactant d9, dα, and dβHTMA, spin probes 11-SL-UTMA, 9-SL-UTMA, 7-SL-UTMA in a molar ratio of 1% to deuterated surfactants were added. Hence totally there are 9 series of samples: magadiite+d9HTMA+11-SL-UTMA, magadiite+d9HTMA+9-SL-UTMA, magadiite+d9HTMA+7-SL-UTMA, and so on for dα and dβHTMA, respectively. Each series of samples includes organomagadiite, PS and PCL composites (Fig.5.2. (A)).

As described in Sec.3.4.2, from Eqn.3.101 T_m, a memory time of relaxation, can be derived by two-pulse ESEEM experiments (Fig.3.19. (A)). By exponential data fitting T_m is calculated from the signal. The results are listed in Tab.5.11.

sample	T_m (ns) dαHTMA series	T_m (ns) dβHTMA series	T_m (ns) d9HTMA series
11-SL-UTMA	393	352	402
11-SL-UTMA+PCL	797	799	832
11-SL-UTMA+PS	684	647	657
9-SL-UTMA	709	597	752
9-SL-UTMA+PCL	988	1081	1210
9-SL-UTMA+PS	935	1081	1127
7-SL-UTMA	707	567	677
7-SL-UTMA+PCL	1223	1185	1255
7-SL-UTMA+PS	1159	1050	1103

Table 5.11: T_m relaxation time from two-pulse ESEEM. T_m can be approximated as the T_2 transverse relaxation time in the high field approximation

Tab.5.11 shows that both polymer composites have a longer relaxation time and T_m is the longest in PCL nanocomposites. This is expected because intercalation of PCL chains can delay relaxation of spin probe to a larger degree than non-intercalated PS. Although PS chains do not intercalate with organoclay layers PS still interacts with surfactant layers. In 9-SL-UTMA series PS and PCL composites even have the same T_m. Furthermore the tail-labeled 11-SL-UTMA spin probe has the shortest relaxation time and the 7-SL-UTMA spin probe in PCL

nanocomposites has the relatively longest relaxation time.

Compared with the 11-SL-UTMA sample with HTMA without deuterated surfactant (magadiite+11-SL-UTMA+HTMA sample), deuterons cause a modulation on a long time scale while proton modulation remains the same (Fig.5.15).

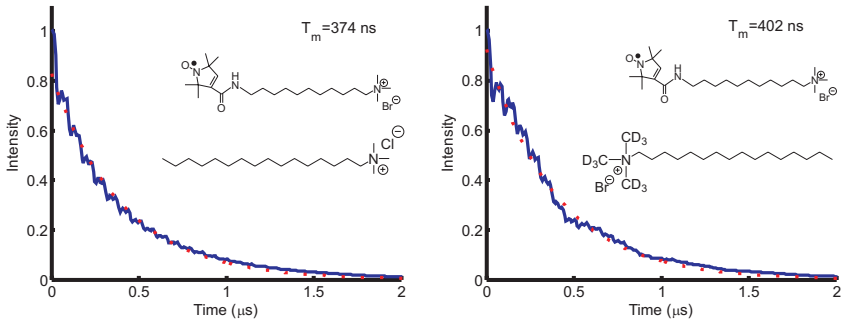

Figure 5.15: Two-pulse ESEEM spectra of samples with non-deturated surfactant HTMA and d9HTMA surfactant with the same spin probe 11-SL-UTMA. (A) T_m = 374 ns for magadiite+11-SL-UTMA+HTMA organomagadiite. (B) T_m = 402 ns for magadiite+11-SL-UTMA+d9HTMA organomagadiite. There is apparent additional modulation from deuterium at long time scales while proton modulation remains the same.

5.7.2 Results from three-pulse ESEEM measurements

By three-pulse ESEEM the relative strength of the hyperfine coupling between electron and deuterons can be measured. It can be calculated from Eqn.3.107 that the Larmor frequency of deuterium in X-band is between 2.0 and 2.5 MHz (for protons it is about 15 MHz). The amplitude of the peak in this range in frequency domain is proportional to the square of the anisotropic electron-deuterium hyperfine coupling. The ESEEM data treatment is shown in Fig.3.19. (B). (C) and (D) and the experimental results after Fourier transformation are shown in Fig.5.16. The relative intensity of the deuterium modulation is labeled in the plot and the results are listed in Tab.5.12.

Generally d9HTMA has the strongest hyperfine coupling because it has 9 deuterons, compared to only two deuterons in dαHTMA and dβHTMA ((C1), (F1), (I1)). Unexpectedly, both PCL and PS exhibit apparent dilution effects on deuteron density although PS does not intercalate into organomagadiite. This result coincides with that from two-pulse ESEEM. PS modifies the surfactant layers although there is no intercalation. For different positions of the spin probe for the same deuterated surfactant there are no significant differences indicating that the 11-, 9-, 7- positions in the alkyl chain have the same extent of contact with the headgroup (d9HTMA) and the 1- and 2- position of the alkyl chain (dαHTMA and dβHTMA). For the same spin probe, as expected d9HTMA has the strongest modulation, in all three cases of organomagadiite, PCL, and PS composites.

5.7.3 Results from four-pulse DEER measurements

Four-pulse DEER is used to measure electron-electron dipolar couplings and get distance distributions by converting data from dipolar coupling space (d) to distance space (r) in analogy to light scattering, where q space is

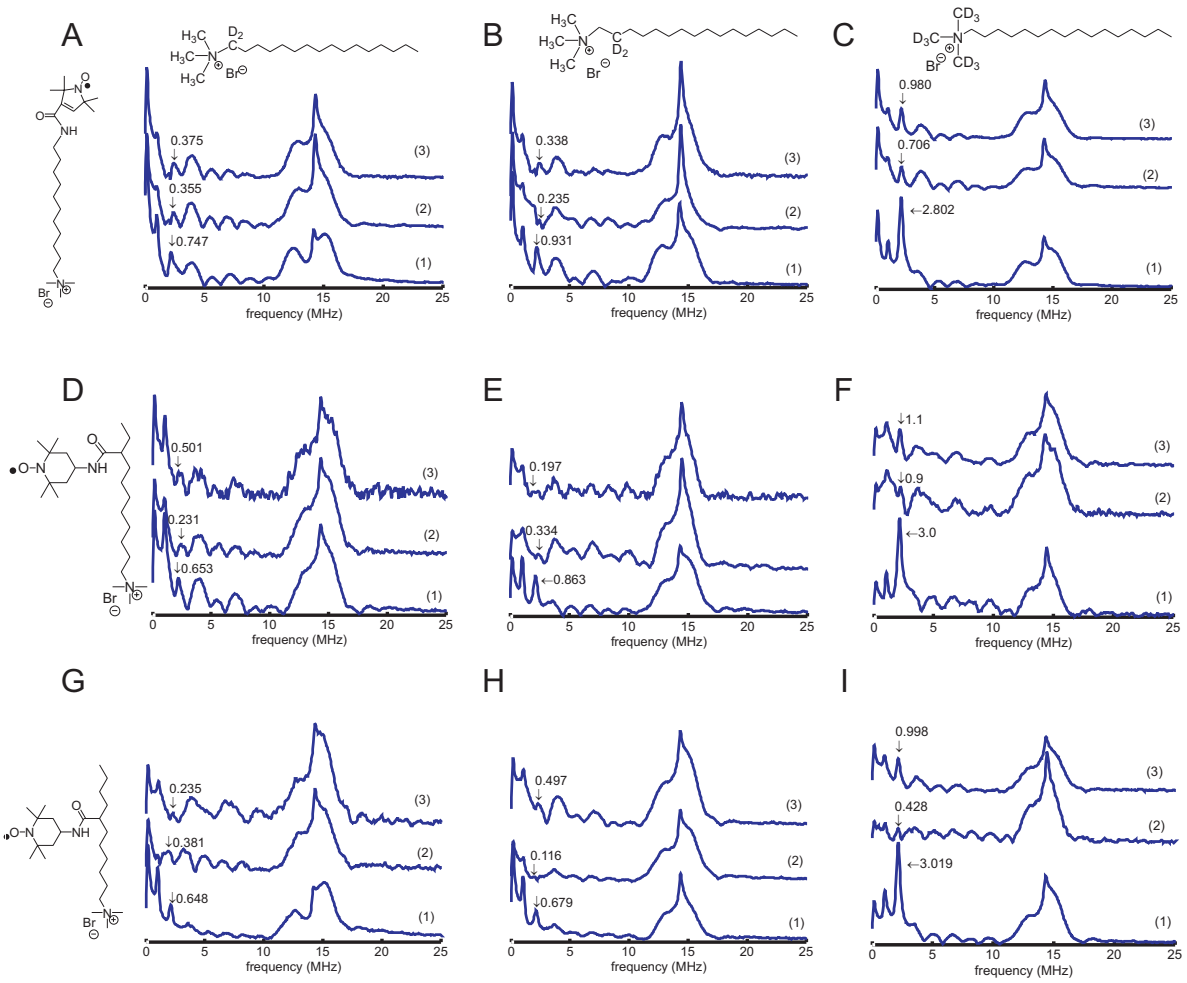

Figure 5.16: ESEEM results in frequency domain. (A) 11-SL-UTMA+dαHTMA series with (1) as organomagadiite, (2) as PCL nanocomposites and (3) as PS microcomposites. (B) 11-SL-UTMA+dβHTMA series; (C) 11-SL-UTMA+d9HTMA series; (D) 9-SL-UTMA+dαHTMA series (E) 9-SL-UTMA+dβHTMA series; (F) 9-SL-UTMA+d9HTMA series; (G) 7-SL-UTMA+dαHTMA series; (H) 7-SL-UTMA+dβHTMA series;(I) 7-SL-UTMA++d9HTMA series.

converted to distance space. For our systems the original signal is very nicely fit by the assumption of a homogeneous distribution in two dimensions (the residue in the middle corresponding to the difference between signal and fitting curve is a flat line in Fig.3.26. (B)). So there is no specific distance distribution because the nitroxides are distributed homogeneously on the surface. By Eqn.3.128, the dimensionality can be derived by application of (30). A density ρ of the nitroxide labels can also be obtained from the decay rate of the dipolar evolution function.

The results of nitroxide density and dimensionality of the spin probe distribution on the silicate surface are listed in Tab.5.13 and shown in Fig.5.17. Part (A) shows, just as the result from three-pulse ESEEM, that both polymers have apparent dilution effects on the spin probe. Nitroxide density differs little between PCL and PS. The dimensionalities of the PS microcomposites are similar for 11-SL-UTMA, 9-SL-UTMA and 7-SL-UTMA however those of PCL nanocomposites are different: PCL with tail-labeled 11-SL-UTMA has the largest dimensionality as 2.6 while in PCL with 9-SL-UTMA and 7-SL-UTMA nitroxides are more strongly confined to a plane. Part (B)

sample	relative strength dαHTMA series	relative strength dβHTMA series	relative strength d9HTMA series
11-SL-UTMA	0.747	0.931	2.802
11-SL-UTMA+PCL	0.355	0.235	0.708
11-SL-UTMA+PS	0.375	0.338	0.980
9-SL-UTMA	0.653	0.863	3.00
9-SL-UTMA+PCL	0.231	0.334	0.900
9-SL-UTMA+PS	0.501	0.197	1.10
7-SL-UTMA	0.648	0.679	3.019
7-SL-UTMA+PCL	0.381	0.116	0.428
7-SL-UTMA+PS	0.235	0.497	0.998

Table 5.12: Relative intensity of hyperfine coupling between electrons and deuterons.

shows that intercalation of PCL influences the distribution of surfactant layers.

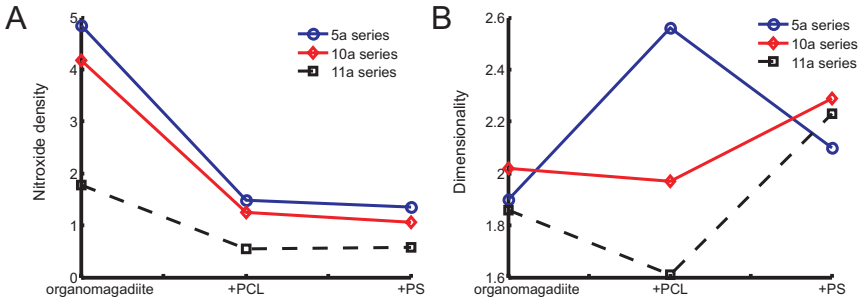

Figure 5.17: Nitroxide density and dimensionality of the nitroxide distribution on the silicate surface. (A) Nitroxide density of organomagadiite, PCL and PS composites. Circles represent the 11-SL-UTMA series; diamonds the 9-SL-UTMA series; squares and dashed lines the 7-SL-UTMA series. (B) Dimensionality of the spin probe distribution on the silicate surface

nitroxide density (mol/element area)				dimensionality		
sample	organomagadiite	+PCL	+PS	organomagadiite	+PCL	+PS
11-SL-UTMA	4.842	1.485	1.356	1.90	2.56	2.10
9-SL-UTMA	4.178	1.256	1.067	2.02	1.97	2.29
7-SL-UTMA	1.770	0.542	0.582	1.86	1.61	2.23

Table 5.13: Nitroxide density and dimensionality of spin probes measured by DEER

5.8 Characterization of HTBP organosilicates by ^{31}P MAS NMR

As described in Sec.5.5.3.3, organomagadiite prepared with the phosphonium surfactant HTBP can be characterized with ^{31}P MAS NMR. In Fig.5.6. (B) there are two peaks in the ^{31}P NMR spectrum. In previous work on organoclay prepared from Somasif and HTBP in excess we also found two peaks in the ^{31}P NMR spectrum. (30) To check whether the two peaks can be assigned to head groups directly attached to the surface (monolayer state) and headgroups remote from the surface (multilayer state), the sample prepared with excess HTBP was

washed several times with ethanol/water (50:50 wt%) and measured with ^{31}P NMR. The washing out effect by ethanol was also proved by EPR as in the organomagadiite prepared with nitroxide spin probes only a very weak CW EPR signal remained if the samples were washed with ethanol overnight. Spin-labeled surfactants are thus washed out preferentially. The parameters of ^{31}P NMR were described in Sec.5.4.4. The FID signal was recorded at $d_1 = 60$ s after $\pi/2$ pulse. Experiments with $d_1 = 30$ s were also tried and the chemical shifts obtained were the same as those in spectra measured with $d_1 = 60$ s. Thus we know that a repetition time $d_1 = 60$ s is sufficient for phosphonium nuclei in single pulse MAS NMR to obtain spectra with correct peak amplitudes.

^{31}P NMR spectra of the sample with excess HTBP (spectrum (1)) and the sample that was washed with ethanol (spectrum (2)) are shown in Fig.5.18. It is noticed that peak 2 (28.9 ppm) in spectrum (1) is weakened in spectrum (2) while peak 1 (30.22 ppm) remains the same. So peak 1 can be assigned to phosphonium nuclei in directly attached headgroups (monolayer state) as it survived after ethanol washing and peak 2 can be assigned to phosphonium nuclei in additional surfactant layers. This assignment is in agreement with the fact that the larger chemical shift in downfield corresponds to phosphonium nuclei with stronger deshielding effects, that may be caused by nearby electronegative groups (e.g. OH^- groups) on the magadiite surface. Strongly bound counter ions (Br^-) on the surface could also contribute to such deshielding effects. The resolution of ^{31}P NMR of organoclay prepared with magadiite is better than that prepared with Somasif as the latter has paramagnetic ions such as Fe^{3+} in the natural silicate structure. (30)

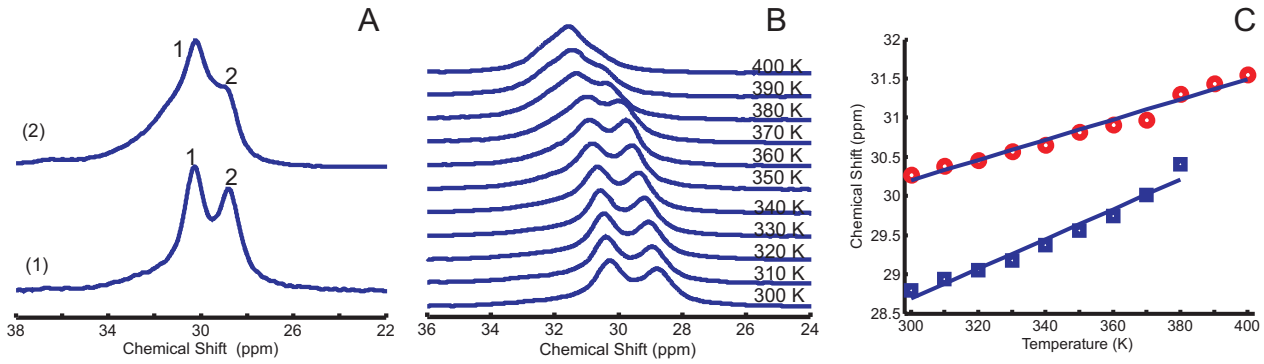

Figure 5.18: ^{31}P single pulse MAS NMR of monolayer and multilayer HTBP surfactants and temperature-dependent ^{31}P NMR of the multilayer sample. (A) (1) ^{31}P NMR signal from the multilayer sample prepared with an excess of HTBP of $200 mmol/100 g$. (2) The signal from the same sample after repeated washing with ethanol/water mixture (wt% 50/50). Peak 1 can be assigned to the signal from a monolayer and peak 2 can be assigned to the signal from additional layers. (B) Temperature dependent ^{31}P NMR. (C) Chemical shift values from (B) with circles represent chemical shifts of peak 1 and squares represent chemical shifts of peak 2. With increasing temperature, the two states of phosphorus from the different layers merge and behave as a single layer with stronger interaction with the magadiite surface. The increase of the chemical shifts with temperature can be fitted linearly.

The sample prepared with an excess of HTBP was also measured with temperature dependent ^{31}P MAS NMR and the spectra are shown in Fig.5.18. (B). The measuring temperature was increased from 300 K to 400 K in steps of 10 K. The chemical shifts corresponding to peak 1 and peak 2 are plotted in (C) with circles representing chemical shifts of peak 1 and squares representing chemical shifts of peak 2. In Fig.5.14. (C), it is clear that with increasing temperature chemical shifts δ are further low field indicating more deshielding effects at higher

temperature. Above 380 K phosphonium nuclei in different states merge and behave as if they were in a single layer (with one broadened peak). These observations can be explained by assuming that at high temperature, when the surfactant is close to a melt state, reordering of the surfactant layers results in a stronger interaction between hydrophilic phosphonium head groups and the surface of the magadiite.

Thus from ^{31}P NMR two states of phosphonium nuclei in surfactant layers can be characterized corresponding to a state in monolayer and an additional layer. At high temperature surfactant layers tend to reorganize to a single layer which has stronger interaction with clay.

5.9 Molecular motion of phosphonium surfactants

5.9.1 Temperature dependent CW EPR spectra

Just like temperature dependent CW EPR experiments were applied to the ammonium surfactant HTMA series, the phosphonium series was also measured with CW EPR to study dynamics of HTBP surfactant layers with 11-SL-UTBP, 9-SL-UTBP and 7-SL-UTBP spin probes (Tab.5.1). Temperature-dependent CW EPR spectra are shown in Fig.5.19.

Generally nitroxide-labeled phosphonium surfactants are more stable than nitroxide-labeled in ammonium surfactants, especially in PCL nanocomposites. The spectrum at 300 K after heating at 450 K has a triplet nitroxide spectrum which is close to that at 300 K before heating. Similar to the HTMA series, HTBP surfactants have the fastest molecular motion in PCL nanocomposites among organomagadiite, PS and PCL composites. However, compared with the HTMA series (Fig.5.11), molecular motion of HTBP in organoclay is generally faster, especially for the close-to-middle labeled 7-SL-UTBP spin probe (Fig.5.19. (G)). For organomagadiite with 9-SL-UTBP and 7-SL-UTBP spin probes only a single component (slow) is present while for ammonium spin probes with increasing temperature there are two components (slow and fast) present in the EPR spectrum (Fig.5.11. (D) and (G)).

$2A'_{zz}$ measured from EPR spectra are shown in Fig.5.20 and T_{50G} and T_{ODT} are also indicated in the plot. Similar to the result for the ammonium surfactant HTMA, for organomagadiite and PS composites $T_{ODT} \approx T_{50G}$. For PCL nanocomposites the actual $T_{ODT} \leq T_{50G}$ is also the same as that of ammonium surfactants.

The T_{ODT} of the samples are listed in the Tab.5.14. PS microcomposites have a higher glass transition temperature and PCL nanocomposites have a lower T_{ODT} than that of organoclay. Compared with T_{ODT} of ammonium samples listed in Tab.5.8, it is found that organoclay prepared from HTBP has higher T_{ODT} than that from HTMA. It should be noticed that HTMA chloride powder has higher melting point (232-234°) than that of HTBP bromide powder (56-58°), so probably HTMA has more crystalline properties. The thermal stability of nitroxide-labeled phosphonium surfactants is higher than that of nitroxide-labeled ammonium surfactants. The T_{ODT} of PCL nanocomposites are very close for ammonium spin probes (9-SL-UTMA, 7-SL-UTMA) and phosphonium spin probes (9-SL-UTBP, 7-SL-UTBP). The tail-labeled ammonium spin probe 11-SL-UTMA is special because it has a slow component in PCL nanocomposites. For PS microcomposites the immobilization effect which results in an increase of T_{50G} is similar for 11-SL-UTBP, 9-SL-UTBP, and 7-SL-UTBP.

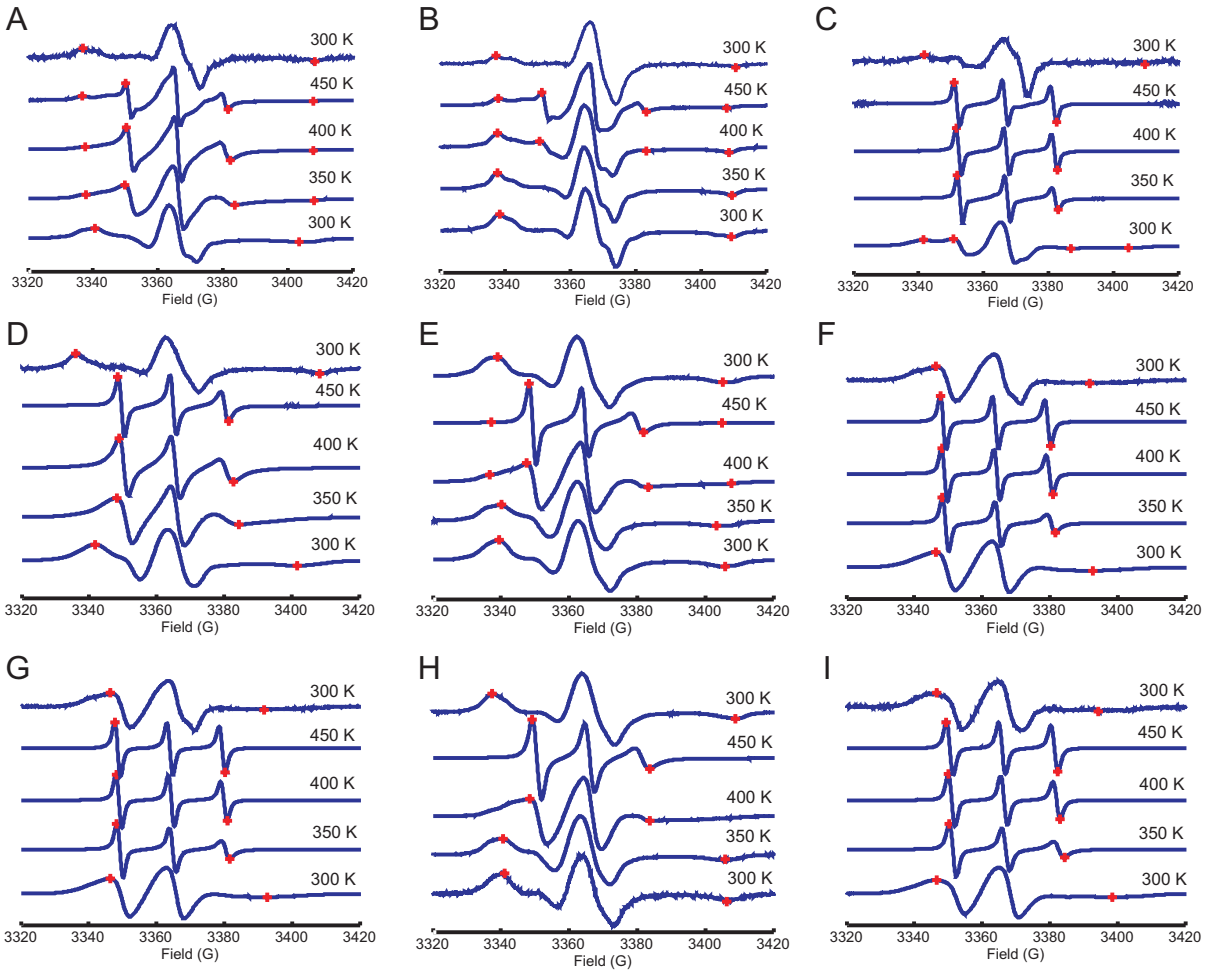

Figure 5.19: Temperature-dependent CW EPR spectra of the phosphonium surfactant HTBP series. (A) Organomagadiite with 11-SL-UTBP (magadiite+11-SL-UTBP+HTBP). (B) PS microcomposites (magadiite+11-SL-UTBP+HTBP+PS). (C) PCL nanocomposites (magadiite+11-SL-UTBP+HTBP+PCL). (D) Organomagadiite with 9-SL-UTBP (magadiite+9-SL-UTBP+HTBP). (E) PS microcomposites (magadiite+9-SL-UTBP+HTBP+PS). (F) PCL nanocomposites (magadiite+9-SL-UTBP+HTBP+PCL). (G) Organomagadiite with 7-SL-UTBP (magadiite+7-SL-UTBP+HTBP). (H) PS microcomposites (magadiite+7-SL-UTBP+HTBP+PS). (I) PCL nanocomposites (magadiite+7-SL-UTBP+HTBP+PCL). The spectra at 300 K on the top were measured at 300 K after cooling down from 450 K.

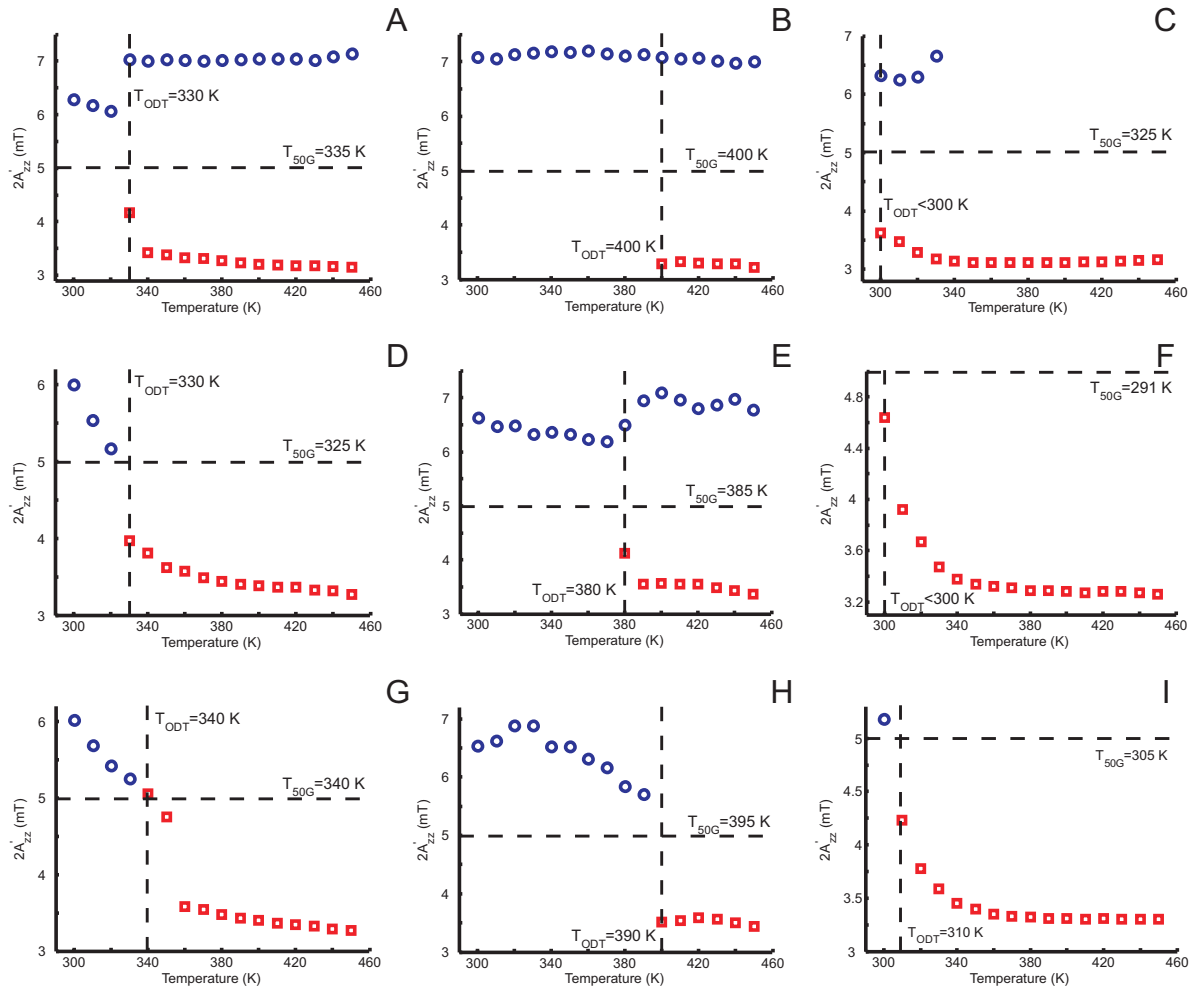

Figure 5.20: $2A'_{zz}$ of temperature dependent CW EPR spectra. (A) Organomagadiite with 11-SL-UTBP (magadiite+11-SL-UTBP+HTBP). (B) PS microcomposites (magadiite+11-SL-UTBP+HTBP+PS). (C) PCL nanocomposites (magadiite+11-SL-UTBP+HTBP+PCL). (D) Organomagadiite with 9-SL-UTBP (magadiite+9-SL-UTBP+HTBP). (E) PS microcomposites (magadiite+9-SL-UTBP+HTBP+PS). (F) PCL nanocomposites (magadiite+9-SL-UTBP+HTBP+PCL). (G) Organomagadiite with 7-SL-UTBP (magadiite+7-SL-UTBP+HTBP). (H) PS microcomposites (magadiite+7-SL-UTBP+HTBP+PS). (I) PCL nanocomposites (magadiite+7-SL-UTBP+HTBP+PCL). Cirles represent molecular motion in the slow tumbling region and squares represent molecular motion in the fast motional region. T_{50G} and T_{ODT} are plotted for comparison.

Sample	T_{50G} (K)	Sample	T_{50G} (K)	Sample	T_{50G} (K)
11-SL-UTBP	335	9-SL-UTBP	330	7-SL-UTBP	340
11-SL-UTBP+PS	400	9-SL-UTBP+PS	385	7-SL-UTBP+PS	395
11-SL-UTBP+PCL	325	9-SL-UTBP+PCL	291	7-SL-UTBP+PCL	305

Table 5.14: T_{50G} values of phosphonium surfactant series.

5.9.1.1 Analysis of the reorientational correlation time τ_c

The CW EPR spectra can also be fitted by simulated spectra to obtain the rotational correlation time τ_c. The experimental and simulated spectra are shown in Fig.5.21. It can be noticed that in the series of organomagadiite, PS microcomposites and PCL nanocomposites the molecular motion is the fastest in PCL and the slowest in PS composites. This is consistent with the result from the ammonium surfactant series. The values of the rotational correlation time τ_c at 300 K are listed in Tab.5.15. The average τ_c of the samples are located in the slow tumbling regime according to the simulations although a component could be in the fast motional regime (squares in Fig.5.20).

Sample	τ_c (ns)	Sample	τ_c (ns)	Sample	τ_c (ns)
11-SL-UTBP	5.79	9-SL-UTBP	4.12	7-SL-UTBP	4.12
11-SL-UTBP+PS	8.17	9-SL-UTBP+PS	5.89	7-SL-UTBP+PS	6.09
11-SL-UTBP+PCL	2.79	9-SL-UTBP+PCL	2.66	7-SL-UTBP+PCL	3.10

Table 5.15: τ_c values of the phosphonium surfactant series at 300 K.

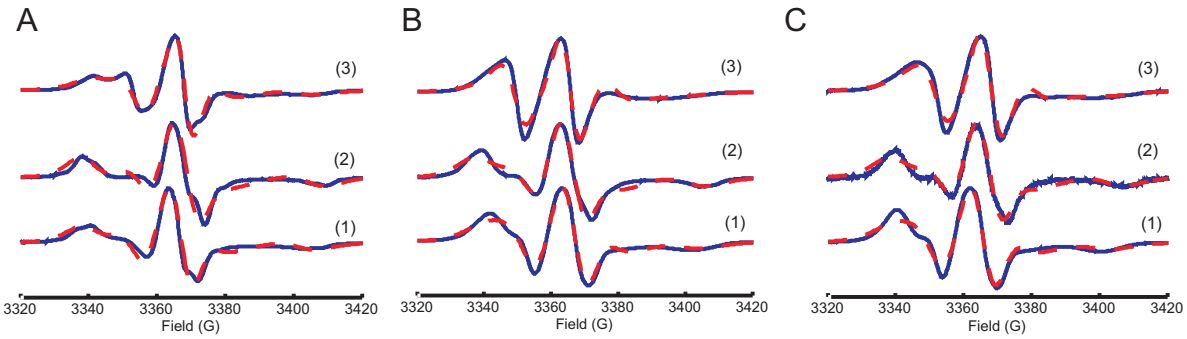

Figure 5.21: Experimental and simulated spectra of the HTBP series at 300 K. Solid lines are experimental spectra and dashed lines are simulated spectra. (A) 11-SL-UTBP series. (B) 9-SL-UTBP series. (C) 7-SL-UTBP series with (1) as organomagadiite, (2) as PS microcomposites and (3) as PCL nanocomposites.

Compared with the data in Tab.5.9, the immobilization effect of PS is stronger in phosphonium surfactant samples than in ammonium surfactant samples however the mobilization effect of PCL for both surfactants is similar.

After τ_c was obtained, the activation energy E_a was calculated from Arrhenius plots as described in Sec.5.6.2.2. The Arrhenius plots are shown in Fig.5.22. The activation energies E_a are listed in Tab.5.16. Compared with samples with ammonium surfactants, generally E_a of the reorientation process of phosphonium surfactant layers

is positive. Spin-labeled phosphonium surfactants are more stable than spin-labeled ammonium surfactants so that regime 2, which occurs for ammonium surfactants, is not observed. The overall reorientation process of 11-SL-UTBP, 9-SL-UTBP and 7-SL-UTBP in organomagadiite has an average E_a of about 2.0 $kJ\,mol^{-1}$. Similar to spin-labeled ammonium surfactants, with increasing temperature phosphonium spin probes undergo two processes in PS and PCL composites. Again the transition temperature between regime 1 and regime 2 of PS microcomposites is close to the glass transition temperature T_g of bulk PS (373 K) and for PCL nanocomposites the transition temperature is close to the melting temperature T_m of PCL (333 K). From E_a values it is noticed that spin probes of 9-SL-UTBP and 7-SL-UTBP behave similarly with increasing temperature however the tail-labeled 11-SL-UTBP behaves a little differently. Both in PS and PCL composites E_a is somewhat smaller as motion of the chain end does not require as much free volume as motion of the whole chain.

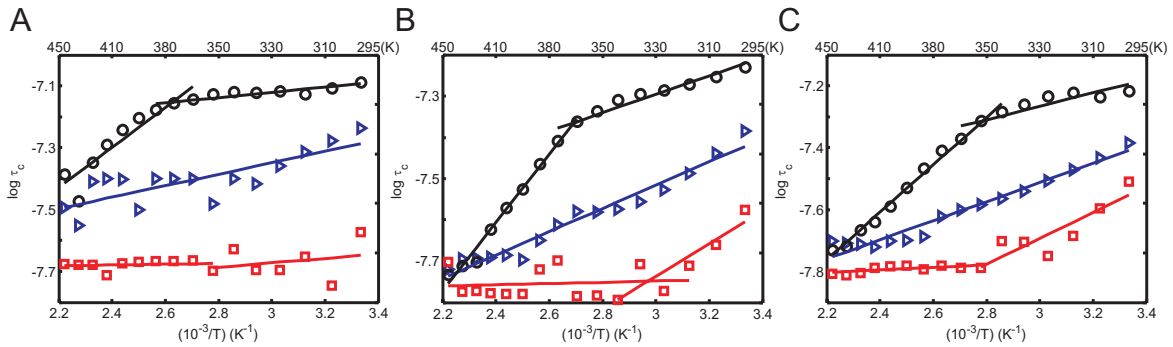

Figure 5.22: Arrhenius plot of the rotational correlation time τ_c. (A) magadiite+11-SL-UTBP+HTBP series. (B) magadiite+9-SL-UTBP+HTBP series. (C) magadiite+7-SL-UTBP+HTBP series. Triangles correspond to organoclay; Circles correspond to PS micrcomposites and squares corresponds to PCL nanocomposites.

Sample	E_{a1} of regime 1 ($kJ\,mol^{-1}$)	E_{a2} of regime 2 ($kJ\,mol^{-1}$)	transition temperature (K)
11-SL-UTBP	1.5	-	-
11-SL-UTBP+PS	0.71	5.4	380
11-SL-UTBP+PCL	0.60	0.09	330
9-SL-UTBP	2.3	-	-
9-SL-UTBP+PS	1.9	6.9	380
9-SL-UTBP+PCL	3.3	0.13	330
7-SL-UTBP	2.6	-	-
7-SL-UTBP+PS	1.8	6.4	360
7-SL-UTBP+PCL	3.5	0.35	330

Table 5.16: Activation energy E_a calculated from Fig.5.22.

5.10 Spatial information obtained from ENDOR

5.10.1 Results from stimulated echo experiments

Samples prepared with phosphonium surfactants can be measured with Electron Nuclear Double Resonance (ENDOR) to obtain the hyperfine coupling between the electron and ^{31}P nuclei. As described in Sec.3.5.2, with the model shown in Fig.3.23, the distance distribution between radicals and ^{31}P nuclei can then be obtained with Eqn.3.117.

Before ENDOR experiments, stimulated echo experiments were performed to derive the optimum interpulse time τ (Sec.3.5.1). From these stimulated echo experiments an approximate transverse relaxation time T_2 can be obtained. In Fig.3.24 the data treatment of the ENDOR experiments is shown. The results of stimulated echo experiments are listed in Tab.5.17. Clearly in PCL nanocomposites the T_2 is larger than that in organoclay and in PS microcomposites. However PS also leads to a longer T_2 of spin probes in microcomposites although it does not intercalate into organomagadiite. The lengthening of T_2 is somewhat smaller than in PCL nanocomposites. This result is consistent with two-pulse ESEEM experiments of samples with ammonium surfactant HTMA (Tab.5.11). In general the stimulated echo experiment yields a longer relaxation time T_2 than a two-pulse ESEEM experiment for the same sample. However samples prepared with HTBP have shorter relaxation times measured with the stimulated echo experiment than T_m of samples prepared with HTMA measured with two-pulse ESEEM even though ESEEM was measured at 80 K, a higher temperature than the 50 K used for the stimulated echo experiments. This can be explained by assuming that the ammonium surfactant has a longer relaxation time because of stronger interaction between the ammonium head group and the silicate surface. For example, for a sample with 11-SL-UTMA and HTMA (without deuterated HTMA, not shown in Tab.5.11), T_m for organomagadiite is 373 ns and for PCL and PS composites the values are 821 ns and 674 ns respectively, while T_2 for the HTBP series are 296 ns, 468 ns and 404 ns respectively (Tab.5.17).

sample	τ (ns)	sample	τ (ns)	sample	τ (ns)
11-SL-UTBP	296	9-SL-UTBP	260	7-SL-UTBP	300
11-SL-UTBP+PCL	468	9-SL-UTBP+PCL	496	7-SL-UTBP+PCL	544
11-SL-UTBP+PS	404	9-SL-UTBP+PS	488	7-SL-UTBP+PS	516

Table 5.17: Interpulse delay τ obtained from stimulated echo experiments. τ can be approximated as transverse relaxation time T_2

5.10.2 Results from ENDOR

The ENDOR data was treated as described in Sec.3.5.2. The results of three series (11-, 9- and 7-SL-UTBP) of samples are shown in Fig.5.23. Generally ENDOR works well for characterization of PLS systems with iron free magadiite. The hyperfine coupling can be measured with very a good signal/noise ratio (Fig.3.24) unlike in work on the commercial layered silicate Somasif. (7) Spectra simulated with the planar distribution model (Fig.3.23, dotted line in Fig.3.24. (D)) fit the experimental spectra quite well.

Fig.5.23 shows that with this model there are two distinct peaks in the distance distribution between the electron spin and ^{31}P nuclei. Theoretically for the end-labeled spin probe 11-SL-UTBP the distance between electron spin and the phosphonium head group in the same molecule is about 1 nm (the main chain length of undecyl-tributyl phosphonium bromide). All preferred distances measured by ENDOR are less than 1 nm. This suggests that the surfactant alkyl chains lie rather flat on the surface of the silicate platelets, as suggested by other experiments in previous work on Somasif. (7) There is little difference between different site-labeled organomagadiites (Fig.5.23. (A1), (B1), (C1)). In principle the middle-labeled spin probe 7-SL-UTBP should have a shorter distance between the electron spin and ^{31}P nuclei however this is not observed in the ENDOR data. This is an even stronger argument for flat-lying alkyl chains, as only in this case the distance between different position in the alkyl chain and the phosphonium head group layer is almost the same. The shorter distance (r_1) should arise from intermolecular contribution between the electron spin and ^{31}P atom in other surfactant head groups on the silicate surface while the longer distance (r_2) is also an intermolecular contribution which arises from ^{31}P in a neighbouring surfactant layer (*middle layer*). The model with a middle layer is presented in more detail in Sec.6.8. The values of r_1 and r_2 and corresponding fractions of the signal are listed in Tab.5.18.

Sample	r_1 (nm)	r_1 fraction	r_2 (nm)	r_2 fraction
11-SL-UTBP	0.38	0.272	0.69	0.728
11-SL-UTBP+PS	0.46	0.213	0.71	0.787
11-SL-UTBP+PCL	0.36	0.466	0.71	0.534
9-SL-UTBP	0.40	0.329	0.69	0.671
9-SL-UTBP+PS	0.45	0.148	0.70	0.852
9-SL-UTBP+PCL	0.39	0.400	0.84	0.600
7-SL-UTBP	0.40	0.357	0.71	0.643
7-SL-UTBP+PS	0.48	0.358	0.75	0.642
7-SL-UTBP+PCL	0.39	0.381	0.88	0.619

Table 5.18: Mean distances r_1 and r_2 of the peaks in bimodal fitting of the ENDOR spectra and corresponding fractions of the two peaks.

Although WAXS data show that there is no intercalation of PS chains into the organomagadiite and the distance between the silicate platelets does not change in PS microcomposites (Fig.5.6. (A)), both PCL and PS have influence on the hyperfine couplings. This result again is consistent with that from two-pulse ESEEM, three-pulse ESEEM, DEER from ammonium surfactant samples and stimulated echo experiments for phosphonium surfactant samples. The longer distance r_2 of 9- and 7-SL-UTBP PCL nanocomposites increases due to intercalation (Tab.5.18). WAXS reveals that the basal spacing of 2.9 nm (space of 1.9 nm between platelets because the thickness of one sheet is approximately 1 nm) in organoclay is enlarged to 3.5 nm (2.5 nm between platelets) in PCL nanocomposites (Fig.5.6. (A)). More space between platelets results in a longer distance r_2 in PCL nanocomposites (Fig.5.23. (B2) and (C2)). The increased r_2 ($[(r_2(\text{PCL}) - r_2(\text{organoclay})]/r_2(\text{organoclay})]$) of 22% is close to that from WAXS data, which is 31% ((2.5 nm − 1.9 nm)/(1.9 nm)) (Tab.5.4). However, the absolute increase in r_2 is only about half as large as the absolute increase of the interlayer distance. This suggests that r_2 is a distance to ^{31}P nuclei in a middle layer. The end-labeled spin probe 11-SL-UTBP is less affected by PCL. This is unexpected, as the chain end should have more conformational freedom than a side chain, it is in agreement with

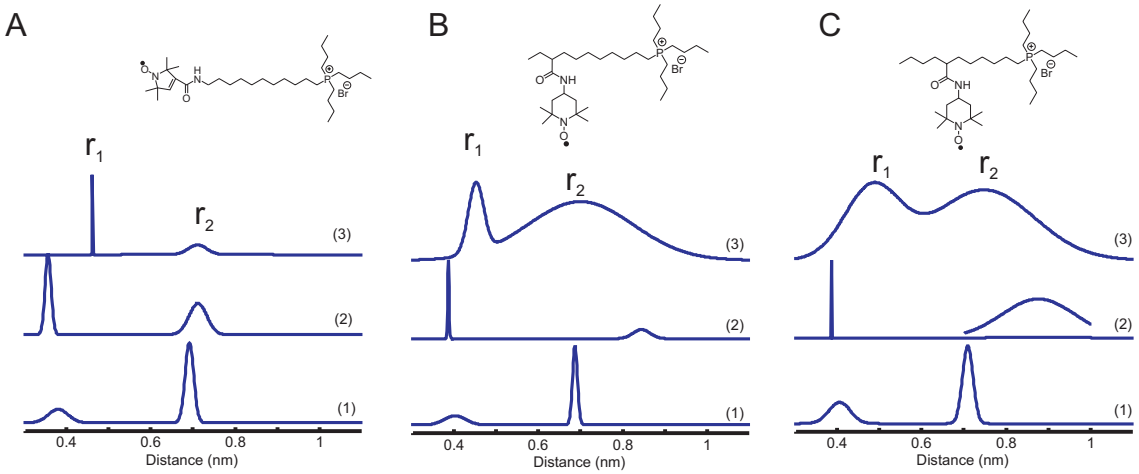

Figure 5.23: Distance distribution between the electron spin and ^{31}P nuclei from ENDOR experiments. (A) the series of samples prepared with the 11-SL-UTBP spin probe. (1) organomagadiite; (2) nanocomposites with PCL; (3) microcomposites with PS. The chemical structure of 11-, 9- and 7-SL-UTBP is shown. (B) the series of samples prepared with the 9-SL-UTBP spin probe. (C) the series of samples prepared with the 7-SL-UTBP spin probe.

CW EPR (Fig.5.21), which shows a stronger mobilization by PCL intercalation for 7- and 9-SL-UTBP than for 11-SL-UTBP. This phenomenon in turn shows that the dimensionality of surfactant layers at the surface differs little between organomagadiite and nanocomposites: the aliphatic main chain of the surfactant molecules does not change very much if the interlayer spacing increases.

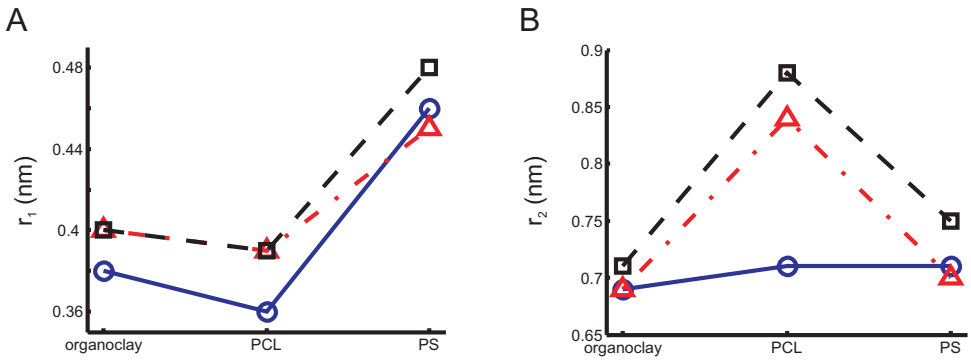

Figure 5.24: Plot of the distances r_1 and r_2 with circles as the 11-SL-UTBP series, triangles as the 9-SL-UTBP series, and squares as the 7-SL-UTBP series. (A) r_1 distance. (B) r_2 distance.

From Fig.5.24. (A) it can be noticed that the distance r_1 increases significantly in PS microcomposites and decreases slightly in PCL nanocomposites. Because r_1 is below 0.40 nm, much less than the theoretical chain length of a single spin probe molecule of 1 nm, r_1 can be assigned to the contribution of the nitroxides coupling to neighbouring phosphonium nuclei in the same layer of surfactant molecules that lie flat on the surface. In this model the dilution effect of PS in microcomposites measured with three-pulse ESEEM and DEER can be explained by increasing of r_1, which corresponds to an increase of the angle (θ) that the alkyl chains make with the silicate surface. In other words, the alkyl chains do not lie that flat on the surface in PS microcomposites as

in the organomagadiite or in PCL nanocomposites (Fig.5.25). The increasing of r_2 which arises from the enlarged distance between organomagadiite layers can explain the dilution effect of PCL nanocomposites measured by three-pulse ESEEM and DEER. ENDOR thus suggests that the mechanism of dilution effects of PCL and PS is different. This is also indicated by a different dimensionality of the homogeneous nitroxide distribution measured with DEER.

A model to explain distance r_1 is presented in Fig.5.25 . Based on these ENDOR results a comprehensive model with a middle layer of surfactant molecules in the gallery between the organomagadiite layers can be introduced, by comparing the combination of distances r_1 and r_2 with the basal distance from WAXS and the chain length of the spin probe. The middle layer model will be discussed in Sec.6.8.

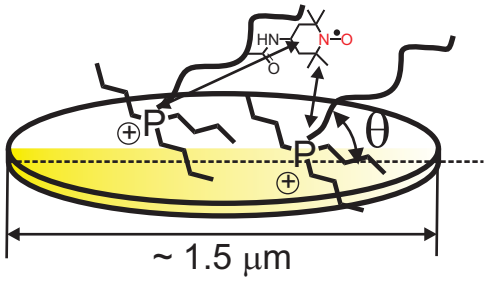

Figure 5.25: The single layer model to explain the distance contribution r_1. Angle θ is the direction of the alkyl chains with respect to the silicate surface. Two vectors represent the intramolecular contribution and intermolecular contribution in the same layer on the surface. From the explaination in the text the intramoleuclar contribution can be neglected and θ should be very small.

As shown in Fig.5.25, the alkyl chains make an angle θ with the silicate surface. In principle θ can be distributed from 0° to 90° in this model. The contributions of distance r_1 could be intramolecular or intermolecular as shown in Fig. 5.25 because r_1 is as small as 0.4 nm. For $\theta = 90°$ for all chains, the intramolecular distance is the shortest distance (≈ 1 nm). For $\theta < 90°$ intermolecular distances are shorter and could be very small if θ is small. There is only *one* ^{31}P nucleus in the same surfactant molecule as the electron spin, but there are *many* ^{31}P in neighbouring molecules that have shorter ($\theta < 90°$) or similar ($\theta \approx 90°$) distances from the electron spin. Because of the much higher number of other ^{31}P nuclei (99 times more than unlabeled surfactant because of the molar ratio (1%) of spin probes in preparation), the intramolecular contribution is negligible. The distance $r_1 \approx 0.4$ nm is close to van-der-Waals contact of the nitroxide group with the tributylphosphonium group. If labels in the 11-, 9-, and 7-position have van-der-Waals contact to head groups, θ must be close to zero. Hence from this single layer model the distance r_1 should be contributed from distances between electrons and ^{31}P nuclei in the neighouring surfactant molecules in the same layer. In this layer surfactant molecules lie rather flat on the surface of the platelet. The distance r_2 contribution is explained by a middle layer model and discussed in Sec.6.8.

Chapter 6

Discussion

6.1 Discussion of magadiite synthesis

By hydrothermal synthesis, magadiite with a well defined layered structure can be synthesized. The critical parameters are the annealing temperature and duration of the reaction under autogeneous pressure in an autoclave, if the composition of reactants is fixed (amorphous silica : NaOH : H_2O = 3 : 1 : 200). Under such conditions the temperature is found to be more critical than the annealing period because the species of product is determined by the temperature. A longer annealing period can however improve regularity of the morphology. The crystal structure and morphology of the products can be characterized by WAXS and SEM. WAXS shows a nice reproducibility of the fine structure of the product at the same temperature. From Tab.6.1 the optimum annealing conditions were found and are summarized as follows.

1. At a relatively low temperature such as 140°C, the reaction duration in the autoclave needs to be as long as 62 hours to 72 hours.

2. If the temperature is set between 150°C and 155°C, annealing for 48 hours is sufficient. A longer period improves the morphology, however at this temperature a longer time also results in admixture of magadiite to the kenyaite.

3. The transition temperature between producing mainly magadiite and producing mainly kenyaite is at about 155–160°C. At 140°C the product is pure magadiite. At 170°C the product is pure kenyaite. In between the product is a mixture of magadiite and kenyaite. Below 155°C the product is dominated by magadiite and above 160°C the product is dominated by kenyaite.

4. If the temperature is far below 140°C the supercritical condition is not achieved and the product is amorphous. If the temperature is far above 170°C the final product is again amorphous quartz.

Although the fine structure of the products is stable, SEM shows that the morphology is rather sensitive to small shifts of the reaction temperature. As described in Sec.5.1, with hydrothermal synthesis, at supercritical conditions in an autoclave, a small shift of temperature could result in a drastic change of the dielectric constant and the equilibrium of reactions (Eqn.5.1 and Eqn.5.2). WAXS shows that the same product is still thermodynamically

stable, but SEM reveals that the morphology is influenced by a small inaccuracy of the temperature control, probably due to a change in the relative rates of nucleation and growth.

6.2 Characterization of adsorption conditions

From titration with HTMA chloride solution, the CEC of magadiite can be roughly determined to be on the scale of 80–120 mmol/100g which is very similar to Somasif, a fluoromica that was used in our previous experiments on PLS nanocomposites, which has a CEC of 80 mmol/100g. Phenomena observed in the titration experiment indicate that the process of adsorption of HTMA on the magadiite surface via electrostatic interaction consists of three basic stages. For the rest of experiments the organomagadiite was prepared with an amount of surfactant of 200 mmol/100g of magadiite to have a complete absorption. Unbound excess surfactant was washed away.

1. Between 30-40 mmol/100g big aggregates (flocculants) were formed fast and low turbidity of the supernatantas was observed.

2. Around 80 mmol/100g minimum turbidity of supernatant was observed. This point probably corresponds to CEC of synthesized magadiite.

3. Above 120 mmol/100g the adsorption of surfactants is saturated. Most of the additional surfactants can be washed out with water. From TGA data (Tab.5.5) the amount of absorbed surfactant HTMA is on the scale of 85 mmol/100g.

In Sec.6.8 a model with a middle layer of surfactants is presented. Although it is based on experimental results for phosphonium surfactants it still gives a reasonable explanation of formation of the middle layer from the general process of adsorption of surfactants. The middle layer in the structure can occur even near electroneutrality or with only a small excess of surfactant. A few surface charges are uncompensated and the excess cationic headgroups form layers in the middle. This might be a balance between entropy and enthalpy.

From WAXS data the intercalation degree of organomagadiite could be defined via the basal spacing, which corresponds to the first order scattering peak d_{001}. The intercalation degree is calculated with Eqn.5.6. The intercalation degree of organomagadiite with excess loading of HTMA (200 mmol/100g) is 340% and for HTBP it is 280%.

The actual amount of adsorbed surfactant can be calculated with TGA data with the assumption that surfactant molecules are all burned out under very high temperature (900°C, air flow 30 ml/min). Such assumption was proved for organoclay prepared with HTBP as the calculated result is very close to that from interpretation of the ^{31}P MAS NMR spectrum. With TGA the amount of HTBP is found to be 60 mmol/100g and with ^{31}P MAS NMR it is found to be 62 mmol/100g. Thus for organomagadiite prepared with HTMA, the amount of adsorbed HTMA calculated from TGA as 85 mmol/100g should be reliable. The larger amount of adsorbed ammonium surfactant and larger intercalation degree compared to phosphonium surfactant could be due to the smaller head group of the ammonium surfactant which provides more space for adsorption. The other aspect is that interaction between

the ammonium surfactant and the magadiite surface is stronger than that between phosphonium surfactant and the magadiite surface due to the higher charge density of the ammonium head group.

6.3 Intercalation with polymers

With the melt method, polymers with different dielectric constants were choosen to test for intercalation with organomagadiite prepared with HTMA and HTBP. WAXS was used to characterize the intercalation degree. Tab.5.4 gives the results of intercalation expreiments. It was found that the dielectric constant is not a significant factor that governs intercalation. Although the polymers we have tried, PEO, PVDF, P4VP, PS, PEMA and PCL were all reported to have intercalation with some organoclay in solution or by in situ polymerization (32), with melt intercalation above the bulk glass transition temperature, the intercalation degree of hybrids (polymer/organomagadiite) are different. PCL was found to have intercalation with both HTMA and HTBP organomagadiite while PEMA was found to intercalate with HTMA organomagadiite only with a smaller intercalation degree than that of PCL nanocomposites. It seems that polymers with a carbonyl group in the *main chain* and a low glass transition temperature are easier to intercalate into organomagadiite. PEMA has a low glass transition temperature ($T_g = 66°C$) but the carbonyl group is on the side chain. It can intercalate with HTMA organomagadiite to a small degree, however it does not intercalate into HTBP organomagadiite.

PS was the first polymer used for the preparation of nanocomposites using the melt intercalation method with alkylammonium cation modified MMT (montmorillonite). (32). It was also used in our previous experiments with Somasif. PS intercalates into HTMA organoclay based on Somasif under the same melt conditions (160°C, 7 MPa) however it does not intercalate into HTBP organoclay based on Somasif. There is not a general rule to decide whether a polymer can intercalate into an organosilicate or not. However from results in this thesis, on melt intercalation into organomagadiite, presence of a carbonyl group and a low glass transition temperature appear to be important factors. The reason is most probably hydrogen bonding between the carbonyl group in the polymer chain and hydroxyl groups on the surface of magadiite. Although the surface of the silicate should be modified with a cationic surfactant to prevent phase separation between silicate and polymers, the properties of functional groups of the polymer and surface of the clay still play an important role in intercalation. If no such interaction exist there is no thermodynamic driving force for the intercalation, although it might still be possible to disperse the organosilicate in the polymer matrix under mechanical stress, thus producing metastable nanocomposites.

6.4 Results on dynamics of the ammonium surfactant layer

6.4.1 General information obtained from ^{2}H NMR and CW EPR

In our previous work, CW EPR was introduced to study the molecular motion of surfactant layers on a time scale of nanoseconds. Pulse EPR techniques (ENDOR, three-pulse ESEEM) were also applied to study hyperfine coupling between nitroxides of spin probes and a deuterated polymer. (6)–(7) The experiments were done with

Somasif, a synthetically modified natural layered silicate which contains paramagnetic ions that enhance relaxation of spin probes because of dipole-dipole coupling between nitroxides and paramagnetic metal species. Also most of the previous experiments were restricted to nanocomposites of an ammonium cation modified Somasif and PS, and microcomposites of a phosphonium organoclay and PS. For PS composites, T_{50G}, the glass transition temperature, is larger than T_{ODT}, the order-disorder transition temperature of the surfactant layer in the pure organoclay. With synthesized iron-free magadiite and PCL, the study could now be extended to nanocomposites whose T_{50G} is below T_{ODT} of pure organosilicate. The method could also be extended to nanocomposites with a phosphonium cation modified organosilicate. Moreover, with iron-free magadiite and site-specific deuterated surfactants ^{2}H solid echo NMR was applied for the first time to access different time scales of motion of the surfactant layers (in scale of tens to hundreds of microseconds).

With magadiite, both ^{2}H solid echo NMR and CW EPR give the same result that the molecular motion of surfactants is faster in PCL nanocomposites than that in organomagadiite and in PS microcomposites. With CW EPR this result is found both for ammonium and phosphonium surfactants. Also with ^{2}H solid echo NMR and CW EPR, it is found that for PS microcomposites, where PS does not intercalate into organomagadiite galleries, molecular motion of surfactant layers differs less from that in pure organomagadiite than for PCL nanocomposites. However the molecular motion in PS microcomposites is not exactly the same as that in organomagadiite but slower and the PS glass transition is clearly revealed in activation plots of the surfactant motion (^{2}H results from Tab.5.6, CW results from Tab.5.9 for HTMA and Tab.5.15). For PLC nanocomposites, the melting temperature of bulk PCL is revealed in Arrhenius plots of temperature-dependent CW EPR.

6.4.2 Discussion of results from ^{2}H NMR

With the site-specifically deuterated ammonium surfactants d9, dα, and dβHTMA (Tab.5.1), ^{2}H solid echo NMR can be applied to study molecular motion of surfactant layers and have a comparison between different sites in surfactant molecules. Motion of deuterons in the head group (d9) and in the alkyl chain (dα and dβ) is divided into four categories (Fig.5.9). The deuterons in d9HTMA could undergo rotation of methyl groups around C–N (motion 1, three-site jump motion), rotation of ammonium head group around N–C (in the alkyl chain) (motion 2, three-site jump motion), rotation of the alkyl chain around the symmetrical axes (motion 3, continuous diffusion motion) and wiggling of the alkyl chain with respect to the ammonium head group (motion 4, continuous diffusion motion).

The deutrons in dα and dβ can only undergo motion 3 and motion 4. Temperature-dependent ^{2}H NMR spectra show that at -80°C (193 K) motion of deuterons is rigid. Motion 1 and 2 are present at temperatures as low as -40°C (233 K) while motion 3 is present at 25°C (298 K) and motion 4 is slightly present at 80°C (353 K). Deuterons in d9HTMA reflect the three-site jump motion because the FWHH of ^{2}H NMR spectra (12.4 kHz) is about one nineth of that of dα and dβHTMA (115-123 kHz) indicating presence of motion 1 and 2 (each reduces quadrupole coupling by a factor of 3). Generally dynamics of deuterons differs little between organomagadiite and PS microcomposites. However for PCL nanocomposites, motion 3 and 4 dominates at lower temperature which is between -40°C and 25°C than that for organomagadiite and PS microcomposites (between 25°C and 80°C).

Although at room temperature surfactant layers are more mobile in PCL nanocomposites than that in organoclay and PS microposites (for d9, dα and dβCTAB), at low temperature of -40°C the line shape and FWHH differ little between organoclay, PCL and PS hybrid composites. The ^{2}H NMR spectra at -40°C (233 K) are shown in Fig.6.1.

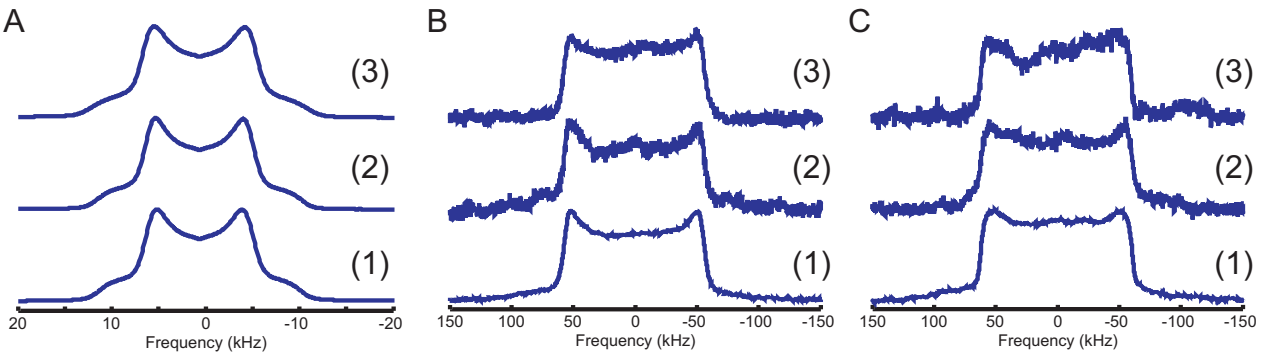

Figure 6.1: ^{2}H NMR spectra at -40°C (233 K) with (1) as organomagadiite, (2) as PS microcomposites and (3) as PCL nanocomposites. (A) d9HTMA series. (B) dαHTMA series. (C) dβHTMA series.

6.4.3 Discussion of results from CW EPR

With site-specific nitroxide spin probes 11-, 9- and 7-SL-HTMA (Tab.5.1), molecular motion of surfactants was characterized by temperature-dependent CW EPR from 300 K to 450 K. Apart from confirming the result of ^{2}H NMR that surfactant layers have more mobility in PCL nanocomposites than in organoclay and in PS hybrids, CW EPR also reveals the relationship between T_{50G}, the EPR glass transition temperature, and T_{ODT}, the order-disorder transition temperature. The rotational correlation time τ_c was derived from simulations and the activation energy E_a was calculated from Arrhenius plots.

Firstly from temperature dependent CW spectra, after cooling down from 450 K, the spectra at 300 K show that decomposition of ammonium surfactant spin probes is enhanced in PCL nanocomposites (Fig.5.11). In organomagadiite and PS hybrid the spin probes also exhibit decomposition, however the slow component can survive (except tail-labeled spin probe 11-SL-HTMA in PS nanocomposites).

From $2A'_{zz}$ plots (Fig.5.12) T_{50G} and T_{ODT} were obtained. For organomagadiite and PS microcomposites T_{50G} is very close to T_{ODT} because $2A'_{zz} = 50$ G is at the transition limit between the slow tumbling and the fast motion regime. For PCL nanocomposites, T_{ODT} of the hybrid is below T_{50G} because the fast component dominates the molecular motion. However T_{50G} of PCL nanocomposites is still higher than the T_g of the bulk polymer PCL ($T_g = -60$°C, (213 K)). Except for 11-SL-UTMA nanocomposites, which exhibit a slow component over the whole temperature range, T_{50G} is below the T_{ODT} of organomagadiite.

From analysis of the rotational correlation time τ_c, the mobility of surfactant layers in PCL nanocomposites and immobility in PS microcomposites are proved (Tab.5.9). Although PS does not intercalate into organomagadiite it influences dynamics of the surfactant layers. Generally with increasing temperature from 300 K to 450 K,

reorientation processes of surfactant layers in PS microcomposites and PCL nanocomposites can be divided into two regimes. The transition temperature between these two regimes for PS microcomposites is around the glass transition tempeature T_g of PS (373 K) (Tab.5.10). For PCL nanocomposites the transition temperature between these two regimes is around the melting tempeature T_m of PCL (333 K). This is a common property for both the HTMA and HTBP series and is more regular for the HTBP series without the except which exists in HTMA series (PCL nanocomposites with 11-SL-UTMA) (Fig.5.14. (A)).

For the organomagadiite HTMA series the reorientation process can also be divided into two regimes, which could be related to the decomposition process. For the HTBP series spin-labeled phosphonium spin probes in the organomagadiite are more stable and have one avtivation energy E_a in the reorientation process with increasing temperature.

6.5 Results of electron spin relaxation and spatial distribution of the ammonium surfactant layer

6.5.1 Results from ESEEM

Pulse EPR techniques (ESEEM, DEER and ENDOR) work much better on the systems based on synthetic iron-free magadiite than on earlier systems based on commercial layered silicates. ESEEM was applied to samples prepared from nitroxide spin probes and deuterated surfactants to measure spin-spin relaxation and hyperfine coupling between nitroxides and deuterons. DEER was applied to samples prepared with nitroxide spin probes to measure the dipole-dipole coupling. ENDOR was used for samples prepared from HTBP and nitroxide spin probes to measure hyperfine couplings between electrons and ^{31}P nuclei.

With two-pulse ESEEM, T_m, the phase memory time of the electron spin of nitroxides, which can be approximated as T_2 under the high field approximation, can be measured. Tab.5.11 shows that both polymer composites have a longer relaxation time than that of organoclay and T_m is the longest in PCL nanocomposites. Thus although PS chains do not intercalate into organomagadiite galleries, the PS matrix is again found to influence the behaviour of the surfactant layer. Remarkably, such an influence is still visible at a temperature of only 80 K where the ESEEM experiments were performed. The table also reveals that the tail-labeled 11-SL-UTMA spin probe has the shortest relaxation time and the close-to-middle labeled 7-SL-UTMA spin probe in PCL nanocomposites has the longest relaxation time. Together with results from ^{2}H NMR, the shortest T_m of the tail-labeled 11-SL-UTMA is expected because nitroxdes at end group is generally more mobile than that attached to the backbone.

By three-pulse ESEEM the relative strength of hyperfine coupling between electrons and deuterons can be measured. From Tab.5.12 generally d9HTMA has strongest echo modulation because it is rich in deuterons. It is noticed that both for PCL and PS hybrids the hyperfine coupling intensity is decreased, corresponding to a dilution of deuterium density. To study the dilution degree the relative intensity can be normalized by intensity of the corresponding organomagadiite. The normalized results are listed in Tab.6.1. In Tab.6.1 it should be noticed

that relative intensities of different organomagadiites are different. To relate the normalized values to the original values, the original values for the organomagadiites are listed in Tab.6.2.

sample	relative strength dαHTMA series	relative strength dβHTMA series	relative strength d9HTMA series
11-SL-UTMA	1	1	1
11-SL-UTMA+PCL	0.47	0.25	0.25
11-SL-UTMA+PS	0.50	0.36	0.35
9-SL-UTMA	1	1	1
9-SL-UTMA+PCL	0.35	0.39	0.30
9-SL-UTMA+PS	0.77	0.23	0.37
7-SL-UTMA	1	1	1
7-SL-UTMA+PCL	0.59	0.17	0.14
11a+dαCTAB+PS	0.36	0.73	0.33

Table 6.1: Relative strength of the deuterium echo modulation between electrons and deuterons normalized by the corresponding data for organomagadiite.

sample	relative strength dαHTMA series	relative strength dβHTMA series	relative strength d9HTMA series
11-SL-UTMA	0.747	0.931	2.802
9-SL-UTMA	0.653	0.863	3.00
7-SL-UTMA	0.648	0.679	3.019

Table 6.2: Original relative intensity of hyperfine coupling between electrons and deuterons of organomagadiite.

From Tab.6.1 there is not a general regularity of dilution effects of PCL and PS. The 11-SL-UTMA series with dβHTMA has similar dilution effects as the d9HTMA series.

6.5.2 Conclusion from DEER

By separating the dipole-dipole coupling from the echo decay, four-pulse DEER measures dipolar evolution data that can be converted to a radial distribution function within the 1 to 10 nanometer length scale. For organomagadiite and PLS systems, the original echo signal is very nicely fit by the assumption of a homogeneous distribution in two dimensions. There is no specific distance distribution between electron spins (Fig.3.26). However from DEER, nitroxide density (amounts of nitroxides per element area) and the dimensionality of the distribution can be derived from the dipolar evolution function (Eqn.3.128). Fig.5.17 and Tab.5.13 clearly show that spin probes are distributed homogeneously in two dimensions especially for the 9-SL-UTMA and 7-SL-UTMA series. PCL nanocomposites with 11-SL-UTMA have the largest dimensionality of 2.56 probably because nitroxides labeled at the tail have more freedom in PCL nanocomposites which has an enlarged distance between layers. It also shows that dilution effects of PCL and PS for spin probes are similar although they have a different mechanism as will be explained by ENDOR experiments.

6.6 States of ^{31}P nuclei of HTBP surfactants characterized with ^{31}P MAS NMR

With ^{31}P MAS NMR, two states of ^{31}P nuclei can be defined from their chemical shifts. They correspond to directly surface-attached headgroups at 30.3 ppm and surface-remote headgroups at 28.8 ppm. In the measurement it was found that a free evolution time d1 after the FID detection of 30 s was long enough for T_1 relaxation. During qualitative measurements d1 was set to 60 s and in quantatitive measurements, in which the sample was a mixture of organomagadiite and ADHP d1 was set to 1800 s. So results from quantative measurements are reliable as all excited ^{31}P can return to their equilibrium state within d1 = 1800 s. Integration of the signal thus gives true relative spin counts and such results were comparable with that from TGA (Sec.5.5.3.3).

Ethanol proved to have the capability to dissolve surfactants adsorbed in organoclay. If samples were washed several times with ethanol/water mixture (50/50 wt%) the EPR signal was very weak. By utilizing this property, the chemical shifts corresponding to directly attached and remote surfactants can be assigned. The sample prepared with an excess of HTBP was measured with ^{31}P NMR and then washed with ethanol/water mixture (50/50 wt%) overnight. Then this washed sample was measured again with ^{31}P NMR. By comparing the NMR spectra the surviving signal was assigned as the signal from surface-attached headgroups (30.3 ppm) and the weakened signal was assigned to surface-remote headgroups (28.8 ppm). This assignment is expected because larger chemical shifts in downfield correspond to phosphonium nuclei with stronger deshielding effects with electronegative groups (e.g. OH^- groups) on the magadiite surface. Remaining counter ions (Br^-) strongly bound near the surface could also contribute to such deshielding effects.

Temperature-dependent ^{31}P MAS NMR from 300 K to 400 K (Fig.5.18) reveals that with increasing temperature, both chemical shifts δ shift to downfield (more deshielding effects) and the difference between the two chemical shifts decreases. Above 380 K the ^{31}P nuclei in different states merge into one broadened peak. At high temperature when the surfactant is close to the melt state, reordering of the surfactant layers seems to result in stronger interaction between hydrophilic phosphonium head groups and the surface of magadiite.

6.7 Results on dynamics of the phosphonium surfactant layer

With site-specific nitroxide spin probes 11-, 9- and 7-UTBP (Tab.5.1), molecular motion of surfactants was characterized by temperature dependent CW EPR from 300 K to 450 K. Nitroxides attached to phosphonium surfactants are more stable than those attached to ammonium surfactants, especially in PCL nanocomposites. The spectrum at 300 K after heating at 450 K is a triplet nitroxide spectrum which is close to that at 300 K before heating (Fig.5.19). Also like in the HTMA series, HTBP surfactants have the fastest molecular motion in PCL nanocomposites among organomagadiite, PS and PCL composites.

For organomagadiite and PS microcomposites, T_{50G} is also very close to T_{ODT} just like in the ammonium (HTMA) series. For PCL nanocomposites $T_{ODT} \leq T_{50G}$. Compared with T_{ODT} of ammonium samples listed in Tab.5.8, it is found that organomagadiite prepared from HTBP has a higher T_{ODT} than that prepared from

HTMA. However the T_{ODT} of PCL nanocomposites are very close for 9-SL-UTMA and 9-SL-UTBP as well as for 7-SL-UTMA and 7-SL-UTBP. The tail-labeled ammonium spin probe 11-SL-UTMA is an exception because it has a slow component in PCL nanocomposites. For PS microcomposites the immobilization effect which results in an increase of T_{50G} is similar for 11-, 9- and 7-SL-UTBP.

By analyzing rotational correlation times τ_c which were derived from spectrum fits, the same result as that from the HTMA series can be obtained: the molecular motion is the fastest in PCL and is the slowest in PS composites in the series. Compared with τ_c of the HTMA series, the immobilization effect of PS is stronger in the phosphonium surfactant sample than in the ammonium surfactant sample, however the mobilization effects of PCL for both surfactants are similar (Tab.5.9 and Tab5.15). The activation energy E_a can also be calculated from Arrhenius plots after τ_c is obtained. Compared with samples with ammonium surfactants, generally E_a of the reorientation process of phosphonium surfactant layers is positive. The apparent negative activation energies in HTMA series (organomagadiite prepared from HTMA, Fig.5.14) can thus be traced back to the decomposition of ammonium surfactants at high temperatures. The behaviour of the reorientation process of HTBP surfactants in PCL and PS composites with increasing temperature is similar to that of HTMA surfactants, which consists of two regimes and the transitition temperatures can be identified with T_g of PS and T_m of PCL respectively.

6.8 Spatial information obtained from ENDOR

Before ENDOR experiments, the stimulated echo experiments were performed to have optimum time of interpulse time τ (Sec.3.5.1). From stimulated echo experiments approximate transverse relaxation times T_2 were obtained. As with the T_m measured by two-pulse ESEEM for the HTMA series, both PCL and PS increase T_2 and PCL T_2 increases to a larger degree. Usually stimulated echo experiments measure a longer apparent relaxation time than two-pulse ESEEM experiment for the same sample. However T_2 measured by the stimulated echo is shorter for the phosphonium spin probe than T_m measured from two-pulse ESEEM for the ammonium spin probe (with similar chemical structure) even though the temperature of 50 K for the stimulate echo experiments is lower than that of 80 K for two-pulse ESEEM. Probably the ammonium surfactant has a longer relaxation time because of stronger interactions between the ammonium head group and the silicate surface.

In contrast to failed earlier attempts with Somasif organosilicates, ENDOR works well to characterize PLS systems with iron free magadiite. The hyperfine coupling can be measured with a very good signal/noise ratio (Fig.3.24). The spectra simulated with a planar distribution model (Fig.3.23) and a bimodal distance distribution (dotted line in Fig.3.24. (D)) fit the experimental spectra well. Thus distance distributions between electrons and ^{31}P nuclei can be obtained. Details of these distance distributions are given in Tab.5.18 and Fig.5.23. With the planar model, ENDOR can access distances as small as 0.35 nm and as large as 1.0 nm.

Simplified model of a single surfactant layer is presented in Fig.5.25 in which the intramolecular contribution to r_1 is negligible and surfactant molecules lie flat on the surface of magadiite. To explain the distance distribution between electrons and ^{31}P nuclei, based on the single layer model, a model with a *middle layer* is presented in Fig.6.2 and the results from ENDOR are relisted in Tab.5.18. The model explains the results taking into account

the HTBP chain length (about 1 nm), the width of the silicate galleries derived from bascal spacing measured by WAXS and the ENDOR distances.

Sample	r_1 (nm)	r_1 fraction	r_2 (nm)	r_2 fraction
11-SL-UTBP	0.38	0.272	0.69	0.728
11-SL-UTBP+PS	0.46	0.213	0.71	0.787
11-SL-UTBP+PCL	0.36	0.466	0.71	0.534
9-SL-UTBP	0.40	0.329	0.69	0.671
9-SL-UTBP+PS	0.45	0.148	0.70	0.852
9-SL-UTBP+PCL	0.39	0.400	0.84	0.600
7-SL-UTBP	0.40	0.357	0.71	0.643
7-SL-UTBP+PS	0.48	0.358	0.75	0.642
7-SL-UTBP+PCL	0.39	0.381	0.88	0.619

Table 6.3: Mean distances r_1 and r_2 of the peaks in bimodal fitting of the ENFOR spectra and corresponding freactions of the two peaks.

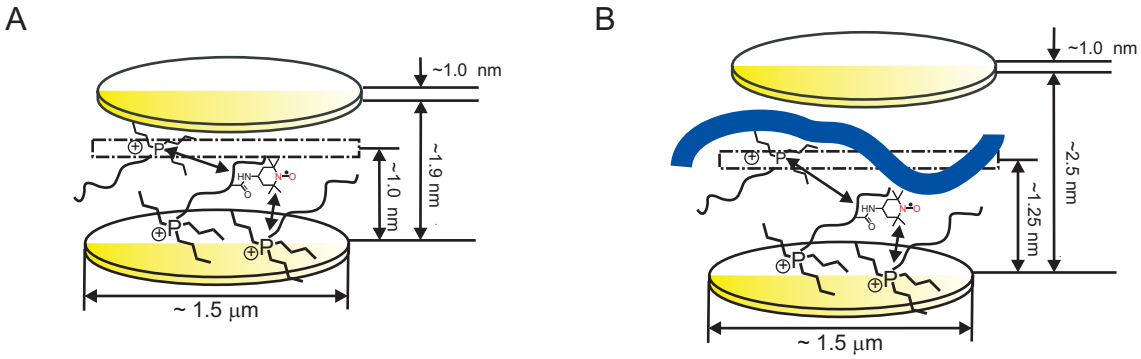

Figure 6.2: Model of intercalation of the phosphonium surfactant HTBP in organomagadiite and in PCL nanocomposites from ENDOR measurements. The dashed line represents a middle layer of HTBP surfactants. The basal spacing is from WAXS measurements. (A) organomagadiite. (B) PCL nanocomposites.

In the model presented in Fig.6.2, r_1 describes the interaction between nitroxides and ^{31}P neighbouring the spin probe *in* the same layer because r_1 is a small length contribution. The longer length contribution r_2 is due to the interaction between the nitroxide and ^{31}P in the *middle layer*. This layer must be in the middle because if it was attached to the surface of the next magadiite platelet the distance should be longer ($1.9 - 0.4 = 1.5$ nm). With this layer located in the middle of the gallery, the distance distributions and their trends on intercalation of PCL are in agreement in this model. The sum of r_1 and r_2 (about 1.0 nm) is approximated to the half of the width of the gallery. The model also fits the data of PCL nanocomposites from 9- and 7-SL-UTBP ($r_1 + r_2 \approx 1.25$ nm) with their enlarged gallery between the magadiite platelets. For 11-SL-UTBP PCL nanocomposites r_2 is a little bit smaller, which could be due to a closer distance between nitroxides labeled at the tail and the middle layer.

For PS microcomposites, the r_2 distribution differs little from that of organomagadiite because the distance between layers of organomagadiite does not change as PS chains do not intercalate into layers. However, the r_1

distribution increases indicating a longer distance between nitroxides and neighbouring ^{31}P nuclei in the same layer. This is reasonable as three-pulse ESEEM also indicates that the labels are more remote from the surfactant headgroups in PS microcomposites than in organomagadiite and DEER indicates that the nitroxide labels distribute over a larger amount of space. The mechanism could be that in PS microcomposites surfactants are more stretched due to the pressure that the PS matrix exerts on the organomagadiite stacks. Thus although both PCL and PS have dilution effects the mechanisms are different. For the PCL nanocomposites, the dilution of nitroxide density is reflected by enlargment of r_2 while for the PS microcomposites the dilution effects is reflected by enlargement of r_1 (Fig.5.24). Although this result is derived from results for the phosphonium surfactant HTBP series, the results from ESEEM and DEER shows that this conclusion can probably be applied to ammonium surfactant HTMA series as well.

The dilution effects in PS microcomposites are illustrated in Fig.6.3. The pressure exerted on silicate layers is due to the thermal expansion property of PS during the preparation of the microcomposites in press. PCL should also have thermal expansion effects however intercalation effects dominate in the PCL nanocomposites.

As illustrated in Fig.6.3, PS matrix exerts pressure on the stack of organomagadiite resulting in reordering the surfactant layers. The middle layer still exists after the pressing.

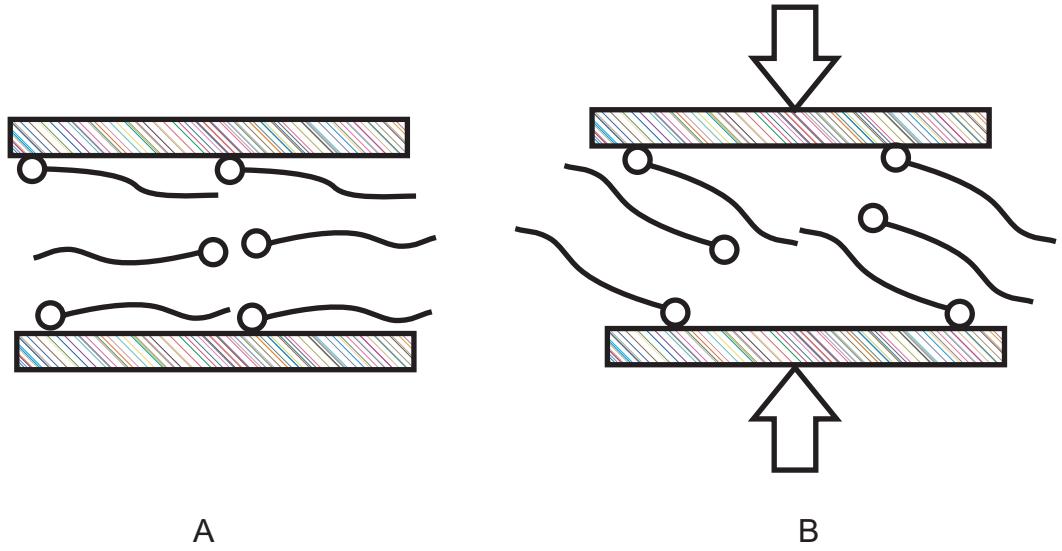

Figure 6.3: Illustration of dilution effects in PS microcomposites. (A) Surfactant molecules lie flat on the surface of silicate (from the conclusion about the r_1 distance. The existance of the middle layer is from the conclusion of the r_2 distance. (B) Due to thermal expansion of PS, which is the tendency to increase in pressure when heated during the preparation of the PS microcomposites in press, PS matrix exerts pressure on the stack of organomagadiite resulting in reordering the surfactant layers.

Chapter 7

Conclusion

Structually well defined magadiite can be synthesized by a hydrothermal method (yield: 61%). With a fixed composition (amorphous silica : NaOH : H_2O = 3 : 1 : 200 in molar ratio) and autogeneous pressure in the autoclave, the annealing temperature is more critical than the annealing time. The product can be characterized with WAXS and SEM and the optimum parameters of synthesis were found (140°, 62 hours or 150-155°, 48 hours). The intercalation degree of the surfactant to prepare organoclay was characterized with WAXS via the bascal spacing between layers. Titration was used to determine the rough range of the CEC to be around 80 mmol/100g. The exact amount of absorbed surfactants, HTMA and HTBP, was found by TGA. The TGA result for HTBP organoclay was compared with the result from quantitative ^{31}P MAS NMR measurement and was found to be in good agreement. From TGA the amount of absorbed HTMA in organoclay, which was prepared with an excess of surfactant of 200 mmol/100g, was about 85 mmol/100g. For HTBP organoclay the amount of HTBP is about 60 mmol/100g. Moreover, for HTBP organoclay, ^{31}P MAS NMR was used to characterize the states of ^{31}P nuclei in surfactant layers. It turns out that there are two different states of ^{31}P corresponding to directly surface-attached and surface-remote ^{31}P nuclei with different chemical shifts. Temperature-dependent ^{31}P NMR revealed that with increasing temperature, ^{31}P nuclei shift to a more deshielding regime and the different layers merge into a single layer.

Different polymers were tested for melt intercalation into magadiite and organomagadiite using WAXS and SAXS characterization. It was found that the dielectric constant of the polymer is not a significant parameter influencing intercalation. A carbonyl group in the main chain and a low glass transition temperature improves the degree of intercalation into organomagadiite. PCL was found to intercalate with both HTMA and HTBP surfactants. WAXS shows that HTMA organomagadiite has a higher intercalation degree with PCL than HTBP organomagadiite, probably because of the smaller head group and thus a better accessibility of surface hydroxyl groups for hydrogen bonding with the carbonyl groups of PCL. SAXS clearly indicates the intercalation of polymers into organoclay.

With site-specific deuterated ammonium surfactants, ^{2}H solid echo NMR was used to study molecular motion of deuterons in surfactant layers. At room temperature surfactants are more mobile in PCL nanocomposites than

those in PS microcomposites and organomagadiite. The motion of deuterons is located in the intermediate to show exchange region by measuring FWHH of ^{2}H NMR lineshape (in a few tens to hundreds microseconds scale).

The deuterons in d9HTMA could undergo rotation of methyl groups around C–N (motion 1, three-site jump motion), rotation of ammonium head group around N–C (in the alkyl chain) (motion 2, three-site jump motion), rotation of the alkyl chain around the symmetrical axes (motion 3, continuous diffusion motion) and wiggling of the alkyl chain with respect to the ammonium head group (motion 4, continuous diffusion motion).

The deuterons in α and β position can only undergo motion 3 and motion 4. Temperature-dependent ^{2}H NMR spectra show that at -80°C (193 K) deuterons are rigid. Motion 1 and 2 are present at a temperature as low as -40°C (233 K) while motion 3 is present at 25°C (298 K) and motion 4 is slightly present at 80°C (353 K). Deuterons in d9HTMA reflect the three-site jump motion because the FWHH of ^{2}H NMR spectra (12.4 kHz) is about one nineth of that of dα and dβHTMA (115-123 kHz) indicating presence of motion 1 and 2 (each reduces quadrupole coupling by a factor of 3). Generally dynamics of deuterons differs little between organomagadiite and PS microcomposites. However for PCL nanocomposites, motion 3 and 4 dominates at lower temperature which is between -40°C and 25°C than that for organomagadiite and PS microcomposites (between 25°C and 80°C).

At a temperature as low as -40°C, the accelerating effect on surfactant layers in PCL nanocomposites is not observed. This indicates that at low temperature below -40°C surfactant molecules are rigid and in pulse EPR experiments dynamic aspects of surfactants can be excluded.

With site-specific nitroxide ammonium and phosphonium spin probes, temperature-dependent CW EPR was applied to obtain further information on molecular motion in the surfactant layers. Compared to previous work on PLS systems with Somasif and PS, in which T_{50G} of the polymer is larger than T_{ODT} of the surfactants in pure organomagadiite, with iron-free magadiite and PCL the work could be extended to nanocomposites where T_g of the polymer is below T_{ODT} of the pure organomagadiite. Coinciding with results from ^{2}H NMR, surfactant layers in such nanocomposites are found to have faster motion than in microcomposites with PS and pure organomagadiite for both the HTMA and HTBP series.

By spectral fitting, rotational correlation times τ_c and then activation energies E_a were derived from Arrhenius plots. In general E_a of the reorientation of surfactants is on the order of a few $kJ\,mol^{-1}$, less than that of bulk polymers which is on the order of tens of $kJ\,mol^{-1}$ (28), indicating a smaller energy barrier of the reorientation of surfactants than that of bulk polymers. HTBP organoclay and PS hybrids have longer τ_c than the HTMA series meaning that HTMA is more mobile than HTBP in organoclay and PS hybrids. However in PCL nanocomposites τ_c of the HTBP series are very close to those of the HTMA series.

Plots of E_a as a function of temperature reveal different processes in the reorientation of surfactant molecules with increasing temperature. Generally with increasing temperature from 300 K to 450 K, the reorientation process of surfactant layers in PS microcomposites and PCL nanocomposites can be divided into two regimes. The transition temperature between these two regimes for PS microcomposites is around the glass transition tempeature T_g of PS (373 K) (Tab.5.10). For PCL nanocomposites the transition temperature between these two regimes is around the melting tempeature T_m of PCL (333 K). This is a common property for both the HTMA and HTBP series. For organomagadiite, an apparent negative E_a in the HTMA series at high temperature can be

related to decomposition while for the HTBP series the phosphonium spin probes are more stable and no negative E_a is observed.

Pulse EPR techniques such as two-pulse ESEEM, three-pulse ESEEM were applied to samples prepared from both site-specific nitroxide spin probes and site-specific deuterated surfactants to study relaxation of ammonium spin probes and the hyperfine coupling between electrons and deuterons. Transverse relaxation times derived from two-pulse ESEEM indicate that both PS and PCL slow down motion of nitroxide spin probes at very low temperature. In PCL nanocomposites the relaxation of nitroxides is the slowest. This result is consistent with that from stimulated echo experiments for the HTBP series. It indicates that in absence of large-scale motion at such a low temperature as 80 K, spin-spin relaxation is delayed by intercalated PCL polymer chains. PS, although it does not intercalate into organomagadiite, still has influence on the surfactant layers. This is proved by three-pulse ESEEM and DEER. Three-pulse ESEEM indicates that both PCL and PS leads to an increase of the mean distance between nitroxide labels in 11-, 9-, and 7- position on the alkyl chains and the deuterated trimethyl ammonium head groups. DEER shows that both polymers dilute nitroxide density to a similar degree. With DEER the dimensionality of the spin probe distribution can be obtained and it turns out that surfactants are distributed homogeneously in both organomagadiite and polymer composites. The two-dimensional model fits the DEER signal well and no preferable electron-electron distance can be derived.

With iron-free magadiite, ENDOR can be applied successfully to a PLS system for the first time to study hyperfine couplings between electrons and ^{31}P nuclei and gives distance distributions between them with the planar model. Two peaks were found in the distance distribution at distances r_1 and r_2 in the scale between 0.4 nm and 1 nm. A model with a middle layer of surfactants between the surface-attached layers explains these distance distributions. In this model r_1 corresponds to intermolecular contributions in the same layer and r_2 is due to the middle layer contribution.

For the first time molecular motion of the surfactant layers was studied by both ^{2}H NMR and CW EPR and information on relaxation and spatial structure was obtained by pulse EPR. Comprehensive information from these techniques can nicely complement information from conventional characterization techniques such XRD and TEM and provide a much more detailed picture of structure and dynamics of the surfactant layer in polymer-layered silicate nanocomposites.

Bibliography

[1] A. Blumstein, *J. Polym. Sci. A.*, **1965**, 3, 2665-2672.

[2] A. Okada, M. Kawasumi, A. Usuki, Y. Kojima, T. Kurauchi, O. Kamigaito; (Eds.:) D. W. Schaefer, J. E. Mark, *Polymer based molecular composites. MRS Symposium Proceedings, Pittsburgh*, **1990**, 171, 45-50.

[3] S. S. Ray, M. Okamoto, *Polym. Sci.*, **2003**, 28, 1539-1641.

[4] A. Okada, Y. Fukushima, S. Inagaki, A. Usuki, S. Sugiyama, T. Kurashi, O. Kamigaitov *U.S. patent 4,739,007*, **1988**, invs.

[5] A. Okada, Y. Kojima, M. Kawasumi, Y. Fukushima, T. Kurauchi, O. Kamigaito, *J. Mater.*, **1993**, 8, 1179

[6] G. Panek, S. Schleidt, Q. Mao, M. Wolkenhauer, H. W. Spiess, G. Jeschke, *Macromolecules*, **2006**, 39, 2191-2200

[7] S. Schleidt, H. W. Spiess, G. Jeschke, *Colloid Polym. Sci.*, **2006**, 284, 1211-1219

[8] K. Beneke, G. Lagaly, *American Mineralogist*, **1977**, 62, 763-771

[9] K. Beneke, G. Lagaly, *American Mineralogist*, **1983**, 68, 818–826

[10] O-Y. Kwon, S-Y. Jeong, J-K. Suh, J-M. Lee, *Bull. Korean Chem. Soc.*, **1995**, 16(8), 737-741

[11] H. Annehed, L. Flth, F. J. Lincoln, *Z. Kristallogr*, **1982**, 159, 203

[12] R. A. Fletcher, D. M. Bibby *Clays and Minerals*, **1987**, 35(4), 318-320

[13] Y. Kim, J. L. White, *Journal of Applied Polymer Science*, **2004**, 92, 1067–1071

[14] H. W. Spiess, *Advanced in Polymer Science*, **1985**, 66, 23–55

[15] C. A. Fyfe, *Solid State NMR for Chemists*, C.F.C. Press **1983**

[16] S. Vandoorslaer, G. Jeschke, *Fluxional Organometallic and Coordination Compounds*, Wiley & Sons Ltd. **2004**

[17] T. Sako, Y. Arai, Y. Takebayashi, *Supercritical Fluids*, Springer **2002**, P. 331

[18] J. Uillaneva-Garibay, K. Mueller, *Lecture. Notes Phys.*, **2006**, 684, 65-86

[19] M. Zanetti, S. Lomakin, G. Camino, *Macromol.Mater.Eng.*, **2000**, 279, 1-9

[20] P. Atkins, J. de Paula, *Physical Chemistry*, Oxford **2002**, P. 583

[21] D. F. Shriver, P. W. Atkins, *Inorganic Chemistry*, Oxford **2002**, p. 366

[22] P. Atkins, R. Friedman, *Molecular Quantum Mechanics,* Oxford **2005**, p. 209

[23] A. Schweiger, G. Jeschke, *Principles of pulse electron paramagnetic resonance*, Oxford. **2001**, 26.

[24] P. Zaeker, G. Jeschke, *The Journal of Chemical Physics* **2005**, 122, 024515

[25] G. Jeschke, A. Koch, U. Jonas, A, Godt, *Journal of Magnetic Resonance* **2002**, 155, 72-82.

[26] G. Jeschke, *DeerAnalysis 2006 User's Manual* **2006**

[27] A. D. Milov, Y. D. Tsvetkov, *Appl. Magn. Reson.* **1997**, 12, 495.

[28] G. G. Cameron, *Pure Appl. Chem.*, **2006**, 54, 483-492

[29] J. A. S. Smith, *Chem. Soc. Rev.*, **1986**, 15, 225–260

[30] G. Jeschke, S. Schlick, *Advanced ESR Methods in Polymer Research (Ed. S. Schlick)*, Wiley-Interscience, Hoboken, **2006**

[31] S. Hayashi, K. B. Hayamizu, *Chem. Soc. Jpn.*, **1989**, 62, 2429-2430

[32] S. S. Ray, M. Okamoto, *Prog. Polym. Sci.*, **2003**, 28, 2429

[33] M. Zanetti, S. Lomakin, G. Camino, *Macromol. Mater. Eng.*, **2000**, 279, 1-9

[34] J-H. Yang, Y-S. Han, J-H. Choy, H. Tatyama, *Journal of Materials Chemistry*, **2001**, 11, 1305-1312

[35] R. A. Vaia, R. K. Teukolsky, E. P. Giannelis, *Chem Mater*, **1994**, 6, 1017-1022

[36] O. Becker, R. Varley, G. Simon, *Polymer*, **2002**, 43, 4365-4373

[37] D. L. VanderHart, A. Asano, J. W. Gilman, *Macromolecules*, **2001**, 34, 3819-3822

[38] X. Zhao, K. Urano, S. Ogasawars, *Colloid Polym. Sci.*, **1989**,267, 899-906

[39] G. Jimenez, N. Ogata, H. Kawai, T. Ogihara, *J. Appl. Polym. Sci.*, **1997**, 64, 2211-2220

[40] N. Ogata, G. Jimenez, H. Kawai, T. Ogihara, *J. Polym. Sci. part B: Polymer Physics*, **1997**, 35, 389-396

[41] A. Morgan, J. Harris, *Polymer*, **2003**, 44, 2113-2120

[42] D. K. Yang, D. B. Zax, *J. Chem. Phys.*, **1991**, 110, 5325-5336

[43] S. K. Sahoo, D. W. Kim, J. Kumar, A. Blumstein, A. L. Cholli, *Macromolecules*, **2003**, 36, 2777-2784

[44] J. S. Beck, J. C. Vartuli, *J. Am. Chem. Soc.*, **1992**, 114, 10834-10843

[45] J. S. Vartuli, C. T. Kresge, M. E. Leonowicz, A. S. Chu, S. B. McCullen, I. D. Johnson, E. W. Sheppard, *Chem. Mater.*, **1994**, 6, 2070-2077

[46] A. Firouzi, D. Kumar, L. M. Bull, *Science*, **1995**, 267, 1138-1143

[47] G. G. Almond, R. K. Harris, K. R. Franklin, *J. Mater. Chem*, **1997**, 7(4), 681-687

[48] S. Stoll, A. Schweiger, *J. Magn. Reson.*, **2006**, 178(1), 42-55

[49] F. Kooli, L. Mianhui, S. F. Alshahateet, F. Chen, Z. Yinghuai, *Journal of Physics and Chemistry of Solids*, **2006**, 67, 926-931

[50] S. Peng, Q. Gao, Z. Du, J. Shi, *Applied Chy Science*, **2006**, 31, 229-237.